Gdańsk University of Technology
Faculty of Civil and Environmental Engineering

mgr inż. Jan Suchorzewski

Badanie efektu skali w betonie na poziomie kruszywa - badania doświadczalne i wyniki obliczeń metodą elementów dyskretnych

Investigations of size effect in concrete at aggregate level - experiments and calculations results using discrete element method

Doctoral thesis

Supervisor: prof. dr hab. inż. Jacek Tejchman

Gdańsk 2019

Contents

Summary

Size effect is a fundamental phenomenon in concrete. It is characterised by decreasing strength and increasing brittleness of concrete with increasing size. The thesis includes experimental and theoretical elements. The main goal of the thesis were investigations of a size effect at the aggregate level by taking fracture into account with the discrete element method (DEM) for various failure modes. Comprehensive experiments on a size effect were carried out for a tensile splitting test. In experiments, the micro-computed tomography (micro-CT) and digital image correlation (DIC) technique were used. The concrete was simulated as a four-phase material composed of aggregate, cement matrix, macro-pores and interfacial transition zones (ITZs) between the aggregate and cement matrix. DEM for concrete was calibrated with the aid of simple uniaxial tests of uniaxial compression and uniaxial tension. In numerical calculations with the real internal concrete structure, the distribution and evolution of inter-particle contacts, inter-particle forces, force chains, rotations, broken contacts and energies was analyzed (depending on the specimen size) for various failure mechanisms: quasi-brittle, brittle and very brittle (snap-back). Experimental results were directly compared with experiments. Good agreement was achieved. In addition, comprehensive size effect experiments on reinforced concrete beams under bending without and with stirrups were carried out that were scaled along the height or length.

Streszczenie po polsku

Efekt skali jest fundamentalnym zjawiskiem w betonie. Charakteryzuje się spadkiem nośności i wzrostem kruchości betonu wraz ze wzrostem wielkości elementów. Rozprawa doktorska zawiera elementy doświadczalne i teoretyczne. Głównym celem pracy doktorskiej było zbadanie efektu skali w betonie na poziomie kruszywa z uwzględnieniem jego pękania przy zastosowaniu metody elementów dyskretnych (DEM) dla różnych mechanizmów zniszczenia. Wykonano obszerne badania doświadczalne efektu skali podczas testu rozłupywania betonu. W badaniach została wykorzystana mikro-tomografia komputerowa (micro-CT) oraz technika korelacji obrazów cyfrowych (DIC). Beton został modelowany na poziomie mezoskopowym jako materiał złożony z czterech faz: kruszywa, zaprawy cementowej, makro-porów i stref przejściowych między kruszywem i zaprawą. Metoda elementów dyskretnych została skalibrowana dla betonu na podstawie prostych testów doświadczalnych jednoosiowego ściskania i jednoosiowego rozciągania. W obliczeniach numerycznych z rzeczywistą wewnętrzną strukturą betonu został wyznaczony rozkład i rozwój kontaktów, sił między-kontaktowych, łańcuchów sił, obrotów, pękniętych kontaktów oraz energii dla 3 różnych mechanizmów zniszczenia (zależnych od wielkości badanego

elementu): quasi-kruchego, kruchego i b. kruchego (snap-back). Wyniki badań doświadczalnych zostały bezpośrednio porównane z wynikami obliczeń DEM. Uzyskano dobra zgodność wyników między doświadczeniami a symulacjami. Dodatkowo wykonano obszerne doświadczenia nad efektem skali ze zginanymi żelbetowymi belkami bez i ze strzemionami, które były skalowane wzdłuż wysokości lub długości.

List of Figures

List of Tables

Chapter 1

Introduction

1.1 Phenomenon and problem

The size effect is a fundamental phenomenon in concrete materials. It denotes that both the: 1) nominal structural strength (corresponding to the maximum load value reached in the loading process) and 2) material ductility (ratio between the energy consumed during the loading process before and after the load-deflection peak) always decrease with increasing element size. These two deformation process parameters are of major importance for the assessment of the element safety and its interaction with adjacent structural elements. Concrete elements exhibit a transition from the snap-through response in the post-critical phase for small size elements to the snap-back response (a catastrophic drop in strength related to a positive slope in a load-deflection softening branch) for large size elements. Usually the size effect has been specified for geometrically similar elements, differing only by the value of the size factor. The physical understanding of size effects is of major importance for civil engineers who try to extrapolate experimental outcomes at laboratory scale to actual structures of practical size range. Since large structures are strongly beyond the range of testing in laboratories, their design has to rely on a realistic extrapolation of testing results with smaller element sizes

Two mechanical size effects are of major importance in concrete under loading: energetic (or deterministic) and statistical (or stochastic) one. The deterministic size effect is caused by the formation of a region of intense strain localization with a certain volume (micro-crack region – called also fracture process zone (FPZ)) that always precedes discrete macro-cracks. The strain localization zone size is not negligible relative to the cross-section dimensions and is large enough to cause significant stress redistribution in the structure, related to energy absorption in localization failure zones and energy release in remaining unloading regions. The energy absorption in localized failure zones is similar but the energy release grows with increasing element size (both normalized by the specimen size) that causes the decrease of nominal strength for larger elements. Thus the nominal structural strength, which is sensitive to the ratio between the size of strain localization zones and the specimen size, cannot be appropriately estimated in laboratory tests since it is different for various specimen sizes (the size of localized zones cannot be experimentally scaled). A statistical (stochastic) effect is caused by the spatial variability/randomness of the local material strength and occurs in concrete structures of a positive geometry. The larger size of the concrete member is, the more weak elements occur. For structures of a practical size, the size effect follows

neither the plastic limit load theory nor linear elastic fracture mechanics. The deterministic size effect is important for moderate size structures. The Weibull statistical size effect is usually smaller and significantly increases as an asymptotic limit for very large size structures. In spite of the ample experimental evidence, the physically based size effect is not taken into account in practical design rules of engineering structures, assuring a specified safety factor with respect to the failure load. Instead, a purely empirical approach is sometimes considered in building codes which is doomed to yield an incorrect formula since physical foundations are lacking. The understanding of a size effect is of major importance to ensure the safety of the structure and to optimize the material behaviour.

Fracture (that is responsible for a deterministic size effect) is a very complex phenomenon, consisting of main macro-cracks with various branches, secondary macro-cracks and micro-cracks. During fracture, micro-cracks first arise in a hardening region on the stress–strain curve which change gradually during material softening into dominant distinct macroscopic cracks up to damage. The fracture process strongly depends upon a heterogeneous structure of materials over many different length scales, changing e.g. in concrete from the few nanometres (hydrated cement) to the millimetres (aggregate particles). In order to properly describe fracture/size effect in detail, the material meso-structure has to be taken into account since it affects in a pronounced way the global results with respect to both the strength and brittleness/ductility.

Commonly, the deterministic size effect investigations in concrete have been performed at the macro-level by using different enhanced constitutive models for concrete, equipped with a characteristic material length (e.g. integral-type non-local models), crack band and cohesive crack approaches. Note that in contrast to DEM, continuum mechanics solutions do not consider cracking from the beginning of deformation, the damage rules have usually a priori assumed sigmoid shape and they are switched on in the softening regime only. Moreover, the heterogeneity of material properties (like stiffness, strength, fracture energy) is reflected in a homogenized sense only. The only link to the meso-structure is the presence of a characteristic length in enhanced continuum laws with softening. The characteristic length is usually chosen as a too large value as compared to experimental results (to speed up the calculations). The realistic curved cracks cannot be obtained without taking the material meso-structure into account.

1.2 Aims

The main objective of the thesis is the description of a size effect in concrete based on experimental and theoretical investigations, by taking different failure modes into account. Two types of

laboratory experiments were performed to study a size effect and related failure modes. The tests were carried out with: a) concrete cylinders of five different diameters that were subjected to splitting tension and b) 33 non-geometrically similar reinforced concrete beams under bending with and without stirrups that varied along the length or height and Theoretically, the size effect was investigated at the meso-scale level using the discrete element method (DEM) by taking the real concrete meso-structure into account. In meso-scale calculations of concrete during uniaxial compression, uniaxial tension, and splitting tension was considered as a 4-phase material conmposed of aggregate, cement matrix, macro-voids and interfacial transition zones (ITZs) between the aggregate and cement matrix. The assumed meso-structure was based on x-ray μCT scans of real concrete specimens. The 2D and 3D DEM calculations were carried out. The different meso-structural events at the aggregate level were studied in detail in the context of a size effect. The numerical results of the size effect in splitting were directly compared with the coresponding experimental outcomes.

1.3 Thesis structure

The thesis consists of 6 Chapters and 2 Appendices. Chapter 1 introduces the phenomenon, problems and aims. In Chapter 2, an overview of the literature concerning a size effect is presented. The experimental studies on the size effect during tensile splitting tests (using the x-ray micro-tomography, scanning electron microscope and digital image correlation (DIC) technique) are described in Chapter 3. Chapter 4 includes the basic formulations of the discrete element method (DEM) for concretes. Chapter 5 presents results of DEM simulations of experimental laboratory tests concerning uniaxial compression, uniaxial tension and splitting tension. In Chapter 6, the most important conclusions and future research directions are offered. The results of experimental tests on the size effect in large reinforced concrete beams (with and without stirrups) are described in two Appendices.

1.4 Innovative elements

The innovative elements of the doctoral thesis are:

1) Application of the discrete element method to concrete with the real internal structure, based on 3D x-ray μCT images using the very advanced micro-tomography system Skyscan 1173. Concrete iwas decsribed as a 4-phase material composed of aggregate, cement matrix, interfacial transitional zones (ITZs) and macro-voids.

2) Investigations of different meso-structural phenomena at the aggregate level in the context of the size effect for different failure modes.

3) Meso-scale analyses of all energy components at a different stress-displacement stage with the dissipated and released portions, referred to the fracture process zone and the remaining unloading specimen region during quasi-brittle and very brittle failure.

4) Comphensive laboratory size effect tests on concrete under splitting tension with different specimen diameters, boundaries conditions at loading/supporting regions and failure modes.

5) Comprehensive aboratory experiments on a size effect in large reinforced concrete (RC) beams (33 beams) under bending that were scaled along the height or length (with and without stirrups).

The experimental and theoretical results described in the thesis were already published in four JCR journals from 'Web of Science': 'Engineering Structures' (2018), 'International Journal of Damage Mechanics' (2018), 'Theoretical and Applied Mechanics' (2018) and 'Granular Matter' (2018). The fifth paper is now under review ('Engineering Structures' (2019)).

The research works were carried out within the project "*Experimental and numerical analysis of coupled deterministic-statistical size effect in brittle materials*" (years 2015-2017) financed by the Polish National Science Centre NCN (UMO-2013/09/B/ST8/03598).

Chapter 2

State of Art

Size effect laws

First empirical observations of a size effect were made by Galileo Galilei based on a study of animal bones. Galileo observed that bones of larger species were relatively weaker than the smaller ones. Weibull (1939) formulated a statistical size effect theory, called the weakest-link theory that postulated that the structure was as strong as its weakest point, i.e. structure failed when the lowest local strength was exceeded. The material's strength decreased for very large elements with respect to a statistical law by Weibull (1939) with an asymptote calculated within linear elastic fracture mechanics (LEFM)

$$f(\sigma)=\begin{cases}\dfrac{m}{\sigma_0}\left(\dfrac{\sigma}{\sigma_0}\right)^{m-1}\exp\left(-\left(\dfrac{\sigma}{\sigma_0}\right)^{m}\right) & \sigma\geq 0\\ 0 & \sigma<0\end{cases}, \tag{1}$$

$$F(\sigma)=1-\exp\left(-\left(\frac{\sigma}{\sigma_0}\right)^{m}\right), \tag{2}$$

where m is the shape parameter (called the Weibull modulus) connected with the Weibull distribution probability density factor, σ_0 is the positive scale parameter and F denotes the cumulative distribution function. The shape parameter is calibrated based on experimental mean values and variation as follows:

$$E[\sigma]=\mu=\sigma_0\Gamma\left(1+\frac{1}{m}\right), \tag{3}$$

$$Var[\sigma]=\sigma_0{}^2\Gamma(1+2)-\mu^2, \tag{4}$$

where $\Gamma(\cdot)$ is the gamma function, $E[\sigma]$ denotes the mean value and $Var[\sigma]$ is the coefficient of variation. The shape parameter m depends on a probability distribution of experimental data. The specific case of the Weibull's law is the LEFM solution where the exponential parameter is equal to $n/m=½$ (Fig.2.1).

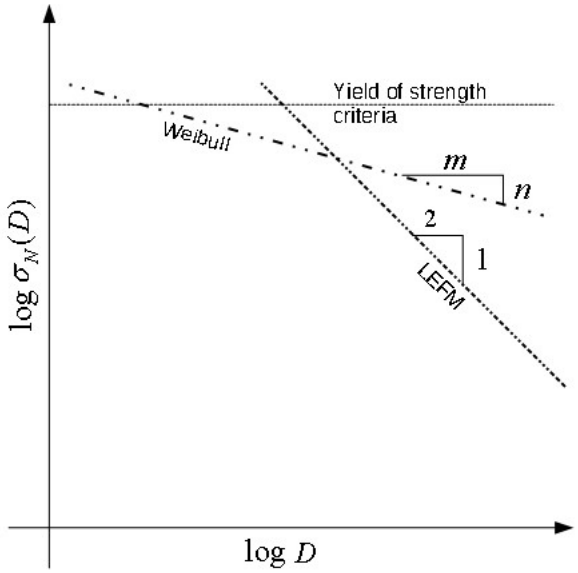

Fig.2.1: Statistical size effect law of Weibull (1939): relationship between nominal strength and element characteristic size (LEFM - linear elastic fracture mechanics)

The size effect law for concrete by Duan and Hu (2004, 2008, 2010) (called also the boundary effect model (BEM)) connects the size effect on the tensile strength to the interaction between a fracture process zone and the nearest specimen boundary. BEM assumes that the change of the FPZ width is due to the crack length variation. The nominal strength is related to a crack length (Fig.2.2a) (Eq.6).

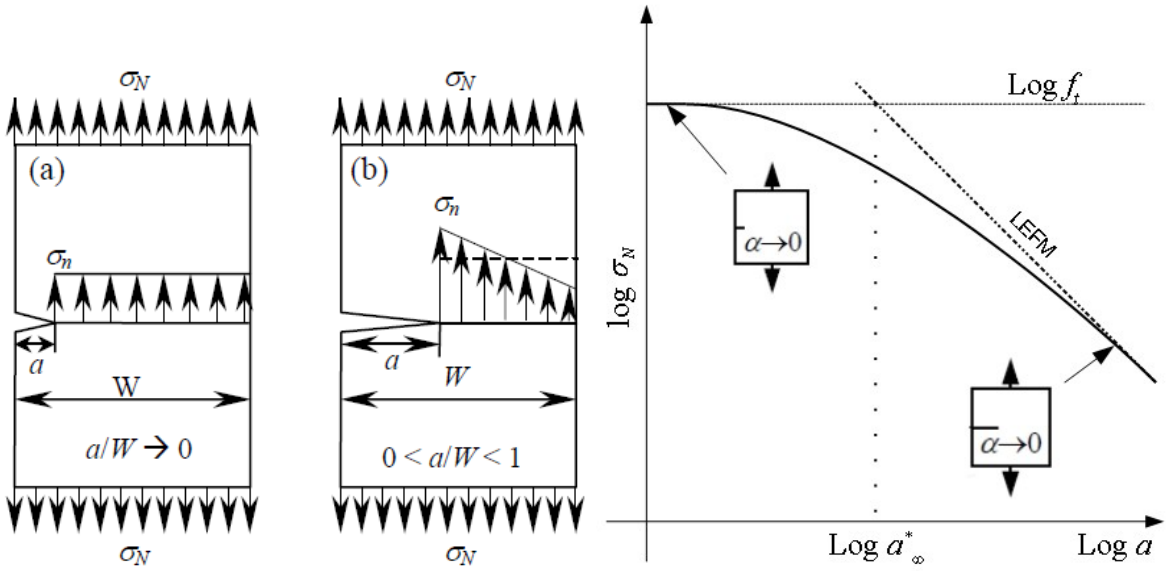

a) b)

Fig.2.2: Boundary effect model (BEM) by Duan and Hu (2008) a) stress distribution ahead of crack and b) relationship between strength and crack length *a*

Considering plastic and elastic fracture of a large metal plate with a pre-existing crack under plane strain conditions (Hu and Wittman 2000), the intersection point of the plastic and elastic solution was found as

$$a^* = \frac{1}{\pi Y^2 (a/W)} \left(\frac{K_{IC}}{\sigma_Y}\right)^2. \tag{5}$$

As the plastic failure is governed with plastic yield strength σ_Y and the elastic strength criterion is described with fracture toughness $K_{IC.}$ W is the specimen size and a denotes the initial crack length and Y is the geometry factor equal to 1.12. Therefore the transition from a plastic to perfectly elastic solution was described with the simplest possible asymptotic function depending on the initial crack length a and the tensile strength f_t'. The strength in BEM was described with the following expression:

$$\sigma_N = \frac{f_t'}{\sqrt{1 + a/a_\infty^*}}, \tag{6}$$

where $a_\infty^* = l_{ch}/1.12^2\pi$ and $l_{ch} = (K_{IC}/f_t')^2$ - the Irwin's characteristic length (Fig.2.2b), K_{IC} is the stress intensity factor and f_t' stands for the tensile strength. The size effect law for concrete was described as:

$$\sigma_N = \frac{\alpha \cdot f_t}{\sqrt{1 + \beta \frac{a}{l_{ch}}}}, \tag{7}$$

where α is the parameter dependent on loading conditions and β is the parameter dependent on the specimen geometry (β contains the geometry factor $Y(a/W)$ and is constant for geometrically similar elements). BEM is capable also to capture size effect on the fracture toughness when a failure mode changes from plastic to brittle. Fracture toughness is usually described in LEFM as

$$K_C = \sigma_N \cdot Y \cdot \sqrt{\pi a} \,. \tag{8}$$

In BEM, the size effect on fracture toughness may be expressed by putting Eq.7 to Eq.8 as

$$\frac{K_C}{K_{IC}} = \sqrt{\frac{\beta_1 \cdot W}{1 + \beta_1 \cdot W}} \,, \tag{9}$$

where K_{IC} denotes the true size-independent fracture toughness and is calculated as $K_{IC} = \sqrt{E \cdot G_F}$ and β_1 is the dimensionless parameter that represents the specimen geometry and loading type, calibrated from the curve fitting. BEM successfully described the size effect on strength and fracture toughness for bending, tension and coupled bending with tension (Fig.2.3.)

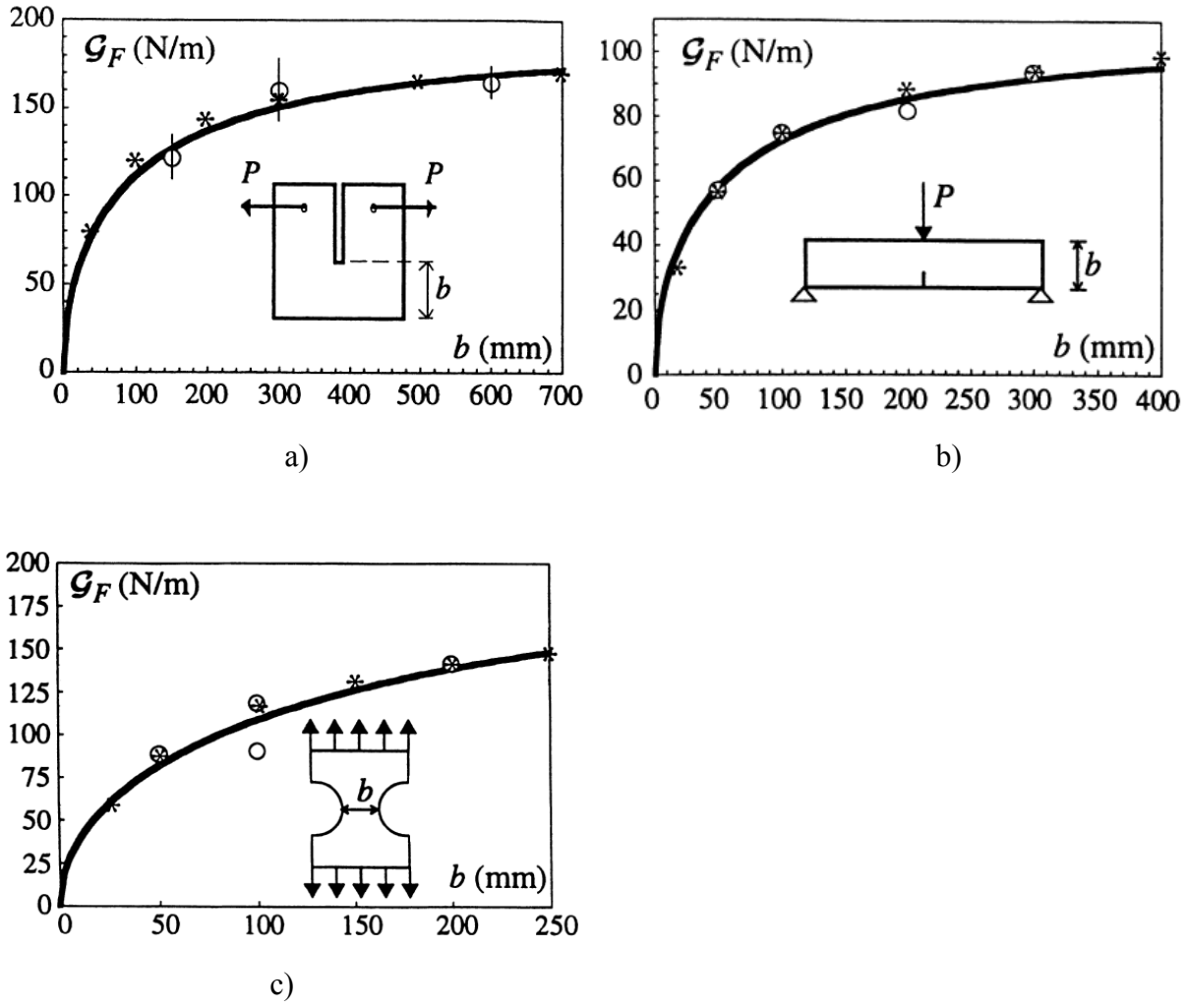

Fig. 2.3: Comparison of fracture energy G_F in function of specimen size remaining ligament b for Boundary Effect Model (BEM) with simple tests on concrete a) wedge splitting test (Wittman et al.

1990), b) three-point bending (Elices et al. 1992) and c) uniaxial tension (Carpintieri et al. 1995) (Hu and Wittman 2000)

BEM includes some incorrect assumptions (the FPZ-boundary interactions, neglecting the energy balance condition and no mathematical basis for asymptotic matching) though it fits the experimental data for fracture mode I (Yu et al. 2010). Moreover, beyond some certain ranges of the ligament and specimen size, the BEM results for G_F and K_{IC} indicate huge errors. Nevertheless, BEM is still under continuous development (Wang 2016, Hu 2017).

The size effect law for concretes proposed by Carpintieri et al. (1989, 1994, 1995) (called the multi-fractal scaling law (MFSL)) postulated that the size effect was due to a fractal nature of both concrete micro-structure and crack surface. The theory was based on scaling the fracture energy G_f with a disorder level (Fig.2.4)

$$\sigma_N(D) = \sqrt{A + \frac{B}{D}}, \tag{10}$$

where D is the characteristic structural size, A is the constant with physical dimensions of the square of stresses ($A = [[F][L]^{-2}]^2$) and B is the constant with physical dimensions of the square of the stress intensity factor ($B = [[F][L]^{-3/2}]^2$), where [F] is the force unit and [L] stands for length unit.

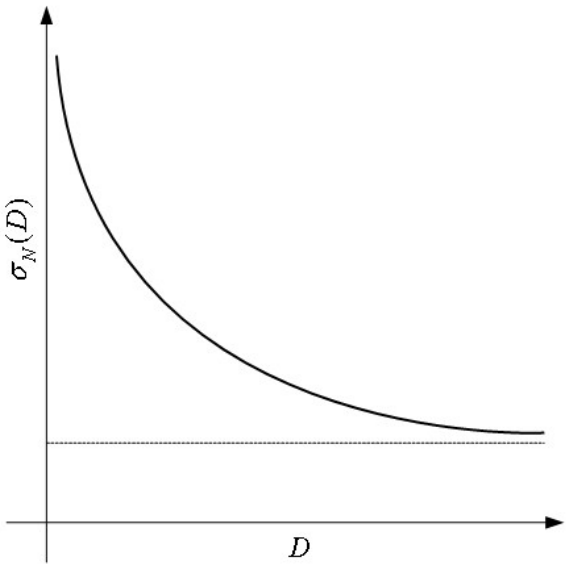

Fig.2.4: Multifractal scalling law by Carpintieri (1989): decrease of nominal strength σ_N with increasing characteristic size D

Both the constants A and B are determined from experiments with the least-squares method (Marquard 1963). The fractal approach has some physical requirements (restrictions):

$$\lim_{d\to\infty}(A+\frac{B}{d})^{1/2}=\sqrt{A}, \tag{11}$$

$$\lim_{d\to 0^{+}}(A+\frac{B}{d})^{1/2}=+\infty. \tag{12}$$

The analytical expression takes a form of:

$$Y(X)=\frac{1}{2}\log(A+\frac{B}{10^{x}}). \tag{13}$$

While the asymptotes are expressed by the flowing formulas for a horizontal line (homogeneous regime - large structures) and vertical line (fractal regime – microscopic dimension X tending to zero):

$$H_1(X)=\log\sqrt{A}, \tag{14}$$

$$H_2(X)=-\frac{1}{2}X+\log\sqrt{B}. \tag{15}$$

Therefore the limit load may be obtained in MFSL only for homogeneous structures. MFSL does not have physical foundations (Bažant and Yavary 2007). Some of them are the following: the fractal nature of fracture surface after failure cannot matter as 99% of energy is dissipated far before the final fracture by micro-cracking and frictional slips in the entire FPZ volume (also away from the fracture surface), and there is no dependence of MFSL coefficients on the structural geometry. Moreover, the same MFSL formulae may be derived from the non-fractal LEFM (Bažant and Yavari 2005).

The most physical and accurate theoretical description of a size effect for geometrically similar concrete structures was given by Bažant (1984). The size effect law (SEL) type I is valid for

unnotched plain concrete or weakly reinforced massive concrete elements (where crack appears suddenly and localisation develops at the moment of crack imitation) and refers to a Weibull's statistical theory. The formulation for SEL type I applies to elements of a positive geometry without an initial notch or a crack, failing at the crack initiation:

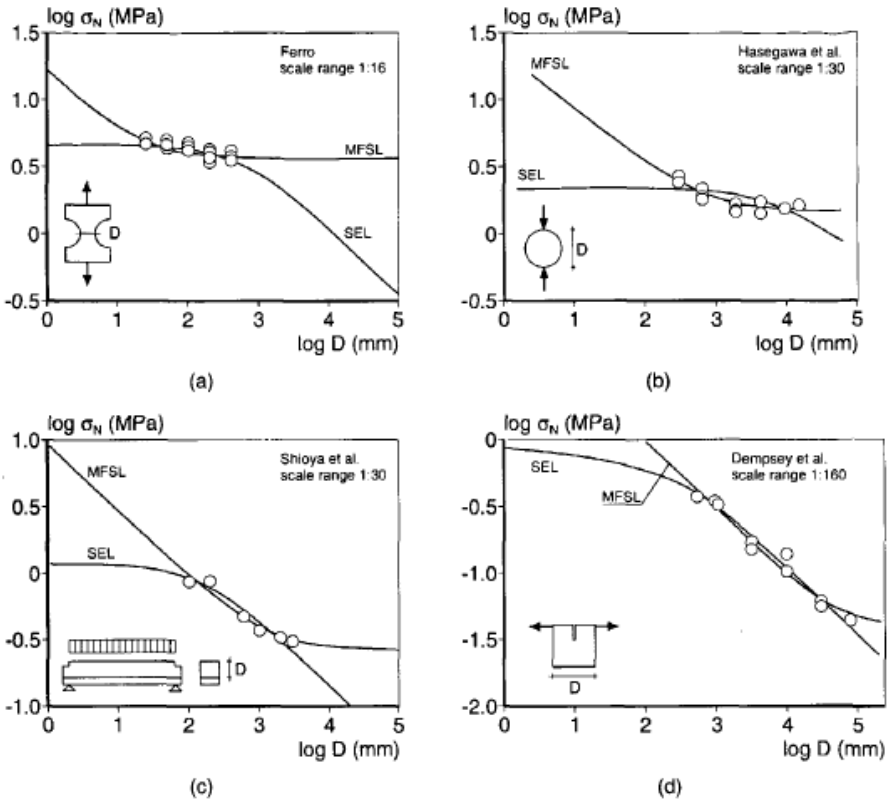

Fig.2.5: Comparison between multi-fractal scalling law (MFSL) by Carpinitieri (1989) and size effect law (SEL) by Bažant (1984) and experiments by: a) Ferro (1994), b) Hasegawa et al. (1985), c) Shioya et al. (1989) and d) Dempsey et al. (1999)

$$\sigma_N(D) = f_r^{\infty}\left(1+\frac{rD_b}{D+l_p}\right)^{\frac{1}{r}}, \tag{16}$$

where r denotes the positive constant parameter (close to 1), f_r^{∞} is the strength limit for very large elements, D_b is the height of the boundary layer of cracking and l_p is the empirical material parameter. The graphical representation of the Bažant's size effect law for geometrically similar elements is shown in Fig.2.6a.

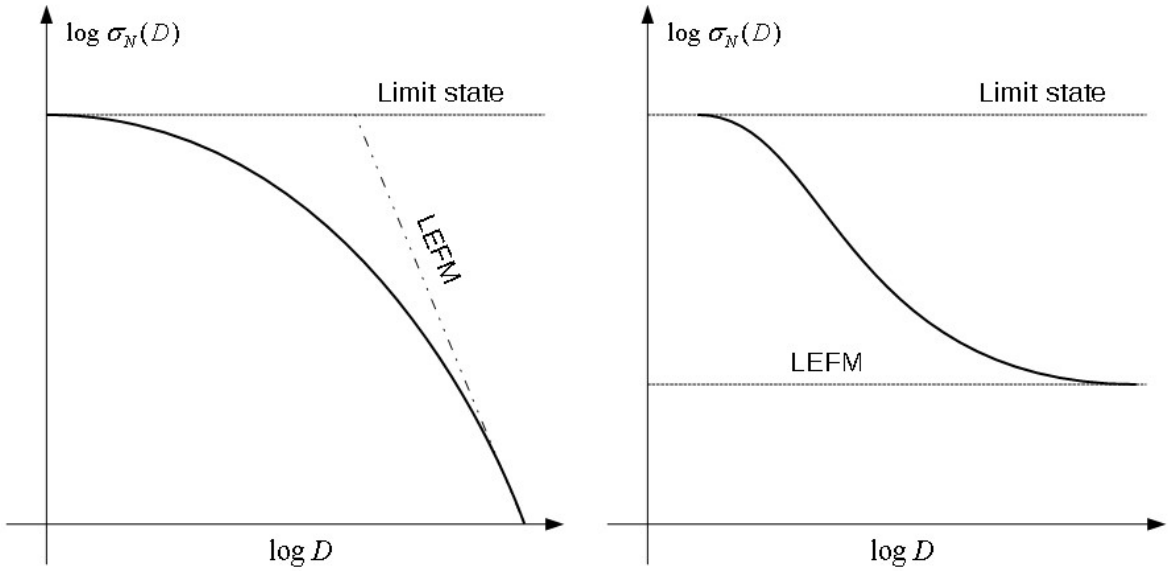

Fig.2.6: Size effect law by Bažant (1984) for geometrically similar elements of a) type I for unnotched elements and b) type II for elements with notches or RC members

The size effect (SEL) type II is applicable to notched concrete specimens or reinforced concrete (all cases with propagating crack)

$$\sigma_N(D) = \frac{Bf_t}{\sqrt{1+\frac{D}{D_0}}} \tag{17}$$

with

$$D_0 = c_f \frac{g'(\alpha_0)}{g(\alpha_0)}, \qquad Bf_t = \sqrt{\frac{EG_f}{c_f g'(\alpha_0)}}, \tag{18}$$

where $\alpha_0 = a_0 / D$ is the normalized crack length, f_t is the tensile strength and c_f is the effective length of FPZ. The function defining the dimensionless energy release function $g(\alpha_0) = D(bK_I / P)^2$ (b – the specimen thickness and P – the applied load) merges the specimen geometry and fracture energy G_f. The ratio D/D_0 corresponds to the brittleness number β. When β=0, the response is plastic as the solution tends to a plastic limit (limit state) and when $\beta \to \infty$ the material response is perfectly brittle and the LEFM solution is reached (Fig.2.6b). Both the SELs have a plastic yield limit for small members and a LEFM limit for very large members.

Bažant (2004, 2007) postulated later that due to material heterogeneity, the solution of SEL type I has to approach a Weibull statistical size effect instead of LEFM. Therefore an extended formula combining both deterministic and statistical size effect is as follows

$$\sigma_N(D) = f_r^{\infty}\left(\left(\frac{L_s}{L_s + D}\right)^{\frac{rn}{m}} + \frac{rD_b}{D + l_p}\right)^{\frac{1}{r}}, \tag{19}$$

where L_s is the characteristic length of micro-structure (that may be determined from experiments and is connected with the concrete micro-structure). The generalised formulation for a combined deterministic-statistic size effect (so-called the universal size effect law) is:

$$\sigma_{Nu}(D) = Bf_t\left[1 + \left(\frac{D}{D_0}\right)^r\right]^{-\frac{1}{2r}}\left[1 + s\frac{2l_f D_0}{(2\gamma l_f + D) + (D_0 + D)}\right]^{\frac{1}{s}}, \tag{20}$$

where r, γ and s are the empirical parameters and l_f is the parameter dependent on the initial crack length. SEL compared to experiments and MFSL is shown in Fig.2.5. Both the theoretical results are in agreement with experiments solely at the laboratory scale.

Experiments

The size effect was widely investigated in experiments on plain and reinforced concrete. The experiments on a deterministic size effect during uniaxial tension were performed among others by van Vliet and van Mier (2000). The concrete specimens had a dog-bone shape to drop failure at boundaries (Fig.2.6). A clear size effect on strength was obtained (Fig.2.7). The size effect was also investigated during 3-point bending (Petersson 1981, Bažant&Pfeifer (1987a), Le Bellego et al.(2003), Skarżyński et al. (2011)) (Fig.2.7). In all experiments, the nominal strength and ductility significantly decreased with increasing specimen size. The size effect was stronger during bending since the stress state was more non-uniform.

The studies on a statistical size effect were performed on plain concrete beams of a different length during 4-point bending by Koide et al. (1999) wherein a constant momentum zone (bending span) was scaled only (Fig.2.9e). The experiments exhibited a constant strength loss with increasing beam length in spite of the same height.

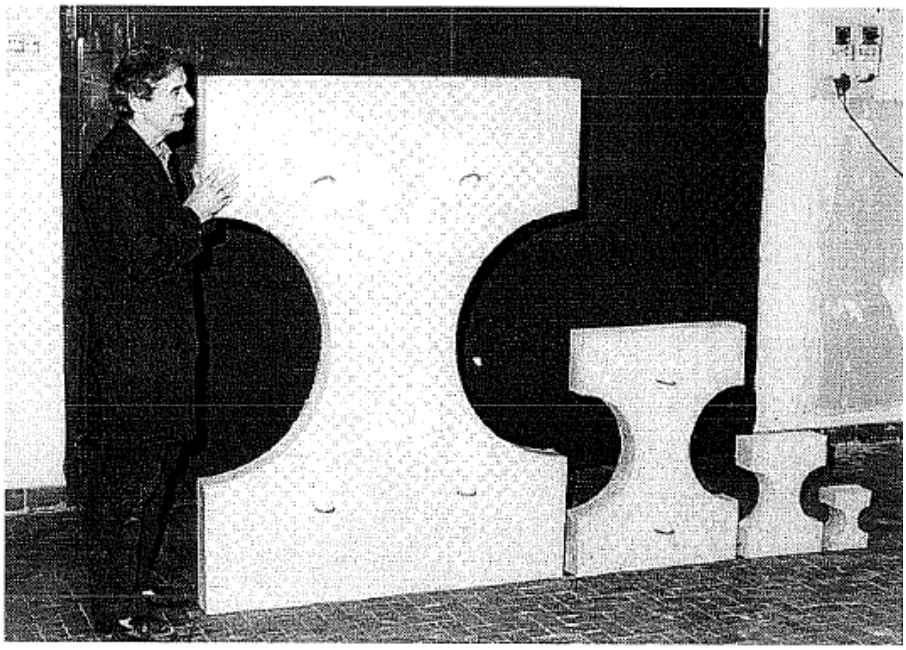

Fig.2.7: Dog-bone shaped concrete specimens tested by VanVliet&van Mier (2000)

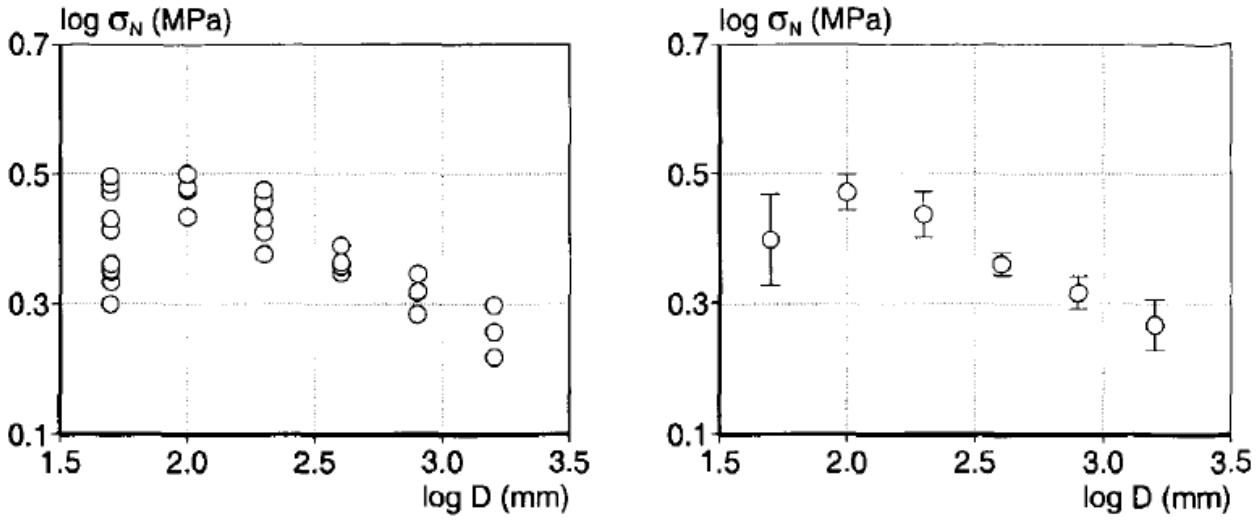

a) b)

Fig.2.8: Strength σ_N versus specimen size D in uniaxial tension for concrete: a) individual values and b) mean values with coefficient of variation obtained (vanVliet 2000)

A strong size effect was experimentally observed in geometrically similar over-reinforced concrete beams without shear reinforcement wherein diagonal shear-tensile failure mode took place in concrete (Petersson 1981, Korol et al. 2014, Walraven&Lehwalter 1994, Kim et al. 1994,

Podgorniak-Stanik 1998, Tan&Lu 1999, Yoshida 2000) (Fig.2.9). The diagonal cracks at failure had in experiments essentially similar paths and relative lengths at the maximum load. The size effect was also observed in reinforced concrete beams with shear reinforcement (Walraven 1994, Zhang&Tan 2007b, Belgin&Sener 2008). In these experiments a diagonal shear-tensile fracture (Zhang&Tan 2007b, Korol 2014) or crushing of a compressive zone (Belgin&Sener 2008) took place in concrete. The experimental results of shear strength were published by Karl - Heinz Reineck et al. (2003). Less than 5% out of about 800 beams tested in shear have the depth greater than D>600 cm. Therefore engineers still lack statistically confirmed results of size effect for large and very large scale structures. SEL compared to experiments and MFSL is shown in Fig.2.10. The theoretical results were again in agreement with experiments solely at the laboratory scale.

Calculations

The size effect in concrete was modelled with the finite element method (Bobiński et al. 2009, Korol et al. 2014b), molecular dynamics (Laubie et al. 2017a,), lattice-particle model (Grassl&Bažant 2009, Laubie et al. 2017b, 2017c) and discrete element method (Suchorzewski et al. 2018b). When using FEM, a deterministic size effect was modelled among others with the second-gradient elasto-plastic model (Pamin&deBorst 1998, Pamin 2004), second-gradient damage model (Simo&Ju 2003) and elasto-plastic model and damage model with non-local softening (Bobiński et al. 2009). The coupled deterministic-statistic size effect was modelled with the nonlocal damage model by Carmeliet&Hens (1994), Frantziskonis (1998), Gutierrez&de Borst (1998), gradient-enhanced model Gutierrez (2006), microplane material model combined with the crack-band model Vorechovsky (2007), Bažant et al. (2007b), Baghini et al. (2007) cohesive crack model Yang and Xu (2008), Grassl and Bažant (2009), elasto-plastic with non-local softening (Bobiński et al. (2009) and Korol et al. (2013)). Vorechovsky (2007) performed a theoretical study on dog-bone specimens (Fig.2.11) tested experimentally by van Vliet (Figs.2.7 and 2.8). He showed that many specimens whose strength was obtained by random sampling was stronger than a deterministic value. With increasing size, the difference between the deterministic and mean statistical strength increased. The deterministic results approached a horizontal asymptote while the statistical one followed the Weibull's weakest link model with the modulus m=7.91. The weakened boundary due to evaporation effects strongly decreased the strength of very small specimens. Depending on the width of the weakened boundary zone, the mean predicted strength decreased and the results' scatter increased.

Korol et al. (2013) performed FEM simulations of 3-point bending test with stochastic elasto-plasticity and non-local softening using random fields describing fluctuations of tensile strength for both plain and reinforced concrete beams. A size effect was obtained on strength and ductility (Figs.2.12-2.14).

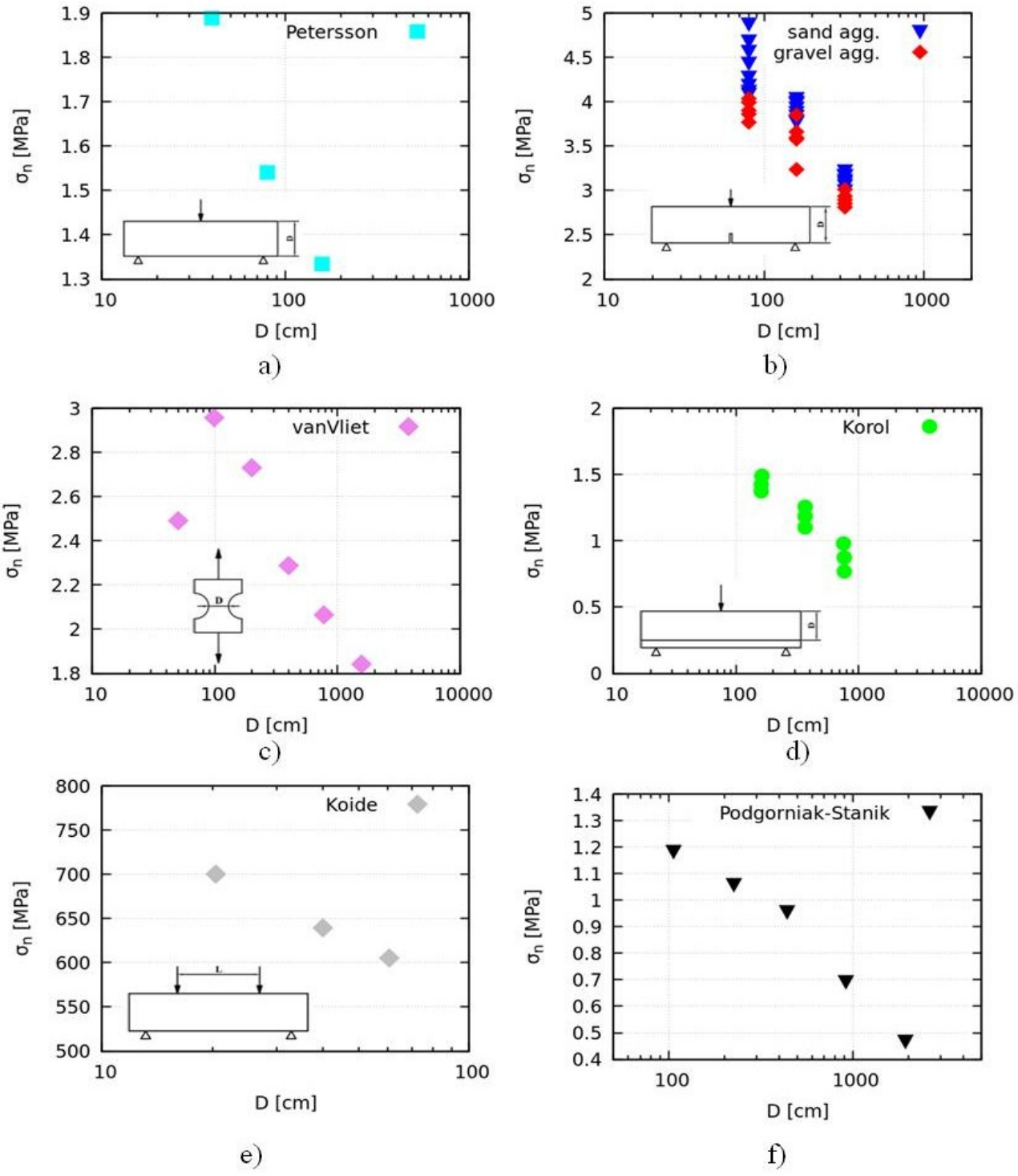

Fig.2.9 Size effect in experiments on plain and reinforced concrete by: a) Petersson (1981), b) Skarżyński et al. (2011), c) van Vliet (2000), d) Korol et al. (2014), e) Koide et al. (1999) and f) Podgorniak-Stanik (1998)

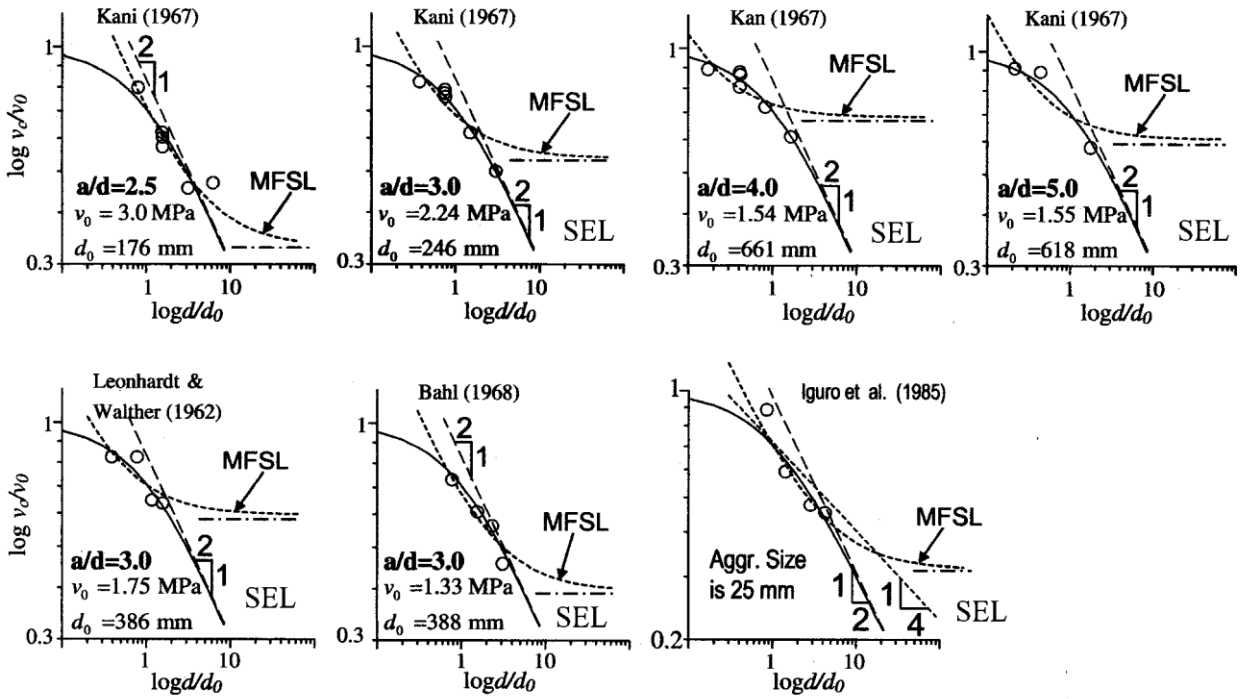

Fig.2.10: Fits of Size Effect Law (SEL) by Bažant et al. (1984) and Multi Fractal Scaling Law (MFSL) by Carpinteri et al. (1994) to experimental data for reinforced concrete beams failing by shear (Bažant and Yavari 2007)

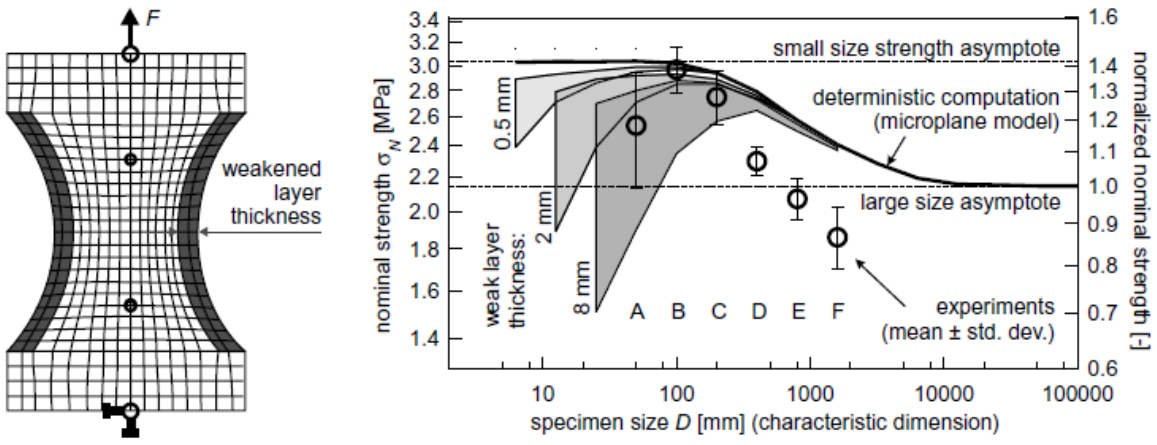

a) b)

Fig.2.11: Size effect calculations by Vorechovsky (2007): a) computational model with boundary weakened layer as compared to experimental data by van Vliet and van Mier (1998) b) results of numerical simulation with various width of weak layers due to shrinkage micro-cracking

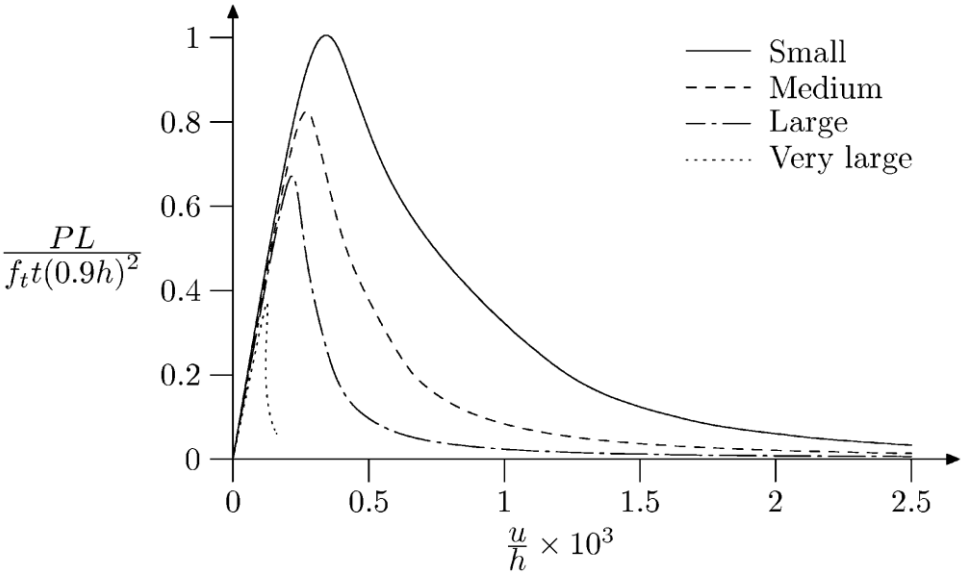

A)

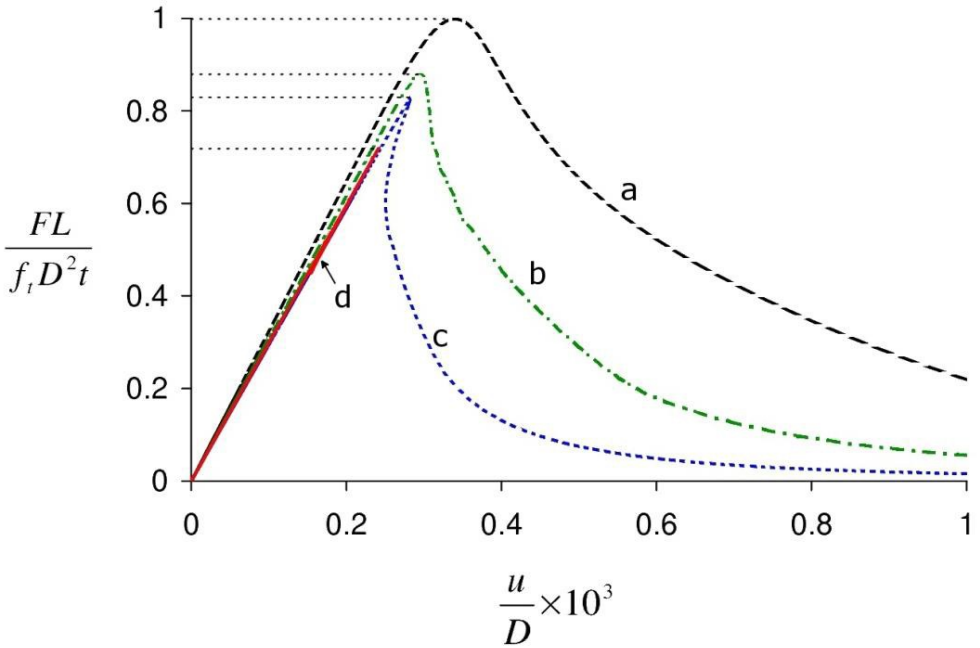

B)

Fig.2.12: Deterministic normalized vertical force-deflection curves with constant values of tensile strength for 4 different concrete beam heights: small D=8 cm (dashed line '*a*'), medium D=16 cm

(dotted-dashed line '*b*'), large *D*=32 cm (dotted line '*c*'), very large *D*=192 cm (solid line 'd') (A) notched beams and B) beams without notch (Korol et al. 2013)

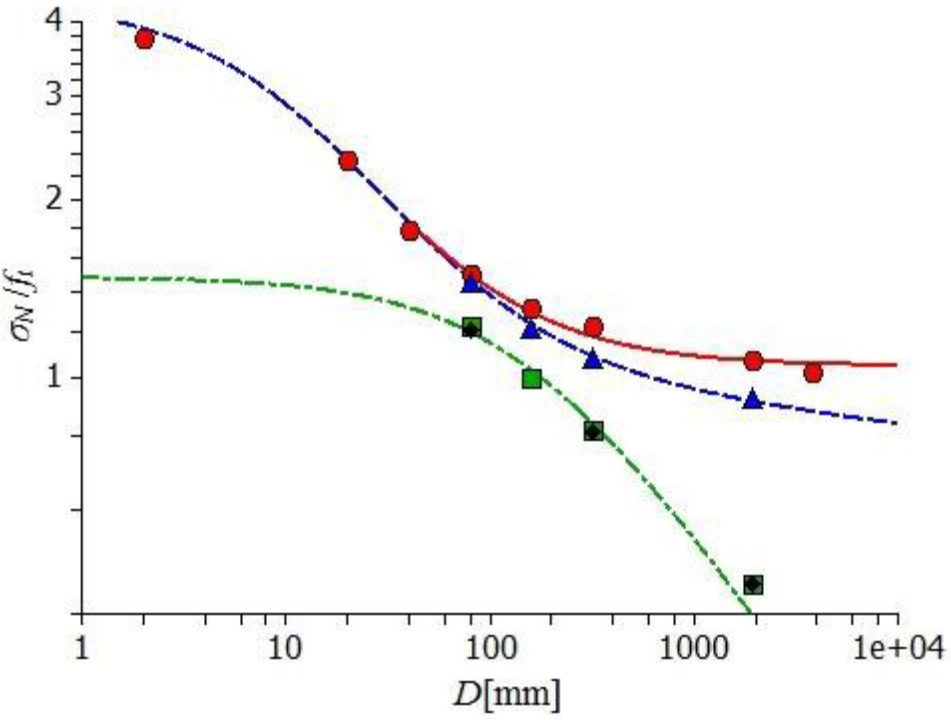

Fig.2.13: Calculated nominal strength *(σ_N (σ_N=1.5FL/(ftD2t))* versus beam height *D* for unnotched concrete beams from deterministic (red circles) and stochastic (blue triangles) and for notched concrete beams from deterministic (green squares) and stochastic (green diamonds) FE calculations compared with deterministic size effect law by Bažant (red solid line), deterministic-statistical size effect law by Bažant (blue dashed line) and deterministic size effect law by Bažant (green dotted-dashed line) (Korol et al. 2013)

Grassl and Bažant (2009) and Laubie et al. (2017b, 2017c) performed simulations with a random lattice-particle model. If the interactions between randomly packed particles had the same strength, a statistical size effect was not obtained. However, it was realistically reproduced when a stochastic distribution of interaction strengths was assumed. Kozicki performed beam lattice model simulations on notched cubic three-phase concrete specimens (Fig.2.15a) under uniaxial tension (Kozicki 2007). The specimen 20×20 cm^2 had the strength lower by 20% and was more brittle in the post-peak range than the small specimen 10×10 cm^2 (Fig.2.15b).

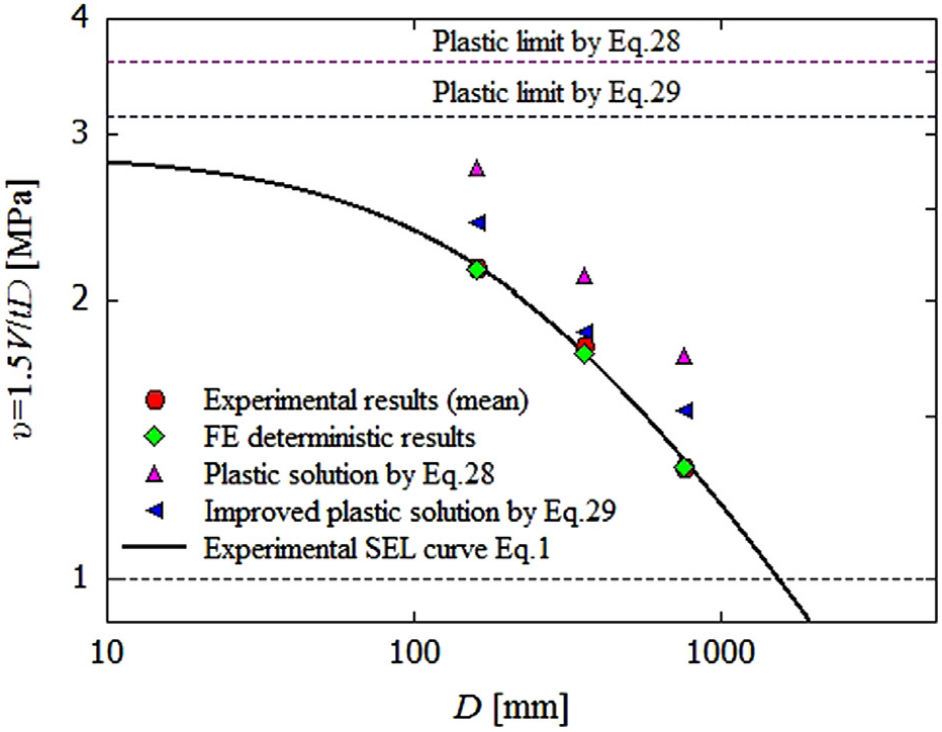

Fig.2.14: FE results of nominal shear strength ν against effective beam depth *D* from deterministic analyses for reinforced concrete beams without shear reinforcement as compared with experiments, size effect law and upper bound plastic theory results

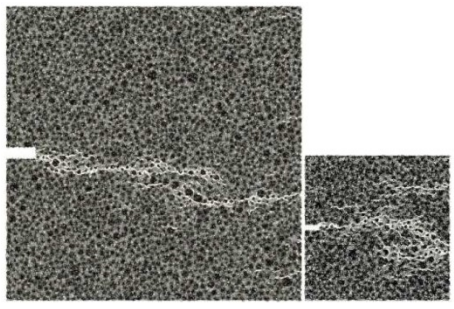

a)

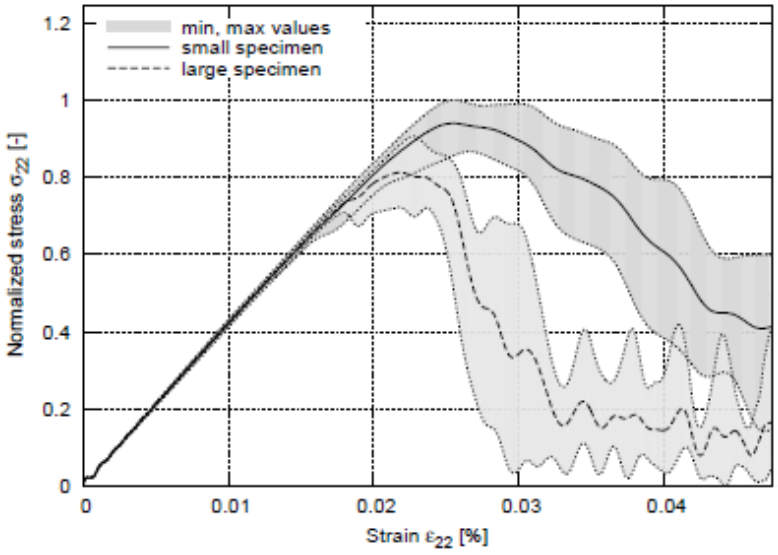

b)

Fig.2.15: Beam lattice model simulation results of uniaxial tension for three-phase concrete material a) fractured specimens and b) solutions variability for small (10×10 cm^2) and large specimen (20×20 cm^2) (Kozicki 2007)

The deterministic size effect was also simulated in compression tests by Cusatis (Cusatis et al. 2006). Prismatic specimens in four different sizes were modelled with the confinement-shear lattice model in two versions (with a v-shaped notch and without it). For unnotched specimens, the size effect in compression was nearly negligible as the nominal strength was reduced only by 7% between specimens with the size of D=50 mm and D=400 mm due to an almost uniform vertical stress distribution. In contrast, for notched specimens, the size effect was very strong and decreased the nominal strength by 23% (Fig.2.16). The authors stated, that compression strength size effect had a crack-initiation type (SEL type I). Moreover, the size effect was very strong in the post-peak region as the brittleness decreased for both notched and unnotched specimens when their size increased.

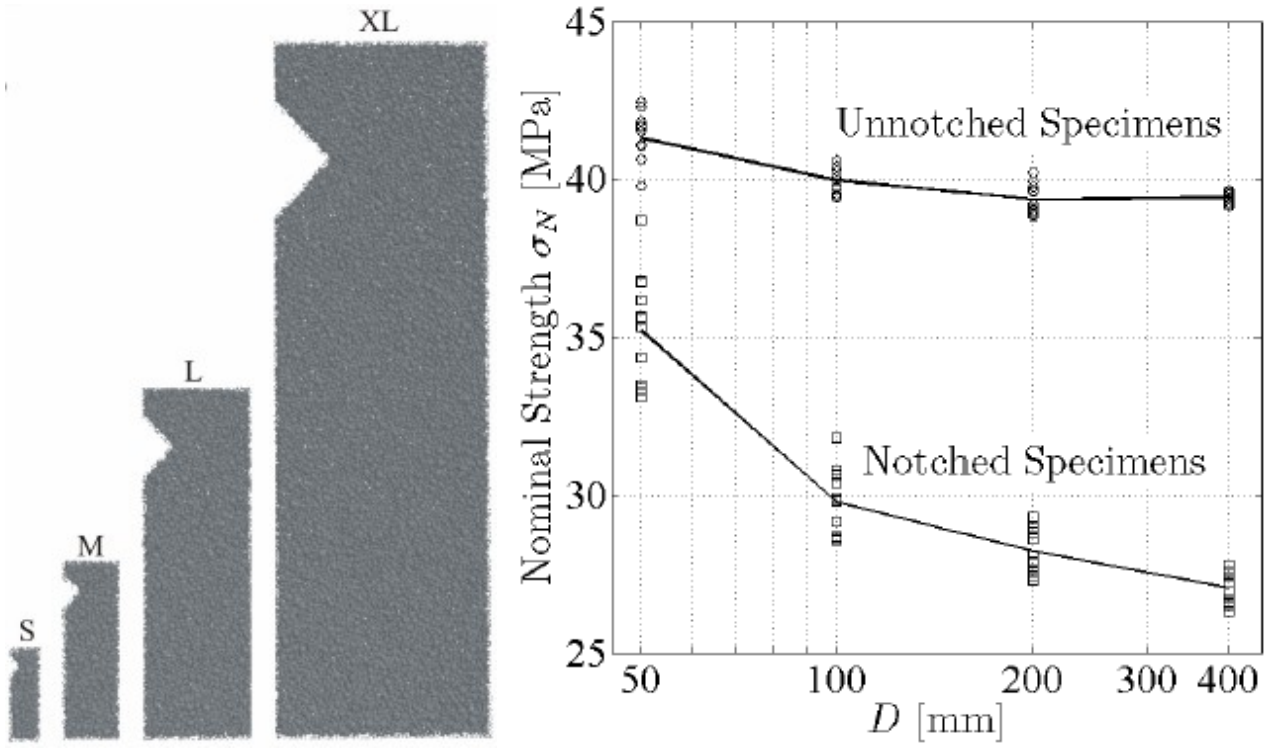

a) b)

Fig.2.16: Results of lattice model simulations of uniaxial compression with and without notch for three-phase concrete material (Cusatis 2006 et al.): a) notched specimens and b) nominal strength σ_N against specimen size D

Chapter 3

Laboratory experiments on concrete fracture

The experimental studies at the laboratory scale are always very important tools for numerical modelling results of concrete fracture at the aggregate level. Three experiments at the small scale were performed for:

1) uniaxial compression (Suchorzewski et al. 2018a),
2) splitting tension with different boundary conditions (Suchorzewski et al. 2018b) and
3) splitting tension with different specimen diameters.

The uniaxial compression test has been chosen since it is the most important experiment for concrete. The splitting tension test has been chosen since it is a very popular simple test to determine the tensile strength of concrete.

3.1 Uniaxial compression

Specimens and test procedure

The uniaxial compression test is described by standards provision as a basic test of the compressive strength of concrete. Cubic specimens with the dimensions of 150×150×150 mm^3 or cylindrical specimens with the diameter of 150 mm and height of 300 mm are used. The specimens used in the research work were however smaller (50×50×50 mm^3) to obtain a better resolution of micro-CT images. The uniaxial compression test is strongly dependent on boundary conditions at ends. When high friction or binding occurs between a concrete specimen and loading plate, the cracks have mainly an x-shape and compressive strength is higher than in the case of free horizontal displacements (van Mier 1997). In the experiments, a very smooth steel loading plate was used and the specimen surface was polished to decrease the wall friction.

The experiments were carried out with concrete including Baltex limestone aggregate (collected on the Baltic seabed) that was round and very smooth due to a long-termed sea activity. The concrete specimens were prepared in the weight proportion 3:1.6:7.1:12.6 (cement 32.5 R: water: sand: aggregate). The minimum aggregate diameter was d_a^{min}=2 mm, maximum aggregate diameter d_a^{max}=10 mm and mean particle diameter d_{50}=5 mm. The sieve aggregate content was 10.2% (diameters 2-4 mm), 78.6% (diameters 4-8 mm) and 11.2% (diameters 8-10 mm). The total particle

(sand and aggregate) volumetric content was 75%. This aggregate was intentionally chosen since it had an oval-like shape that was easier to be simulated in DEM simulations.

The load machine ZWICK Roller HB BPS-FB0250.20.12 was used. The quasi-static tests were performed with a controlled vertical displacement rate of 0.0005 mm/s. Two concrete specimens were scanned by the 3D x-ray micro-tomograph Skyscan 1173 (Skarżyński and Tejchman 2016, Skarżyński et al. 2019) in order to obtain the detailed 3D image of concrete meso-structure in a non-damaged (initial state) and damaged state.

ITZs

Concrete is generally referred to as a heterogeneous and discontinuous material that may be considered at the meso-scale as a composite material wherein four germane phases (constituents) may be isolated: cement paste, aggregate, macro-voids and interfacial transition zones (ITZs) between aggregates and cement paste. ITZs reveal pronounced compositional differences as compared to the cement paste which are the most significant in the vicinity of the aggregates' surface and gradually diminish away from aggregates to become insignificant at a certain distance (15-100 μm) (Scrivener et al. 2004). ITZs differ from the cement paste in porosity, pore size and also in the complementary anhydrous cement and C-S-H (calcium silicate hydrate) contents. In general, ITZs contain more and larger pores, smaller particles and higher porosity, less anhydrous cement and (calcium silicate hydrate, C-S-H) gel, resulting in higher transport properties (i.e., permeability, diffusivity and conductivity) in contrast to the cement paste. ITZs stem from the wall effect of packing of cement grains against the relatively flat aggregate surface which disrupts the packing of cement grains and is responsible for the features of ITZs, particularly for their higher porosity. Another origin of ITZs is a micro-bleeding effect where ITZs accumulate free water around aggregates, especially under large aggregates, and increases the local porosity (Wang et al. 2009). The ITZ-thickness is usually around 20-50 μm and depends strongly on the water to cement ratio, aggregate type, size and age of micro-structure (Elsharief et al. 2003).

It is very difficult to perform experimental tests on ITZs due to their very small size. Therefore ITZs are mainly investigated based on scanning electron microscope (SEM) images. The quantitative data are usually obtained by image post-processing with different techniques. The porosity of ITZ was estimated as 15% at the aggregate edge using the mercury intrusion porosimetry (MIP). It decreased non-linearly down to 5% at the distance of 35 μm from aggregates (Ollivier et al. 1995). The Wood's metal was used at the University of Berkeley to analyse the three-dimensional structure

of ITZs (Srivener&Nemati 1996). The liquefied metal was intruded at the concrete specimen surface under pressure and saturated micro-pores and fractures. Then the images were taken by the backscatter scanning microscope (BSE) in regions surrounding aggregate grains. The width of zones with fractures and micro-pores varied between 30-100 μm, however, the pores interconnected in 3D were located not further than 20 μm from the aggregate edge. The most recent studies of ITZ properties are based on nanoidentation tests and atomic force microscopy. Nanoindentation is a simple mechanical test of pressing a very hard tip (usually made of diamond) with three-sided geometry into a specimen. At the applied force, the displacement is measured. Based on those data, the hardness and modulus of elasticity may be determined. The atomic force microscopy may be used for a surface roughness inspection and together with nanoindentation for analyses of cracking in quasi-brittle materials to determine the stress intensity factors. The ITZ-modulus of elasticity was measured with nanoindentation and was equal to 80% of the cement matrix (Xiao et al. 2013). ITZs were also observed in fibre reinforced concrete around steel fibres and had the thickness of 10-30 μm (Wang et al. 2009). Unfortunately, none of the mentioned methods is able to provide the information on the ITZ-strength. The experimental study of the aggregate-cement interface was performed with a specimen of limestone aggregate with 2 mm layer of the cement paste on it. The specimens were tested in direct tension and shear (Jebli et al. 2017). The strength and stiffness of this composite and pure cement were compared in various hydration times. The composite cohesion was smaller by 25% than for pure cement. Some theoretical studies were also performed to investigate the mechanical properties of ITZs like strength and modulus of elasticity. The multiscale approach of calibration of ITZ properties was realized by Koniegsberger et al. (2014, 2018) based on a thermo-mechanical analysis. The stress state was downscaled from the cement paste level in the aggregate neighbourhood down to the "hydrate needle phases", where the Druker-Prager like criterion was solved for stress peaks at the hydrates level. Afterwards, the stresses were upscaled back to the cement paste level. The necessity of including ITZs at the meso-level was noted with different possible ITZs failure modes (debonding from aggregate, ITZ failure and cement ITZ interface breakage). It is very popular to handle ITZs as layers with different properties with the finite element method (FEM. Grondin&Matallah (2014) stated that TIZ might have high or low density depending on the aggregate type and that concrete macroscopic strength might be reproduced with ITZ properties almost identical as cement paste while the lower ITZ-strength gives results similar to the experimental microscopic phenomenon. ITZs act as "the weak link in the chain when compared to the bulk cement paste and aggregates

In order to measure the width of ITZs in non-damaged specimens, the scanning electron microscope (SEM) HITACHI TM3030 with the maximum magnification factor 30'000 was used. The small specimens cut out from the initial concrete block with a size 40×40×1.5 mm^3 were used. The specimen surface was polished with a grinding stone. ITZs around particles were characterised by an extremely thin and porous structure. Due to a very smooth aggregate surface, their width was merely 2-3 μm, i.e. significantly smaller than in usual concretes (30-50 μm) (Skarżyński et al. 2015) ITZs appeared mainly around aggregate (Fig.3.1A) but they were also visible around some large cement matrix particles (Fig.3.1B). The width of ITZs was not dependent upon the aggregate diameter.

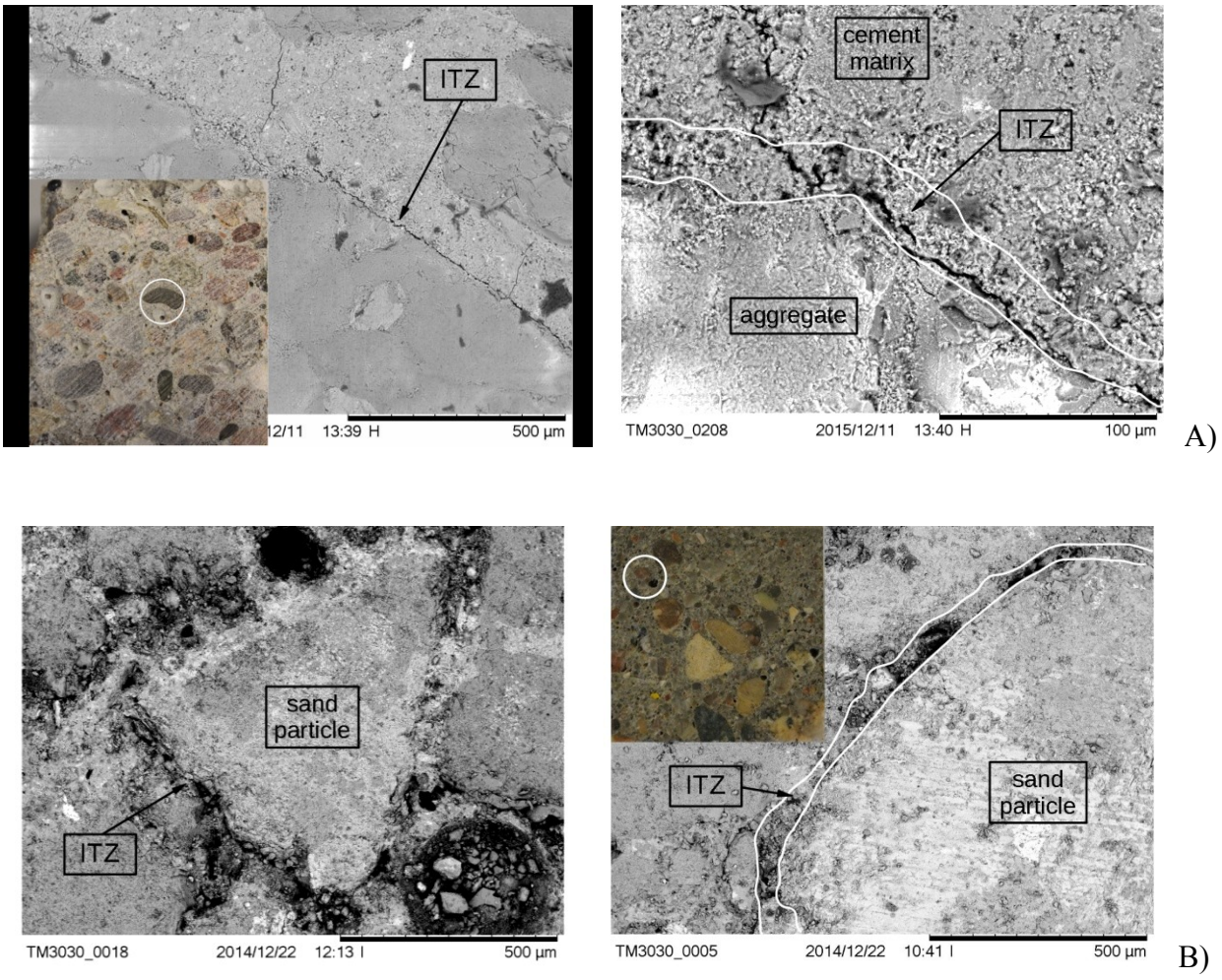

Fig.3.1: Images of ITZs between aggregate and cement matrix in concrete specimen '1' using scanning electron microscope: A) around aggregate particle of diameter d_a=3 mm and B) around sand particle of diameter d_{cm}=0.4 mm (a) magnification factor 200 and b) magnification factor 1000)

Stress-strain curves

The typical experimental stress-strain curves for 4 concrete specimens are shown in Figure 3.2 (for the specimens '1' -'4'). The tests for the specimens '3' and '4' were stopped (ε=0.12% and ε=0.08%) for scanning by micro-CT. The mean concrete strength in compression was about 32 MPa for the specimens '1'-'3' and the mean modulus of elasticity was 32 GPa. The behaviour of the specimen '1' was brittle and '2' was quasi-brittle in the post-peak regime. The different stress-strain responses were probably due to a specific aggregate shape and smoothness.

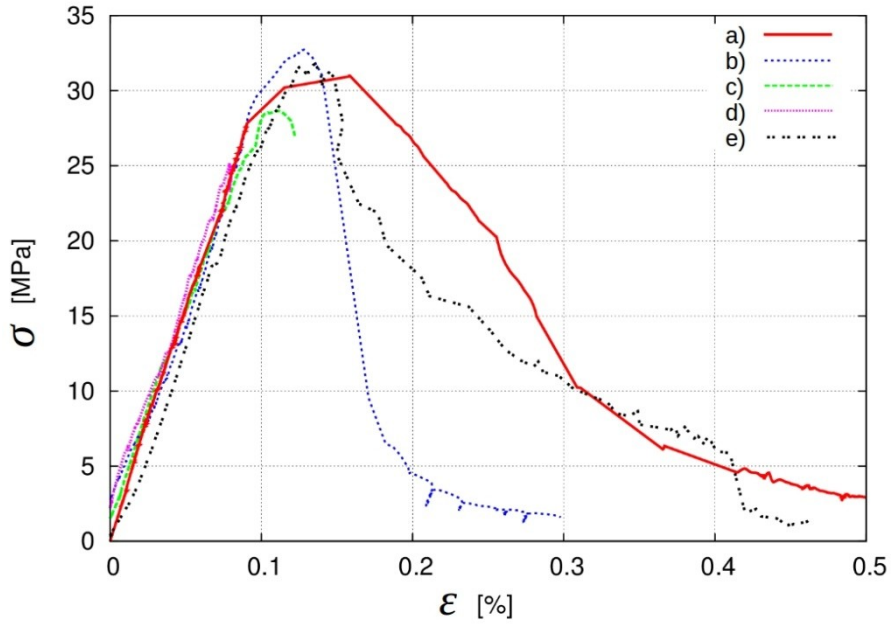

Fig.3.2: Five different stress-strain curves $\sigma=f(\varepsilon)$ from laboratory tests on concrete specimens under uniaxial compression: a) specimen '1', b) specimen '2', c) specimen '3', d) specimen '4' and e) specimen '5' under uniaxial compression (σ - vertical normal stress and ε - vertical normal strain)

The concrete specimen '3' before the test and after the peak stress (ε=0.12%) is presented in Fig.3.3. After compression, the failure surface was very non-uniform (Fig.3.3b). The edges were separated from the specimen core.

a) b)

Fig.3.3 View on face side of specimen '1' a) before test and b) after failure

Micro-CT scans of fracture

The x-ray micro-tomography (called briefly micro-CT) is a 3D imaging technique which uses x-rays to create cross-sections of a physical object that is used to recreate a virtual model (3D model) without destroying the original object (Proudhon 2010, Skarzynski and Tejchman 2016). The micro-CT consists of x-ray emission gun, rotating stage and flat panel sensitive to x-ray emission detecting the x-ray magnitude. The analysed specimen is being rotated around vertical axis with small rotation step. At each step, a 2D black-white image of a specimen with the density map (based on the x-ray absorption) is saved in the computer's memory. To create 3D image of specimens internal structure, a total rotation of 180° is necessary. For specimens with a higher density (large x-ray absorption), the rotation of 360° is used. After that, the 2D image is reconstructed in every horizontal section from individual 2D scans. the reconstructed specimen images may be then rendered and analysed both qualitatively and quantitatively in 3D. The x-ray micro-tomograph Skyscan 1173 in our department represents a new generation in high-resolution desktop X-ray micro-tomography systems (Skarzynski and Tejchman 2016, Skarzynski et al. 2019). The scans were completed up to ten times faster with the same resolution and image quality as compared to previous micro-CTs with a fixed source-detector design. The scanner was equipped with the newly developed 130 keV microfocus x-ray source with a very stable focal spot position and flat panel sensor of a large format (5 Mpx) with special protection by a lead-glass fibre-optic window. As compared to usual X-ray micro-tomographs, this scanner has two basic advantages: a) large

specimens up to 200 mm in diameter may be scanned and b) the specimens are scanned with higher precision (2-3 microns). Note that a continuous investigation of the entire fracture process under deformation with the X-ray micro-tomograph (without breaks for scanning) was not possible for technical reasons yet. Now it is possible to shoot continuous scans during deformation.

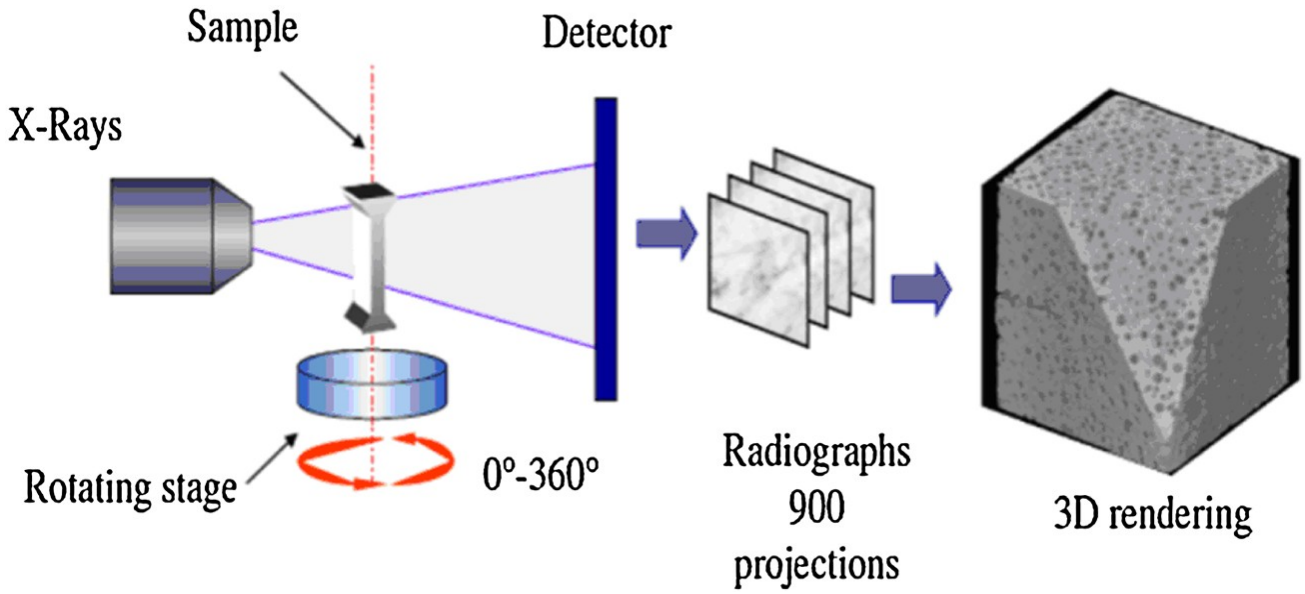

Fig.3.4: The working scheme of micro- CT (Proudhon 2010)

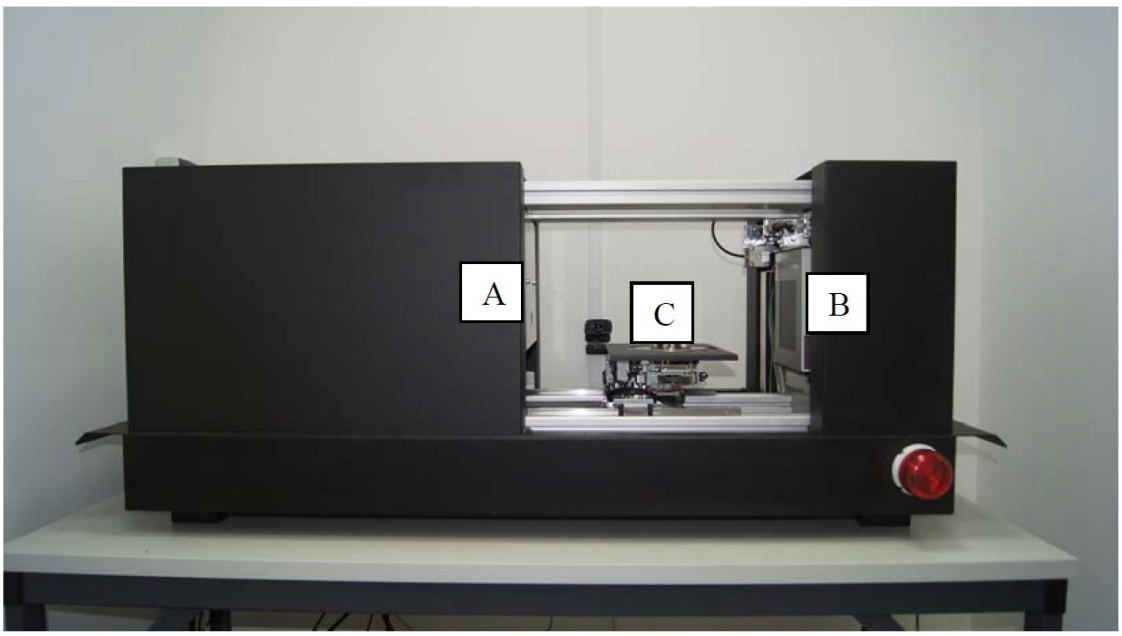

Fig.3.5 Overview on X-ray micro-tomograph Skyscan 1173: A) X-ray source, B) flat panel (detector) and C) precision object manipulator (positioning stage) (Skarżyński and Tejchman 2016, Skarżyński et al. 2019)

The basic outcome of CT scans is a greyscale image (Fig.3.6a) representing the objects densities (the whiter is the object, the higher is its density). In the first step, the region of interest has to be chosen to pick the area for further analyses (Fig.3.6b). Then to distinguish the desired phase (aggregate, cement matrix, pores or crack), a suitable threshold has to be applied, based on density histograms (Fig.3.6a). Choosing high densities, aggregate may be analysed (Fig.3.6c). Finally, aggregate morphology may be quantitatively measured (Fig.3.6d). The parameters as each object surface, volume (Fig.3.7b), porosity (opened and closed pores), centre of gravity, orientation in 3D, major diameter, sphericity, moments of inertia and many others may be extracted from the micro-CT scans.

All concrete specimens were scanned with the same parameter setting. The X-ray source voltage of the micro-CT scanner was set to 130 keV, the current was 61 μA and exposure time was equal 2000 ms. The pixel size of the micro-CT was 39,68 μm. The X-ray projections were recorded with the rotation increment of $0{,}2^{o}$ within 180^{o}. To reduce the noise in the captures X-ray projections, the frame averaging option was set to be 4 and random movement option was 10. The scanning time was approximately 6 hours.

Figure 3.8 demonstrates the 3D micro-CT-images of the 2 cracked cubical concrete specimens '3' and '4' in the region of the peak stress (ε=0.12% and ε=0.08%). The cracked vertical cross-sections of the concrete specimen '3' for the vertical deformation ε=0.12% are shown in Figure 3.8. All cracks were strongly curved mainly due to a random presence of aggregate grains (Figure 3.8 and Figure 3.9). The first crack occurred at the bottom right edge of the specimen on the front side (Figure 3.9a). It propagated through a weak aggregate and then along the left edge of the large aggregate particle. Next it branched into two cracks surrounding two aggregate particles above. Next a central crack was created on the front side (Fig.3.9a) which was not visible on μCT scans as it closed due to unloading. However it was observed during deformation with the aid of the manual digital microscope. In the case of the vertical section at the specimen mid-depth, more vertical cracks were created (Fig.3.9b). They appeared in each specimen region.

The maximum crack width on the specimen front side was w=0.18 mm (measured by the manual digital microscope). The cracks were slightly narrower on micro-CT-scans (w=0.13 mm) due to the specimen unloading during scanning. Initially, the volume of closed voids (voids that are not connected with the specimen edges) in the specimen '3' was 2.04% and of open voids (voids that

are connected with specimen edges) was 2.43%. After cracking (ε=0.12%), the volume of closed voids was 0.8% and open voids 4.05%. The volume reduction of closed voids was caused by a crack propagation through them that turned them into open voids.

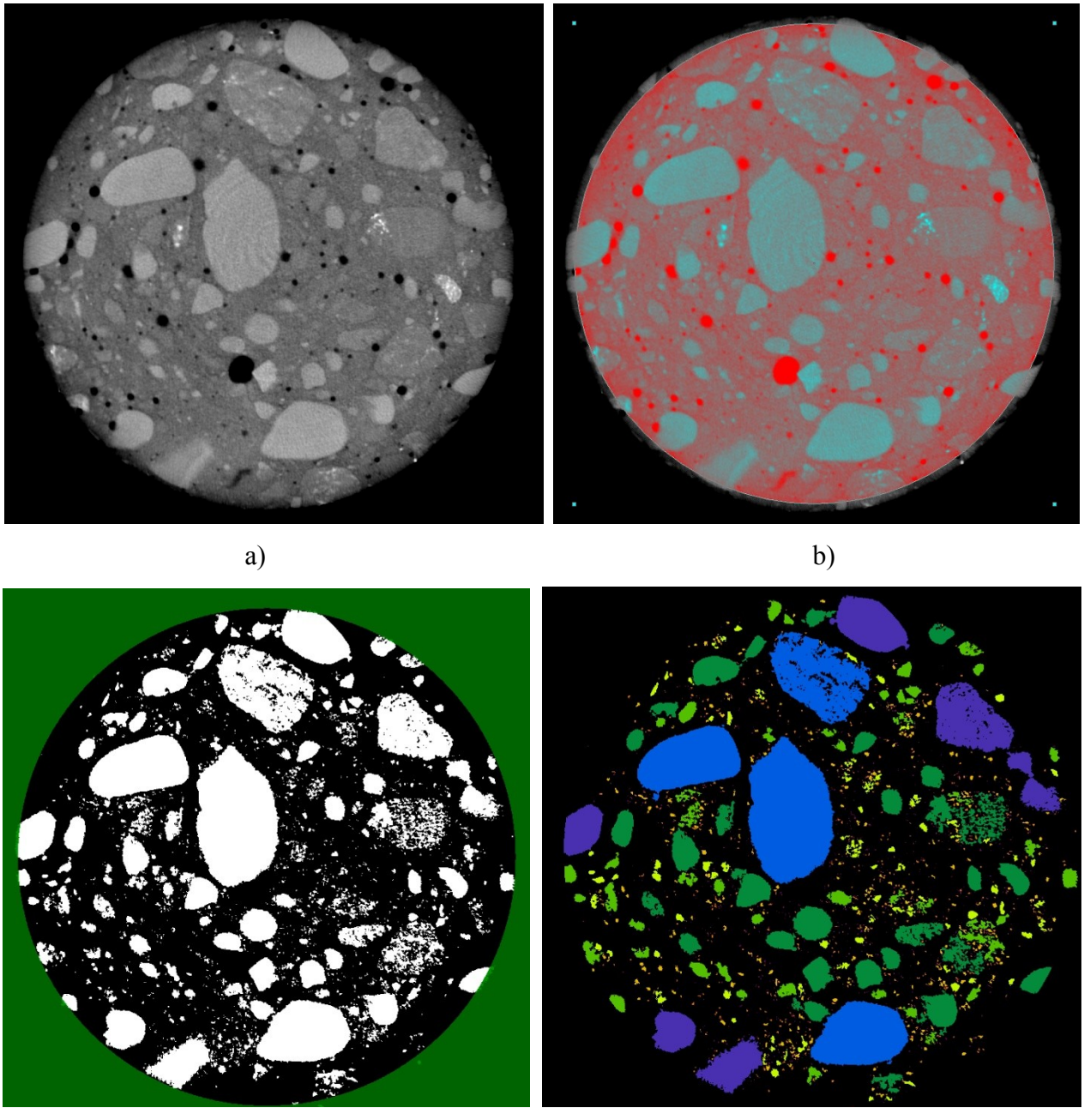

Fig.3.6: Mid-section of specimen with diameter D=74 mm: a) original scan image, b) region of interest (ROI) for further analyses, c) aggregate visible after applying threshold (histogram at Fig.3.7a) and d) morphology analysis of aggregate (histogram at Fig.3.7b).

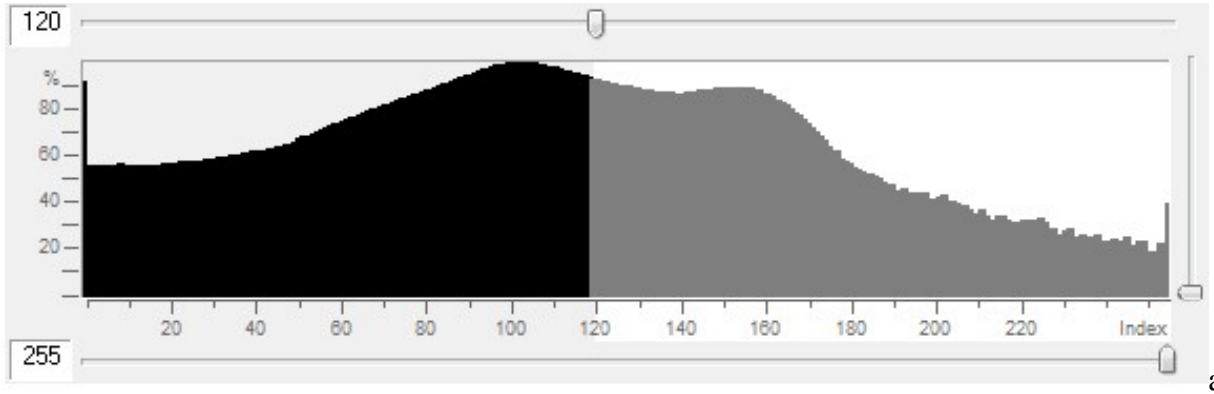

a)

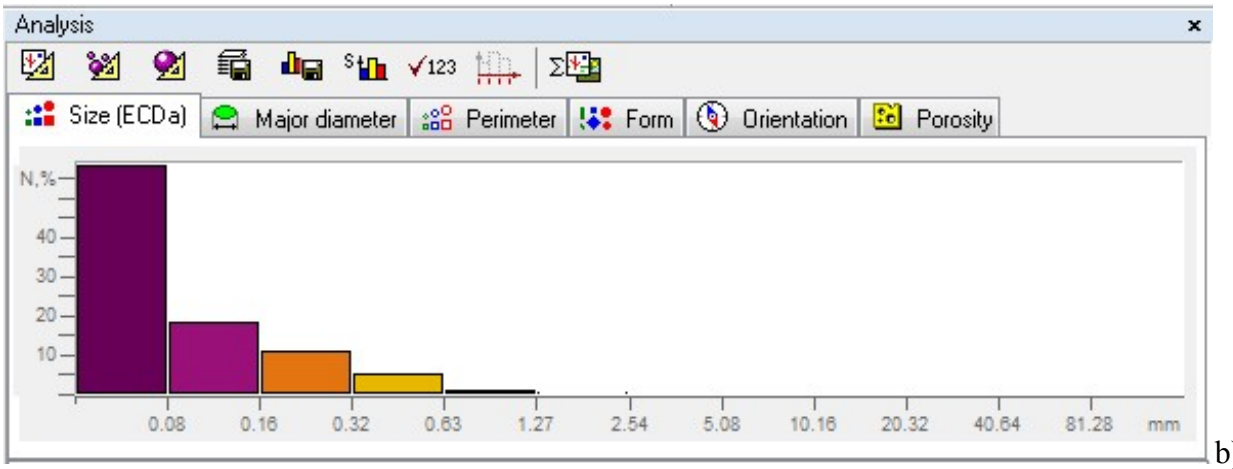

b)

Fig.3.7 Histograms of a) specimen density with applied threshold for aggregate analysis (120 – 255), and b) morphology analysis of aggregates size (horizontal axis presents aggregate size and vertical axis presents frequency)

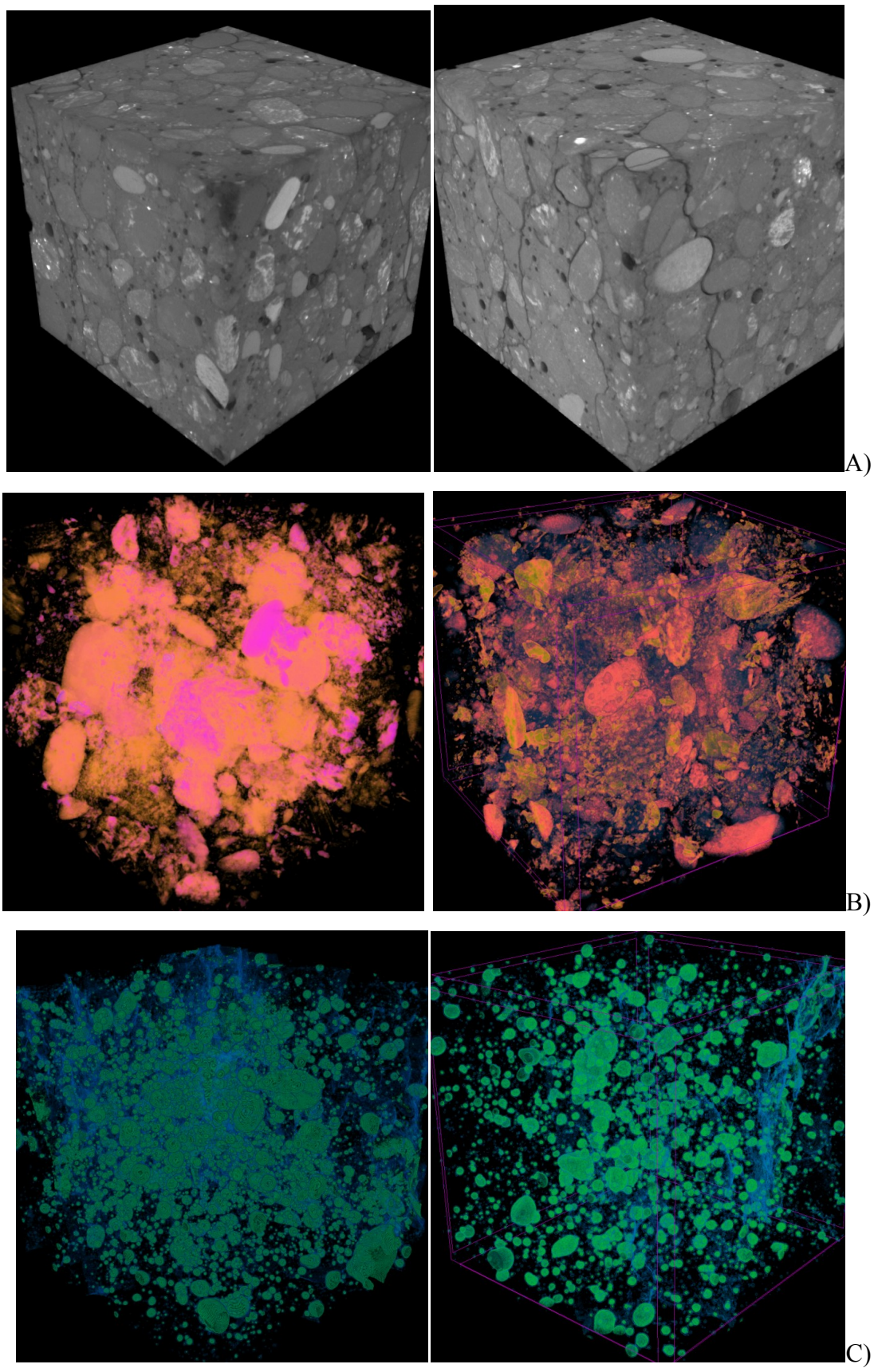

Fig.3.8: 3D micro-CT-scans of 2 cracked cubic concrete specimens '3' (A) and '4' (B) close to peak stress for ε=0.10% and ε=0.12%: a) general view (black spots - voids), b) marked aggregate in red and c) marked macro-voids in green and cracks in blue

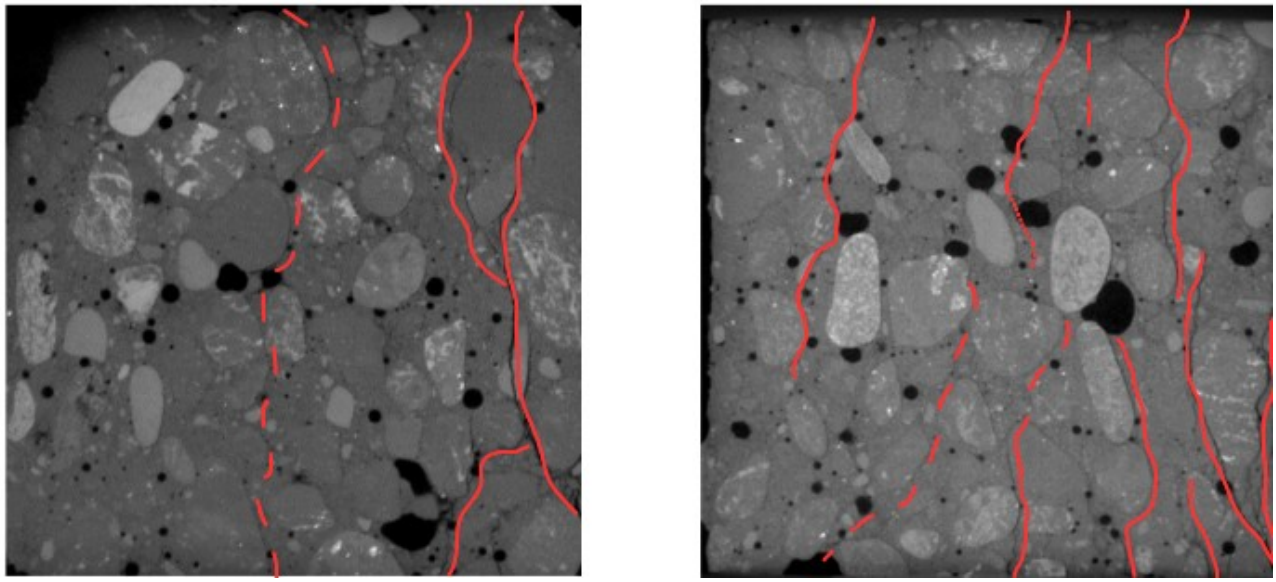

a) b)

Fig.3.9: 2D μCT-scans of cracked cubic concrete specimen '3' of Fig.3.3A for ε=0.12% (cracks are in red: continuous lines obtained on μCT-scans and dot lines by manual microscope , black spots denote voids), a) specimen face and b) vertical mid-depth section

Initially, the volume of closed voids in the specimen '3' was 2.04% and of open voids was 2.43%. After cracking (ε=0.12%), the volume of closed voids was 0.8% and open voids 4.05%. The volume reduction of closed voids was caused by a crack propagation through them that turned them into open voids.

All cracks mainly propagated through ITZs along aggregate particles since they were the weakest phase in concrete. Thus micro-cracking occurred first in ITZs. When two interfacial cracks occurred around adjacent aggregates, a crack inside the cement matrix initiated to bridge the interfacial cracks so that a connected crack path was formed (Fig.3.10). The cracks propagated very rarely through weak aggregate particles and macro-voids (Fig.3.11a). As it was earlier mentioned, a crack branching was also observed (Fig.3.11b). The maximum crack width on the specimen front side was w=0.18 mm (measured by the manual digital microscope). The cracks were slightly narrower on micro-CT-scans (w=0.13 mm) due to the specimen unloading during scanning.

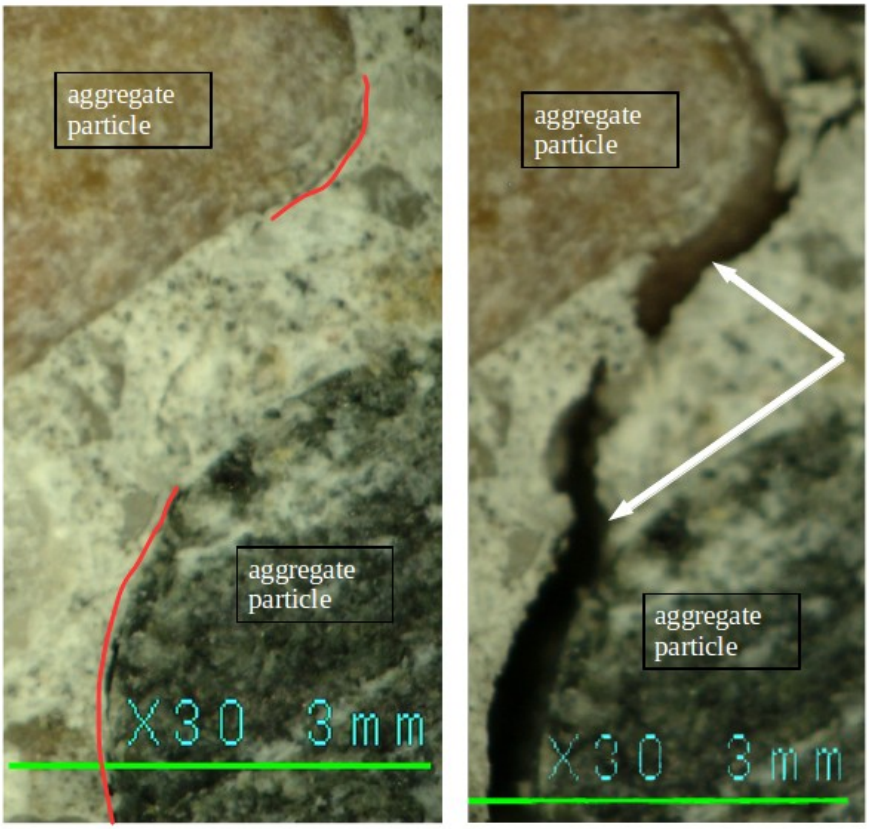

a) b)

Fig.3.10: Crack bridging mechanism on concrete face surface during deformation: a) initial micro-cracks in ITZs of 2 neighbouring aggregate particles (marked in red) and b) developed macro-crack between 2 neighbouring aggregate particles (manual microscope, magnification factor 100)

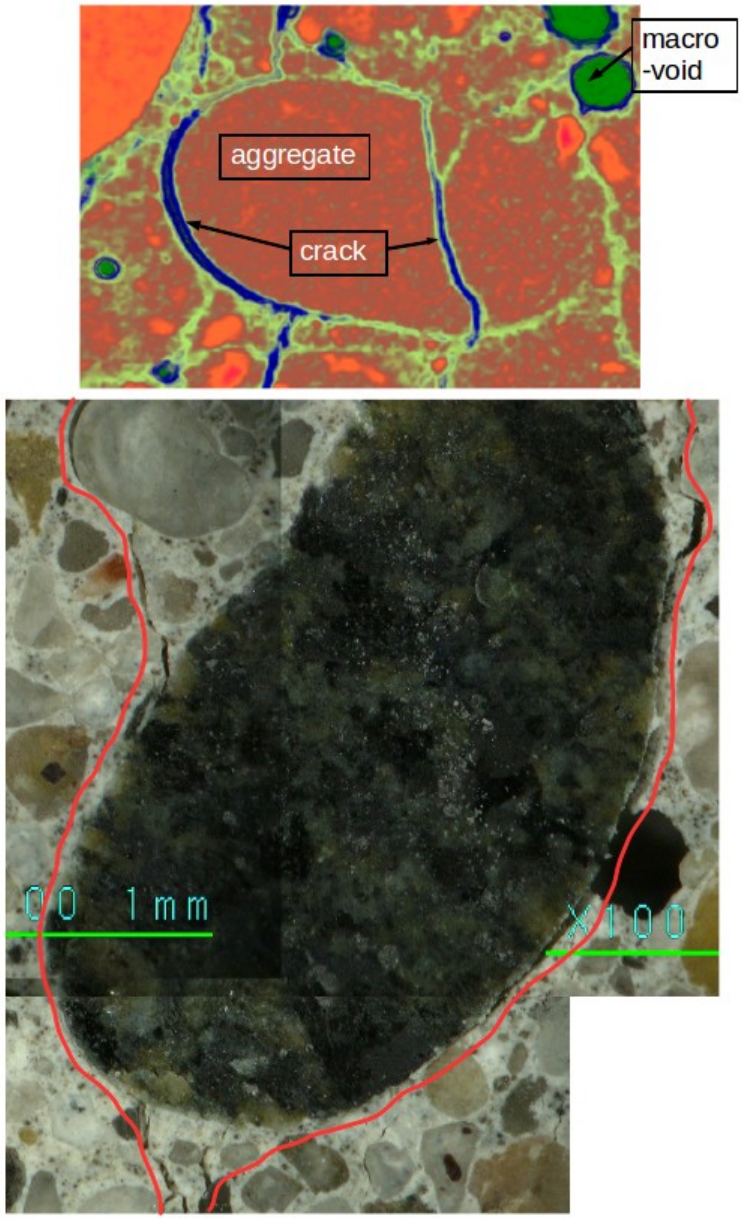

Fig.3.11: Crack propagation in concrete: a) through aggregate particle (d_a=2.5 mm) observed by 3D micro-CT system (red colour denotes aggregate, green/yellow – cement matrix, dark green – voids and blue/light green – crack) and b) branching around aggregate particle (da=3.0 mm) observed by manual digital microscope (magnification by factor 100, main crack is marked in red)

3.2 Tensile splitting tests with different boundary conditions

Specimens and test procedure

The tensile splitting test (Brazilian splitting) is the most popular experimental method of determination of concrete tensile strength due to the simplicity of the load application as compression and standardized the same specimen geometry as in compression strength test and

determination of modulus of elasticity. However, the test is very sensitive to boundary conditions (Rocco et al. 1995, 1999, 2001) and to the positioning of the specimen. Figure 3.12 presents the positioning the apparatus recommended by ASTM to set a cylinder axis perfectly parallel to the loading plate. All standards recommend plywood or hardboard strips for a uniform distribution of compressive stresses under the loading point (ASTM and EN). Moreover, the test is subjected to a size effect since the stress distribution is non-uniform.

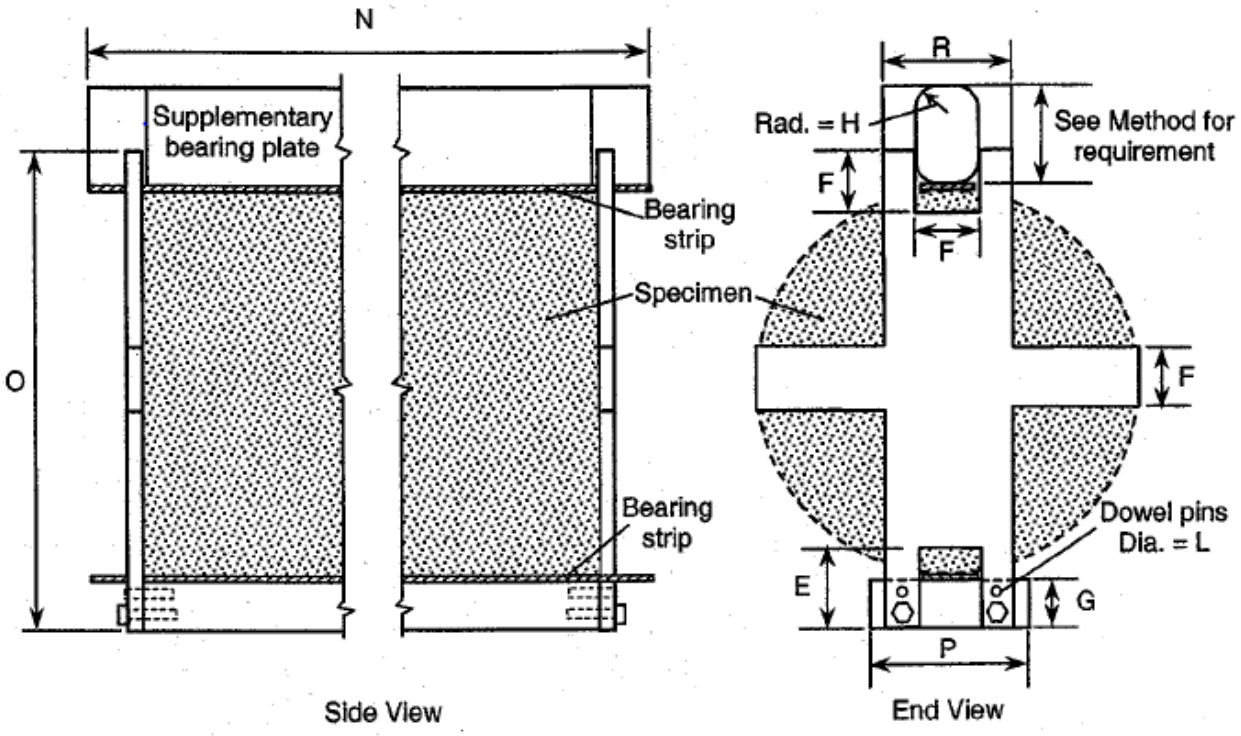

Fig.3.12: Positioning of specimen in splitting tensile test according to ASTM standard (ASTM C 496/C 496M-04)

This test consists of applying a distributed compressive force along the length of a concrete cylinder, which induces a primarily tensile stress perpendicular to the loading plane of the specimen's cross-section with a sharp compressive stress near the load points. The splitting tensile strength is greater than the direct tensile strength and lower than the flexural strength. The recommended standard cylindrical specimen sizes are: diameter D=0.15 m and length L=0.3 m. The tests by Carmona (Carmona et al. 1998) and Lamond (Lamond 2006) showed the specimen length did not influence fracture in splitting tensile tests if the specimen length was equal or larger than 5 times the maximum aggregate diameter. The tests are however sensitive to boundary conditions related to the width (Rocco et al. 1995, 1999, 2001), shape (Kuorkoulis et al. 2013a, 2013b, Salami et al. 2015) and stiffness (Miguel et al. 2016) of the loading strip. With growing loading strip width

b, the concrete strength increased (Rocco 1995, 1999, 2001). The shape's change of the loading strip from a rectangular strip to a curved one made the specimen strength higher by increasing the contact surface (Kuorkoulis et al. 2013a, 2013b, Salami 2015). The loading strip stiffness turned out to be significant for $b/D<0.25$ (very stiff loading strip increased the strength in experiments by Miguel et al. (Miguel et al. 2016)). The effect of boundary conditions on the initial global stiffness and post-peak behaviour of concrete specimens (strength-displacement curve, fracture) has not been investigated yet.

The fracture process in the splitting test with standard loading strips consists of two main stages: 1) a main macro-crack formation in the central vertical zone and 2) secondary cracks connecting the main vertical crack with edges of loading plates (Miguel et al. 2016, Ruiz et al. 2009). In addition, the test outcomes are subjected to a size effect, expressed by a decrease of both the nominal strength and ductility with increasing specimen diameter (Carmona et al. 1998, Bažant et al. 1991, Hasegawa et al. 1985, Kadlecek et al. 2002, Torrent 1977). The European standard (EN12390-6: 2000) defines loading strips as made of a hardboard of the density of 900 kg/m^3 and dimensions: width b=10 mm and thickness t=4 mm whereas the standard (ASTM C 496/C 496M-04) (Fig.3.13) proposes loading strips of plywood: b=25 mm wide and t=3.2 mm thick.

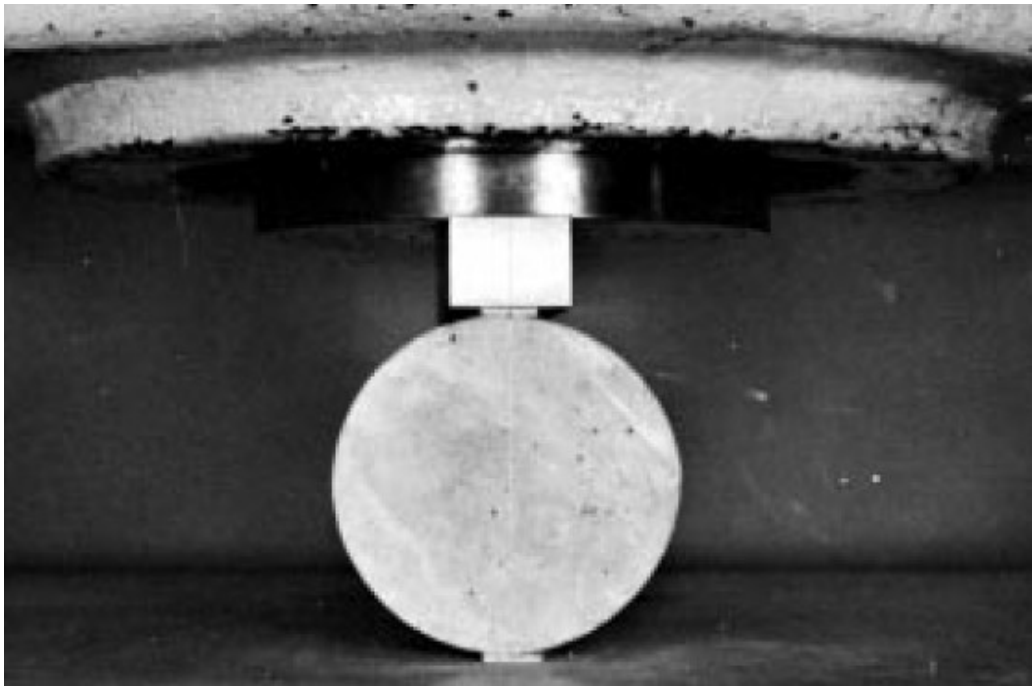

Fig.3.13 The specimen in splitting tensile test according to ASTM standard (ASTM C 496/C 496M-04)

The experimental and theoretical research works were aimed now at understanding the concrete behaviour at the meso-scale during different failure modes in quasi-static splitting tension, depending upon the specimen diameter. Based on preliminary experiments, a quasi-brittle concrete behaviour took place with small specimen diameters (D=5 cm). For larger diameters (D=10 cm), a brittle concrete behaviour occurred. Finally, for very large diameters (D>15 cm), a snap-back instability was observed (that is described by a positive slope in a stress-strain softening branch) (Bažant et al. 1987b, Biolzi et al. 1989, Tanabe et al. 2004, Korol et al. 2013). This instability is typical for large and slender concrete structures, low fracture toughness and high tensile strength (Biolzi et al. 1989, Tanabe et al. 2004, Korol et al. 2013, Carpintieri et al. 2010). In these cases, the energy absorption in failure zones is smaller than the energy release in remaining unloading regions under decreasing load (Tanabe et al. 2004).

Initially, the cylinders with one diameter of D=0.15 m were experimentally and theoretically investigated. During laboratory tests, a snap-back instability occurred. Therefore the test had to be performed under CMOD-control conditions. The vertical load was transferred to concrete specimens through: 1) a plywood board (in the form of surface contact) according to ASTM (ASTM C 496/C 496M-04) and 2) a steel cylinder (in the form of a line contact) to eliminate the effect of boundary conditions. Fracture was monitored using a high resolution and non-destructive technique in the form of the 3D x-ray micro-computed tomography (using Skyscan 1173 (Skarżyński 2016, Suchorzewski 2017b). In addition, the manual 2D digital microscope 'Scalar' was used. The main goal of those preliminary research works was twofold: 1) to check the effect of different boundary conditions on the strength and fracture (expressed by the different loading and supporting strip type) and 2) to investigate in detail the concrete behaviour during quasi-static splitting tension at the meso-scale level.

The splitting tensile experiments were performed in the static loading machine ZWICK Roaller Z400 (Fig.3.14). The machine was equipped with a crack opening extensometer (Sandner EXR10-2x) within the measurement range of ±2 mm with the maximum error of 2%. The extensometer base was equal to 40 mm. The extensometer was located at the mid-height of the concrete specimen and glued to the specimen front side (Fig.3.2.3). The quasi-static tests were performed under the CMOD-control (CMOD - crack mouth opening displacement) with the displacement rate of 0.00001 (1×10^{-5}) mm/s. Two types of loading/supporting strips were used: deformable plywood boards with the thickness of t=3 mm and width of b=25 mm (Fig.3.2.3b) and

rigid steel loading/supporting cylinders with the diameter of 20 mm (Fig.3.2.3a). The first loading/supporting strip is recommended by ASTM (ASTM C 496/C 496M-04). In the second case, the effect of boundary conditions was eliminated. Thus, the vertical load was respectively transferred to specimen through a surface contact or line contact.

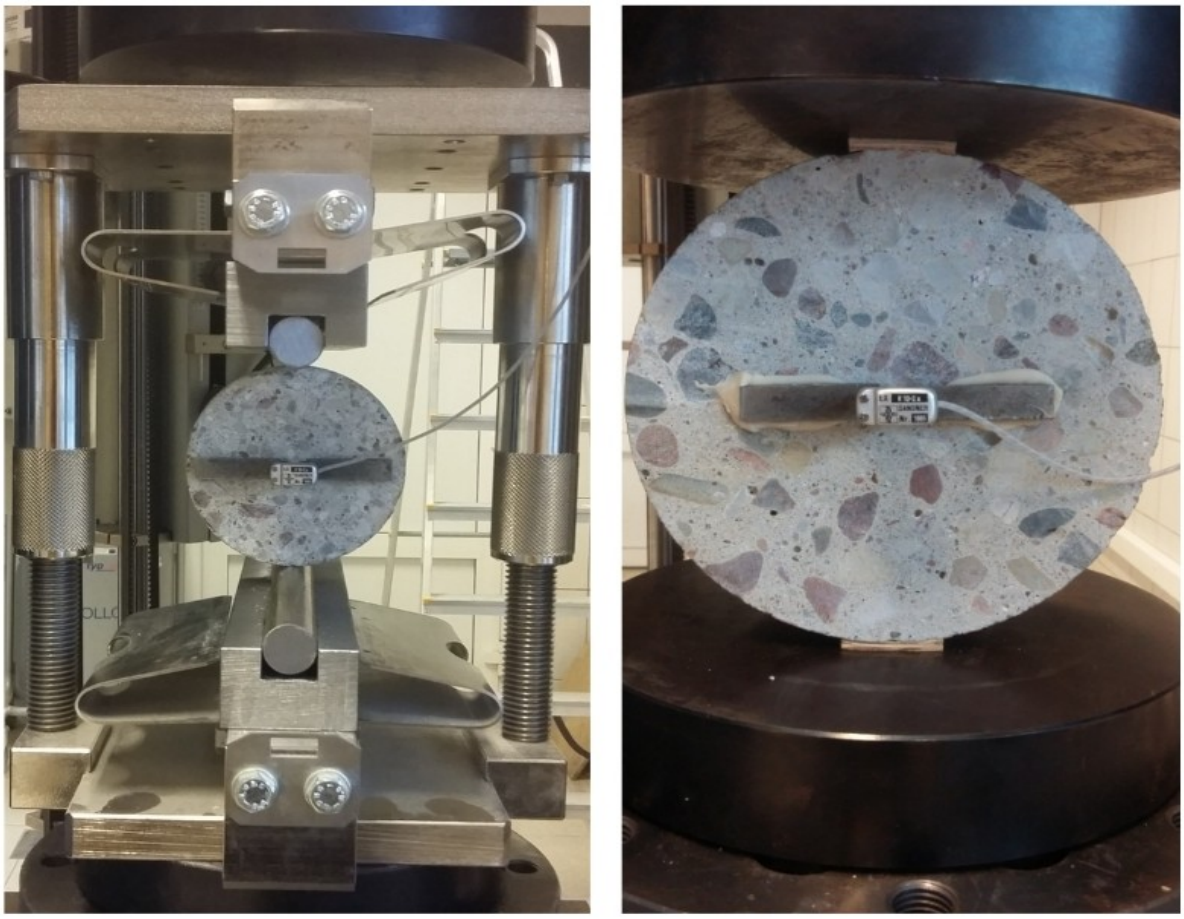

a) b)

Fig.3.14: View on loading machine Zwick Z400 with cylindrical concrete specimen of diameter D=150 mm and length L=60 mm for quasi-static splitting tensile tests: a) specimen loaded through steel cylinders and b) specimen loaded through plywood boards

Concrete was prepared in the weight proportion 3:1.6:7.1:12.6 (cement 32.5R, water, sand, aggregate). The minimum aggregate diameter was d_a^{min}=2 mm, maximum aggregate diameter was d_a^{max}=12 mm and mean aggregate diameter d^a_{50}=5 mm. The volumetric aggregate sieve content was 31.2% (diameter 2-8 mm), and 16.6% (diameter 8-12 mm). Thus, the aggregate volumetric content was 47.8%. The total particle volumetric content (sand and aggregate) in concrete was 75%. The concrete specimens with the diameter of D=150 mm were used. Based on experiments by Carmona et al. (Carmona et al. 1998) and Lamond (Lamond 2011), the minimum specimen length was

assumed L=60 mm (=5×d_a^{max}). The mean standard compressive strength of concrete tested on 3 cubic specimens 150×150×150 mm^3 was equal to $f_{c,cube}$=49.6 MPa and mean standard modulus of elasticity tested on 3 cylindrical specimens D=150 mm and length L=300 mm was E_c=33.1 GPa. Some papers (Lamond 2006, Carmona et al. 1998, Wu et al. 2018) report, the length of the cylinder does not influence the test results if the length is not shorter than 5 times the maximum diameter of aggregate 5xd_{max}. Nevertheless, the influence of cylinders length was checked experimentally on two specimens with the diameter D=150 mm (Fig.3.15A). Figure 3.15B presents two representative curves of specimens length a) L=100 mm and b) L=300 mm. The length of the cylinder neither influenced the strength nor the softening curve (as in the literature).

A)

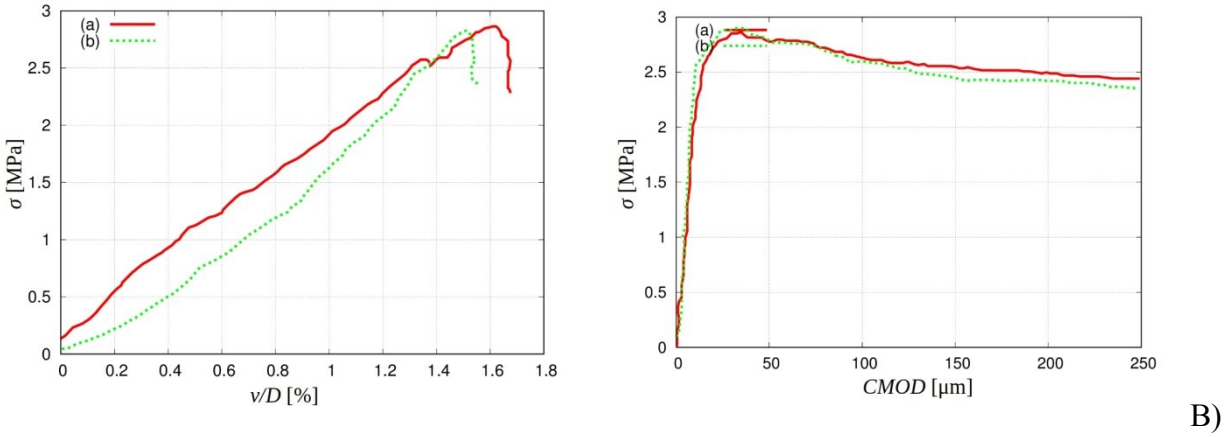

B)

a) b)

Fig.3.15: The specimens view A) and B) tensile stress σ versus a) normalised vertical displacement curves versus v/D in splitting tensile test for various specimen length: a) L=100 mm and b) L=300 mm

Stress-strain curves

Several splitting tests on concrete were carried out: 6 with plywood boards and 5 with steel cylinders. The splitting tensile strength was calculated as $\sigma=2P_{max}/\pi DL$ (P_{max} - the maximum vertical piston force). The maximum and minimum splitting tensile strengths were 3.44 MPa and 3.68 MPa with the standard deviation of 0.22 MPa for plywood boards and 3.26 MPa and 3.54 MPa with the standard deviation of 0.30 MPa for steel cylinders.

Figure 3.16A presents the experimental evolution of the representative splitting tensile stress versus the CMOD curve for concrete specimens using two types of the loading/supporting strip along the specimens (steel cylinders and plywood boards). The CMOD evolution during loading was perfectly linear in time. The splitting tensile strength varied between 3.26 MPa (P_{max}=47.2 kN, v=0.45 mm, CMOD=18 μm) and σ=3.64 MPa (P_{max}=51.2 kN, v=1.15 mm, CMOD=22 μm) for the steel loading/supporting cylinders (line contacts) and plywood loading/supporting boards (surface contacts), respectively. Thus, the splitting tensile strength was higher by about 10% for the plywood boards. Looking at the curve of the stress σ versus CMOD (Fig.3.16A), initially, concrete elastically behaved up to 70% of the maximum tensile stress σ and later slightly non-linearly up to the peak load. After the peak, the pronounced material softening occurred up to the residual state to failure. The residual stress was reached for σ=2.3 MPa (plywood boards) and σ=1.9 MPa (steel cylinder) for CMOD=110 μm. When considering the experimental splitting tensile stress - vertical piston displacement diagram $\sigma=f(v)$ (Fig.3.16B), the clear snap-back mode of failure occurred for v=1.15 mm (plywood boards) and v=0.45 mm (steel cylinders), expressed by a simultaneous reduction of the stress and displacement. Shortly before the test end, the displacement v slightly increased due to the specimen de-fragmentation.

In all tests, the main vertical macro-crack first occurred at the mid-height of the specimen in the central vertical zone (Fig.3.17). Then it propagated towards both the specimen top and bottom. Later depending upon the loading and support strip type it reached the top and the bottom of the specimen (Fig.3.17a) or branched to form a wedge directly under the plywood boards (Fig.3.17b). At the failure, the concrete specimen was divided into two halves.

Interfacial transition zones (ITZs)

ITZs around particles were characterized by a porous structure as compared to the cement matrix (Fig.3.1.3). Their width varied between 10 μm and 25 μm. They appeared around all aggregate grains (d_a≥2 mm) and usually covered about 80-90% of the aggregate circumference (Fig.3.18A) that was caused by a formation of water lenses beneath aggregate grains during mixing (Wang 2009). The width of ITZs was not connected with the aggregate diameter (Figs.3.18B-C).

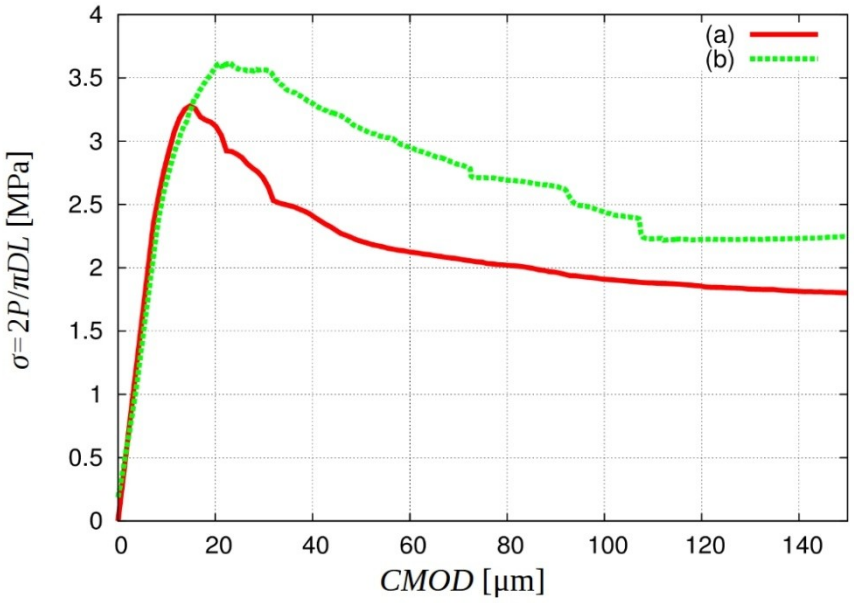

A)

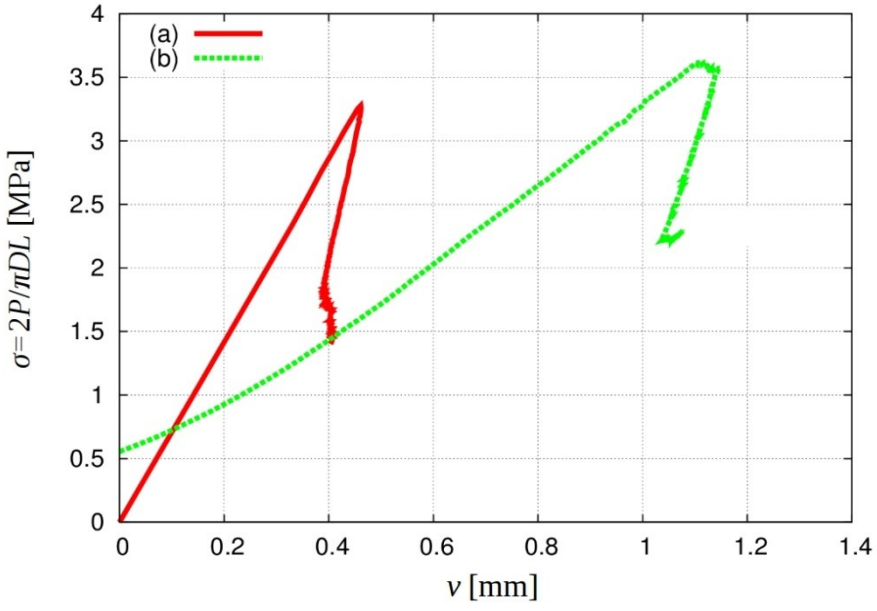

B)

Fig.3.16: Experimental curves for concrete specimens with diameter D=0.15 m): A) splitting tensile stress $\sigma=2P/(\pi DL)$ versus CMOD and B) splitting tensile stress σ versus top vertical displacement v for 2 different loading systems: a) through steel cylinder and b) through plywood board (P - vertical force, L - specimen length)

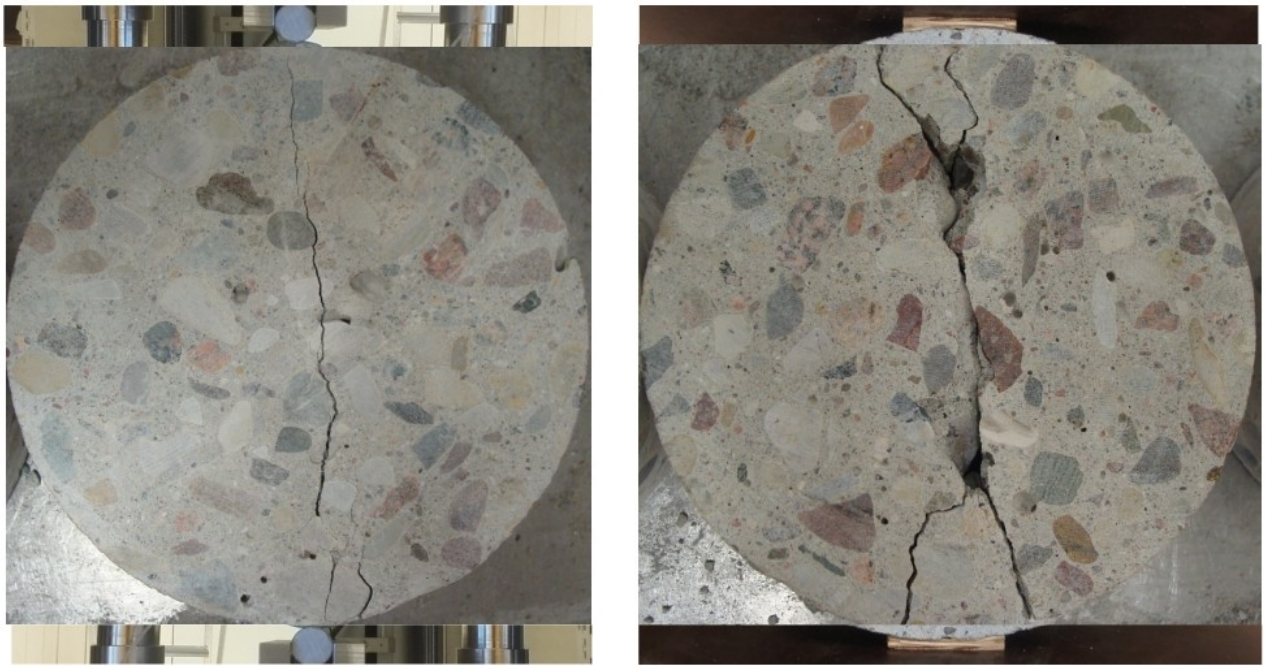

a) b)

Fig.3.17 Final crack pattern in concrete specimens after splitting tensile test with 2 different loading/supporting systems: a) through steel cylinder and b) through plywood board

Micro-CT scans of fracture

In order to measure more precisely the concrete porosity, a smaller concrete specimen (D=50 mm and L=60 mm) was cut out from the same concrete block and scanned by means of the 3D X-ray micro-tomograph Skyscan 1173 (Skarżyński et al. 2015) (Fig.3.19a). The particular phases of the concrete specimen (macro-voids, aggregate and cement matrix) are shown in Fig.3.19b (undamaged) and Fig.3.20A (damaged). The measured total volume of voids was p=3.2% and the measured volume of voids with the equivalent diameter d_p<1 mm was p=1.6% (Fig.3.19c).

The macro-crack images by means of the 3D x-ray micro-tomograph Skyscan 1173 are depicted in Fig.3.20 for the damaged specimen after the test (D=0.15 m, L=0.06 m). In order to obtain better accuracy in the X-ray micro-tomograph, the specimen width was diminished to 0.08 m after the test.

The particular phases are shown in Fig.3.20A. The macro-crack was curved along the vertical and horizontal plane due to a random presence of aggregate grains (Figs.3.20B-D). Sometimes it also propagated through macro-voids and aggregate. On the specimen front side, the macro-crack crossed e.g. 3 aggregate particles (Fig.3.21a). Please note that thus phenomenon occurred also under quasi-static conditions. The crack branching also occurred (Figs.3.22a b, specimen bottom).

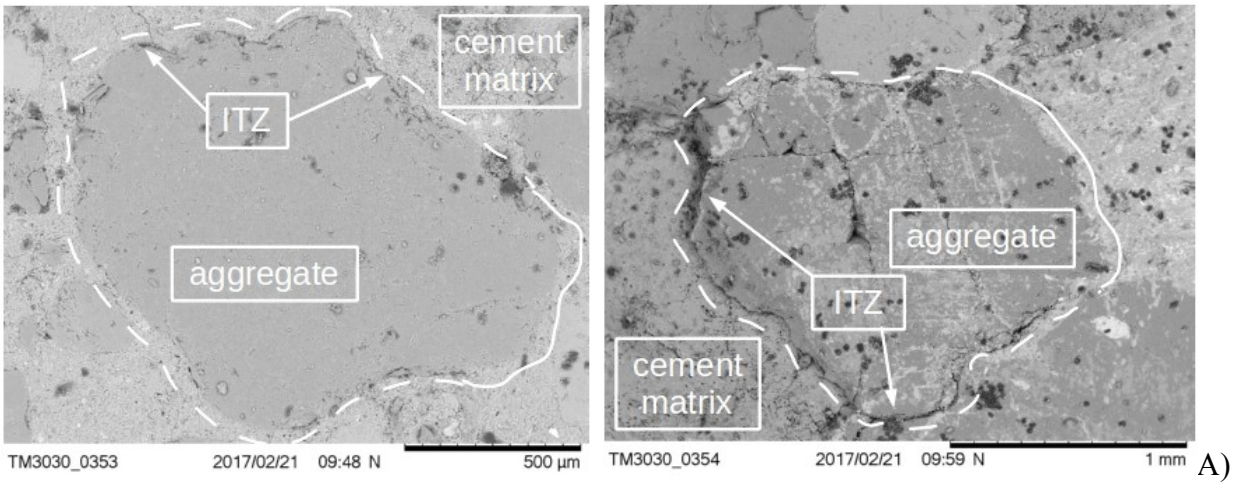

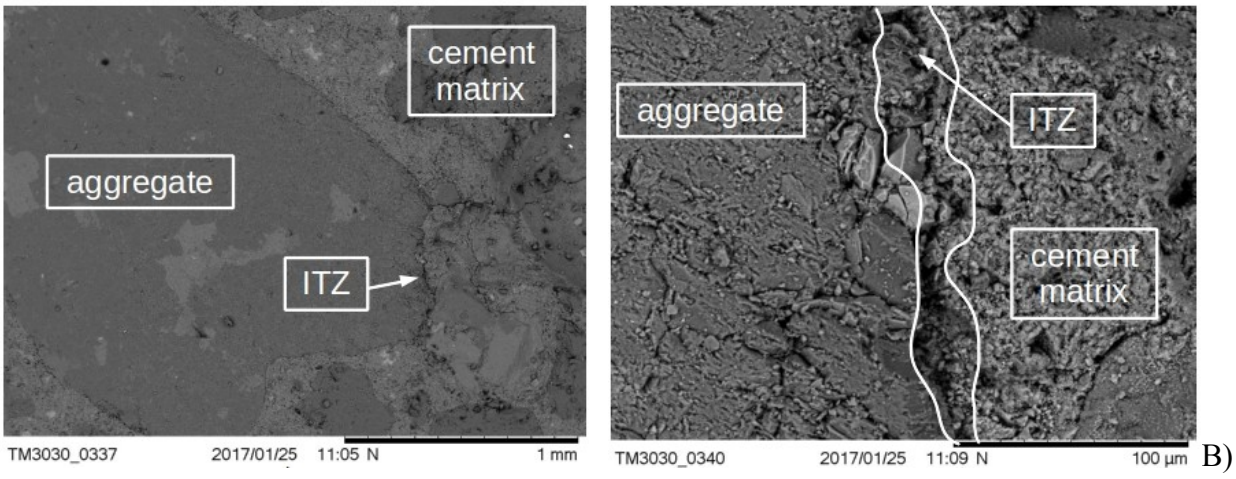

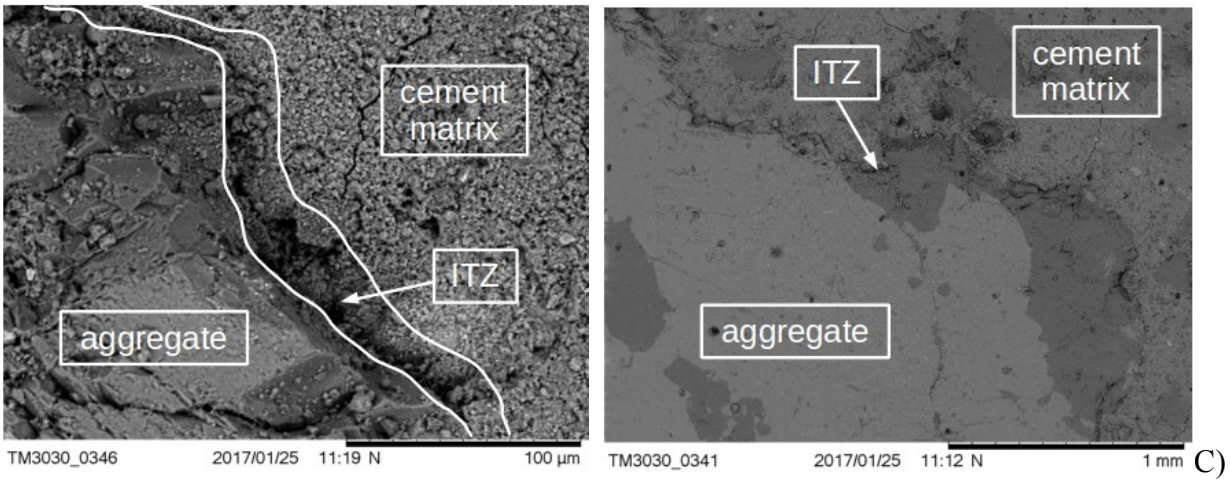

a) b)

Fig.3.18: Images of ITZs between aggregate and cement matrix in concrete specimen using SEM: A) view on arbitrary aggregate particle (continuous lines indicate no clear ITZs and dashed lines denote clear ITZs), B) view on aggregate particle of diameter d_a=2 mm and C) view on aggregate particle of diameter d_a=6 mm (a) magnification factor 100x and b) magnification factor 1000x)

The micro-cracks always initiated in ITZs along aggregate particles since they were the weakest phase in concrete (Fig.3.22a). When two interfacial cracks occurred around adjacent aggregates, a crack inside the cement matrix initiated to bridge the interfacial cracks so that a connected crack path was formed (Fig.3.22b).

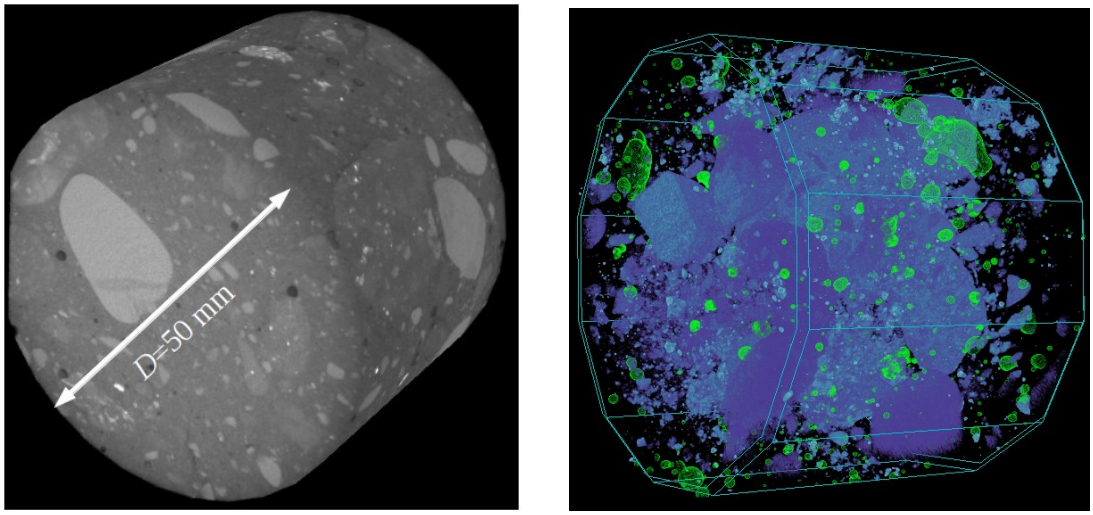

a) b)

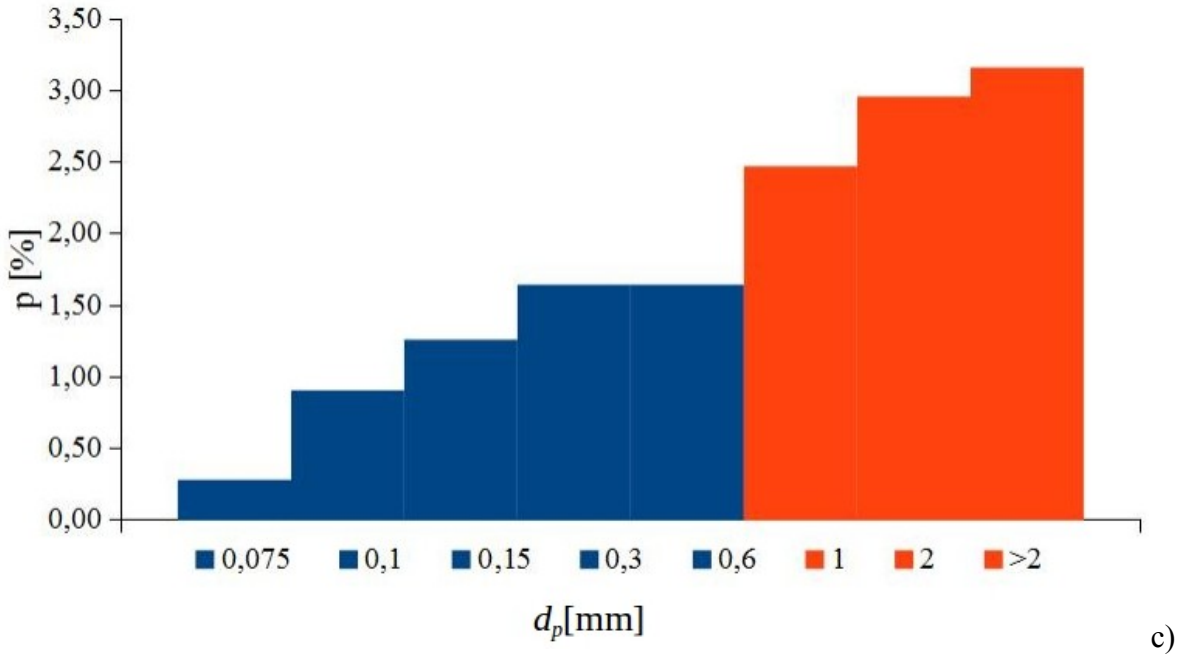

c)

Fig.3.19: Results of μCT for concrete cylinder specimen with diameter of D=50 mm a) general view, b) voids and aggregate particles in specimen (blue colour denotes aggregate and green voids) and c) volume of pores p with different diameter d_p (blue colour denotes micro-voids (d_p<1 mm) and red colour denotes macro-voids (d_p>1 mm), d_p - void equivalent diameter)

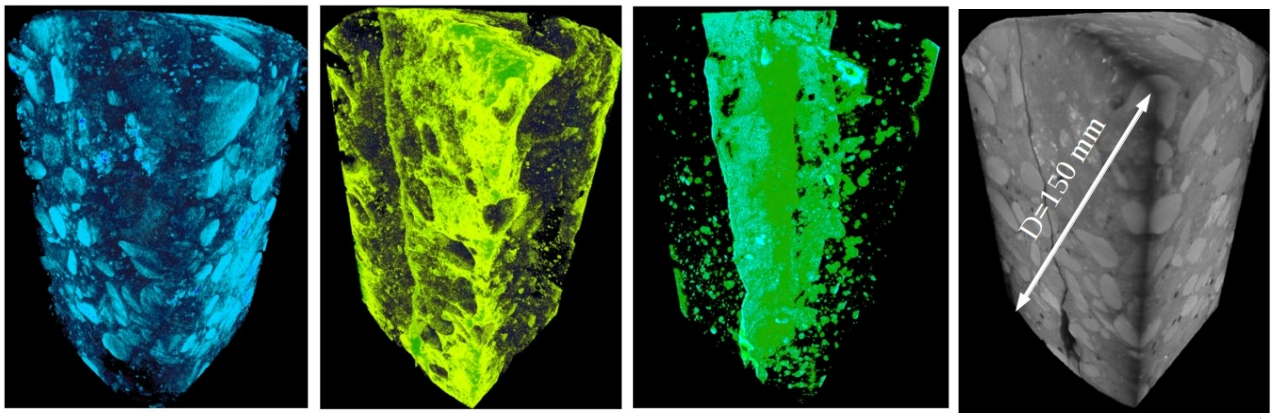

A)

a) b) c) d)

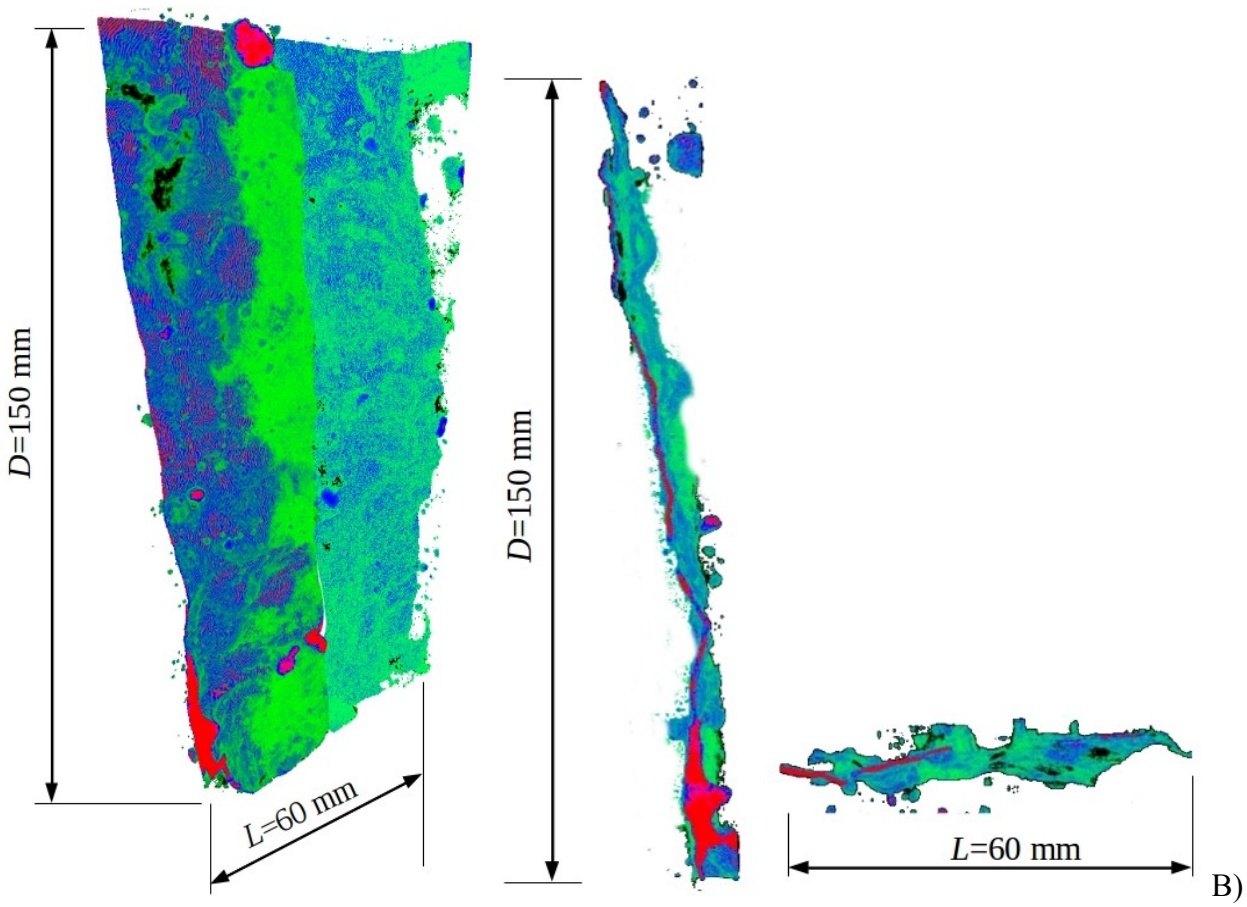

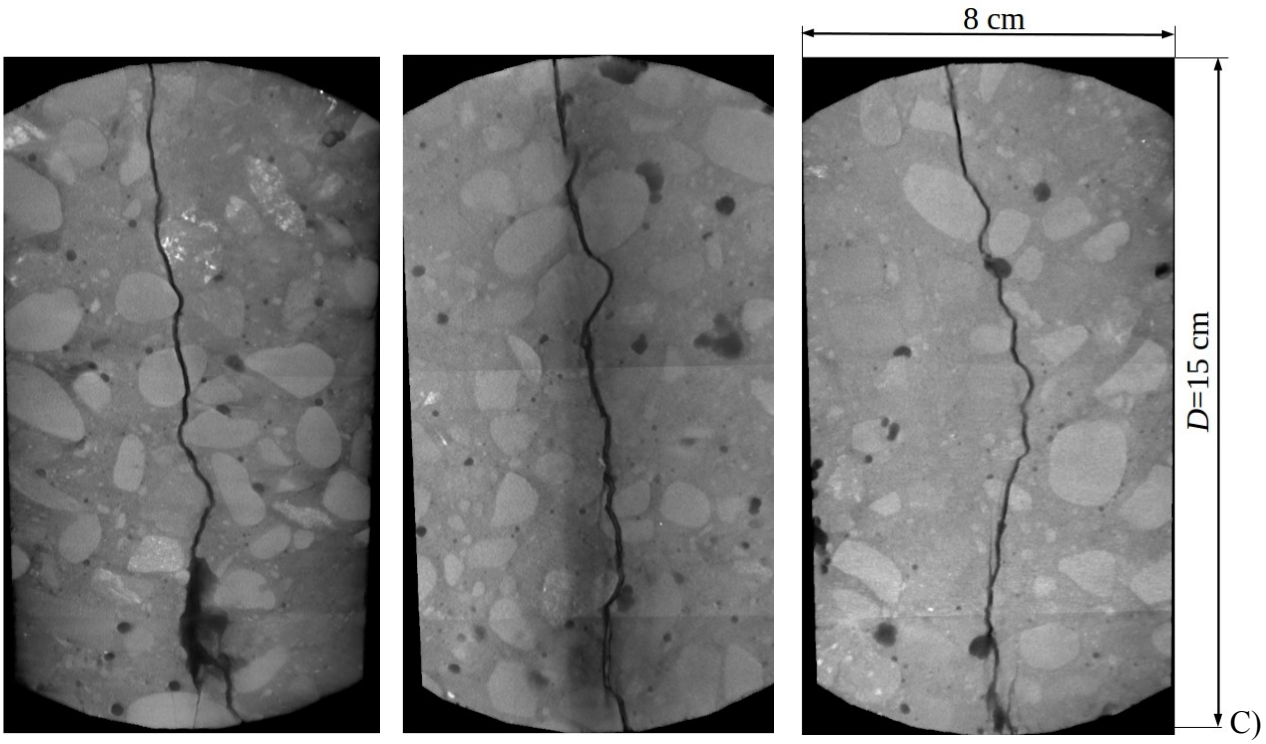

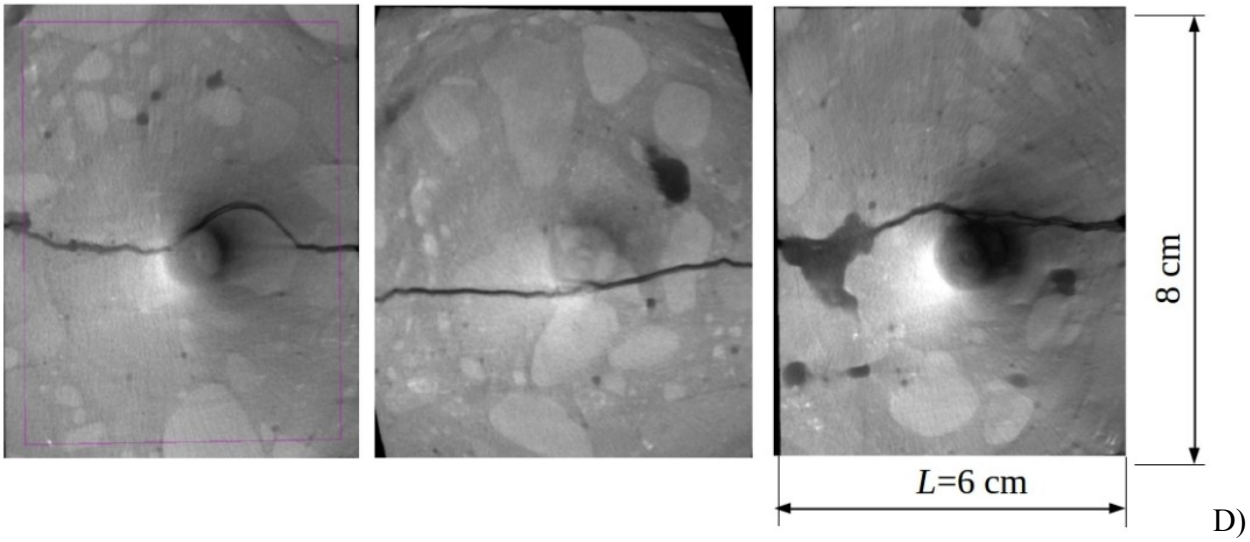

Fig.3.20: 3D μCT scan of concrete cylinder specimen with diameter of D=150 mm: A) view on specimen and phases (a) original scan, b) aggregate, c) cement matrix, d) voids and crack), B) 3D view on macro-crack (a) front view b) side view and c) top view (colours denote crack width w_c; w_c>200 μm (red colour), 50 μm≤w_c≤200 μm (green colour) and w_c<50 μm (blue colour))), C) vertical cross-sections (a) front surface, b) mid-length surface and c) rear surface) and D) horizontal cross-sections (a) mid-height, b) bottom and c) top)

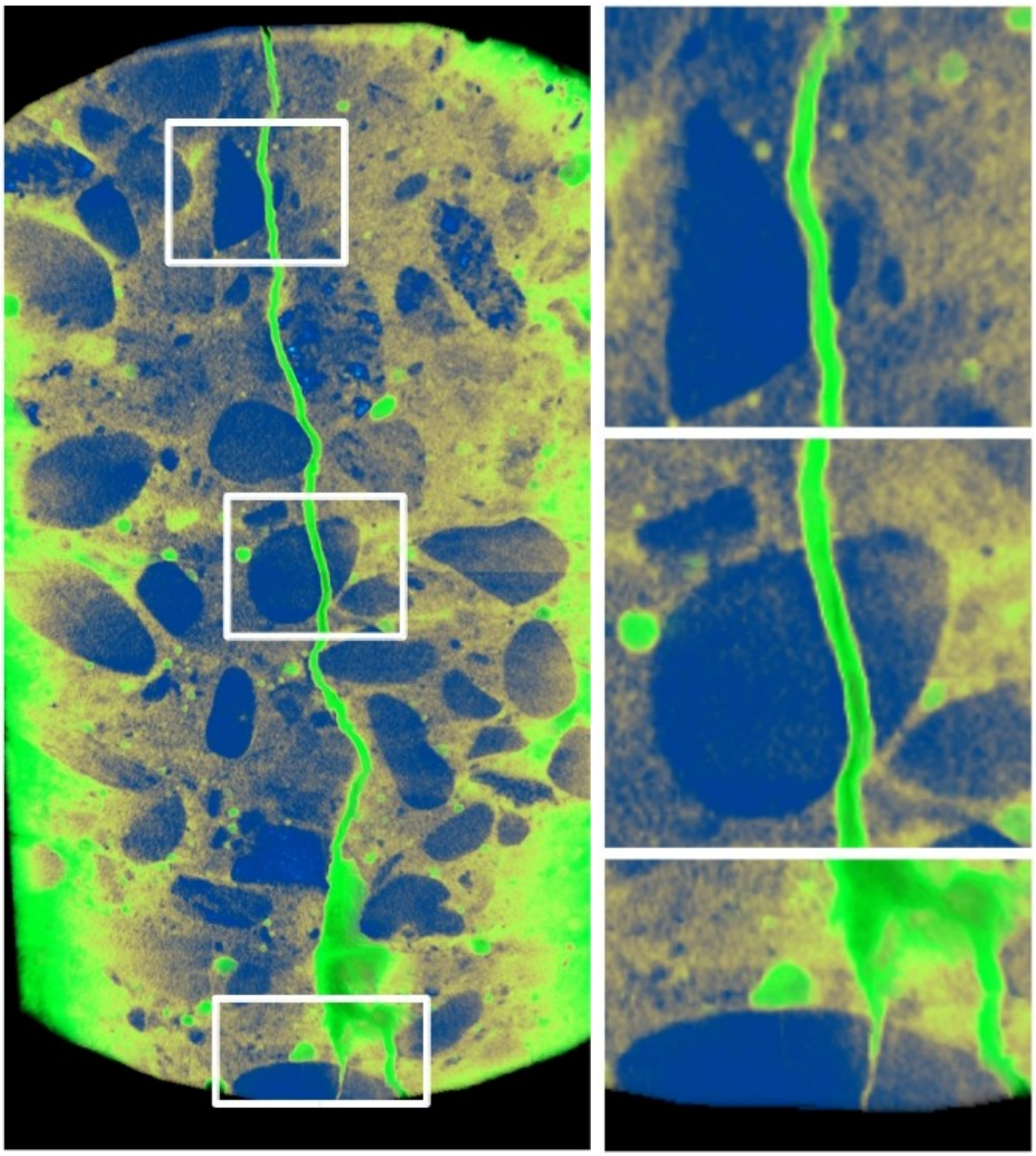

a) b)

Fig.3.21: 3D μCT scan of concrete specimen (D=150 mm) with propagating macro-crack: a) specimen front surface and b) zoom on macro-crack crossing aggregate particles (blue – aggregate, yellow – cement matrix and green - voids and crack)

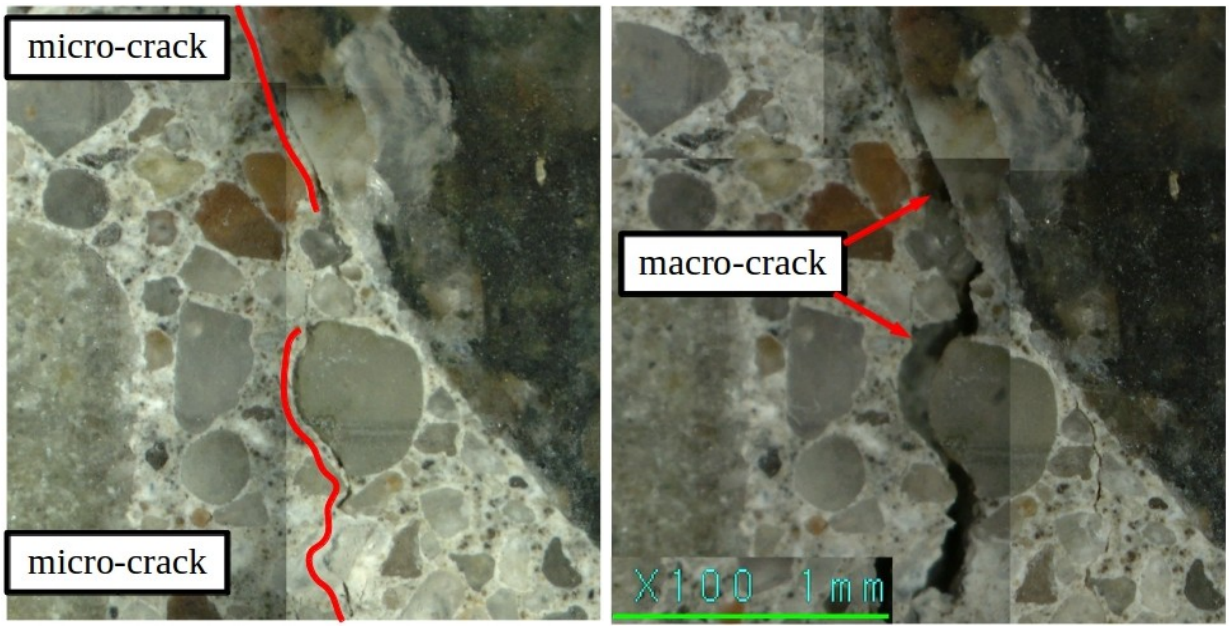

a) b)

Fig.3.22: Crack bridging mechanism on concrete front surface during laboratory test: a) initial micro-cracks in ITZs of 2 neighbouring aggregate particles (marked in red) and b) developed discrete macro-crack between 2 neighbouring aggregate particles (using manual microscope, magnification factor 100)

The Digital Image Correlation (DIC) technique was applied to visualize a fracture process zone (FPZ) on the rear side of the concrete specimen. DIC is a well-known velocity measuring non-invasive procedure, originally developed for fluid mechanics and used for the analysis of displacements in tests on soil and rock models (Rachenmacher&Finno 2004, Bhandari&Inoue 2005, Słomiński et al. 2007). It operates by tracking spatial variations of brightness within an image (divided into a mesh of patches) by comparing successive images so that displacement data can be extracted from sequences of images, and strains then calculated from gradients of measured displacements. The capability of DIC for measuring the shape and width of fracture process zones in concrete was confirmed in the experimental research results by Skarżyński et al. (Skarżyński et al. 2011, 2013a, 2013b). The digital camera Nikon D800 with the image resolution of 36 MPix was used. The images were taken every 2 seconds with the length resolution of 95 pixels/mm. The search patch of 15 pixels was used. FPZ appeared in the specimen mid-height at 80% of the peak-force and increased vertically and horizontally almost up to the peak (Fig.3.23). Afterwards, a macro-crack started to form. In order to calculate the width of a localized zone w_{lz}, the calculated particle displacements were fitted first by the error function ERF (Skarżyński et al. 2011):

$$ERF(x) = \frac{2}{\sqrt{x}} \int_0^x e^{-t^2} dt \,. \tag{21}$$

The halved error function evaluated at $\frac{x}{s\sqrt{2}}$ for the positive x-values gives the probability that the measurement under the influence of normally distributed errors with the standard deviation s has a distance smaller than x from the mean value. The fitting function parameter s in Eq.21 was used to determine the width of a localized zone w_c. Based on experimental results regarding concrete beams (Skarżyński et al. 2011), the width w_{lz} might be calculated from the equation $w_{lz}=4s$. Thus, 95% of the values of the normal distribution function area were within the distance of $2s$ in the both directions from the mean value. The measured width of FPZ was about 3.41 mm ($0.28\times d_a^{max}$) just before the peak (later a macro-crack was created).

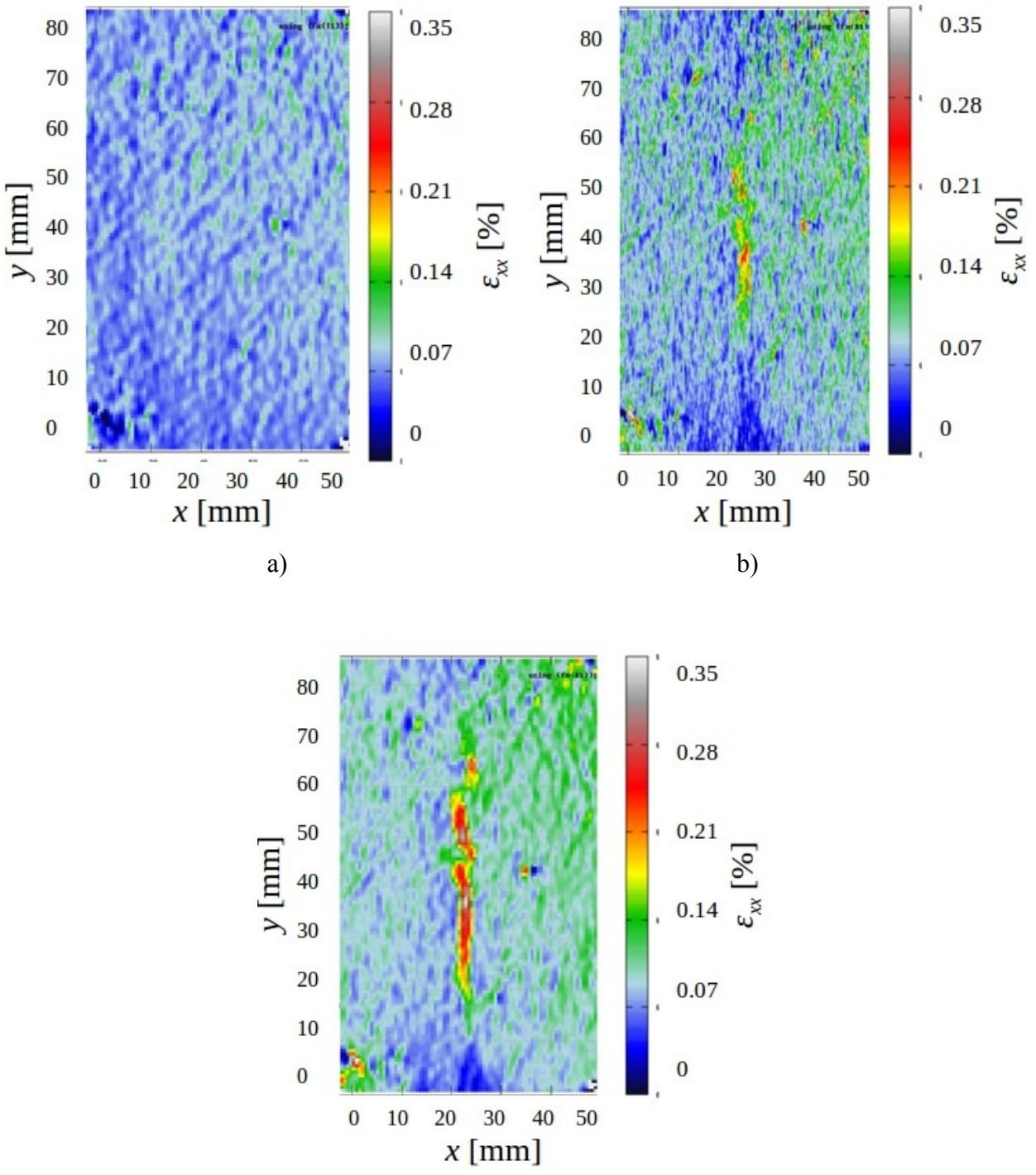

Fig.3.23 Evolution of horizontal strain maps of ε_{xx} based on Digital Image Correlation (DIC) technique in concrete specimen mid-height during increasing vertical force P: a) 50% of P_{max}, b) 90% of P_{max} and c) before peak (98% of P_{max}) for concrete specimen with plywood loading board (colours indicate strain magnitude, x - horizontal coordinate, y - vertical coordinate)

3.3 Tensile splitting tests with different specimen diameter

Specimens and test procedure

It was experimentally proven that a splitting tensile test is subjected to a size effect depending on the cylindrical specimen diameter (Fig.3.24) due to a non-uniform distribution of the tensile stress, caused by compression regions at the loading/supporting points. However, to the authors knowledge, no experimental data was published considering a brittleness increase with increasing diameter in Brazilian splitting test. Whereas, size effect is characterised by both the strength and ductility reduction with increasing specimen size. Therefore, the own experimental campaign was performed to measure the size effect both on strength and brittleness

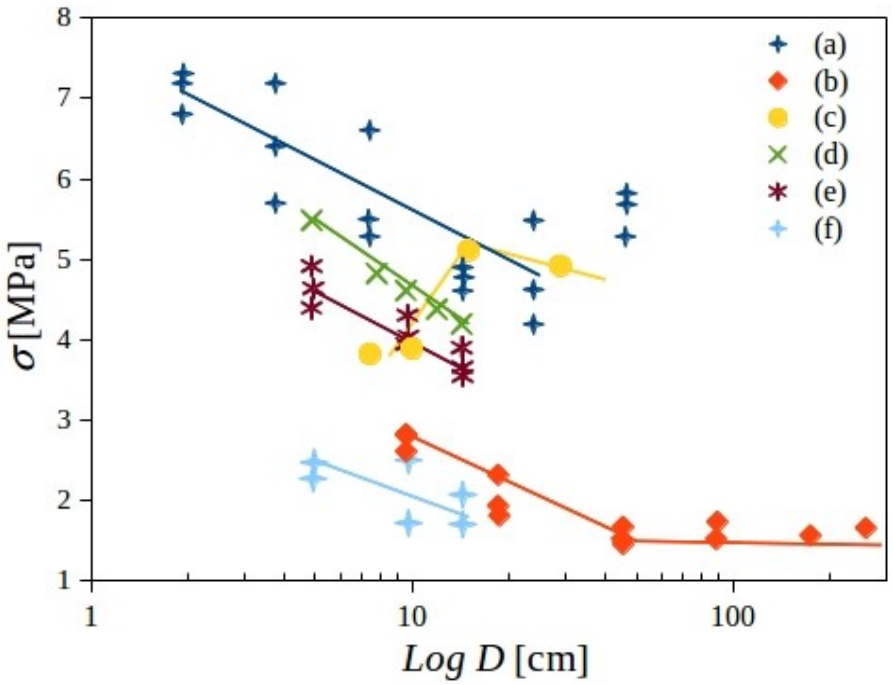

Fig.3.24: Relationship between maximum tensile stress $\sigma=2P_{max}/(\pi DL)$ and specimen diameter D (in logarithmic scale) in splitting tensile tests on plain concrete from laboratory experiments: a) Bažant et al. (Bažant 1987), b) Hasegawa et al. (Hasegawa 1985), c) Carmona et al. (Carmona 1998), d) Kadlecek et al. (Kadlecek 2002) and e) and f) Torrent (Torrent 1977) (continuous lines are trend lines) (P - vertical splitting force, D - specimen diameter, L - cylindrical specimen length)

The experimental programme on splitting tensile with specimens of the diameter D=74, 100, 150, 192 and 250 mm under the CMOD control were carried out (Fig.3.25). Two plywood board as loading strip were used and scaled proportionally with the specimen diameter. The strength and

ductility decreased with increasing specimen diameter. For large specimens D>100 mm, a clear snap-back occurred. The strain maps were obtained with digital image correlation DIC for various specimen sizes. During the test, a micro-cracking process was observed with the digital microscope. The interfacial transitional zones (ITZs) were investigated by scanning electron microscope. The specimens were sawed out from one concrete block with the dimension 200×200×20 cm^3 after 28 days from casting to obtain results independent of drying and shrinkage (Vorechovsky 2007). The concrete receipt was presented in Tab.3.1. The maximum aggregate diameter was 16 mm. The *w/c* ratio was equal to 0.77 and the sand point was 43.7%.

Tab.3.1 Concrete mixture receipt for 1 m^3

Concrete mixture for 1 m^3			
Ingredient	Type	Amount [%]	Mass [kg]
cement	CEM III 42.5 N		230
water	mixing		176
aggregate	sand 0-2	45	817
	gravel 2-8	25	454
	gravel 8-16	30	545
admixtures	MasterPolyheed219	0,7	1,61
ash EDF			70

Fig.3.25: The specimens with plywood strips scaled proportionally with specimens diameter (*b/D*=const.)

The specimens were loaded with loading/supporting strip according to europen codes []. The hardboard with the dimensions: *b*=10 mm and *t*=4 mm for *D*=150 mm (according to the European provisions) was used. For other diameters, the strips width *b* was proportionally scaled with the diameter (*b/D*=const.) to drop the influence of boundary conditions (Rocco 1999).

The specimens were loaded with static loading machine ZWICK Roaller Z400. The CMOD measurements and test parameters were the same as in Section 3.2. The test was performed with CMOD-control to obtain the snap-back behaviour for large specimens. The CMOD-time relationship was perfectly linear in all tests (Fig.3.26). The CMOD rate was not scaled with the specimen diameter since the loading had a static character.

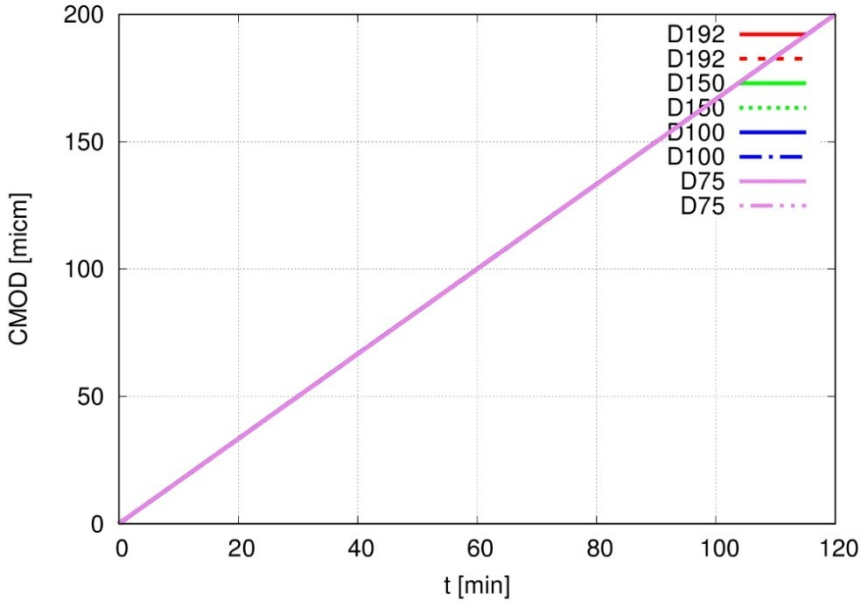

Fig.3.26: Relationship between crack opening *CMOD* and time *t* in experiments

Results

The tensile stress versus the normalised crack opening is presented in Fig.3.27. The clear decrease of strength with increasing diameter was observed. Also the large specimens were more brittle after the peak. The specimen of the diameter D=74 mm reached the average tensile strength of σ=4.35 MPa, for D=100 m - σ=3.55 MPa, for the standard diameter D=150 mm - σ=3.22 MP and for the largest diameter D=192 mm = σ= 2.8 MPa.

Figure 3.28 presents the evolution of the tensile stress σ versus the normalized vertical displacement v/D for the different specimen diameter. The results' scatter decreased with increasing specimen diameter D. Apart from the decreasing strength, the brittleness increased significantly after the peak load was obtained. For the specimens D=74 mm and D=100 mm, it was characterised by the increasing displacement after the peak while for D=150 mm, D=196 mm and D=250 mm, by the decreasing displacement after the peak.

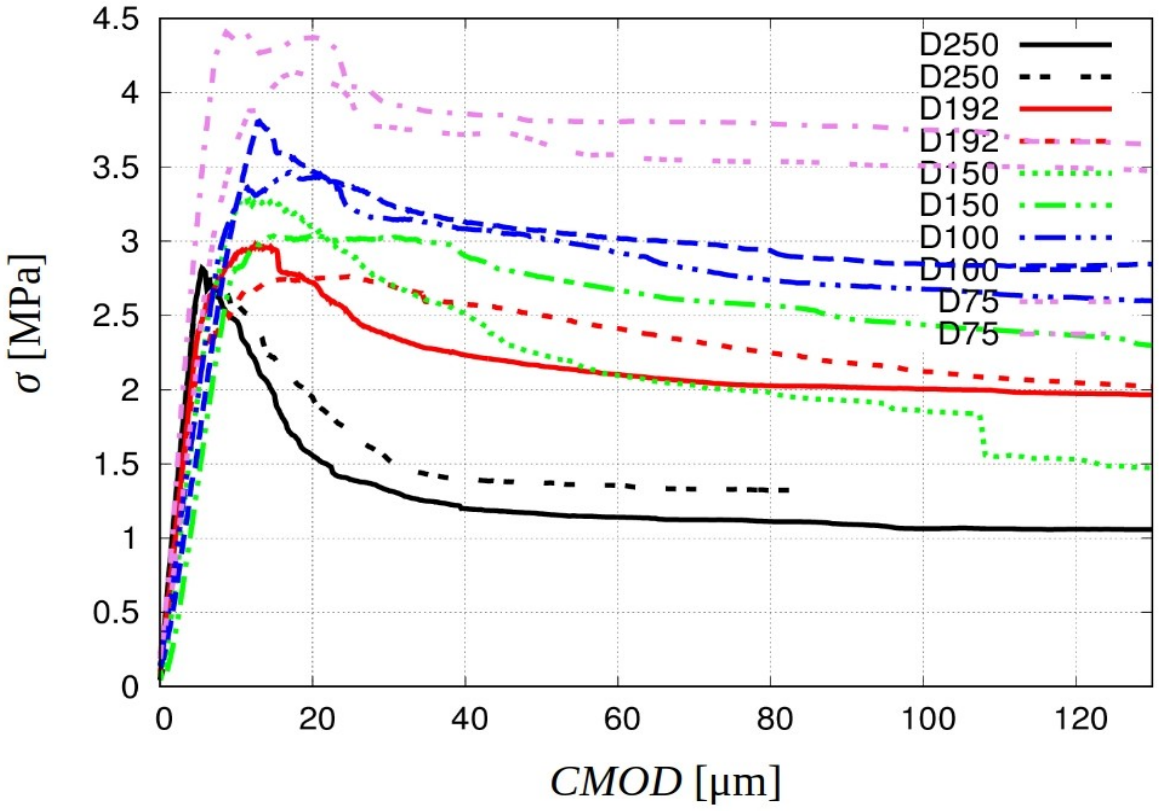

Fig.3.27: Tensile stress σ versus CMOD in splitting tensile tests with various specimen diameter D

The crack patterns are shown in Figure 3.29 for all tested specimens diameters. For the specimen D=74 mm with a higher peak load, the crack had two branches dividing a central part of the specimen from the other two halves (Fig.3.29Aa). For the second specimen with the same diameter, no wedges were observed under supports, however, a secondary crack occurred at the right top of the specimen at the circumference (Fig.3.29Ab). For the rest of the specimens, a single crack occurred with characteristic wedges under loading/supporting strips. The larger specimen diameter was, the less crack was curved.

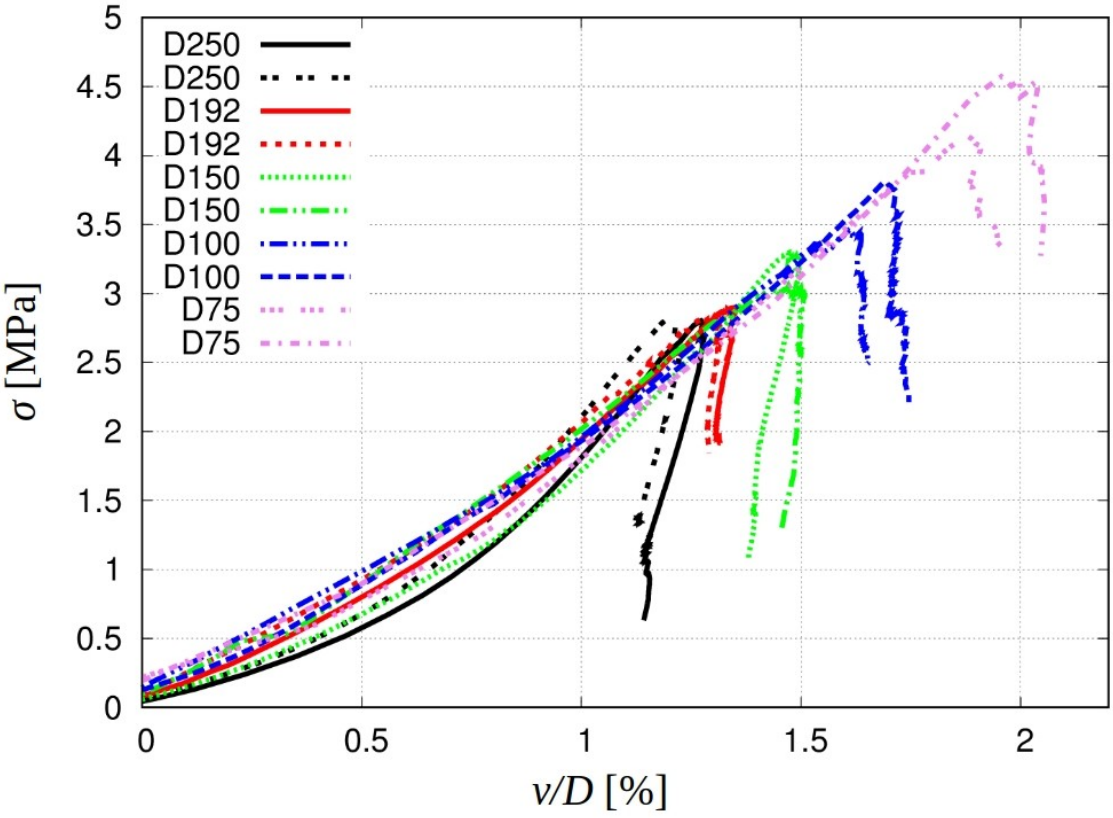

Fig.3.28: Tensile stress σ versus v/D in splitting tensile tests for different specimen diameter

Micro-CT scans of fracture

One specimen of each diameter was scanned with micro-CT before loading. Then the specimen was loaded until CMOD=200 μm and scanned again. The mid-sections of the specimen D=74 mm were carefully analysed and compared with the undamaged state.

The basic three phases of concrete were determined from 3D micro-CT images (Fig.3.30a): aggregate (Fig.3.30b), cement matrix (Fig.3.30c) and voids (Fig.30d). Moreover, the aggregate size distribution and pores structure were analysed. The segmentation was performed with the CTAn 1.17.7.2 software delivered by the firm SkyScan Bruker (the producer of the micro-tomograph). The bottom and top threshold used for each phase was: 0-63 (pores and cracks), 63-112 (cement matrix) and 112-255 (aggregate). After thresholding, fine particle "despeckle" was used to remove the objects finer than 10 voxels (in volume) except pores.

A)

B)

C)

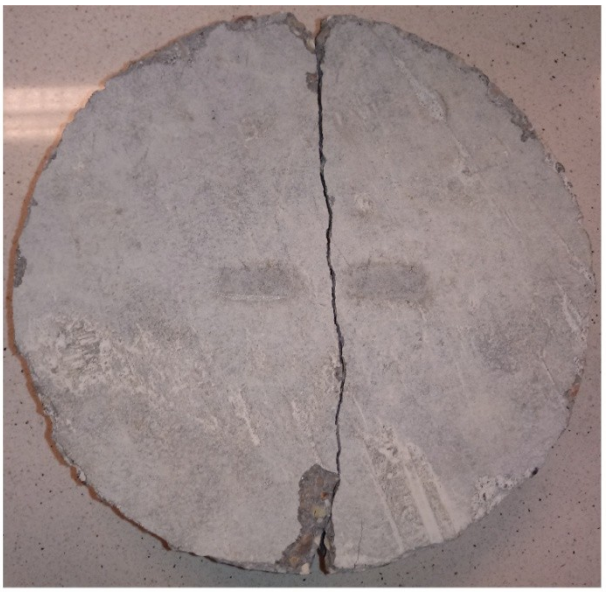

D)


E)

Fig.3.29: The crack patterns for specimens diameters A) *D*=74mm, B) *D*=100 mm, C) *D*=150 mm, D) *D*=192 mm and E) *D*=250 mm for each tested specimen

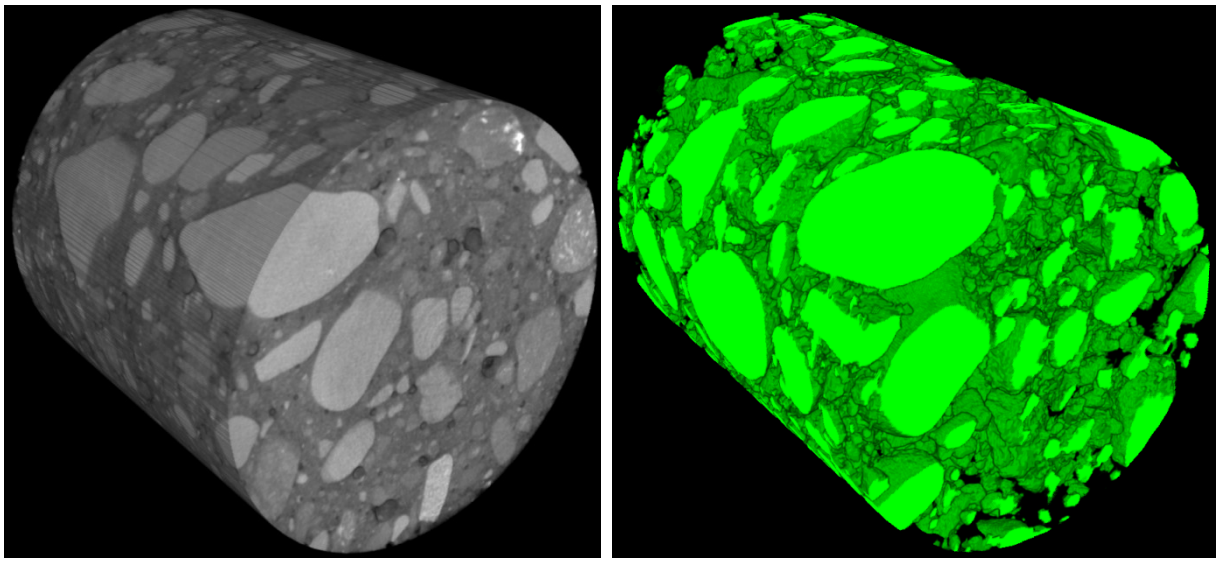
a) b)

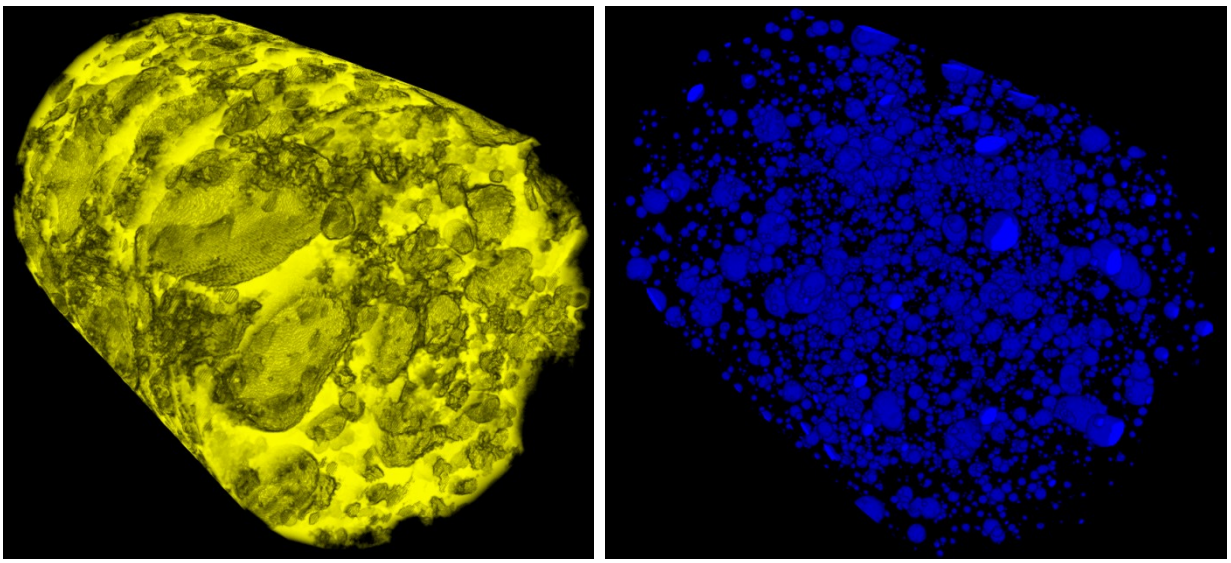

c) d)

Fig.3.30: 3D image of small specimen with dimater of D=74 mm before test: a) original image and visible phases, b) aggregate, c) cement matrix and d) voids

The crack surfaces of all specimens were segmented and the cracks' volume was determined. Some cracks were connected with inner pores during fracture what increased the cracks' volume. For the specimen D=74 mm, the main crack was the most curved (Fig.3.31a). The crack did not crush aggregate particles. The total crack volume was V=117.10 mm^3 and the average crack width was w=0.19 mm. The crack in the specimens D=150 mm and D=250 mm was less curved and exhibited typical wedges oat the specimens top and bottom under the loading/bearing strips (Fig.3.3.1b-c). The crack volumes were V=103.53 mm^3 and V=78.74 mm^3 and the average crack widths w=0.086 mm and w=0.039 mm for the specimens D=150 mm and D=250 mm. Moreover, in the specimen D=250 mm, the crack had a few fine branches in the zones ahead of wedges (Fig.3.31c). The crack volume and average crack width decreased with increasing specimen diameter. In the specimens with D>74 mm, the crack intersected 6 (D=150 mm) and 11 aggregate particles (D=250 mm).

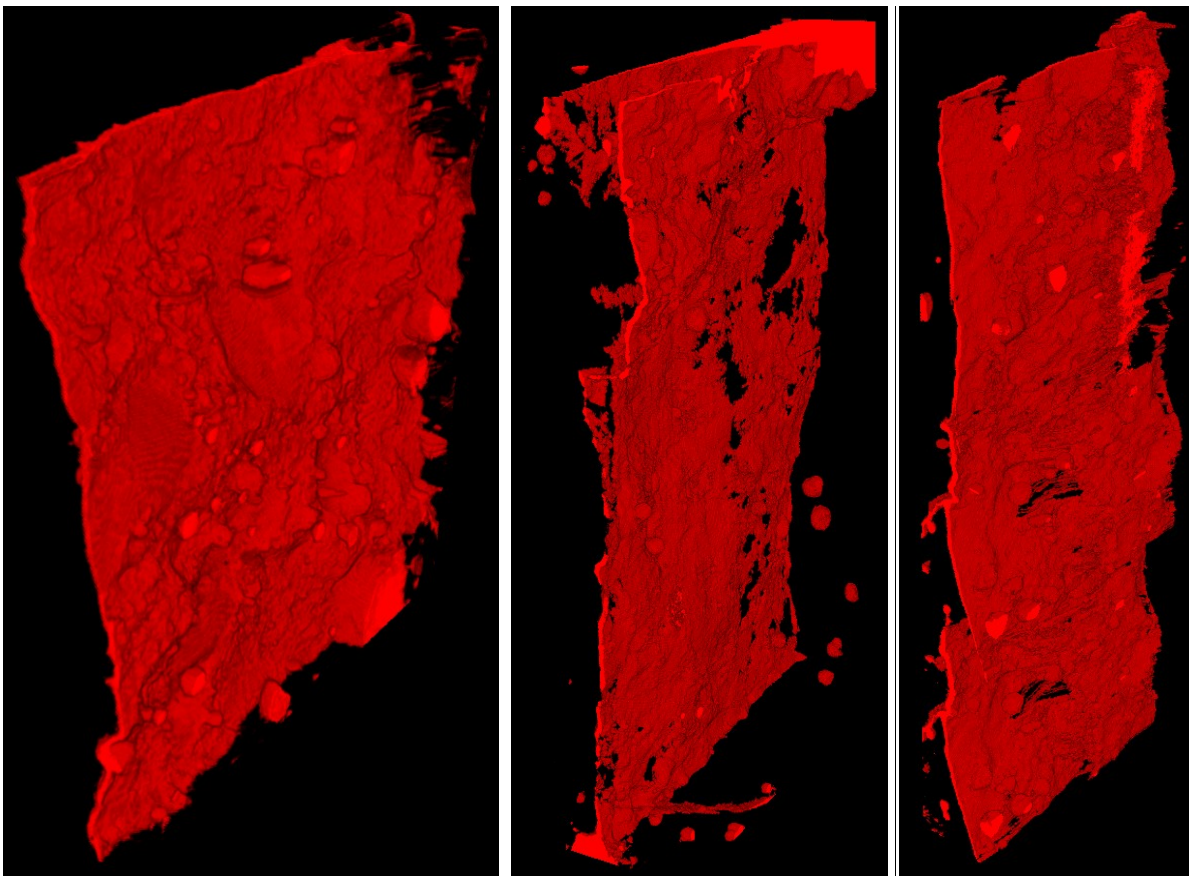

a) b) c)

Fig.3.31: 3D image of crack for specimens: a) *D*=74 mm, b) *D*=150 mm and c) *D*=250 mm after test

The cracks are also presented in Fig.3.32 with the marked thickness. The image was segmented in CTAn and exported to CTvox in 4 files representing each structure thickness (red w>0.2 mm, green 0.2 mm > w > 0.1 mm and blue 0.1 mm > w > 0.05 mm). It was extremely difficult to segment cracks finer than 0.05 mm (50 μm) since they were close to the used image resolution. The higher thickness of the crack for specimen *D*=74 mm was clearly visible as the red colour dominated over the others in the almost entire specimen (Fig.3.32a). The crack in the specimen *D*=150 mm was typical for splitting tension with the largest width in the specimen mid-height. Clear wedges both at the specimen top and bottom occurred (Fig.3.32b). In the specimen *D*=250 mm, the crack width was non-uniform with a high crack opening at the 3/4 height and wide opening on the front side (Fig.3.32c).

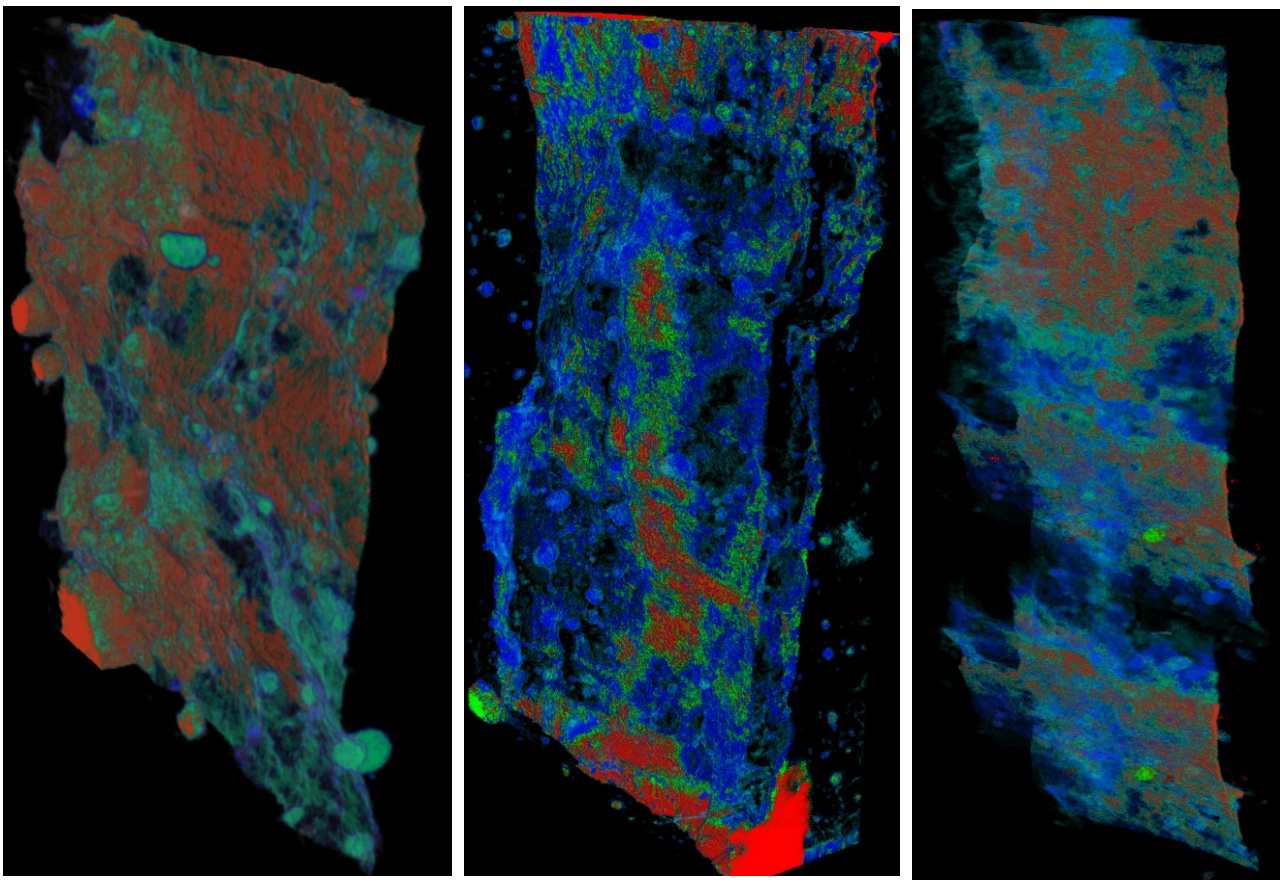

a) b) c)

Fig.3.32: 3D images of crack for specimens: a) D=74 mm, b) D=150 mm and c) D=250 mm after test (the colours represent crack width: red w>0.2 mm, green 0.2 mm > w > 0.1 mm and blue 0.1 mm > w > 0.05 mm)

Size effect

During the experimental campaign, the clear size effect occurred with respect to strength (Fig.3.33) and brittleness (Fig.3.34). The strength decreased the most for small specimens from σ=4.4 MPa (D=74 mm) to σ=3.6 MPa (D=100 mm), so by 15%. The strength decreas was the smallest for largest specimens (by only 3% between D=192 mm and D=250 mm). The brittleness was defined the angle between horizontal axis and the stress-strain curve in a counter-clockwise direction. The relation of brittleness to the diameter was opposite with very similar trend (Fig.3.34), however the angle α change by 9% (between D=74 mm and D=100 mm) and 5% (between D=192 mm and D=250 mm).

The results of own experiments on splitting tension were compared with the size effect law by Bažant's (SEL type I for unnotched specimens). The parameters of the size effect were calibrated

with a regression at the point D=150 mm and corresponding mean strength of f_t=3.13 MPa: B=5.40 and D_0=5.39 (Fig.3.35). The experimental results were in good agreement with theoretical solution except of the largest specimen D=250 mm, where the strength's reduction was smaller by 30% than the one predicted by SEL.

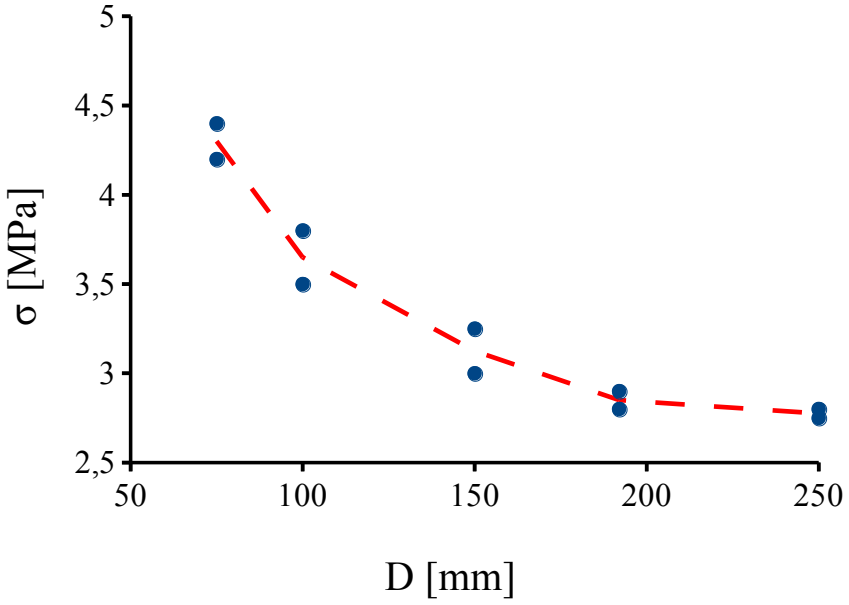

Fig.3.33: Experimental results of tensile strength σ against specimen diameter D (dots) and mean value trend (dashed line)

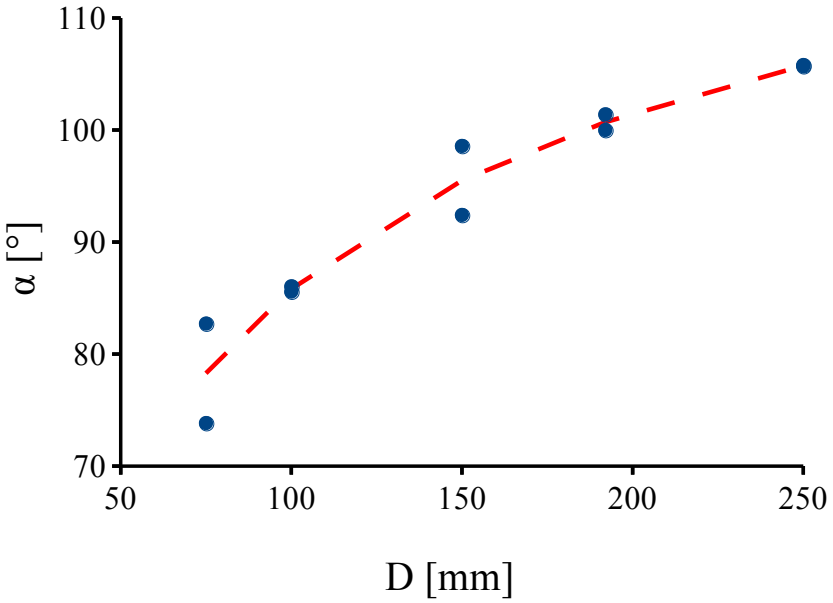

Fig.3.34: Softening parameter α versus specimen diameter D (dots) and mean value trend (dashed line)

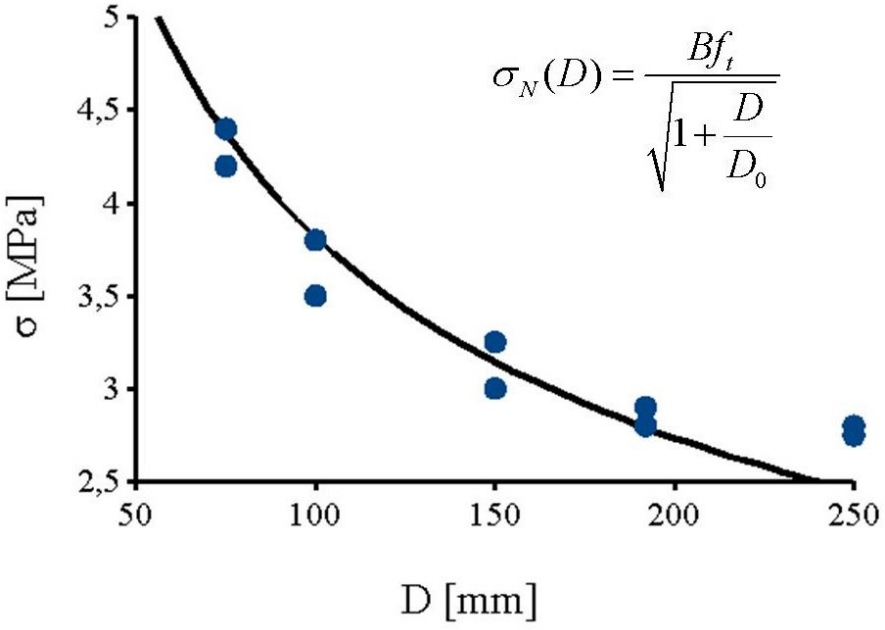

Fig.3.35: Comparison between experiments and SEL type I by Bažant (1987): tensile strength σ versus specimen diameter D

Chapter 4

DEM model for concrete

The discrete element method (DEM) was chosen due to its evident advantages in studying a meso-scale concrete behaviour at the aggregate level (Skarżyński et al. 2005). In general, DEM has the following advantages:

1) DEM can directly simulate the materials' heterogeneous meso- or micro-structure by taking into account different material phases, their random properties and distributions.
2) DEM is an effective tool for deep studies of fracture including initiation, growth and propagation of micro-cracks (strain localization) and discrete macro-cracks.
3) DEM may be used for effective calibration of continuum models for concrete with respect to a characteristic length of micro-structure, crack opening width, instant formation of a discrete macro-crack, effective elastic and inelastic parameters, damage evolution rule, fracture toughness and micro- and macro-cracking.

The shortcomings of DEM are: 1) the enormous calculation times due to a huge number of discrete elements to properly reproduce the meso-structure of materials and 2) the difficulties with respect to calibration due to the lack of suitable meso-scale laboratory experiments. In this thesis, the 2D and 3D material meso-structure was mainly obtained by very advanced micro-tomography system.

DEM comes from molecular dynamics methods used in physics since the early 50. The original DEM was formulated by Cundall and Strack (1979). Next, it was successfully used in analyses of different particulate materials in the powder, mining, milling, pharmacy, ceramics and composite industry et ca. (Fleissner et al. 2007, Ketterhagen et al. 2009, Nosewicz et al. 2013, 2019). DEM considers a material as consisting of particles interacting with each other through a contact law and Newton's 2nd law via an explicit time-stepping scheme. Outstanding advantages of DEM include its ability to explicitly handle the modelling of particle-scale properties including size and shape which play an important role in the concrete fracture behaviour (Donze et al. 1999). DEM does not use a set of differential or integral equations for describing the problem (in contrast to FEM). The discrete calculations may generally use two types of particles: hard particles and soft particles. The hard-particle approach makes an assumption of the contact duration time equal to zero, perfectly corresponding to the kinetic theory of instantaneous contacts. This approach may fail numerically with the 'inelastic collapse' (McNamara and Young 1994) when the time between particle collisions

is very small and the contacts density is very low (or contacts are constant). This assumption is true for gases, some fluids or sparse (non-dense) granular media wherein collisions are rare. For solids, it is rather incorrect as contacts take usually finite times and they are not discrete events. There are numerical methods of handling inelastic collapse problem, however, they always need to be validated with soft-particle DEM (Luding 2008). The hard-particle approach is very time-efficient as the integration time may be as large as the time between collisions by introducing the event-driven scheme. The soft-particle approach is more commonly used and is not limited to short-lasting contacts. Therefore, the soft-particle approach may be used in complex discrete systems with multiple long-lasting contacts. The rigid particles in this approach may deform during the contact existence. The deformation is usually realised as a particles' overlap and rarely as particles' deformation. The forces are calculated for each contact based on a force-displacement relationship that defines the contact stiffness. The disadvantage of soft-particle approach is a very small time step necessary to correctly integrate numerically the equations of motion, resulting in a huge calculation cost (Ketterhagen et al. 2009).

The motion equations of DEM are:

$$m_i \ddot{} \quad \cdot \quad m_i^* g_x - \Sigma^n F_x^{i,j} \tag{22}$$

$$m_i \ddot{} \quad \cdot \quad m_i^* g_y - \Sigma^n F_y^{i,j} \tag{23}$$

$$0.5 m_i R_i^2 \ddot{} \quad \cdot \quad \Sigma^n M_A^{i,j} \tag{24}$$

where m_i is the particle mass, c_i is translation and d_i rolling damping coefficient, g_x and g_y stand for gravity acceleration, f are the external translation (f_x, f_y) and angular (f_A^i) forces acting on the sphere, ¨ and ˙ are the normal acceleration and velocity and ¨ and ˙ stand for the angular acceleration and velocity. F_x and F_y are the internal forces acting on the sphere and M_A is the internal momentum.

The simplest discrete approach used for concrete modelling is a truss-model where every interaction connecting a pair of particles transmits translational degrees of freedom (Kosteski and Iturrioz 2013). The rods are removed when cracking occurs. To better reproduce the material softening, beams instead of rods have to be used that include also rotational degrees of freedom (Schlangen and Garboczi 1997, Kozicki and Tejchman 2008, Tran et al. 2007, 2011). The introduction of different phases with various strengths supports a non-linear behaviour and provides more realistic

results with respect to the post-peak material behaviour (Kozicki 2007, Kozicki and Tejchman 2008).

4.1 Calculation procedure

The calculation procedure of DEM is simple and correspond to explicit solutions in FEM. First, the bodies are defined with their position (*x,y,z*), shape (for spheres defined with one variable - radius *R*) and material parameters (like mass density *m*). After that, the initial forces existing in a discrete system from the previous step are reset. Then, based on the geometry, the particle interactions are found for every pair of overlapping particles. If new interactions appear, they are updated. According to the contact material law, the tangential and normal forces are computed. After that the additional forces like gravity or connected with boundary conditions are added. The forces are generalised for each discrete particle. After that, through second Newton's law of motion, the acceleration *a* of each particle is calculated simply as $a=F/m$ (where *F* is force vector). Then owing to the equations of motion integration, the velocities and displacements are calculated and applied for each particle. This loop (Fig.4.1) is being repeated with a small time increment up to the simulation end.

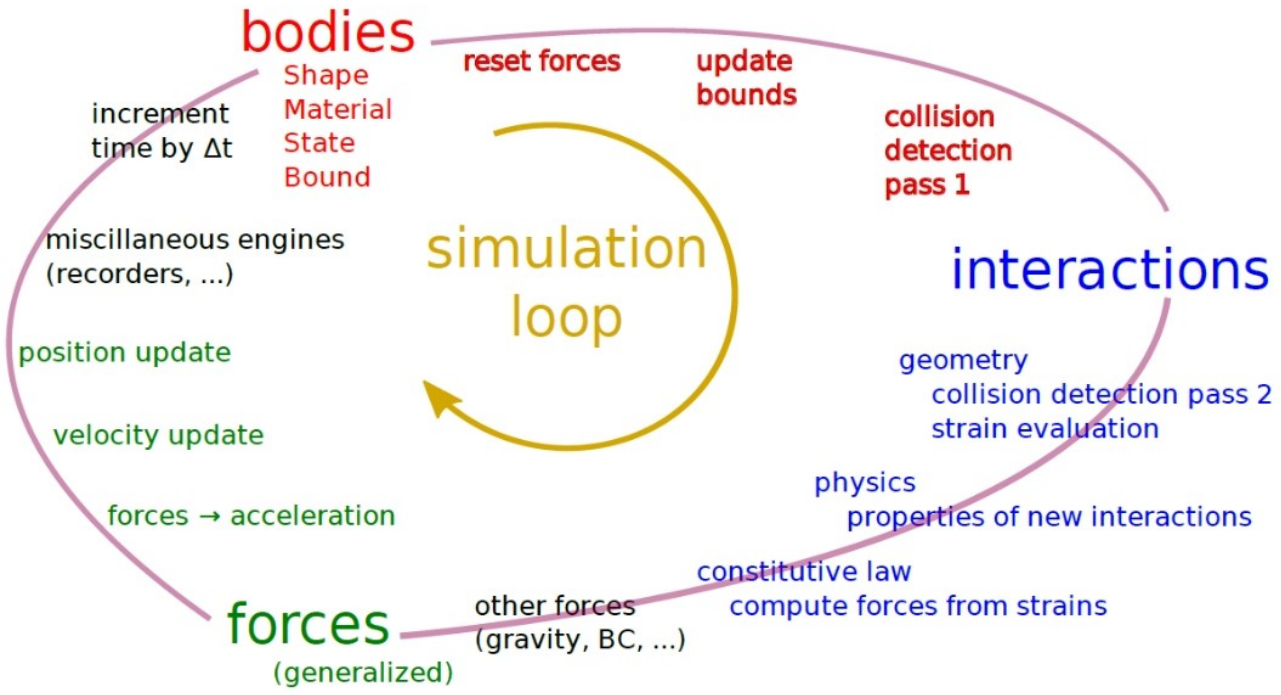

Fig.4.1: Typical simulations' loop (each step begins with "bodies" and continues clockwise with time increment update) (Smilauer et al. 2015)

The deformation of particles is assumed as very small as compared with the entire deformation system, therefore the particles move as rigid bodies and may overlap according to their size. For a simple contact of two discs (marked as particle '1' and '2') approaching to each other with a constant velocity v in time steps Δt, small enough that the discs cannot pass through each other and the overlap increment can be calculated as $\Delta n = v\Delta t$ (Fig.4.2). Knowing the positions of both discs $A_1(x_1,y_1)$ and $A_1(x_2,y_2)$, the contact point may be calculated as the mid-point between the discs' positions. The relative displacement Δn is connected through a force-displacement law (Fig.4.2.2) with contact force with the following expression:

$$\Delta F_n = k_n \Delta n \,, \tag{25}$$

where k_n represents the normal contact stiffness related to the contact Young modulus E_c, Poisso's ratio ν and disc radii R_1 and R_2 and ΔF_n is the increment of the normal force. Assuming the positive direction of the force from the element '1' to the element '2', the forces acting on each particle are:

$$F_{x1} = k_n \Delta n \text{ and } F_{y1} = -k_n \Delta n \,. \tag{26}$$

The forces in Eq.26 allow for determining the new accelerations using the second Newton's law as:

$$\ddot{x}_1 = F_{(1)x} / m_1 \text{ and } \ddot{y}_1 = F_{(2)} / m_2 \,, \tag{27}$$

where $\ddot{x}_1$ and $\ddot{y}_1$ represent 2' the accelerations of the discs '1' in the direction of the applied velocity v and m_1 and m_2 stand for the particles masses. The accelerations calculated by those equations are assumed to be constant over the small time step Δt. By transformation and simplification (no gravity, no external forces, no moments) of the general DEM equations of motion (Eq.22-24) the accelerations may be integrated to compute the velocities $[\dot{x}_1]$ and $[\dot{y}_1]$ as:

$$[\dot{x}_1] = [F_{(1)x} / m_1]\Delta t \text{ and } [\dot{y}_1] = [F_{(1)y} / m_1]\Delta t \,. \tag{28}$$

Afterwards, the relative displacements increments $\Delta n_{(i)}$ at the contact *i*=A, B and C may be calculated with another integration in time:

$$\Delta n_{(A)} = (v - [F_{(1)x} / m_1]\Delta t)\Delta t \tag{29}$$

$$\Delta n_{(B)} = ([F_{(1)x} / m_1]\Delta t - [F_{(2)x} / m_2])\Delta t \,, \tag{30}$$

$$\Delta n_{(C)} = ([F_{(2)x} / m_2]\Delta t - [-v])\Delta t \,, \tag{31}$$

where $\Delta n_{(i)}$ is taken as positive for compression. The cycle is repeated for a large assembly of particles in each existing contact until a final solution is obtained.

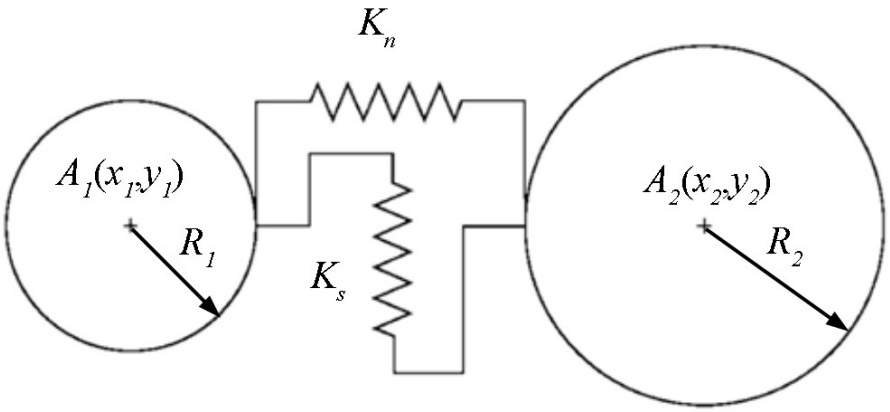

Fig.4.2: Simple elastic interaction with normal and tangential contact stiffness

The geometry and contact model are the most important parts of DEM simulation of the material response. The contact model may be the same or miscellaneous for normal, tangential (forces) and rotational degrees (angular moments) of freedom. For the same contact model, various material parameters may be used to simulate different materials. There are different approaches foe the contact treatment in DEM. The first one postulates that the contact area is proportional to the size of interacting spheres and is not dependent on the force transmitted. The second one is more realistic and takes into account the particles' deformation (Rojek et al. 2000). The contact surface is then proportional to the force acting between the particles.

The DEM calculations in this thesis were performed with the three-dimensional spherical discrete element model YADE which was developed at the University of Grenoble (Kozicki et al. 2008, Kozicki 2009). The 3D spherical discrete element method takes advantage of the so-called soft-

particle approach (i.e. the model allows for particle deformation that is modelled as an overlap of particles). During the simulations, particles may overlap that can be interpreted as a local contact deformation. The model was successfully used for describing the behaviour of granular materials by taking shear localization into account (Widuliński et al. 2011, Kozicki et al. 2012, 2013, 2014, Kozicki and Tejchman 2017, 2018). It demonstrated also its usefulness for fracture simulations in concrete (Skarżyński et al. 2015, Nitka and Tejchman 2018, Suchorzewski et al. 2018a, 2018b, 2019). In our calculations of concrete, the contact moments were neglected.

4.2 Contact law

The material models used for concrete modelling in DEM are usually complex as they intend to describe a fracture process independently of the meso-structure of concrete. Thus, they homogenise the material properties that change with developing fracture (stiffness, strength, plasticity). Rocha et al. (1991) proposed a bilinear constitutive law for a truss-like DEM model. This constitutive law aims to capture irreversible effects of crack nucleation and propagation by accounting for the reduction in the element load carrying capacity (Kosteski et al. 2010). The integration under the F-ε curve OAB represents the energy density causing fracture in single elements and its surrounding. The energy under curve OPC is reversible elastic energy while AOP is the dissipated energy due to fracture (Fig.4.3a). The bilinear model was then developed to take into account elasto-plasticity, resulting in a tri-linear constitutive model (Fig.4.3b). The dissipated energy is associated not only with the fracture energy as in the bi-linear model but also with the energy dissipation due to the plastic deformation (Kosteski et al. 2010).

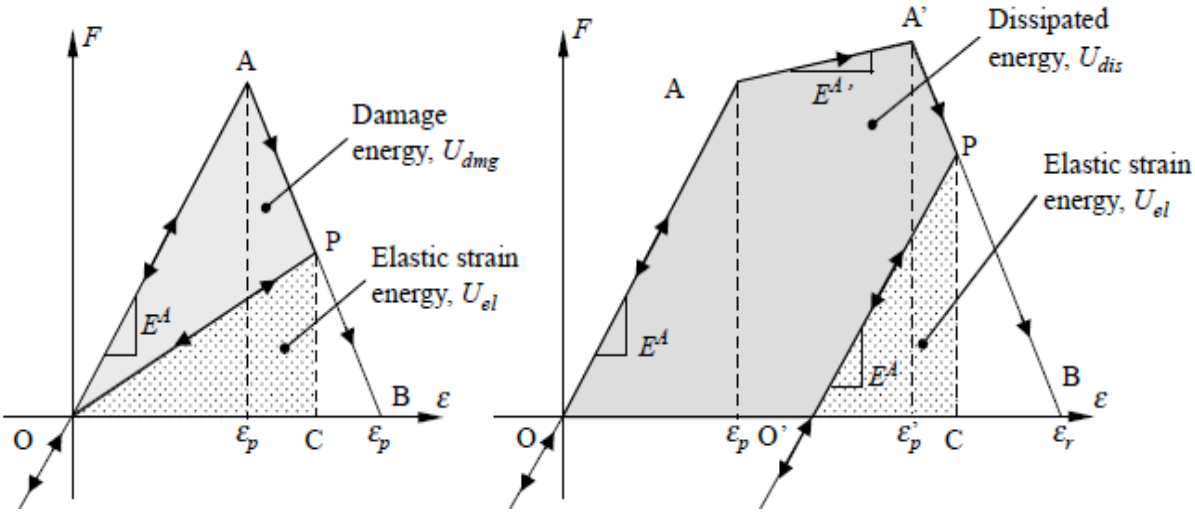

Fig.4.3: Constitutive models for concrete a) bilinear and b) tri-linear (Kosteski 2010)

Another approach for concrete constitutive model in DEM was introduced by Tran et al. (Tran 2010) and Poinard et al. (Poinard 2011). It splits the constitutive relations into tensile and compressive components. The model introduces an additional softening parameter ζ in tension that decreases stiffness after the maximum tensile force is obtained (Fig.4.4). In compression, compaction of particles is taken into account, as this behaviour happens below the level of the used discretization.

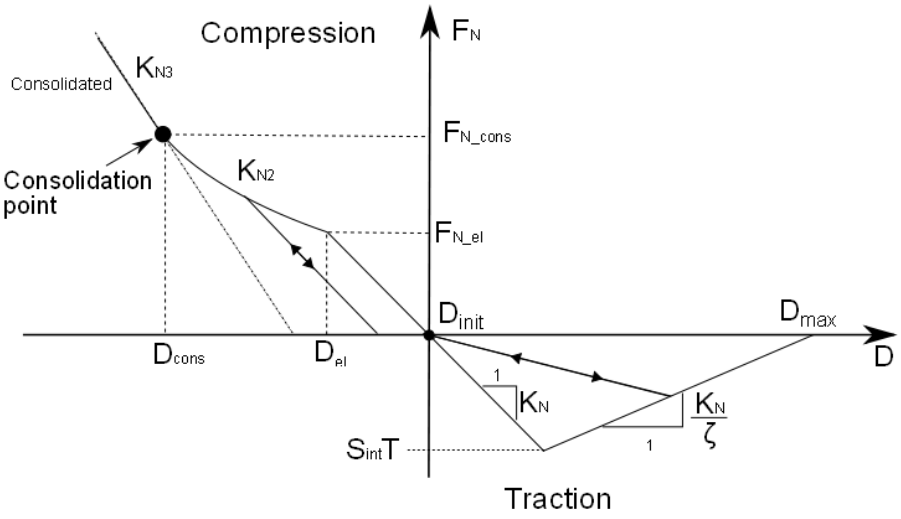

Fig.4.4: Normal contact force law by Tran et al. (2010)

The other approach for concrete interaction was developed by ITASCA Consulting Group in the commercial Particle Flow Code (PFC). It uses simple force-displacement relationships and introduces additional springs (Fig.4.5). The single springs may be broken in different calculations steps what increases ductility with keeping the material law linear with a limit in tension and bi-linear in shear. The particles in PFC may move in normal, tangential and angular directions. The rotations cause additional moments (Cho et al. 2007).

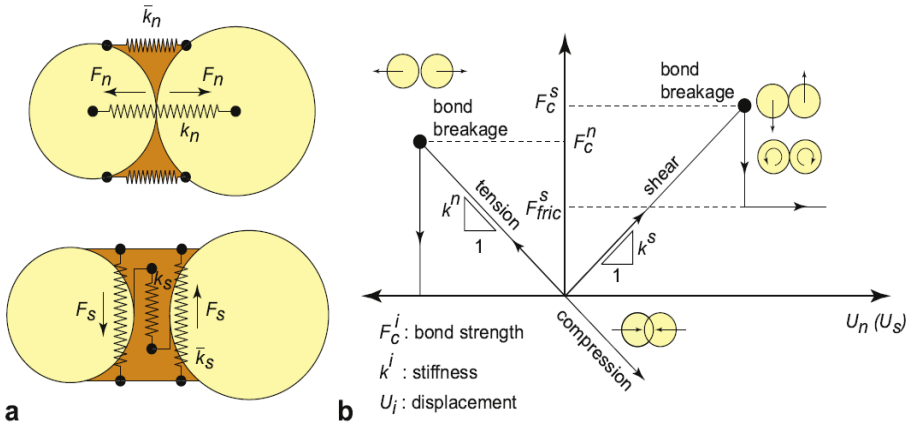

Fig.4.5: Normal contact law by Cho et al. (2007)

The model used in this thesis is the simplest possible for concrete modelling. A linear normal contact model under compression was used. The interaction force vector representing the action between two spherical discrete elements in contact was decomposed into a normal and tangential vector, respectively. The normal forces acting on spheres were modelled by an elastic law with cohesion. The normal and tangential forces were linked to the displacements through the normal stiffness K_n and the tangential stiffness K_s (Fig.4.6a-c) (Kozicki&Donze 2008)

$$\vec{F}_n = K_n U \vec{N}, \tag{32}$$

$$\vec{F}_s = \vec{F}_{s,prev} + K_s \Delta \vec{X}_s, \tag{33}$$

where U is the overlap between spheres, $\vec{N}$ denotes the normal vector at the contact point, $\Delta\vec{X}$ is the increment of the relative tangential displacement and $\vec{F}_{s,prev}$ is the tangential force from the previous iteration. The stiffnesses K_n and K_s were computed as the functions of the modulus of elasticity of the grain contact E_c and two neighbouring grain radii R_A and R_B (to determine the normal stiffness K_n) and the modulus of elasticity E_c and Poisson's ratio υ_c of the grain contact and two neighbouring grain radii R_A and R_B (to determine the tangential stiffness K_s), respectively (Kozicki&Donze 2008)

$$K_n = E_c \frac{2R_A R_B}{R_A + R_B} \quad \text{and} \quad K_s = \upsilon_c E_c \frac{2R_A R_B}{R_A + R_B}. \tag{34}$$

If two grains in contact have the same size ($R_A=R_B=R$), the numerical stiffness parameters are equal to: $K_n=E_cR$ and $K_s=\upsilon_cE_cR$, respectively (thus $K_s/K_n=\upsilon_c$). A simple linear elastic contact law was assumed in normal contacts. The contact forces $\vec{F}_s$ and $\vec{F}_n$ satisfied the cohesive-frictional Mohr-Coulomb equation (Fig.4.6d)

$$\left\|\vec{F}_s\right\| - F_{max}^s - \left\|\vec{F}_n\right\| \times tan\,\mu \le 0 \qquad \text{(before contact breakage)} \qquad (35)$$

and

$$\left\|\vec{F}_s\right\| - \left\|\vec{F}_n\right\| \times \tan\mu \le 0 \qquad \text{(after contact breakage),} \qquad (36)$$

where μ denotes the inter-particle friction angle and F_{max}^s is the cohesive force between spheres. The normal force might be negative down to the minimum value of F_{min}^n (tension) if there was no a geometrical contact between elements. If this minimum normal force between spheres F_{min}^n was reached, the contact was broken. Moreover, if any contacts between grains re-appeared, cohesion between them was not taken into account. A crack was considered as open if cohesive forces between grains (Eqs.35 and 36) disappeared when a critical threshold was reached. The movement of fragments (mass-spring systems with cohesion) was similar to the rigid body movement. A choice of a very simple constitutive law was intended to capture on average various contact possibilities in real concrete. The cohesive force and tensile force were assumed as a function of the cohesive stress C (maximum shear stress at pressure equal to zero), tensile normal stress T and sphere radius R (Kozicki and Donze 2008)

$$F_{max}^s = C \times R^2 \qquad \text{and} \qquad F_{min}^n = T \times R^2. \qquad (37)$$

For two elements in contact, the smaller values of C, T and R were used. A local non-viscous damping scheme was applied in order to dissipate excessive kinetic energy in a discrete system. The damping parameter α_d was introduced to reduce the forces acting on the spheres

$$\vec{F}_{damped}^{\,k} = \vec{F}^{\,k} - \alpha_d \cdot sgn(\vec{v}^{\,k}) \,|\, \vec{F}^{\,k} \,|, \qquad (38)$$

where $\vec{F}^{\,k}$ are the k^{th}-components of the residual force and translational velocity, respectively. A positive damping coefficient α_d was smaller than 1 (sgn(•) returns the sign of the k^{th} component of

velocity). The equation could be separately applied to each k^{th} component of the 3D vector x, y and z. Note that material softening was not assumed in advance in the DEM model.

The particles may have complex shapes in DEM calculations. The geometry definition may be realized by an analytical description (Fig.4.7) of the particle geometry or by connecting spheres in clusters (Fig.4.8). Thus, multiple shapes may be reproduced with DEM in order to faithfully reproduce the particles' shapes. In the thesis, the second approach was used to take the realistic geometry of aggregates and voids in concrete. The spheres were connected into the clusters of spheres as the rigid bodies. The radius of the clump was taken into account while calculating the contact stiffness and strength (cohesion forces between aggregate and cement matrix particles.

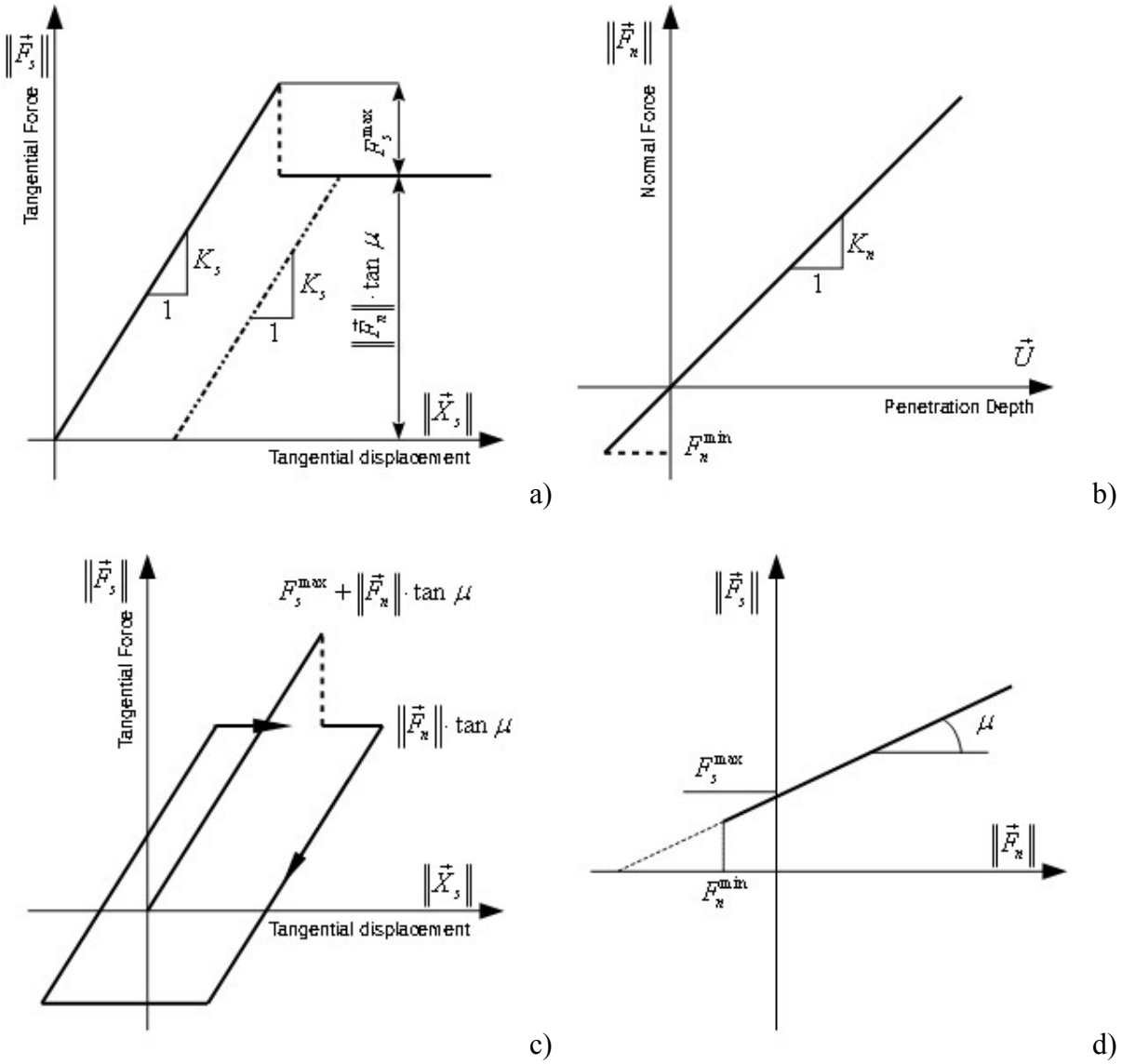

Fig.4.6: Mechanical response of DEM: a) tangential contact model, b) normal contact model, c) loading and unloading path in tangential contact model and d) modified Mohr-Coulomb model (Nitka and Tejchman 2015)

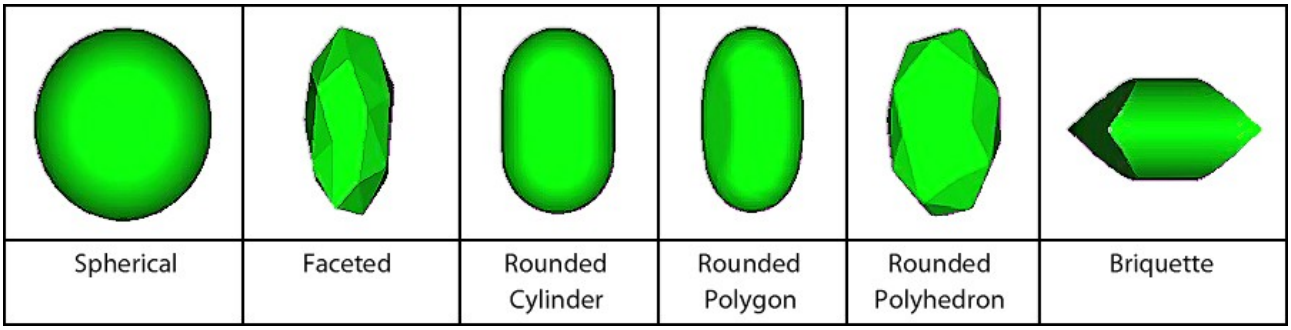

Fig.4.7: Shapes created in DEM with mathematical description (RockDEM 2018)

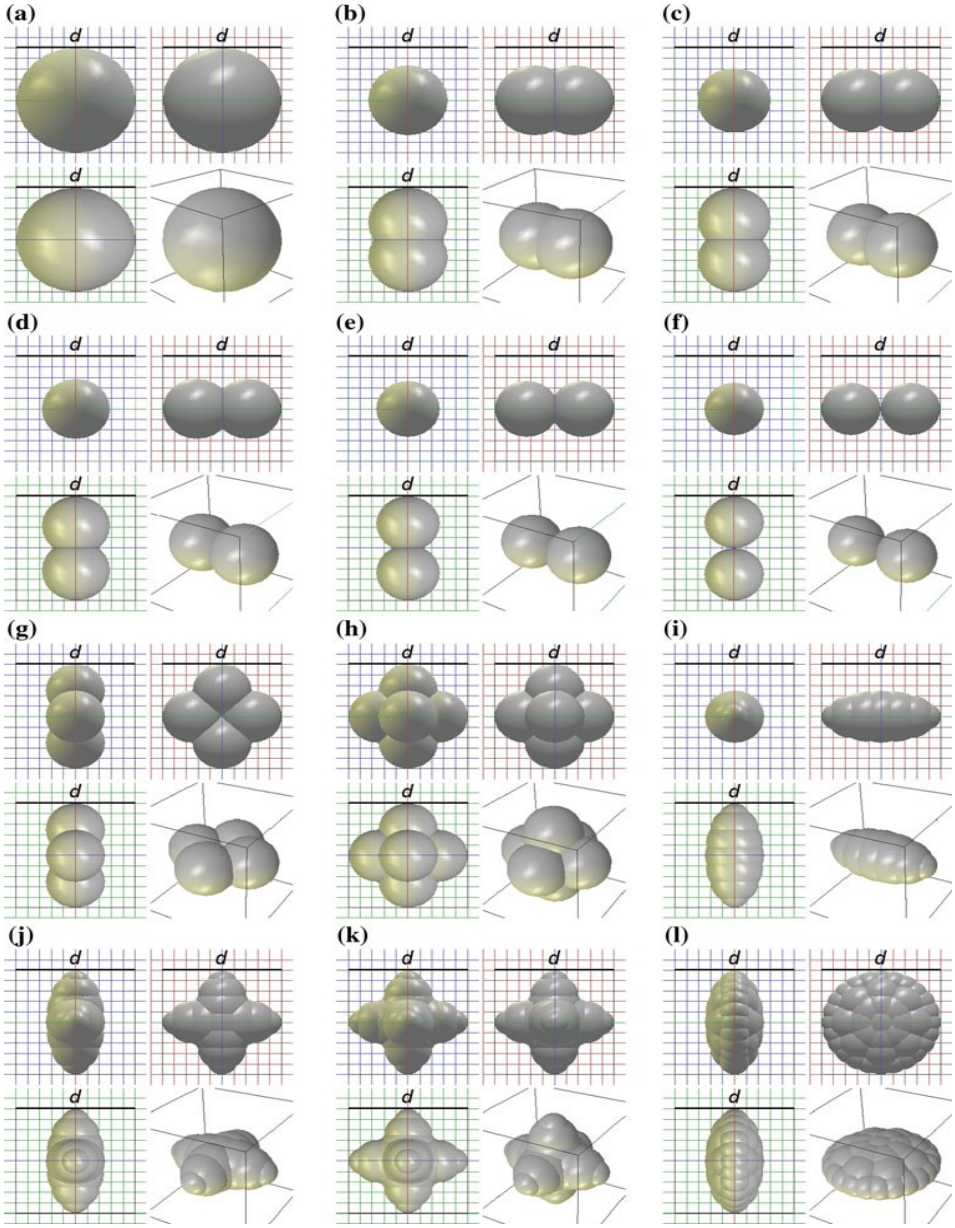

Fig.4.8: Shapes created by assembling clusters of spheres (clumps) to describe sand grains (Kozicki et al. 2012)

Chapter 5

DEM calculations

The numerical simulations of own experiments on concrete (uniaxial compression and splitting tension) were performed with DEM. In addition, uniaxial tension was analyzed. The concrete 4-phase meso-structure was mainly obtained by means of a X-ray micro-computed tomography system (Skarżyński and Tejchman 2016, Skarzyński et al. 2019).

5.1 Uniaxial compression

Preliminary calibration tests

The first numerical simulations were performed for uniaxial compression (Suchorzewski et al. 2018a). In order to study the effect of some DEM parameters on the concrete behaviour, some preliminary calculations on uniaxial compression and uniaxial tension tests under 2D conditions were carried out. Two physical parameters (the number of ITZs expressed by the minimum aggregate diameter with ITZs $d_{a(ITZ)}^{min}$ and the strength of ITZs expressed by the ratio C_{ITZ}/C_{cm}) and one numerical parameter (minimum sphere diameter in the cement matrix $d_{cm(min)}$ were investigated. The strain-strain evolution results were compared with the corresponding tests by van Vliet and van Mier (2000) and van Mier et al. (1986). The 2D specimens were quadratic 100×100 mm^2 (compression) or had a dog-bone-shape 150×100 mm^2 (tension). Only the spheres were used for simulation of the cement matrix and aggregate (Fig.5.1). The sphere minimum diameter was d_{min}=0.25-1.0 mm. The aggregate sieve curve was the same as in the experiment: d_a^{max}=12 mm in compression and d_a^{max}=8 in tension. The spheres with the d_a=0.4-2 mm were treated as the aggregate grains with ITZs and the spheres with d_{cm}<0.4-2 mm as the cement matrix particles. The particle area was 75%. The cement matrix grains filled the concrete specimen in 95% (Nitka and Tejchman 2015). The macro-voids (d>0.5 mm) were assumed in a random way as the empty spaces (their volume/area was 2% of the specimen volume/area). The main DEM parameters were the same as those in Section 2. The ratio of T_{ITZ}/T_{cm} was always the same as the ratio of C_{ITZ}/C_{cm} (=0.5). The top and bottom boundaries were very smooth (i.e. horizontal displacements were free). Figs.5.2 and 5.3 show the results for uniaxial tension and Figs.5.4 and 5.5 for uniaxial compression (stress-strain curves and cracked specimens).

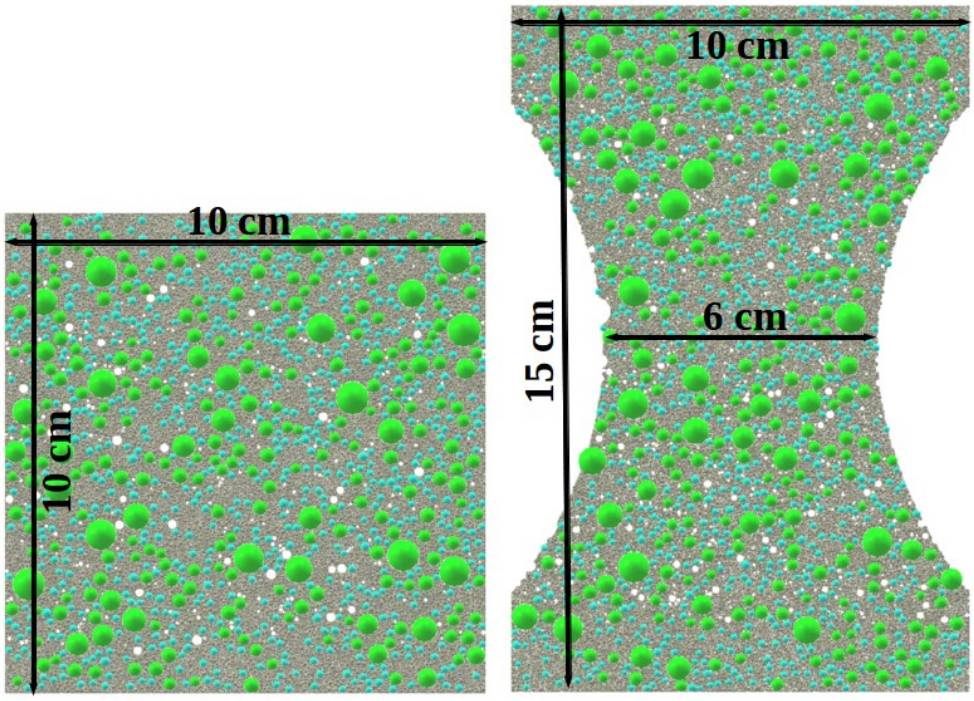

a) b)

Fig.5.1: Concrete 2D specimens (d_{cm}^{min}=0.25 mm) during: a) uniaxial compression and b) uniaxial tension (white colour - macro-voids, green colour - aggregate with $d_a \leq 2$ mm and ITZs, blue colour - cement matrix with 1 mm $\leq d_{cm} <$2 mm and grey colour - cement matrix with 0.25 mm $\leq d_{cm} <$1 mm)

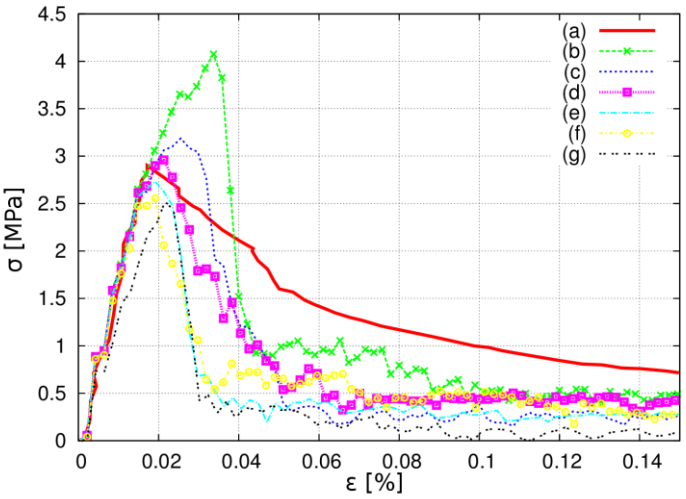

A)

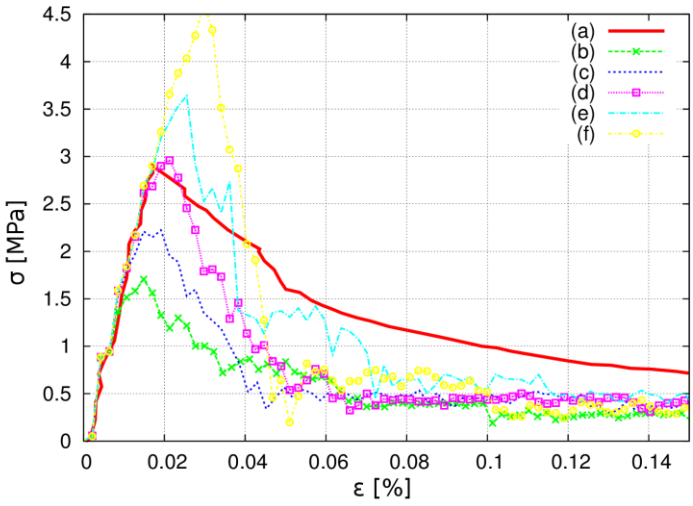

B)

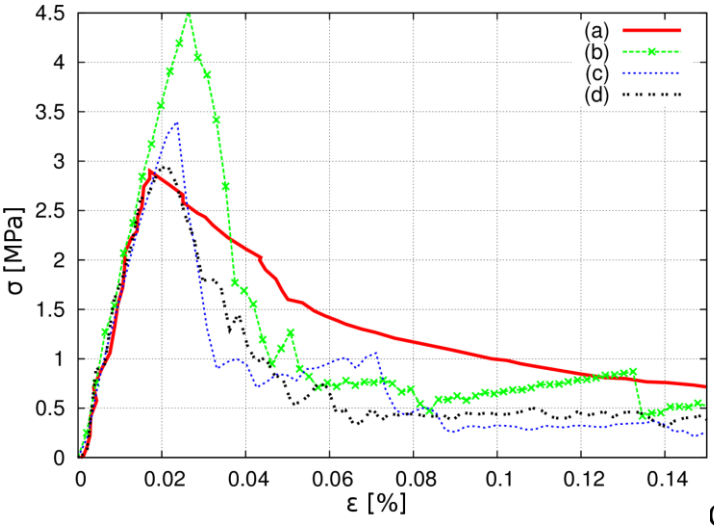

C)

Fig.5.2: Stress-strain curves σ=f(ε) for uniaxial tension from 2D DEM (σ - vertical normal stress and ε - vertical normal strain): effect of: A) minimum sphere diameter including ITZs (a) experiment, b) $d_{a(ITZ)}^{min}$ >2 mm, c) $d_{a(ITZ)}^{min}$ >1 mm, d) $d_{a(ITZ)}^{min}$ >1.6 mm, (e) $d_{a(ITZ)}^{min}$ >1.2 mm, f) $d_{a(ITZ)}^{min}$ >0.8 mm, g) $d_{a(ITZ)}^{min}$ >0.4 mm, B) ratio C_{ITZ}/C_{cm} (a) experiment, (b) C_{ITZ}/C_{cm} =0.3, (c) C_{ITZ}/C_{cm} =0.4, (d) C_{ITZ}/C_{cm} =0.5, (e) C_{ITZ}/C_{cm} =0.6, (f) C_{ITZ}/C_{cm} =0.7, C) minimum sphere diameter in cement matrix (a) experiment, b) d_{cm}^{min} =0.75 mm, c) d_{cm}^{min} =0.5 mm and d) d_{cm}^{min}=0.25 mm (red colour - experiments by van Vliet and van Mier 2000

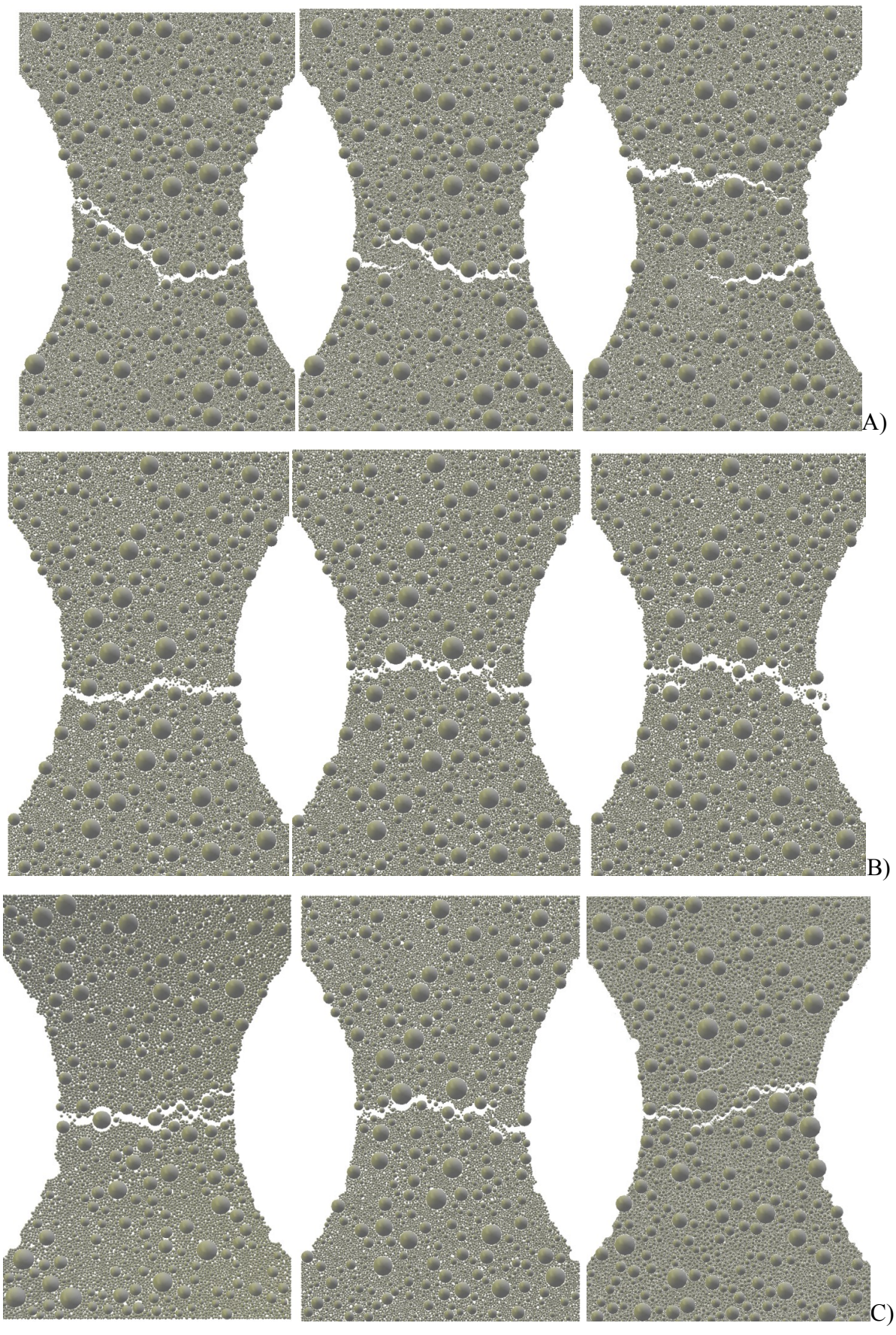

Fig.5.3: Cracked concrete specimens for uniaxial tension from 2D DEM with displacements magnified by factor 20 (ε=0.04%): A) minimum sphere diameter with ITZs a) $d_{a(ITZ)}^{min}$>2 mm, b) $d_{a(ITZ)}^{min}$>1 mm, c) $d_{a(ITZ)}^{min}$>1.6 mm, B) ratio C_{ITZ}/C_{cm} a) C_{ITZ}/C_{cm}=0.7, b) C_{ITZ}/C_{cm}=0.6, c) C_{ITZ}/C_{cm}=0.5, C) minimum sphere diameter in cement matrix a) d_{cm}^{min}=0.75 mm, b) d_{cm}^{min}=0.5 mm, c) d_{cm}^{min}=0.25 mm

All calculated 2D stress-strain curves during tension were too brittle as compared to the experimental one. The reason was the lack of 3D calculations and the minimum cement particles d_{cm}^{min} were too large (Nitka and Tejchman 2015). By increasing the minimum sphere diameter with ITZs from 0.4 mm up to 2 mm, the ratio C_{ITZ}/C_{cm} from 0.2 up to 0.6 and the minimum sphere diameter in the cement matrix from 0.25 mm up to 0.75 mm, the peak tensile stress increased from 2.5 MPa up to 4 MPa (Fig.5.2A), from 1.6 MPa up to 4.5 MPa (Fig.5.2B) and from 3 MPa up to 4.5 MPa (Fig.5.2C). The material ductility became larger mainly with decreasing ratio C_{ITZ}/C_{cm}. For the specimen with larger spheres including ITZs, the cracks were obviously less curved (Fig.5.3A) and the number of broken contacts decreased by 0.5%. A decrease of the ratio C_{ITZ}/C_{cm} increased the number of micro-cracks (Fig.5.3B); the number of broken contact increased by 1.4 %. When reducing the minimum sphere diameter of the cement matrix, more cracks appeared (Fig.5.3C) and the number of broken contacts increased by 2%.

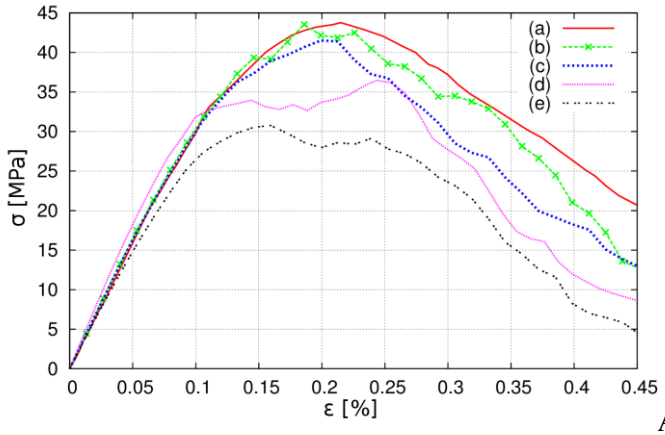

A)

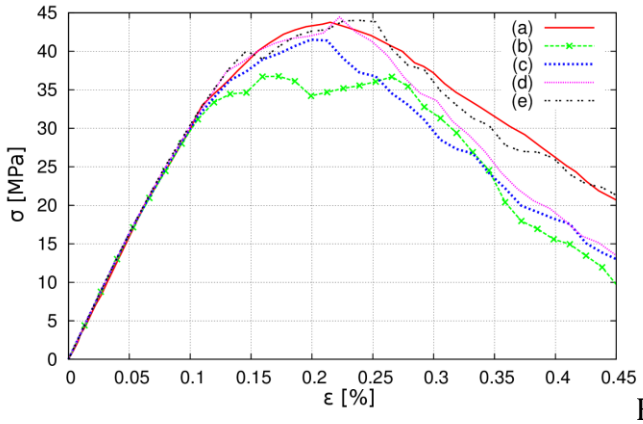

B)

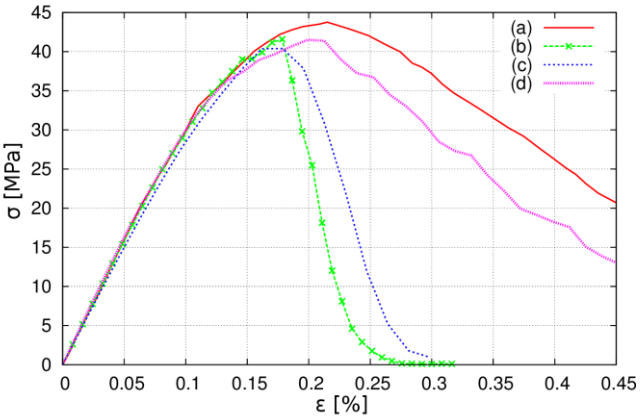

C)

Fig.5.4: Stress-strain curves $\sigma=f(\varepsilon)$ for uniaxial compression from 2D DEM (σ - vertical normal stress and ε - vertical normal strain): effect of: A) minimum sphere diameter with ITZs (a) experiment, b) $d_{a(ITZ)}^{min}$>4 mm, c) $d_{a(ITZ)}^{min}$>2 mm, d) $d_{a(ITZ)}^{min}$ >1.6 mm, e) $d_{a(ITZ)}^{min}$ >1.2 mm, f) $d_{a(ITZ)}^{min}$ >0.8 mm, g) $d_{a(ITZ)}^{min}$ >0.4 mm, B) ratio C_{ITZ}/C_{cm} (a) experiment, b) C_{ITZ}/C_{cm}=0.3, c) C_{ITZ}/C_{cm}=0.4, d) C_{ITZ}/C_{cm}=0.5, e) C_{ITZ}/C_{cm}=0.6, f) C_{ITZ}/C_{cm}=0.7 and C) minimum sphere diameter in cement matrix (a) experiment, b) d_{cm}^{min} =0.75 mm, c) d_{cm}^{min} =0.5 mm, d) d_{cm}^{min} =0.25 mm (red colour - experiments by van Vliet and van Mier 2000)

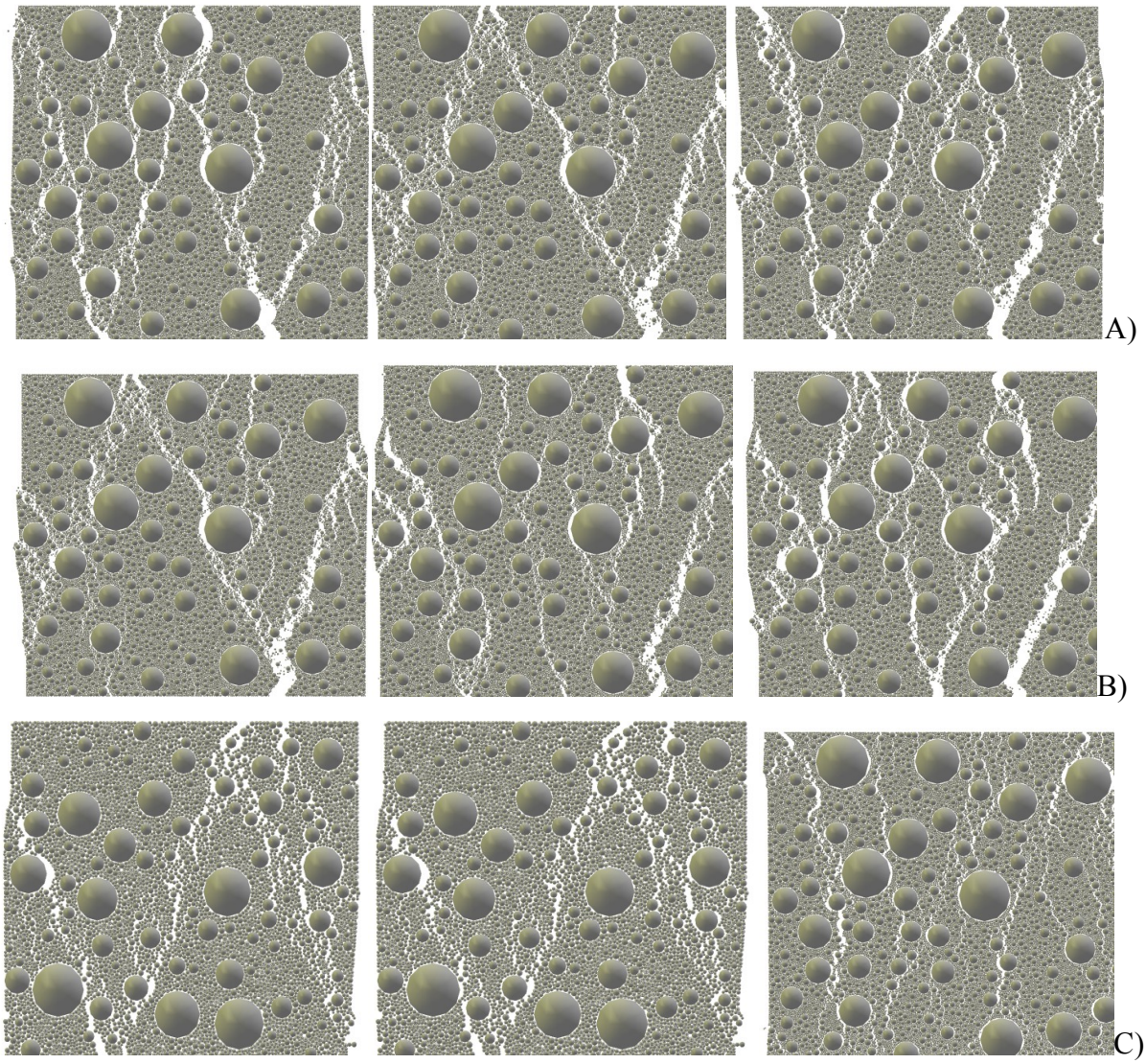

Fig.5.5: Cracked concrete specimens for uniaxial tension from 2D DEM with displacements magnified by factor 20 (ε=0.25%): A) minimum sphere diameter with ITZs (a) $d_{a(ITZ)}^{min}$>2 mm, b) $d_{a(ITZ)}^{min}$>1.6 mm, c) $d_{a(ITZ)}^{min}$>1 mm), B) ratio C_{ITZ}/C_{cm} a) C_{ITZ}/C_{cm}=0.8, b) C_{ITZ}/C_{cm}=0.6, c) C_{ITZ}/C_{cm}=0.4 and C) minimum sphere diameter in cement matrix a) d_{cm}^{min} =0.75 mm, b) d_{cm}^{min}=0.5 mm and c) d_{cm}^{min} =0.25 mm

During compression by increasing the minimum sphere diameter with ITZs from 1.4 mm up to 3 mm, the ratio C_{ITZ}/C_{cm} from 0.2 up to 0.8 and the minimum sphere diameter in the cement matrix from 0.25 mm up to 0.75 mm, the peak stress increased from 30 MPa up to 45 MPa (Fig.5.1.4A), from 35 MPa up to 45 MPa (Fig.5.1.4B) and was about 42 MPa (Fig.5.1.4C). The material ductility increased when increasing minimum sphere diameter in the cement matrix d_{cm}^{min} (Fig.5.1.4C). The

number and distribution of cracks did not change with varying minimum sphere diameter with ITZs (Fig.5.1.5A). The decrease of the ratio C_{ITZ}/C_{cm} produced more cracks (that were mainly straight cracks) (Fig.5.1.5B). More inclined wide cracks occurred for the minimum sphere diameter of the cement matrix d_{cm}^{min}=0.75 mm and more straight cracks occurred for d_{cm}^{min}=0.25 mm (Fig.5.1.5C). The most contacts were obviously broken for d_{min}=0.25 mm.

In summary, the investigated parameters (2 physical and 1 numerical) had a pronounced effect on the concrete behaviour (strength, brittleness, cracking). The most realistic DEM results were obtained for $d_{a(ITZ)}^{min}$≥1.6 mm, C_{ITZ}/C_{cm}=0.5 and d_{cm}^{min}=0.25 mm during tension and $d_{a(ITZ)}^{min}$≥2 mm, C_{ITZ}/C_{cm}=0.5 and d_{cm}^{min}=0.25 mm during for compression.

2D calculations with real meso-structure

Figures 5.6b and 5.6c present the vertical cross-sections of 50×50 mm^2 of the concrete specimen (front side and mid-depth section) with the real aggregate distribution of Fig.5.6 modelled either by clusters of spheres and by spheres with the equivalent area based on the 3D micro-CT scans of Fig.5.6a. The minimum cement matrix particles was d_{cm}^{min}=0.1 mm. The calculated stress-strain curves are demonstrated in Fig.6.1.1.2A ($E_{c,cm}$=11 GPa, C_{cm}=140 MPa, T_{cm}=22.5 MPa, $E_{c,ITZ}$=8.8 GPa, C_{ITZ}=70 MPa and T_{ITZ}=11.25 MPa, Section 3). The number of broken contacts imitating the crack propagation is described in Fig.5.7B. Figure 5.8 presents the cracked specimen with broken contacts marked in red.

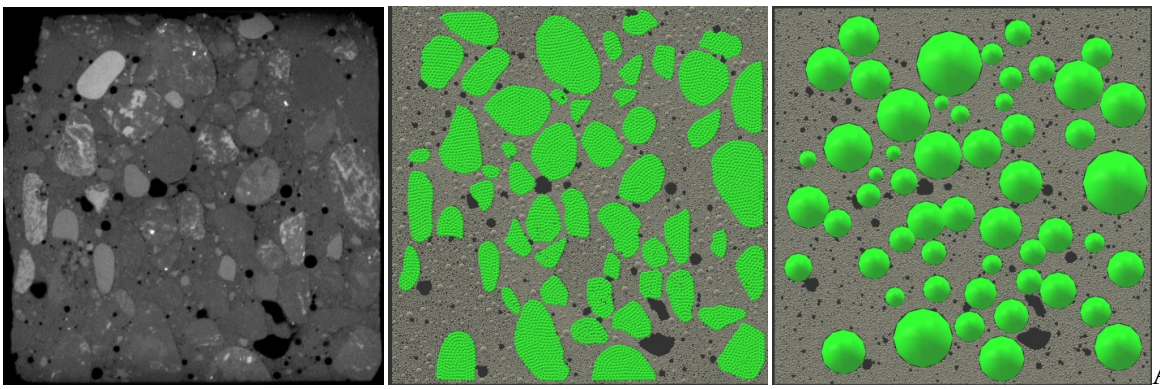

A)

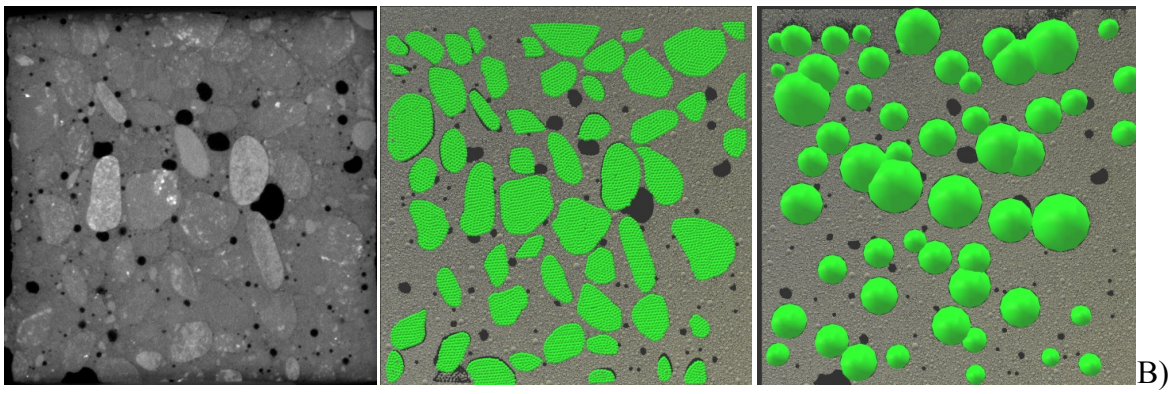

Fig.5.6 2D micro-structure of concrete vertical-sections of 50×50 mm 2 (front side (A) and mid-depth section (B): a) experiments (μCT image, specimen '3') and DEM with aggregate modelled as: b) clusters of spheres and c) spheres with equivalent cross-sectional area and position (green colour - aggregate $d_{a(ITZ)}^{min}$ >2 mm with ITZs, grey colour - cement matrix and black colour - macro-voids)

The calculated curves are in satisfactory agreement with the experimental ones with respect to the modulus of elasticity and strength (Fig.5.7A). They are also close to the experimental curve '1' with respect to the specimen brittleness. As compared to the curve '2', they are too ductile. The strength was larger by 10% for spheres than for clusters of spheres due to stress concentrations for the real aggregate with sharp edges that contributed to the smaller strength and faster cracking. Initially, the number of broken contacts was higher for irregularly shaped aggregate particles and later for round particles (Fig.5.7 B). The stress evolution was thus connected to the number of broken contacts (the larger the peak stress, the smaller was the number of broken contacts). According to Kim and Abu Al-Rub (2011) using a meso-scale FE model, the aggregate shape had a weak effect on the ultimate strength of concrete and on the strain to damage-onset but significantly affected the crack initiation, propagation and distribution. The stress concentrations at sharp edges of polygonal particles caused that the ultimate tensile strength and strain at the damage onset were the highest for circular grains model. The same conclusions were derived by He et al. (2009) and He (2010) using a similar approach. Skarzynski and Tejchman (2013) indicated in FE analyses that the effect of the aggregate shape on the strength was strongly connected with the grain size distribution curve.

3D calculations with random meso-structure

The 3D DEM calculations were performed with aggregate particles simulated as spheres located in the specimen at completely random positions. In order to shorten the calculation time, the minimum

sphere diameter in the cement matrix was d_{cm}^{min}=0.75 mm (instead of d_{cm}^{min}=0.1 mm). The initial macro-void volume was 4.25%. The calculated stress-strain curve as compared to the experimental curve is shown in Fig.8A ($E_{c,cm}$=11 GPa, C_{cm}=140 MPa, T_{cm}=22.5 MPa, $E_{c,ITZ}$=8.8 GPa, C_{ITZ}=70 MPa and T_{ITZ}=11.25 MPa, Section 5.1). Figure 5.8B shows the porosity change (defined as the ratio between the void space volume and the total specimen volume). The change of the broken contacts is depicted in Fig.5.8C.

The calculated 3D strength was too high by 10% only (Fig.5.8A). The calculated strain corresponding to the peak stress was also too large (ε=0.02% against ε =0.015%) (Fig.5.8A). The calculated softening rate was similar as in the experiment for the specimen '2' and too weak as compared with the specimen '1'. The specimen after the initial compaction was subjected to dilatancy due to cracking (Fig..5.8B). The calculated porosity changed its volume from the initial value of p_0=4.25% up to p=4.4% in the strain range up to the peak stress, ε =0-0.2% (in the experiment from p=4.47% up to p=4.85% for ε =0-0.12%) and up to p=6-7% in the range of ε =0-0.4%. The number of broken contacts was significantly higher (by 40%) in 3D calculations (Fig.5.8C) than in 2D calculations (Fig.5B).

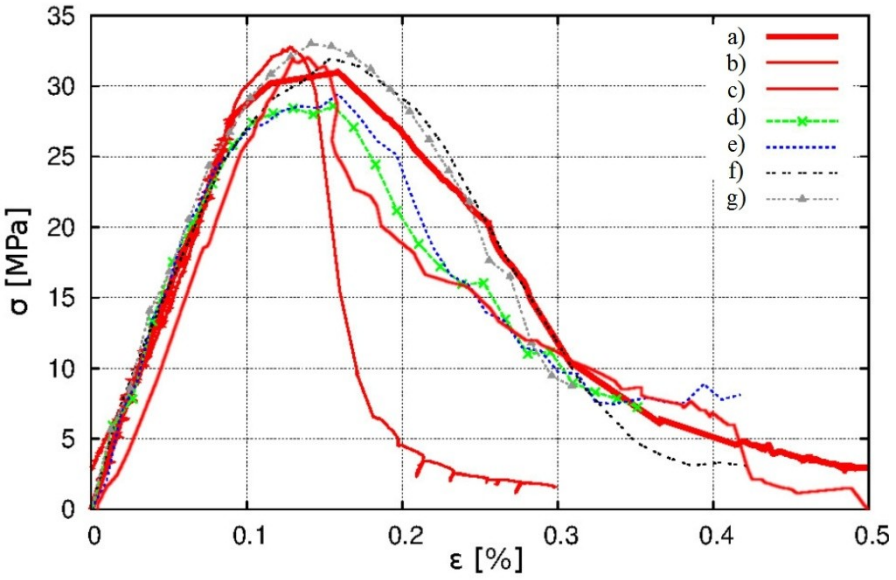

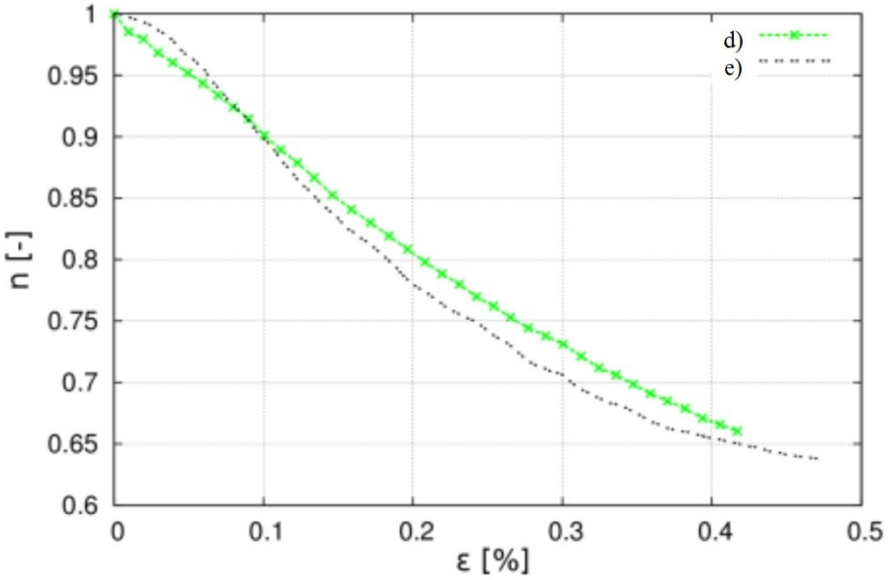

Fig.5.7: 2D DEM results: A) calculated stress-strain curves $\sigma=f(\varepsilon)$ ('d'-'g') as compared to experiments (curves 'a', 'b' and 'c' of Fig.1) and B) relative change of contact number with respect to initial state (d) curve for real aggregate (clusters of spheres) on specimen front side, e) curve for real aggregate (clusters of spheres) in specimen mid-depth section, f) curve for real aggregate (spheres) on specimen front side and g) curve for real aggregate (spheres) in specimen mid-depth section

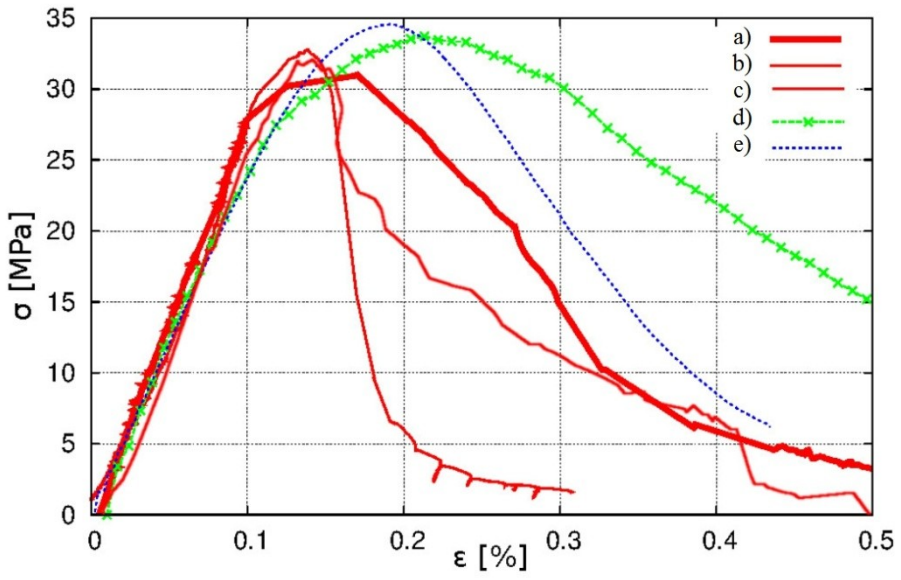

A)

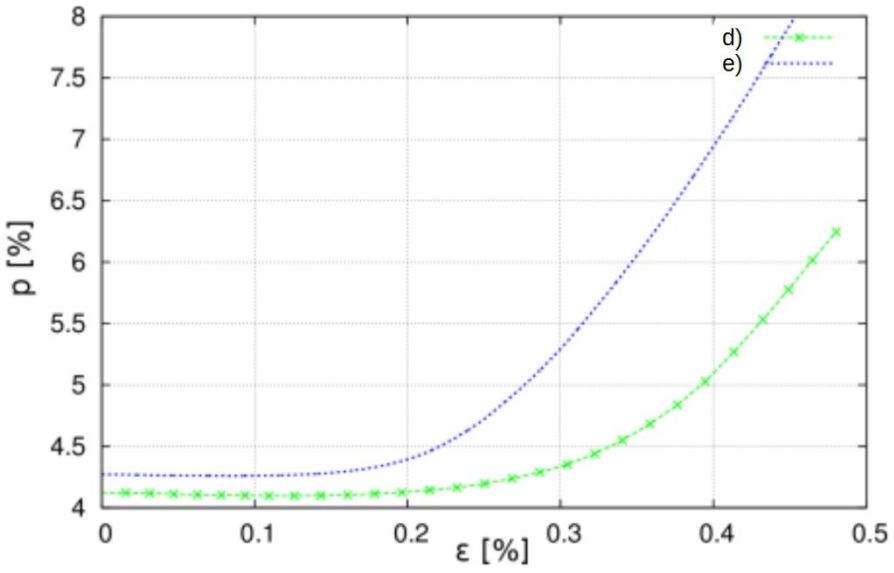

B)

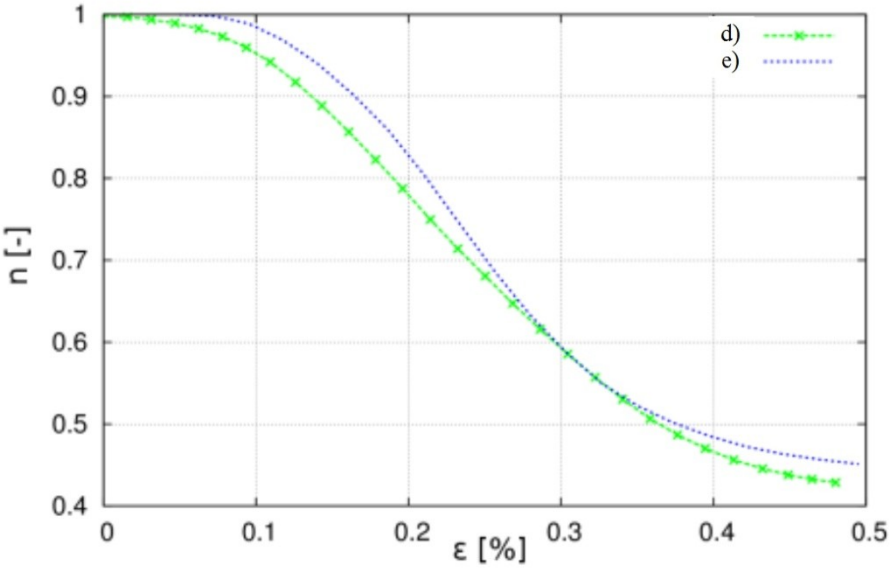

C)

Fig.5.8: 3D DEM results for spheres at random position in concrete specimen: A) stress-strain curves $\sigma=f(\varepsilon)$ (a-c) experiments for specimens '1'-'3' and d-e) calculations) and B) porosity change $p=f(\varepsilon)$ and C) relative change of contact number with respect to initial state $n=f(\varepsilon)$

Meso-scale phenomena

The calculated crack pattern with clusters composed of spheres on the specimen front surface (Fig,5.9Ab) was approximately similar as in the experiment (Fig.5.9Aa). In DEM, both the main experimental cracks appeared in the same regions (right part and central part). The calculated crack

at the right edge side did not obviously propagate through a small aggregate grain. However, a further crack shape was realistically reproduced including branching around two grains at the specimen. The calculated central crack also occurred at the same position. The width of the calculated main crack on the right side of the specimen was w=0.22 mm (clusters of spheres) and w=0.20 mm (spheres) (in the experiment the width was w=0.18 mm). The calculated small cracks on the left side were not visible in micro-CT-scans since the specimen was subjected to unloading for scanning purposes. However, they were observed during deformation with the manual digital microscope. The calculated crack pattern with spheres was different (Fig.5.9Ac) than this with clusters of spheres. The cracks were more straight and their number was higher.

For the specimen mid-depth section, the calculated crack pattern (Fig.9Bb) was in a worse agreement with the experiment (Fig.5.9Ba) due to the fact the real aggregate shape was not reproduced in the calculations. The main crack visible in micro-CT scans on the right specimen side appeared in DEM at the bottom aggregate particle but next then changed its direction to a macro-void. The second crack on the right side was correctly reproduced and propagated to the void. In the central part, a top crack solely corresponded to micro-CT scans. The number of cracks was again higher for round aggregate particles (Fig.5.9Bc).

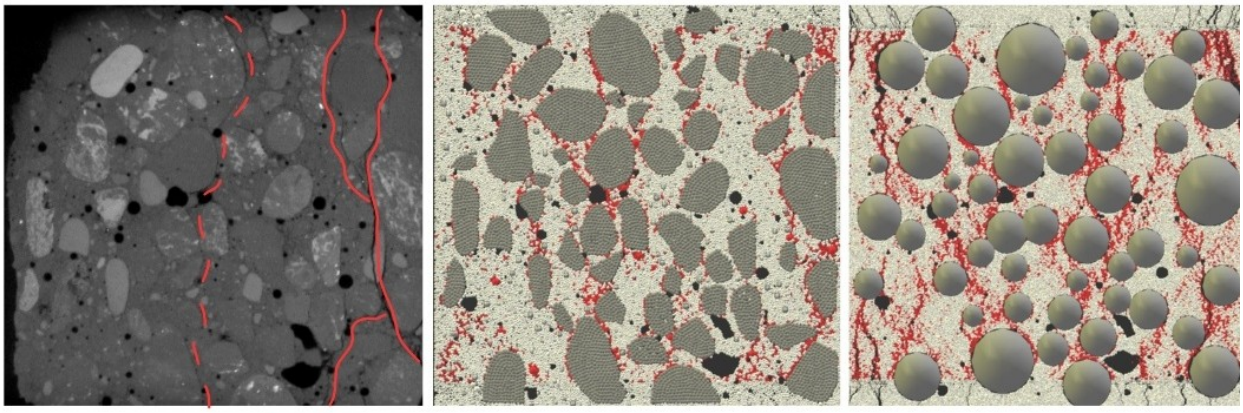

A)

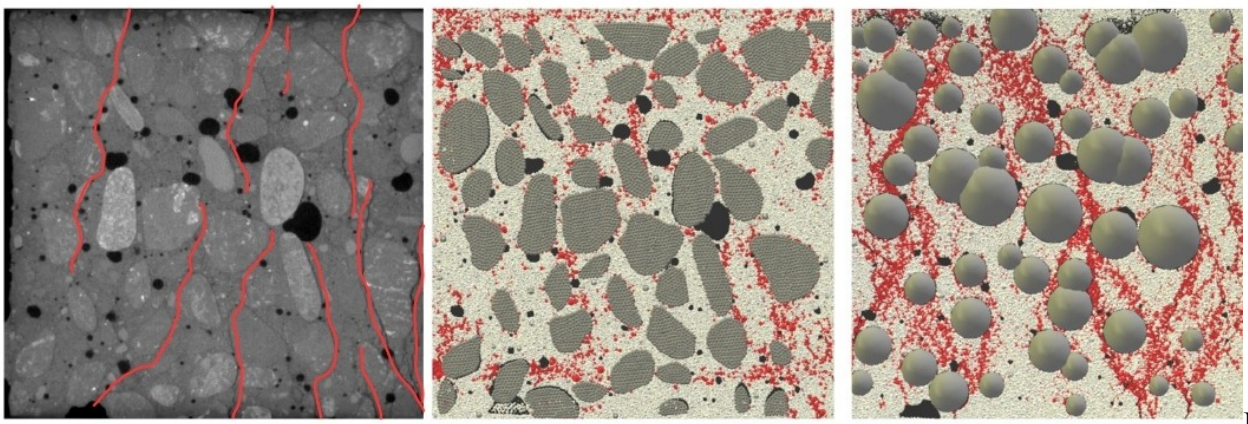

B)

a) b) c)

Fig.5.9: 2D cracked specimen (ε=0.12%): a) experiment (micro-CT image for specimen '3'), b) DEM for real aggregate (clusters of spheres) and c) DEM for real aggregate (spheres) (red colour – cracks, black colour – voids, dark grey colour - aggregate, light grey colour - cement matrix) (*A* – specimen front side and *B* – specimen mid-depth section)

The calculated evolution of cracks on the specimen front side is shown in Figs.5.10a-f. First, broken contacts occurred around aggregate particles, mainly at vertical edges where tensile forces were the largest. Then they developed along the aggregate edges. Afterwards they connected with each other in the cement matrix by bridging (similarly as in the experiment, Section 3.1). The crack branching also occurred in the aggregate surrounding (Fig.5.10f).

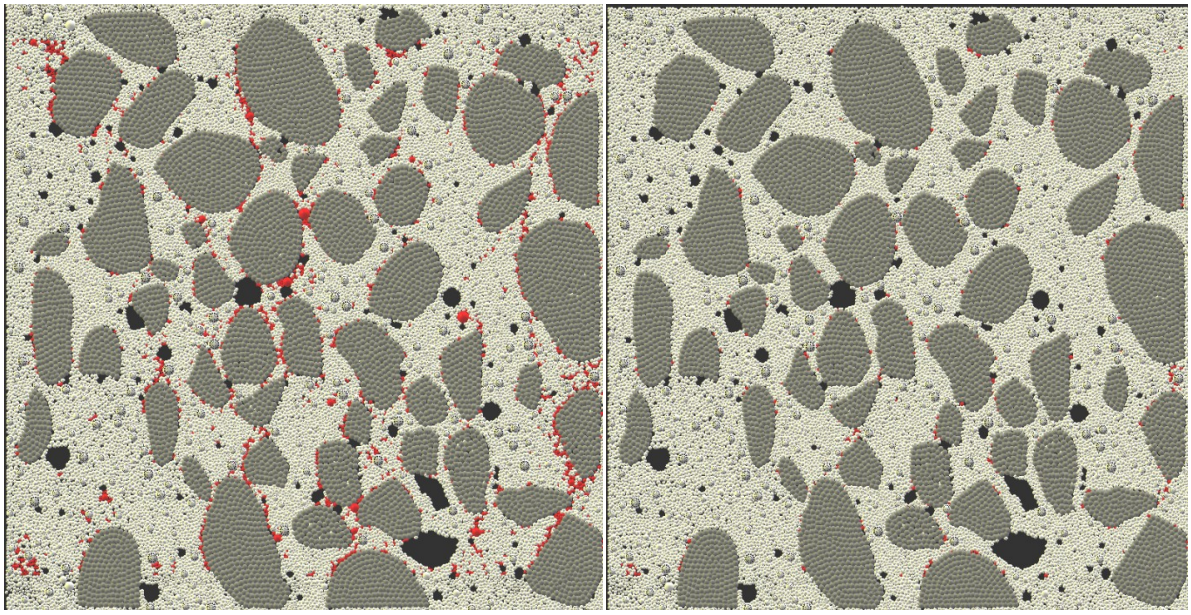

a) b)

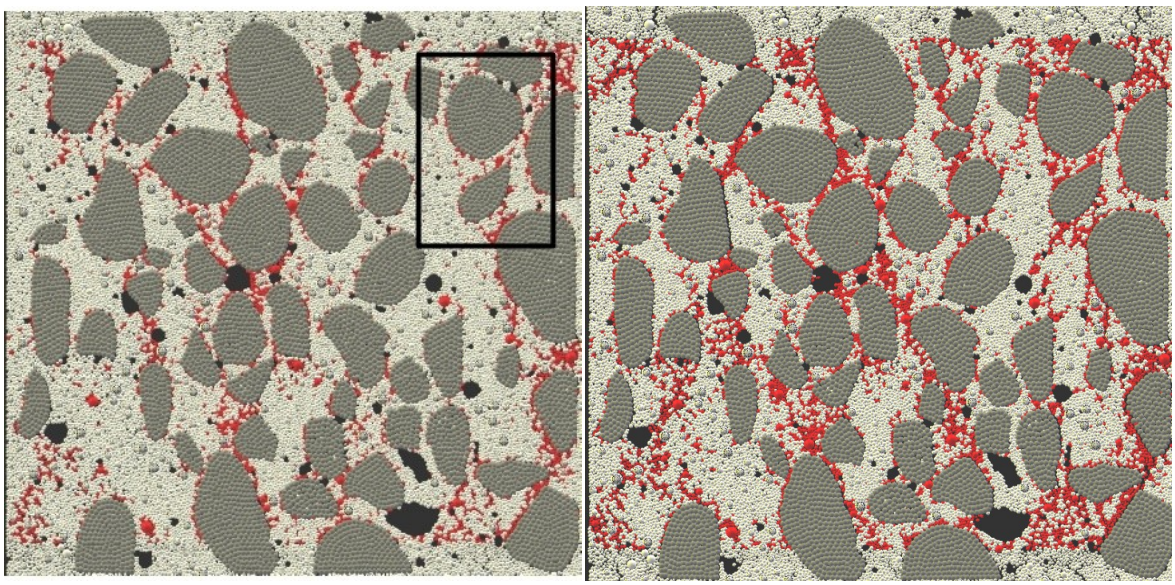

c) d)

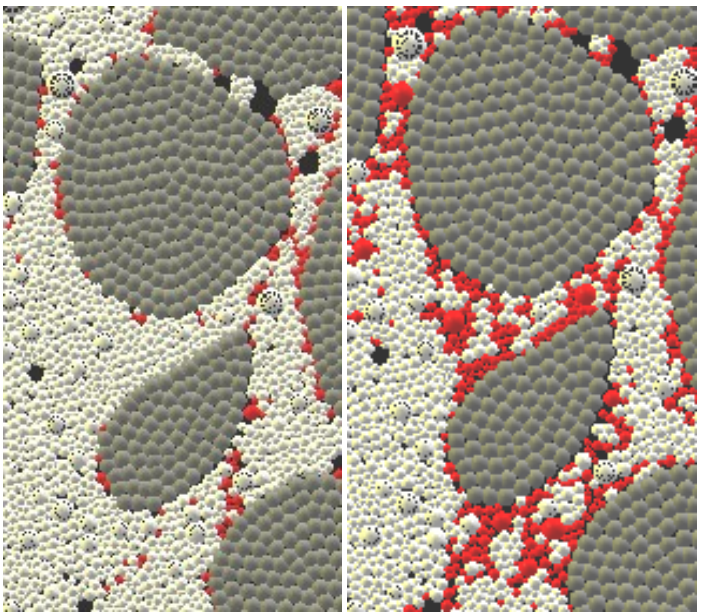

e) f)

Fig.5.10: Crack pattern evolution (marked by red colour) on specimen '3' front side from DEM with clusters of spheres: a) ε=0.03%, b) ε=0.06%, c) ε=0.12% and d) ε=0.20% (dark grey colour - aggregate, light grey colour - cement matrix, black colour – voids) and zoomed crack evolution in area marked with black rectangle (e) ε=0.06% and f) ε=0.2%)

Figure 5.11 demonstrates the evolution of the normal contact forces in the concrete specimen. The red lines in Fig.5.11 correspond to the compressive forces and the blue lines to the tensile forces. The thickness of the lines in Fig. 5.11 represents the magnitude of the normal contact force

between two particles. The external vertical load was transmitted via a network of vertical compressive normal contact forces which formed clear force chains. The tensile forces were horizontal. The compressive force chains carried the load majority and transmitted it on the entire system and were the predominant structure of internal forces at the meso-scale. Their distribution due to the grain re-arrangement during cracking became strongly non-uniform. The maximum compressive normal single force was about 320 N and maximum tensile normal single force was 19 N.

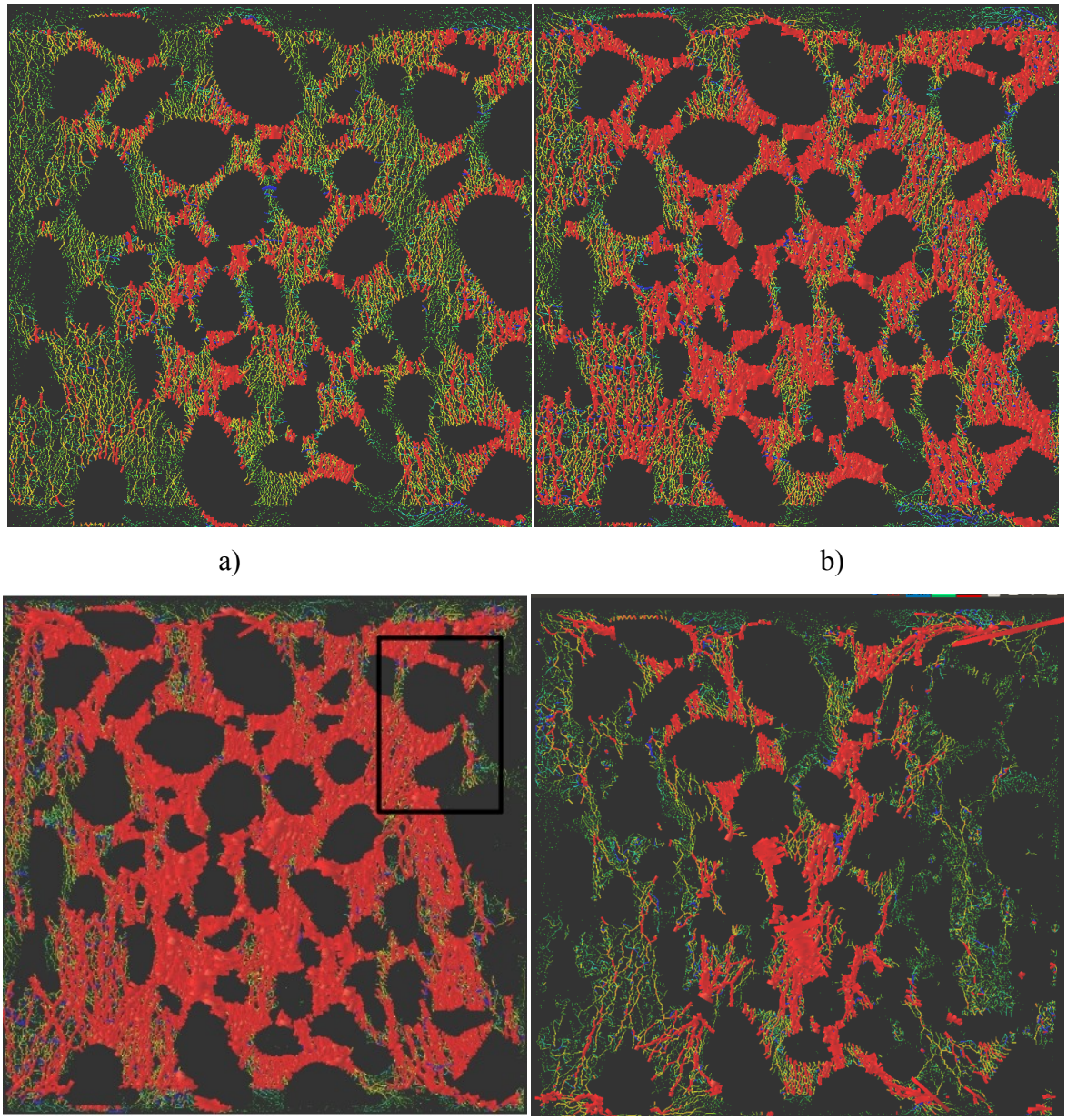

a) b)

c) d)

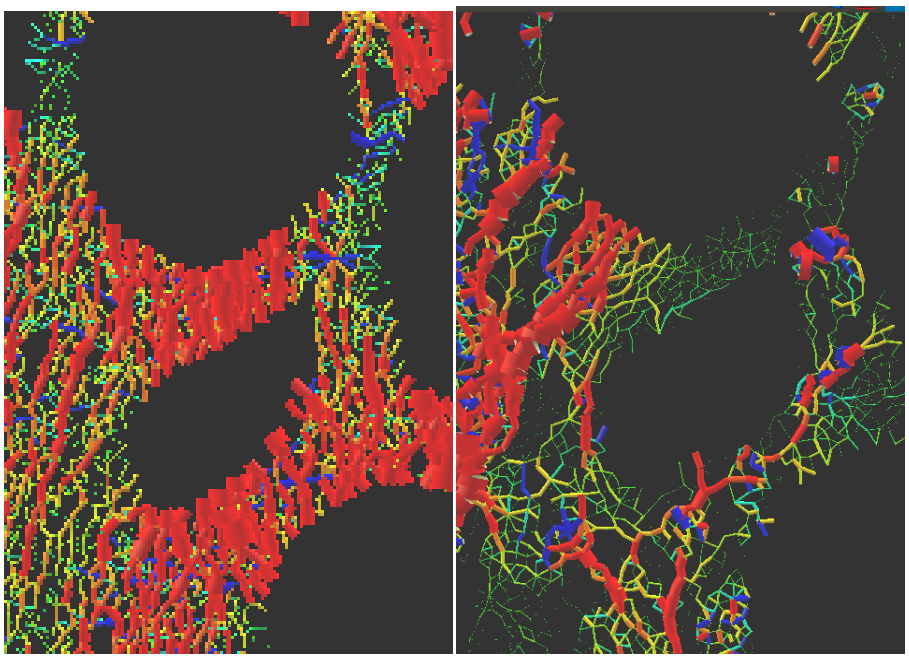

e) f)

Fig.5.11: 2D evolution of compressive and tensile normal contact forces during deformation in DEM for clusters of spheres (specimen '1', front side): a) ε=0.03%, b) ε=0.06%, c) ε=0.12% and d) ε=0.20% (red lines - compressive forces, blue lines - tensile forces) and zoomed normal forces evolution in area marked with black rectangle (e) ε=0.06% and f) ε=0.2%)

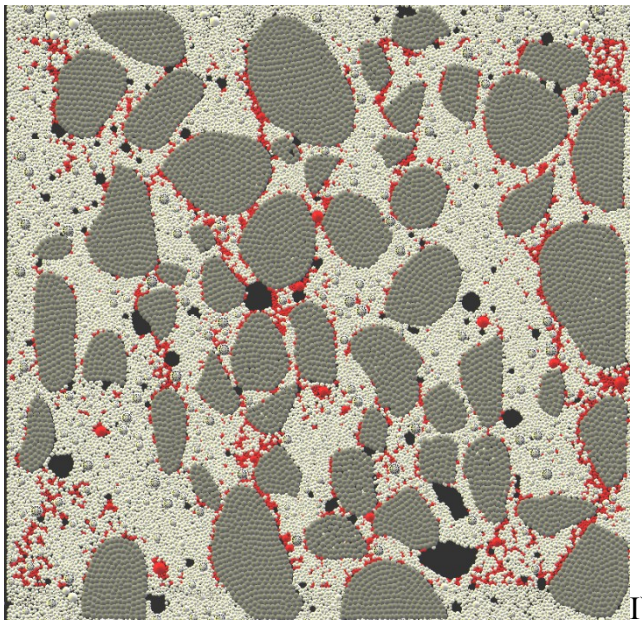

I)

II)

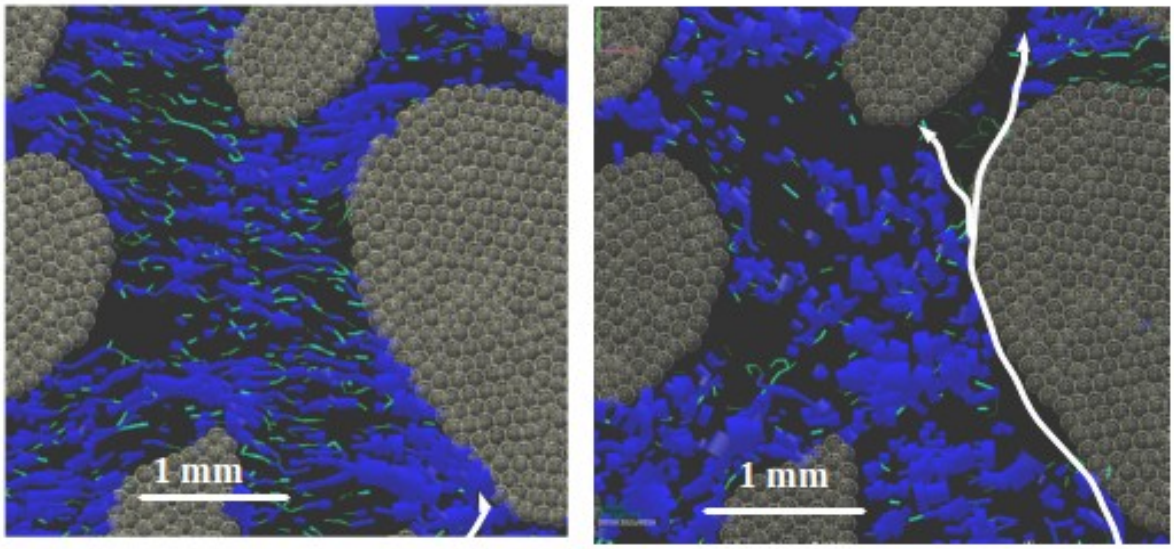

A)

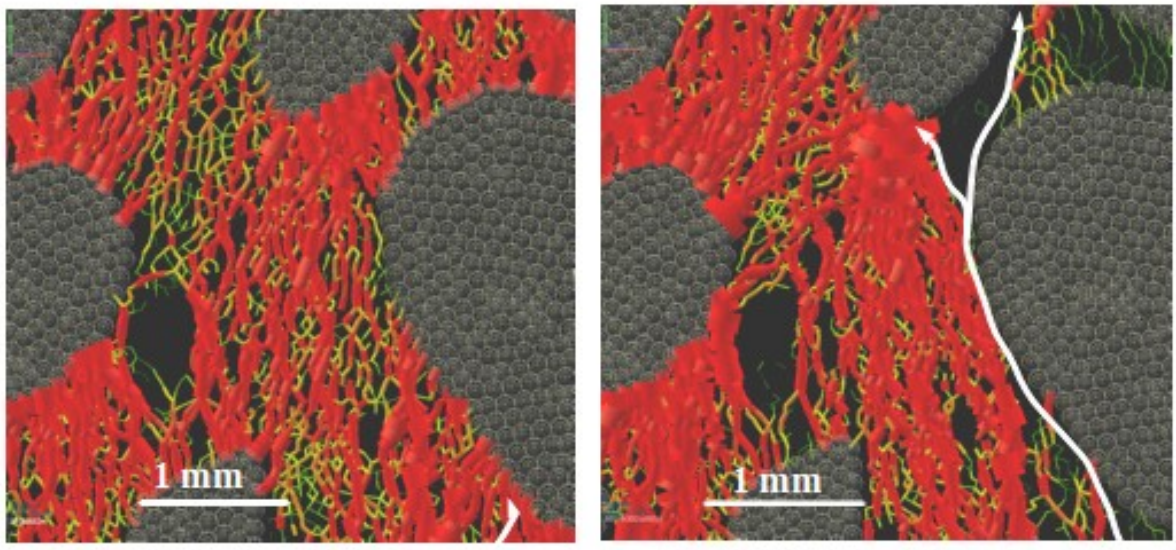

B)

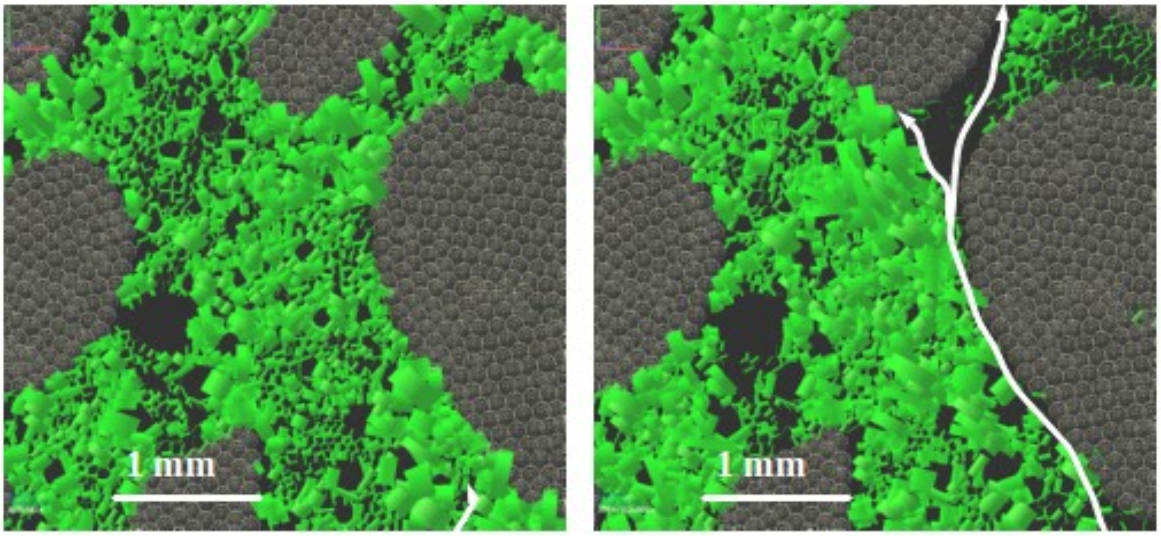

C)

Fig.5.12: DEM calculation results of contact forces between particles (clusters of spheres): I) cracked specimen front surface with marked zoomed region (black rectangle), II) evolution of: A) tensile, B) compressive and C) tangential contact forces between particles at crack in zoomed region for normal strain ε: a) ε=0.06% and b) ε=0.12% (A) tensile forces in blue, B) compressive normal forces in red, C) tangential forces in green) (white arrows indicate crack position, grey spheres indicate aggregate)

The evolution of normal and tangential contact forces along a propagating crack in the concrete specimen '3' is described in Fig.5.13. The outcomes show that the tangential forces also occurred along the propagating crack due to interlocking caused by a non-regular rough crack (Fig.5.13B).

The calculated 3D crack geometry in 3 different vertical cross-sections are presented in Fig.5.15. The occurrence mechanism of cracks (Fig.5.15) was the same as in 2D computations. The cracks in 2D and 3D studies are different in shape due to the different d_{cm}^{min}. The calculation outcomes cannot be directly compared with experiments due to the assumption of round aggregate particles and their different location.

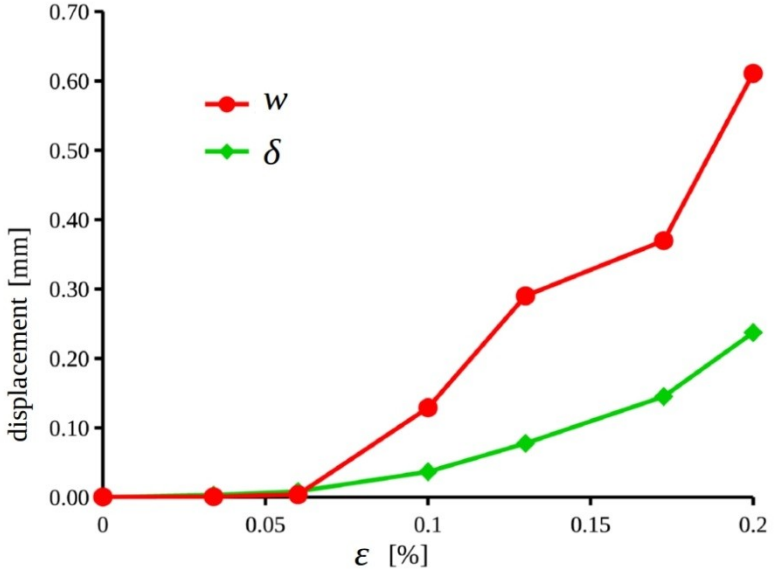

A)

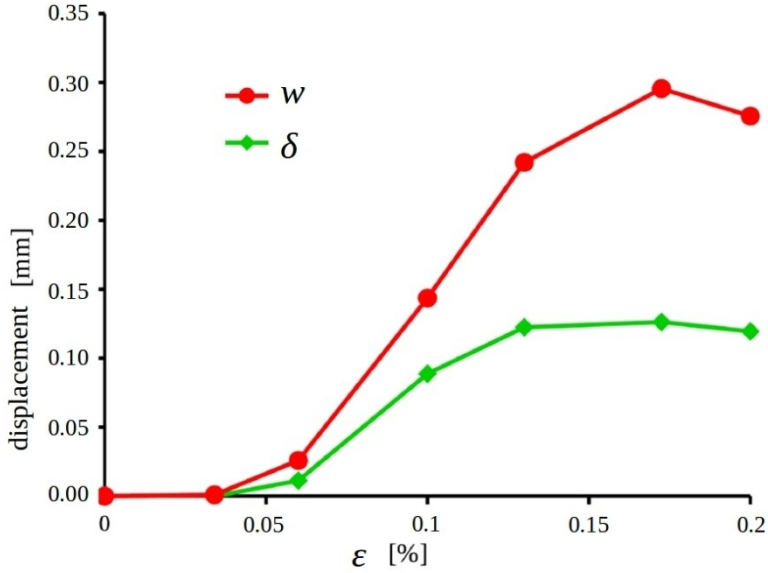

B)

Fig.5.13: Crack displacements w and δ versus global vertical normal strain ε from DEM analyses with clusters of spheres (w - normal crack displacement and δ - tangential crack displacement) for a) central vertical crack of Fig.5.2.1.3Aa and b) left inclined crack at right bottom corner of Fig.5.2.1.3Aa.

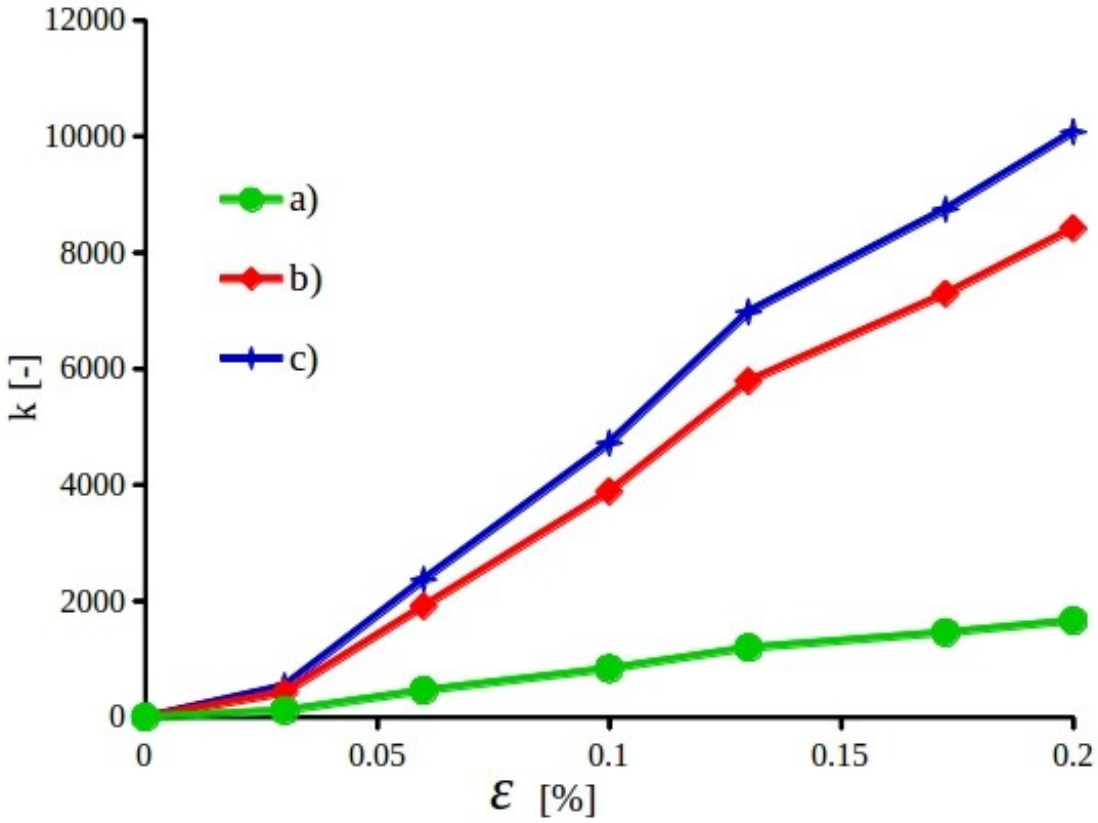

Fig.5.14: 2D DEM results: change of broken normal contact number *k* for real aggregate (clusters of spheres) on specimen front side against global vertical normal strain *ε:* a) normal contacts in ITZs, b) normal contacts in cement matrix and c) all normal contacts

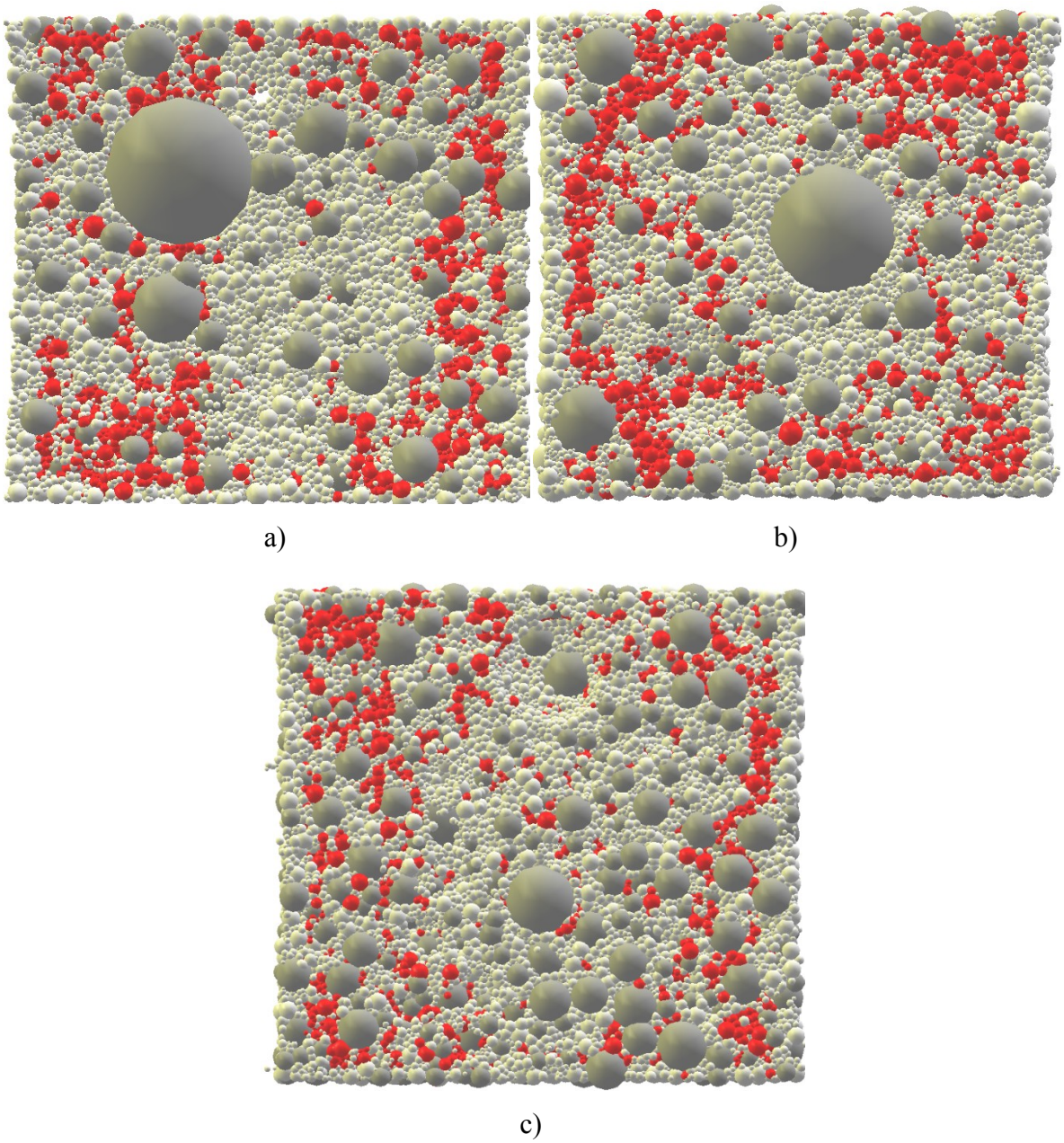

Fig.5.15: Crack patterns in vertical-sections at depth of 0.5 cm (A), 1.5 cm (B) and 3.5 cm obtained by 3D DEM with aggregate as spheres located at random (ε=0.12%) (spheres with broken normal contacts are in red, dark grey colour denotes aggregate with ITZ)

5.2 Splitting tension

The DEM calculations were carried out for concrete splitting with different boundary conditions (Suchorzewski et al. 2018b). The following parameters of the cohesion and tensile strength were used in all DEM analyses of tensile splitting: cement matrix ($E_{c,cm}$=15 GPa, C_{cm}=140 MPa and T_{cm}=25 MPa) and ITZs ($E_{c,ITZ}$=12 GPa, C_{ITZ}=112 MPa and T_{ITZ}=20 MPa) based on earlier

calculations regarding bending and uniaxial compression. ITZs were obviously the weakest phase. The ratio $E_{c,ITZ}/E_{c,cm}$=0.8 was chosen based on the experiments by Xiao et al. (Xiao 2013). The remaining ratios were also assumed as 0.8: C_{ITZ}/C_{cm}=0.8 and T_{ITZ}/T_{cm}=0.8 (Section 4) due to the lack of experimental results. Note that there were no contacts between aggregate grains (d_a□2 mm). The remaining parameters were constant for all phases and regions: υ_c=0.2 (Poisson's ratio of grain contact), μ=18^o (inter-particle friction angle), α_d=0.08 (damping parameter) and ρ=2.6 kG/m^3 (mass density). The prescribed damping parameter α_d and velocity did not affect the results during bending (Skarżyński et al. 2016). In the case of α_d<0.08, the too excessive kinetic energy was always created during fracture (the tensile numerical test could not be performed without numerical damping due to excessively high velocities of particles after fracture. In turn, the effect of the α_d-value on global results for α_d≥0.08 became insignificant. The calculated mean nominal inertial number I for the maximum vertical load (that quantifies the significance of dynamic effects) was <10^{-4} that always corresponded to a quasi-static regime. The 2D concrete specimen (D=0.15 m) under tensile splitting included in total about 20,000 spheres. The detailed calibration procedure was described by (Nitka and Tejchman 2015) based on real preliminary laboratory uniaxial compression and tension tests of concrete specimens (Fig.5.16).

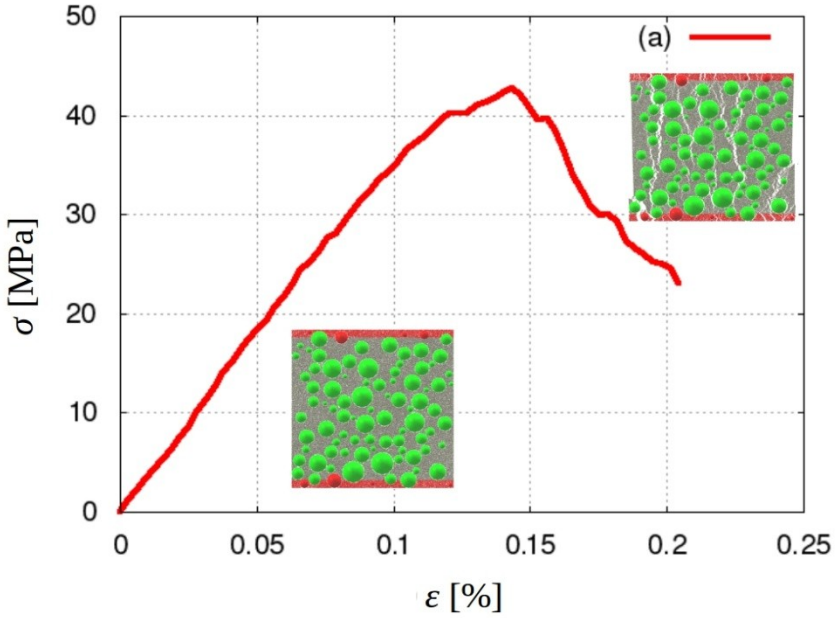

Fig.5.16: Stress-strain $\sigma=f(\varepsilon)$ evolution for 2D uniaxial compression test on square specimen 15×15 cm^2 from DEM with view on specimen before and after failure

Using these material parameters, a very good agreement was achieved between numerical and experimental results for D=0.15 m with respect to stress-displacement curve and fracture geometry

(Fig.5.17) (Nitka and Tejchman 2015). The rigid cylinder of steel at the top and bottom of the specimen was created by a single sphere of the diameter of 20 mm with the 10-times higher stiffness than concrete. The deformation was induced by prescribing the vertical top displacement in such a way that the changes of CMOD (crack mouth opening displacement) were approximately linear in time (as in experiments). CMOD was calculated as a horizontal displacement at the specimen mid-height between mid-points of two regions with the area of A=5×15 mm^2. The mid-points were at the distance of 40 mm as in the experiment. The time step was dt=10^{-8} s.

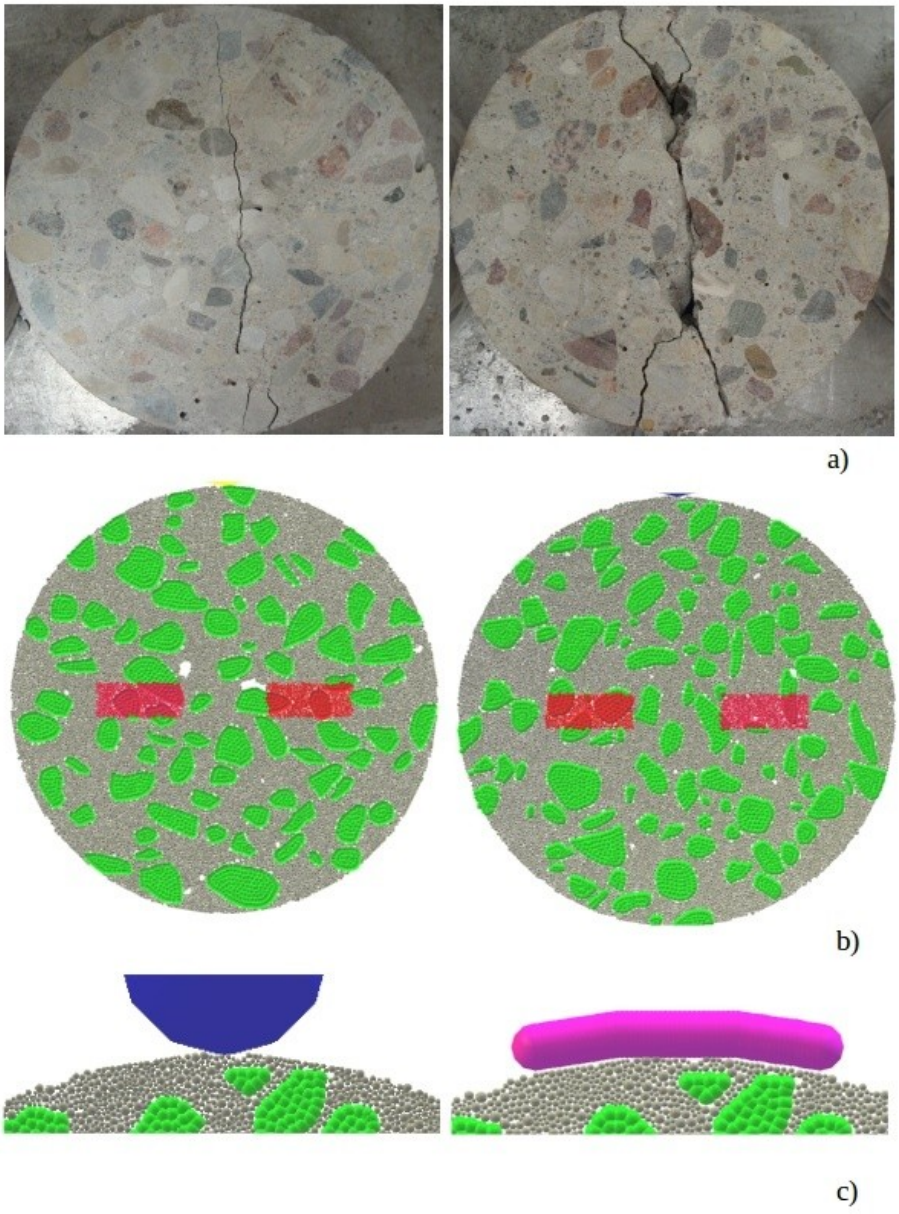

Fig.5.17: Front side of concrete specimens: A) specimen with steel cylinder and B) specimen with plywood, a) experiments, b) DEM (entire specimens) and c) DEM (upper region of specimen) (grey colour denotes cement matrix d_a<2 mm, green spheres denote aggregates with ITZ

(2 mm ≤d_a≤ 12 mm), white spots - macro-voids, blue colour - steel loading cylinder, violet colour - plywood loading plate and red areas are regions for CMOD measurements at specimen mid-height)

Stress-strain curves and fracture process

Figure 5.18 presents the DEM results of the strength compared to the experiments. The evolution of the vertical normal stress σ versus CMOD and v was satisfactorily reproduced (Figs.5.18A and 5.18B). The calculated maximum tensile stress was by 2% too low for the steel loading/supporting cylinders and by 10% too high for the plywood loading/supporting boards than in experiments. The calculated residual tensile stress was the same for the steel cylinders and by 30% too high for the plywood boards. The calculated rate of softening was similar for the steel cylinders and too small for the plywood boards. The differences between numerical and experimental results are probably caused by the different stiffness of plywood boards than in experiments and some slight deviations between the calculated and theoretical CMOD evolution (Fig.5.18C).

Next, the calculations were carried out with the different ratio of T_{ITZ}/T_{cm} and C_{ITZ}/C_{cm}, different intergranular friction angle μ in ITZs and different minimum particle diameter d_{min} (see also Chapter 5.1) in the cement matrix (Fig.5.2.1.4). By diminishing the ratio T_{ITZ}/T_{cm} from T_{ITZ}/T_{cm}=0.9 down to T_{ITZ}/T_{cm}=0.5, the splitting tensile strength decreased from σ=3.20 MPa down to σ =2.55 MPa. The specimen brittleness slightly decreased (Fig. 5.19A). However, a decrease of the ratio C_{ITZ}/C_{cm} from C_{TZ}/C_{cm}=0.9 down to C_{ITZ}/C_{cm}=0.5 did not affect the results (Fig. 5.19B) since the tensile failure dominated during splitting tension. The change of μ (expressing the different aggregate roughness) did not also affect the results (Fig. 5.19C). By reducing the minimum particle diameter in the mortar from d_{min}=1.0 mm down to d_{min}=0.35 mm (Fig. 5.19D), the splitting tensile strength decreased from σ=3.70 MPa down to σ=3.05 MPa (reduction by 15%) and ductility increased. However, if d_{min} reduced from 0.35 mm down to 0.25 mm, the splitting tensile strength merely diminished by 5%. Therefore the value of d_{min}=0.35 mm was used in computations. Note that lower values of d_{min} strongly increase the computation time (for d_{min}=0.25 mm the computation time became longer by the factor 4 as compared to d_{min}=0.35 mm).

The cracked concrete specimens are shown in Fig.5.19 for plywood boards and steel cylinders (DEM versus experiments). Figure 5.20 presents the calculated fracture evolution in the concrete specimen with the plywood boards. The main calculated mechanism of a crack propagation at the meso-level is depicted in Fig.5.22.

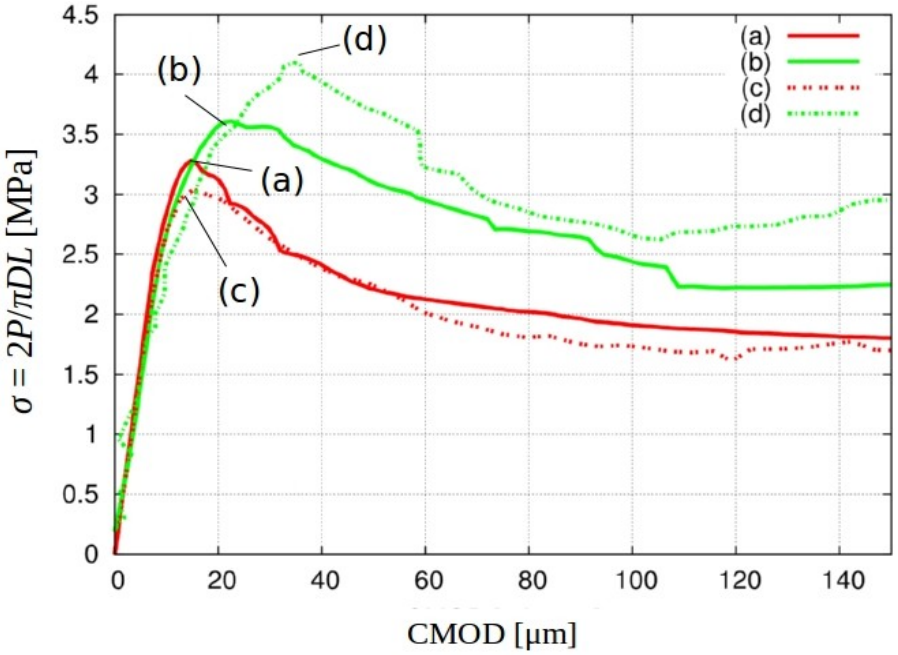

A)

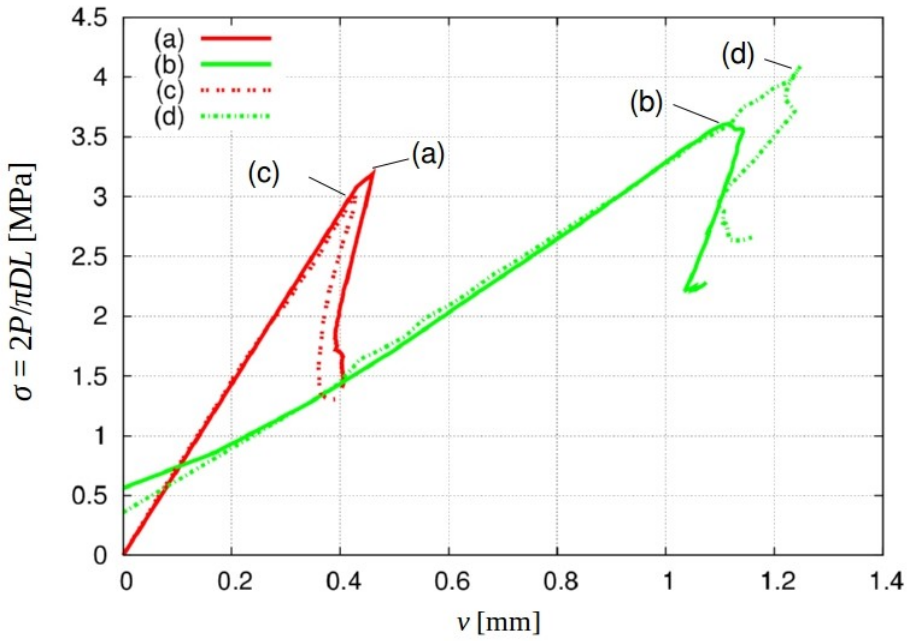

B)

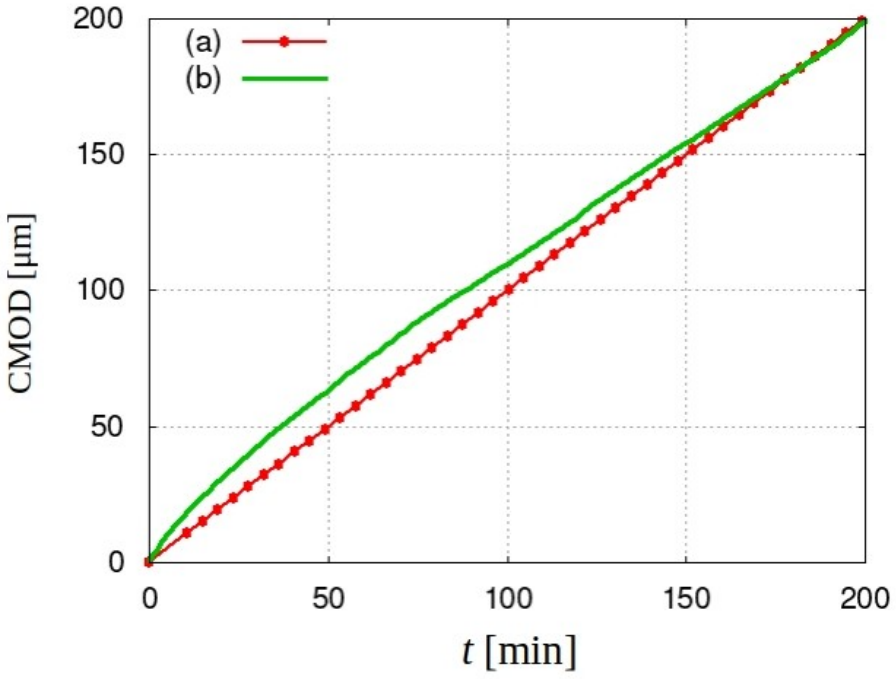

C)

Fig.5.18: Calculated DEM results against experimental ones: A) vertical normal stress σ against CMOD, B) vertical normal stress σ against top vertical displacement v (curves 'a' and 'b' - experiments, curves 'c' and 'd' - DEM, red lines - steel loading cylinder, green lines - plywood loading/supporting boards) and C) relationship between CMOD and loading time in experiment (a) and DEM (b) (continuous lines - experiments, dashed lines - DEM)

The calculated crack patterns were very similar to the experimental ones (Fig.5.19). In DEM calculations with the plywood strip (Figs. 5.19Bb and 5.19Bc), the macro-crack followed exactly the same path as in experiments (Fig. 5.19Ba). It also branched into rigid wedges at the same height (25% of D from the top and bottom). However, the crack shape in the wedge often followed the other side of the aggregate particle. In DEM calculations with the steel cylinder (Figs. 5.19Ab and 5.19Ac), the macro-crack was more curved than in experiments (Fig. 5.19Aa) and followed the opposite edges of aggregates in the lower specimen half. The large aggregate grain at the specimen bottom crushed in the experiment in contrast to DEM outcomes (the model has not included grain crushing yet).

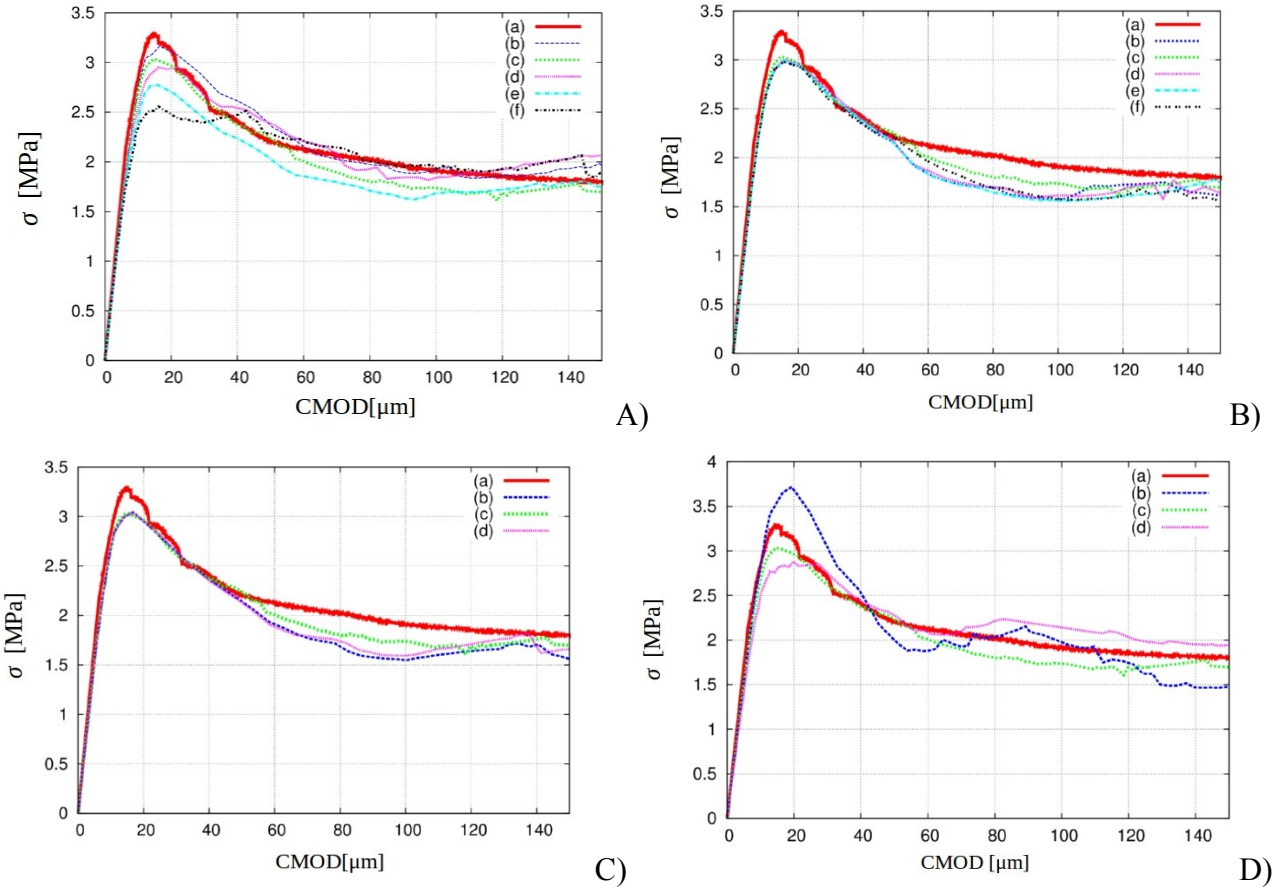

Fig.5.19: Evolution of vertical normal stress σ versus *CMOD* from DEM results for steel loading cylinder with different ratio of T_{ITZ}/T_{cm} (A) and C_{ITZ}/C_{cm} (B) (b) $T_{ITZ}/T_{cm}=C_{ITZ}/C_{cm}=0.9$, c) $T_{ITZ}/T_{cm}=C_{ITZ}/C_{cm}=0.8$, d) $T_{ITZ}/T_{cm}=C_{ITZ}/C_{cm}=0.7$, e) T_{ITZ}/T_{cm} $C_{ITZ}/C_{cm}=0.6$ and f) $T_{ITZ}/T_{cm}=C_{ITZ}/C_{cm}=0.5$), different intergranular friction angle μ in ITZs (C) (b) $\mu=8°$, c) $\mu=18°$, d) $\mu=30°$) and different minimum diameter of cement sphere d_{min} (b) $d_{min}=1.0$ mm, c) $d_{min}=0.35$ mm and d) $d_{min}=0.25$ mm) as compared to experimental curve 'a'

In DEM simulations, initially, several single micro-cracks occurred in the entire specimen (Fig.5.20a). The broken contacts first occurred always in ITZs at corners of aggregate particles wherein tensile forces were the largest. They developed next in ITZs along aggregate edges. Later the micro-cracks started to concentrate in the vertical central zone at the specimen mid-height (Fig.5.20b). Afterwards, they connected with each other in the cement matrix by bridging and created a discrete macro crack in the vertical central zone (similarly as in the experiment) (Fig.5.20c). The crack propagated towards the top and bottom of the specimen for CMOD=150 μm (Fig.5.20d). At the top and bottom, it branched by creating a clear wedge under the

loading/supporting plywood boards. At the test end (CMOD>150 μm), the specimen was almost symmetrically de-fragmented.

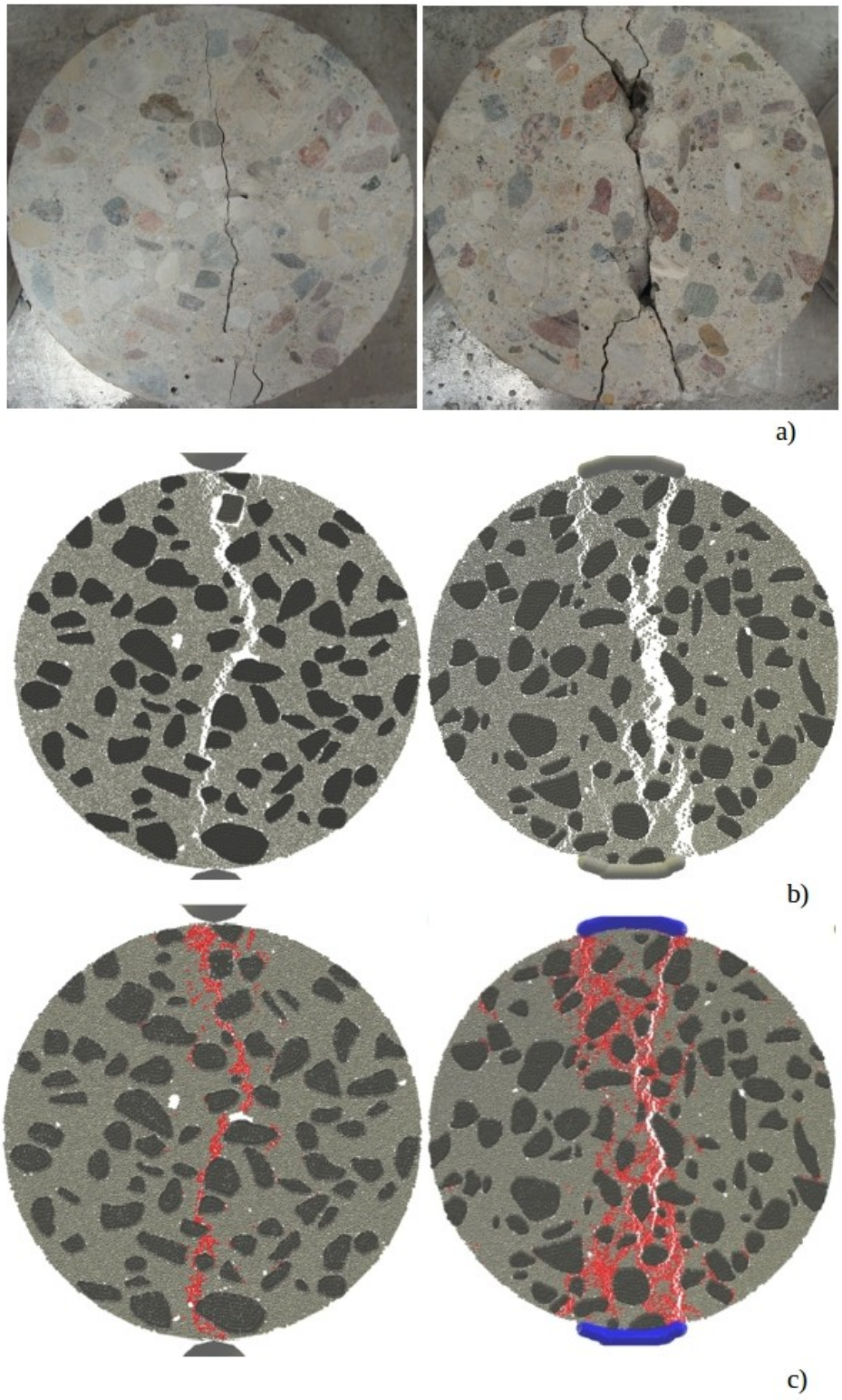

Fig.5.20: Experimental and calculated fractured specimens at residual state for CMOD>150 μm: a) experimental cracks and b) and c) calculated cracks by DEM (red colour corresponds to broken contacts) for A) steel loading/supporting cylinders and B) plywood loading/supporting boards

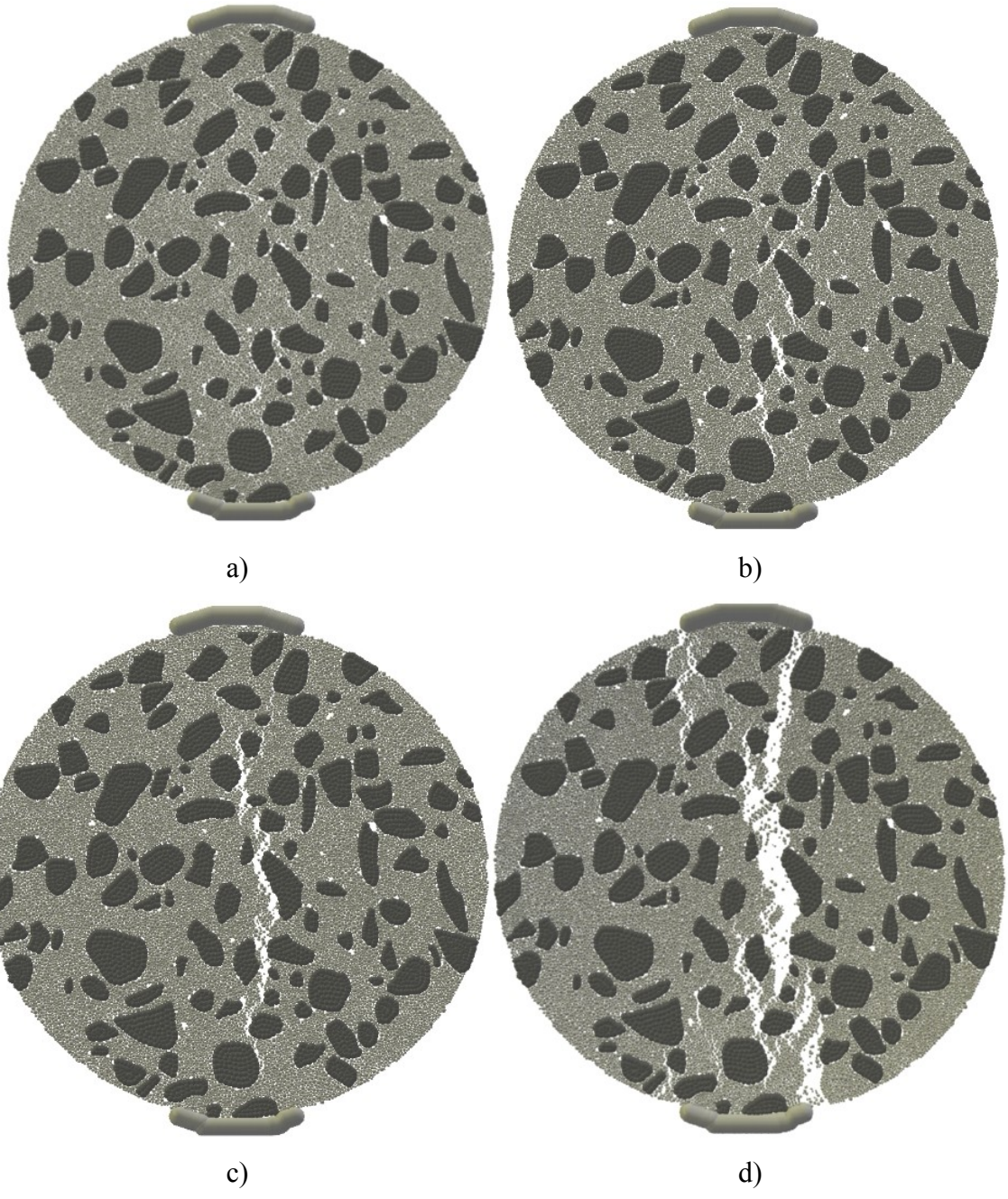

Fig.5.21: Calculated evolution of cracking in concrete specimen versus CMOD for plywood loading/supporting boards: a) CMOD=10 μm, b) CMOD=20 μm, c) CMOD=30 μm and d) CMOD=150 μm (black colour indicates aggregates, grey colour represents cement matrix and white colour is opened macro-crack (displacements were magnified by factor 200)

Meso-scale phenomena

The macro-crack was always created by bridging interfacial micro-cracks (Fig.5.22).

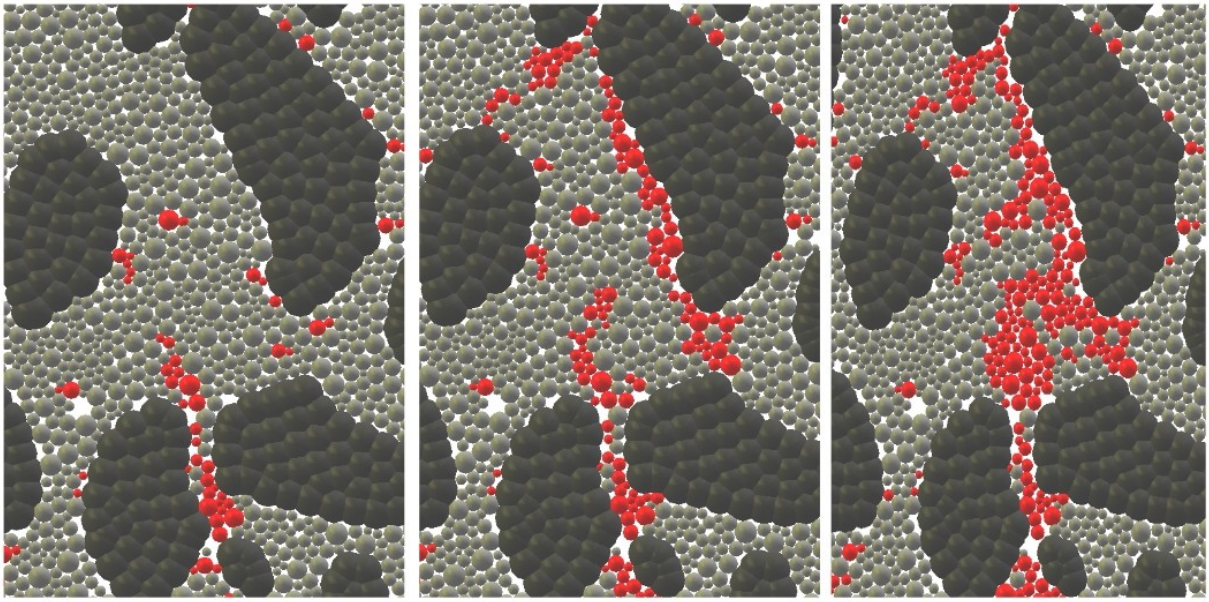

a) b) c)

Fig.5.22: Mechanism of macro-crack creation in concrete specimen by bridging interfacial zones for plywood loading board using DEM: a) CMOD=10 μm, b) CMOD=15 μm and c) CMOD=20 μm (spheres in red indicate broken contacts, dark grey corresponds to aggregate)

The calculated resultant particle displacements from the quadratic cell equal to $5d_{50}\times5d_{50}$ moved by 2 mm (d_{50}=2 mm - the mean particle diameter) across a localized zone (FPZ) are depicted in Fig.5.23. In order to realistically calculate the width of a localized zone w_{lz}, the calculated particle displacements were again fitted first by the error function ERF (Section 3, Eq.21). The calculated width of a localized zone was w_{lz}=3.9 mm based on the displacement jump shown in Fig.18 (i.e. $0.33\times d_a^{max}$ and $0.8\times d^a_{50}$). It was slightly larger than the experimental result obtained by means of DIC (w_{lz}=3.4 mm, Fig.5.23).

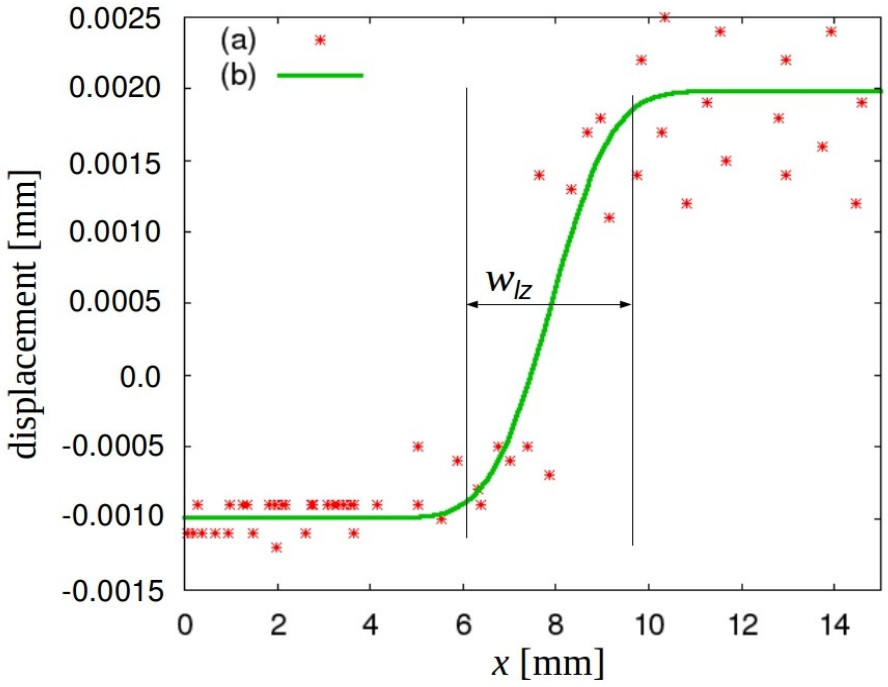

Fig.5.23: Calculated horizontal displacement profile at specimens mid-height for CMOD=25 μm (with plywood loading strip) versus horizontal coordinate *x* across localized zone from DEM (points '*a*' correspond to DEM results and solid line '*b*' corresponds to error function ERR)

Figure 5.24 presents the evolution of inter-particle normal contact forces. The blue lines indicate tensile and red lines compressive forces. The line thickness is proportional to the force magnitude. The external vertical splitting force was transmitted via a network of normal contact forces which formed force chains. They carried the majority of the loading and transmitted it on the entire system and were the predominant structure of internal forces at micro-scale. Initially, large vertical compressive normal contact forces were created in the almost entire specimen (Fig.5.24a). Tensile normal forces occurred in a perpendicular (horizontal) direction. In the boundary regions, compression obviously dominated over tension. Before the peak of the vertical force, the compression and tensile forces increased, however, some single tensile forces started to break due to the contact damage (Fig.5.24b). After the load peak, the horizontal tensile forces started to be smaller (Fig.5.24c). When a vertical macro-crack ocrossed the specimen, the compressive forces concentrated in the specimen mid-region and the tensile forces became located mainly along the specimen circumference due to the compression of two separated specimen halves (Fig.5.24d). The maximum single compressive force was 75 N and tensile one was 8 N. Some compressive forces appeared also along the non-uniform macro-crack edge due to aggregate inter-locking (Skarżyński et al. 2016, Elias et al. 2012, Scholtes&Donze 2013).

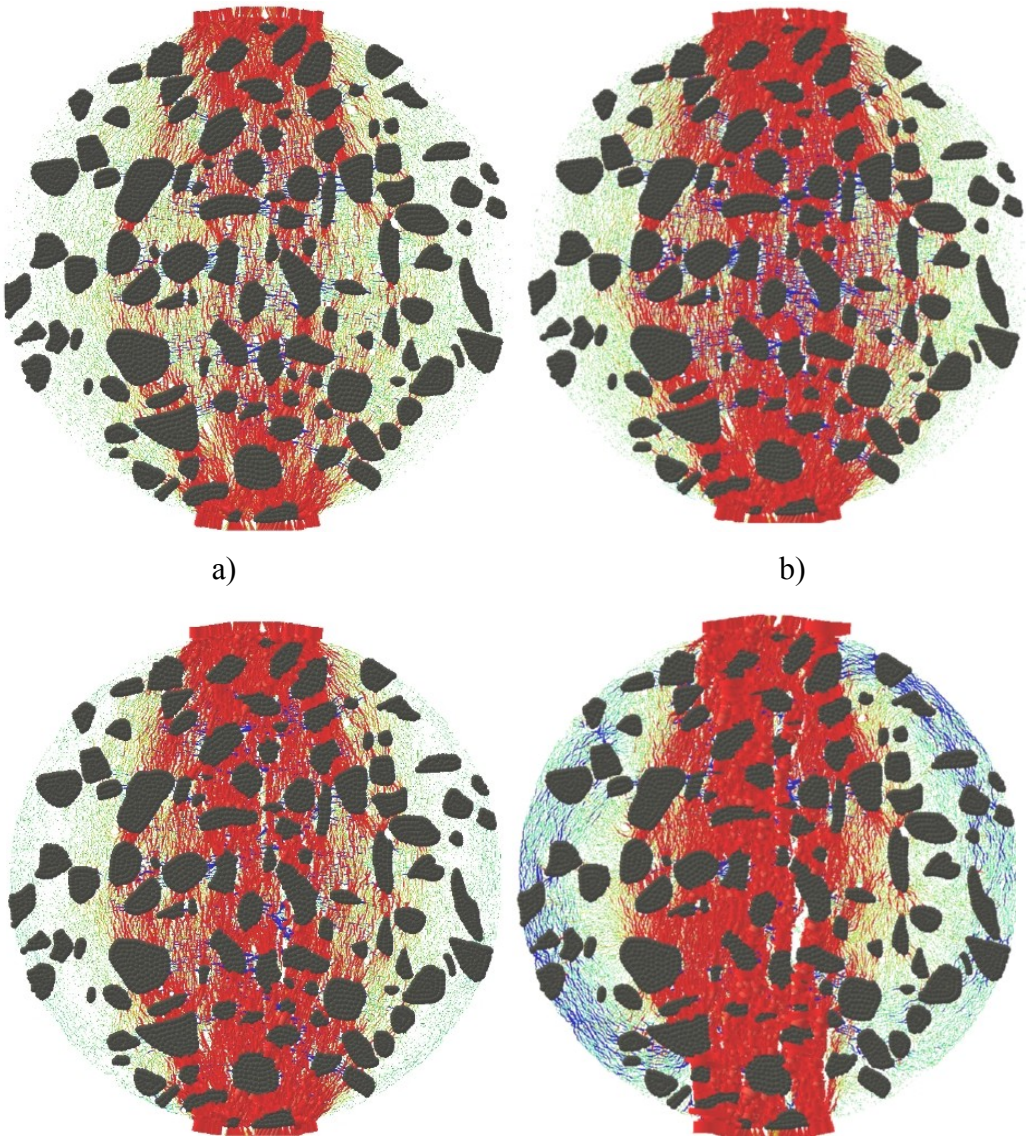

Fig.5.24 Inter-particle tensile (blue lines) and compressive (red lines) normal contact forces in DEM calculations for concrete specimen with plywood boards versus CMOD: a) CMOD=10 μm, b) CMOD=20 μm, c) CMOD=30 μm and d) CMOD=150 μm (green colour denotes small values of internal forces)

The evolution of the number of broken normal contacts is demonstrated in Fig.5.25A. For the force line contact, the total number of broken normal contacts was always lower by about 10% than for the force surface contact. The total number of broken contacts was approximately 1750-2100 (Figs.5.25Ac and 5.25Af). The number of broken normal contacts in ITZs (n=420-450) (Figs.5.25Aa and 5.25Ad) was 3.5-4 times smaller than in the cement matrix (n=1400-1750) (Figs.5.25Ab and 5.25Ae). Nearly 30-40% (cement matrix) and 90% (ITZs) of normal contacts

were damaged before the peak load due to micro-cracking. The rate of the normal contact breakage with increasing CMOD was always smaller in ITZs. At the deformation beginning, the mean coordination number (number of contacts per particle) was N=4.75-4.80 (Fig.5.25B). Up to the peak, the mean coordination number reduced to N=4.65-4.70 due to micro-cracking. Before the loading end, it decreased further to the value of N=4.57-4.59 due to macro-cracking.

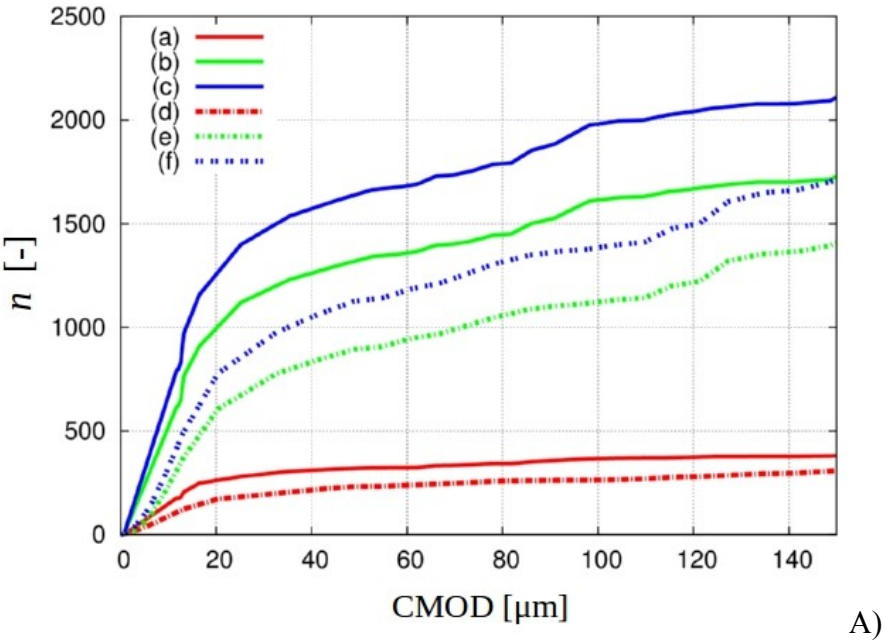

A)

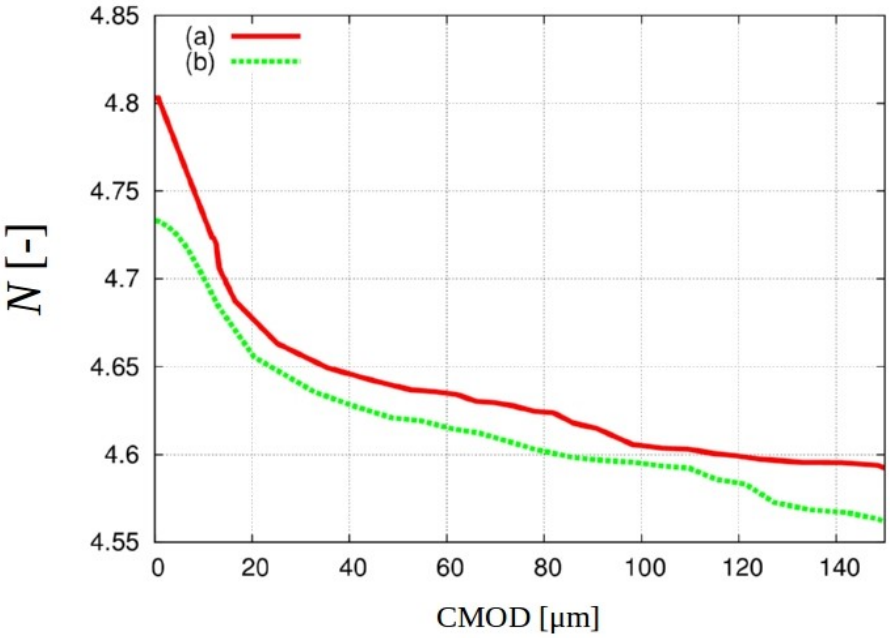

B)

Fig.5.25: DEM results: A) evolution of broken normal contacts n against CMOD in concrete specimen with plywood loading/supporting boards (continuous lines) and steel loading/supporting cylinders (dashed lines): a) and d) in ITZs, b) and e) in cement matrix and c) and f) in concrete

specimen and B) evolution of coordination number N versus CMOD (a) plywood loading board and b) steel loading cylinder)

The calculated horizontal normal stress based on normal and tangential contact forces between particles along the vertical central line is demonstrated in Fig.5.26. The stress was determined from the formula (Love 1927):

$$\sigma_{ij} = \frac{1}{V_p} \sum_{c=1}^{n} x_i^c f_j^c , \tag{39}$$

wherein x_i^c - the i-th component of the branch vector connecting the centre of the particle mass of the particle p with the contact point c, f_j^c - j-th component of the total force in that contact point and V^p - the particle volume (area in 2D). In order to avoid too strong stress fluctuations, the stresses were calculated from the cell $5d_{50}\times5d_{50}$ which was moved by d_{50}. The calculated stress was compared with experimental measurements by Ferrara and Gettu (Ferrara 2001) (using a cardboard loading/supporting strip) and theoretical elastic solution by (Timoshenko 1977). The calculated stresses obviously indicated a certain fluctuation due to the presence of aggregate particles. The calculated maximum tensile normal stresses (curves 'a and 'b' in Fig.5.26) were very similar as the measured one (Ferrara&Gettu 2001) (curve 'c' in Fig.5.26) and the theoretical one (Timoshenko1977) (curve 'd' in Fig.5.26). In the case of the maximum compressive normal stress at horizontal boundaries, the theoretical value described by the curve 'b' was higher by 30% than the measured one (curve 'c').

Figure 5.27A presents the evolution of the average normal and shear displacement along the main central macro-crack at the mid-height. In the elastic range, the shear crack displacement dominated over the normal crack displacement. However, the normal crack displacement was later dominant. After the peak load (CMOD>30 μm), the shear crack displacement reached an asymptote for δ=39 μm, while the normal displacement linearly grew up. The failure had a clear tensile type.

The distribution of particle rotations in the concrete specimen is demonstrated in Fig. 5.27B for CMOD=150 μm. The rotations obviously occurred only if cracks appeared after the bond breakage. The maximum particle rotations at the test end were about 0.7°. The number of particles rotating clockwise and counter-clockwise was similar.

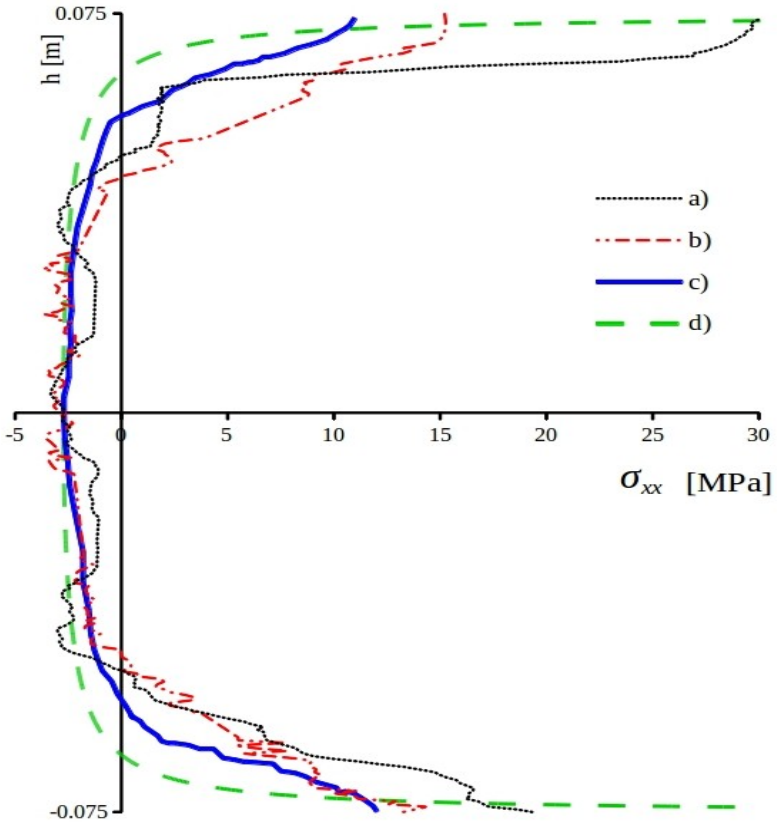

Fig.5.26: Distribution of horizontal normal stress σ_{xx} in concrete specimen along height h=D=0.15 m for CMOD=18 μm: a) DEM (steel loading/supporting cylinders), b) DEM (plywood loading/supporting boards, c) measurements by Ferrara (Ferrara&Gettu 2001) and d) analytical solution by (Timoshenko 1977)

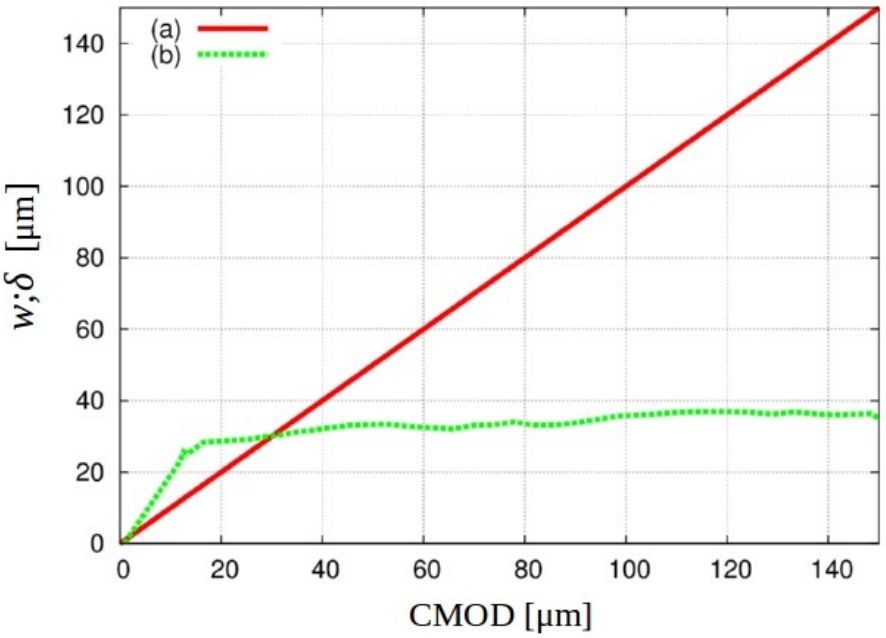

A)

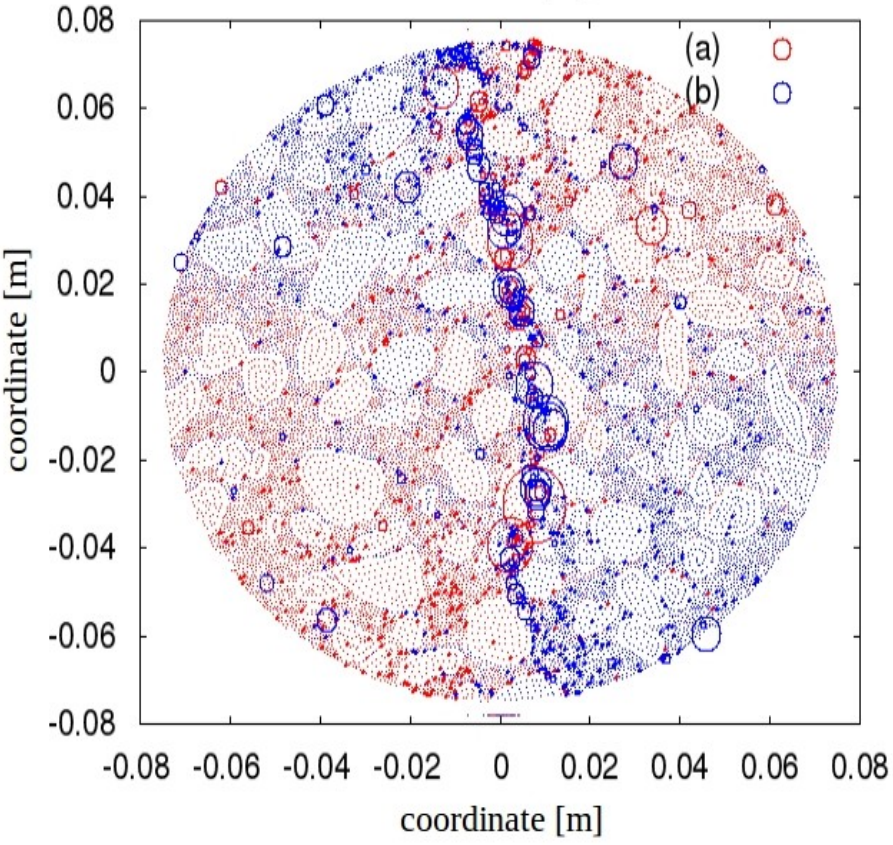

B)

Fig.5.27: DEM results (plywood boards): A) evolution of crack displacement versus CMOD in central macro-crack (a) normal direction w and b) shear displacement δ) and B) distribution of particles rotations for CMOD=150 μm (a) red circles indicate clockwise and b) blue circles show counter-clockwise rotation, circle diameter is proportional to particles rotation)

5.3 Meso-scale size effect analyses

The size effect on strength and brittleness was investigated on two concrete 2D specimens with the different diameter D (D=0.15 m and D=0.05 m) during a splitting test (Suchorzewski et al. 2019).

Stress-strain curves and fracture process

For size effect simulations, the concrete specimen with the 3 times smaller diameter (D=0.05 mm) was artificially constructed by cutting it out from the specimen D=0.15 m in order to eliminate the statistical effect in concrete (Fig.5.28). This specimen included totally 2 500 spheres. The deformation was induced by prescribing the vertical displacement at the specimen top. In addition, one simulation was performed with the cut-out specimen of the diameter of D=0.05 m with the reduced minimum sphere diameter in the cement matrix d_{cm}^{min}=0.10 mm (instead of d_{cm}^{min}=0.35 mm).

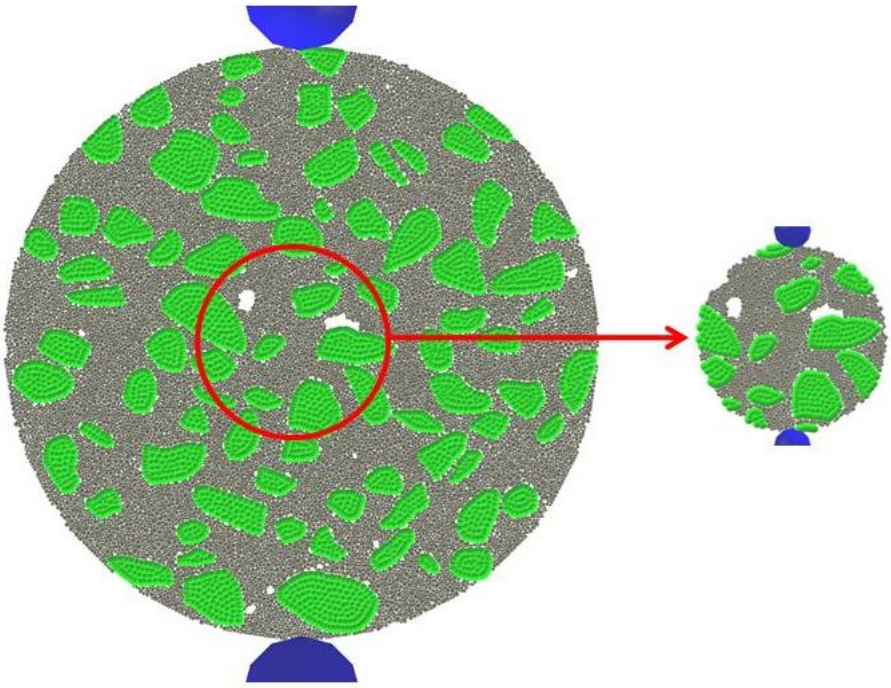

a) b)

Fig.5.28: Numerical construction of smaller 2D concrete specimen from larger specimen for DEM calculations (a) D=0.15 m and b) D=0.05 m)

Figure 5.29 presents the DEM results of the evolution of the tensile splitting stress σ versus vertical piston displacement v for two different specimen diameters D: D=0.05 m and D=0.15 m. In contrast to calculations with D=0.15 m, the numerical test for D=0.05 m was carried out by prescribing the vertical displacement v. The results of Fig.5.3.1.1 indicate a clear size effect regarding both the

strength and brittleness. The calculated maximum tensile splitting stress was higher by about 17% (3.5 MPa against 3.0 MPa) and normalized vertical piston displacement v/D corresponding to maximum tensile splitting stress was higher by about 20% (v/D=0.36 against v/D=0.30) for the smaller specimen diameter D=0.05 m than for the larger specimen D=0.15 m. The specimen with the smaller diameter D indicated a quasi-brittle failure mode and the specimen with the higher diameter D indicated a very brittle failure mode with the snap-back instability. The smaller minimum sphere diameter, d_{cm}^{min}=0.1, mm did not affect the peak stress, however, it slightly increased the concrete ductility due to the relatively small number of particles in the entire specimen of D=0.05 m (Fig.5.29b).

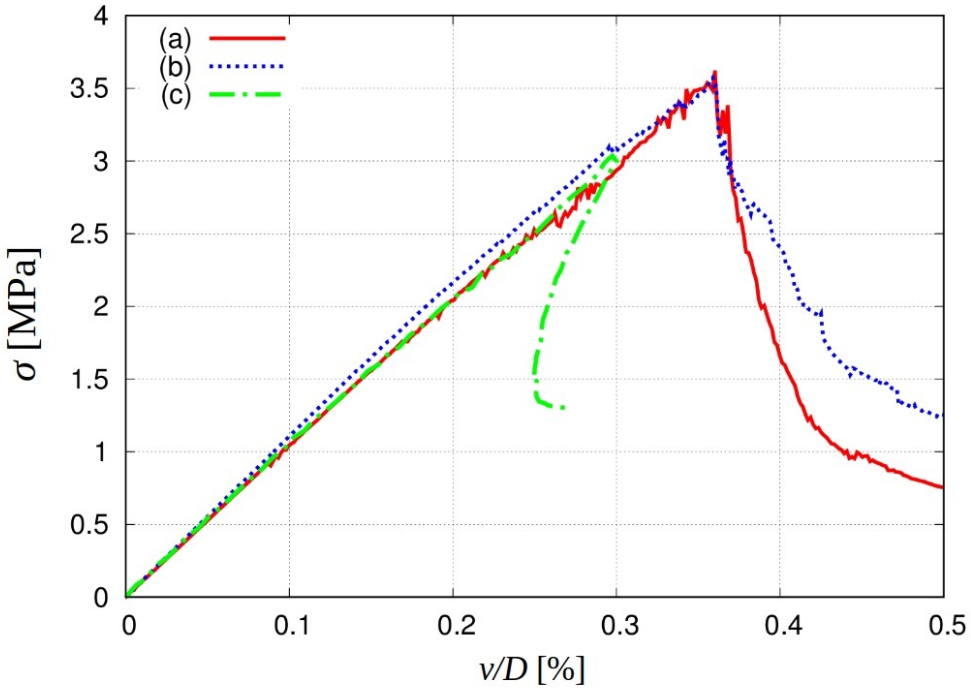

Fig.5.29: DEM results: evolution of nominal tensile splitting stress $\sigma=2P/(\pi DL)$ against normalized vertical piston displacement v/D for two different specimen diameters D and minimum particle diameters d_{cm}^{min}: a) D=0.05 m with d_{cm}^{min}=0.35 mm, b) D=0.05 m with d_{cm}^{min}=0.10 mm and c) D=0.15 m with d_{cm}^{min}=0.35 mm

Figure 5.30 demonstrates the fractured specimens. The width of the fracture region (marked in blue in Fig.5.29) was assumed to be about 4 mm and was equal to the width of FPZs in experimental measurements and previous DEM calculations (Suchorzewski et al. 2018a).

Initially, several single micro-cracks occurred in the entire specimen. Later micro-cracks started to concentrate in the vertical central zone at the specimen mid-height. Afterwards they connected with each other in the cement matrix by bridging in order to create a discrete macro-crack in the vertical central zone (similarly as in the experiment). The macro-crack propagation way was similar in both concrete specimens (Fig.5.30).

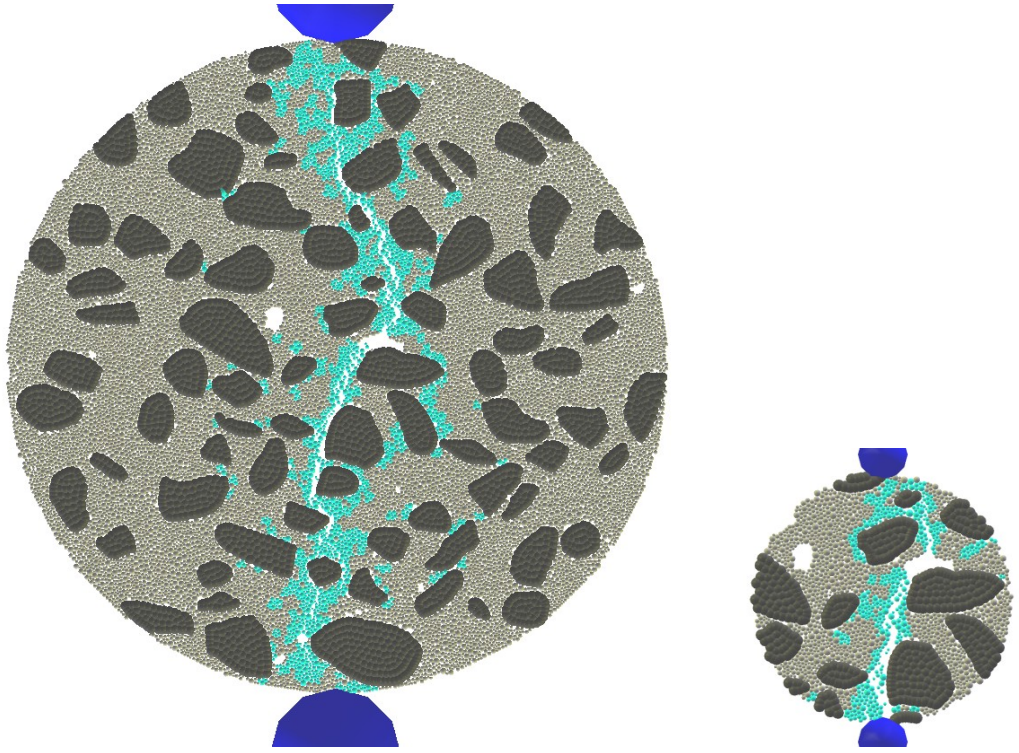

a) b)

Fig.5.30: Calculated fracture in concrete specimen for residual splitting tensile stress of σ=1.5 MPa for 2 different specimen diameters: a) D=0.15 m and B) D=0.05 m (black colour indicates aggregates, grey colour represents cement matrix, white colour shows macro-pores, cyan colour denotes area with broken contacts and blue colour shows supports (displacements were magnified by factor 100)

Evolution of broken normal contacts

The evolution of the number of broken normal contacts for two concrete specimens D=0.05 m and D=0.15 m during deformation is demonstrated in Figs.5.31. Figure 5.32 shows the distribution of broken normal contacts up to peak (Fig.5.32a) and between the peak load and failure (Fig.5.32b) for two different specimen diameters D.

The number of broken contacts obviously increased during deformation in particular after the peak load (Fig.5.31). The total number of broken contacts was n=350 (D=0.05 m) and n=1200 (D=0.15 m) in the considered range of v/D. With respect to the specimen diameter, the total normalized number of broken contacts was n/D=350 and n/D=400, respectively. The relatively more contacts were broken before the peak load for D=0.15 m (850/1200=0.71) than for D=0.05 m (180/350=0.51) and after the peak load up to the failure for D=0.05 m (170/350=0.49) than for D=0.15 m (350/1200=0.29) (Figs. 5.31 and 5.32). Therefore the numerical damping and kinetic energy were higher for D=0.05 m after the peak. It is visible that the pronounced continuous cracking process started in D=0.05 m slightly before the peak load for v/D=0.33 (Fig.5.32A) and in the specimen of D=0.15 m clearly before the peak load v/D=0.25 (Fig.5.32B). During the snap-back behaviour (D=0.15 m) relatively less contacts were broken after the peak load than during the plastic behaviour in the specimen of D=0.05 m (Figs.5.32) that caused that the post-peak behaviour was also more ductile in the smaller specimen (ductility increases with a longer crack propagation way related to the growth of broken contact number (Nitka 2015, Suchorzewski 2018a). The number of broken normal contacts in ITZs (n=60/220) was about 5 times smaller than in the cement matrix (n=300/1000) (Fig.5.32). Nearly 50%/70% (cement matrix) and 50%/90% (ITZs) of normal contacts were damaged before the peak load for D=0.05 m and D=0.15 m due to micro-cracking. The rate of the normal contact breakage was always smaller in ITZs.

Figure 5.33 confirms that for the smaller concrete specimen of D=0.05 m (Fig.5.33A) less contacts (relatively to the total cross-section area) were broken up to the peak (connected with the higher elastic energy) and relatively more contacts were broken in the softening region (connected with the smaller elastic energy) as compared to D=0.15 m (Fig.5.33B).

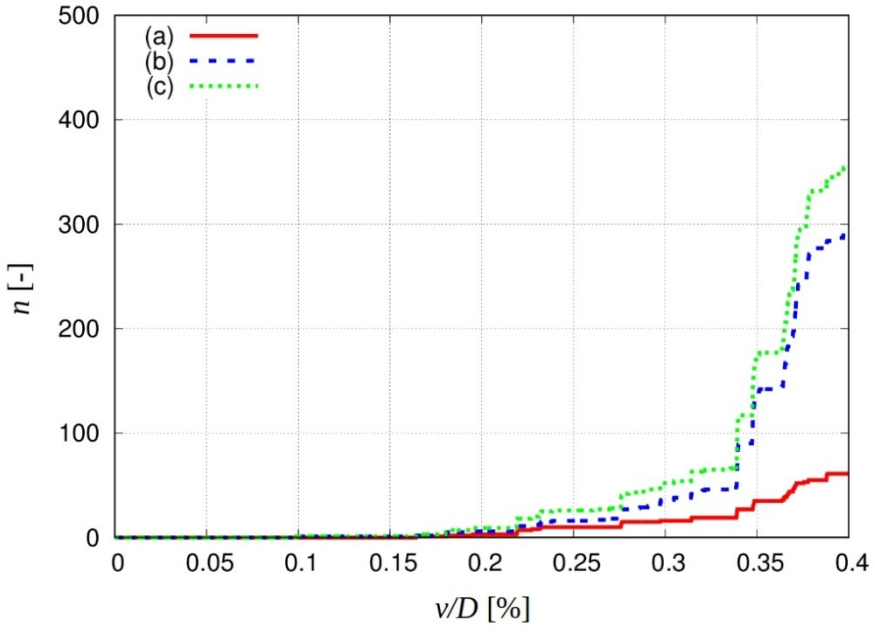

A)

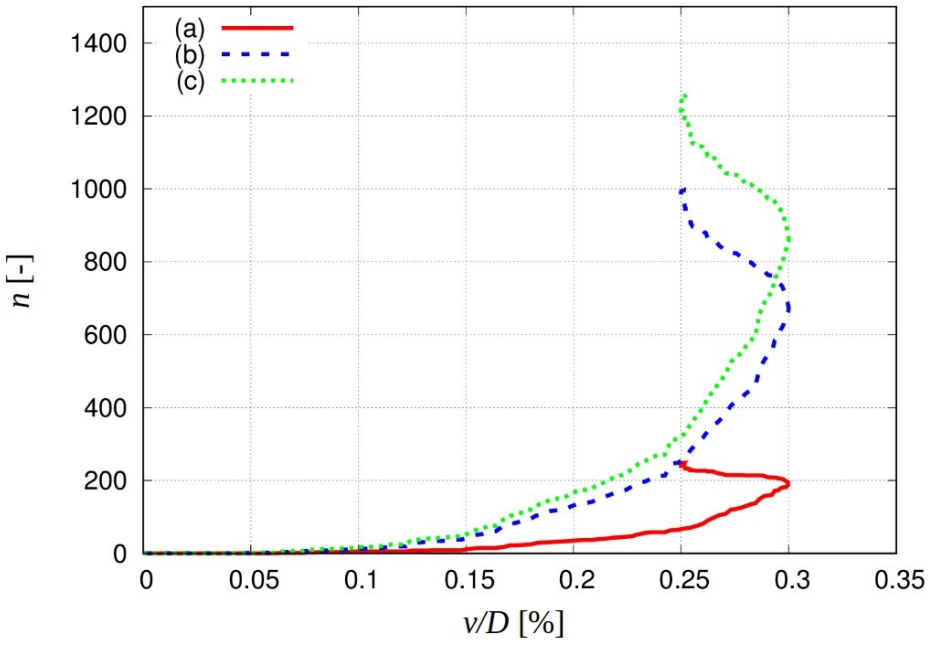

B)

Fig.5.31: 2D DEM results: evolution of broken normal contacts *n* against normalized vertical displacement *v/D* in: a) ITZs, b) cement matrix and c) concrete specimen (A) *D*=0.05 m, B) *D*=0.15 m)

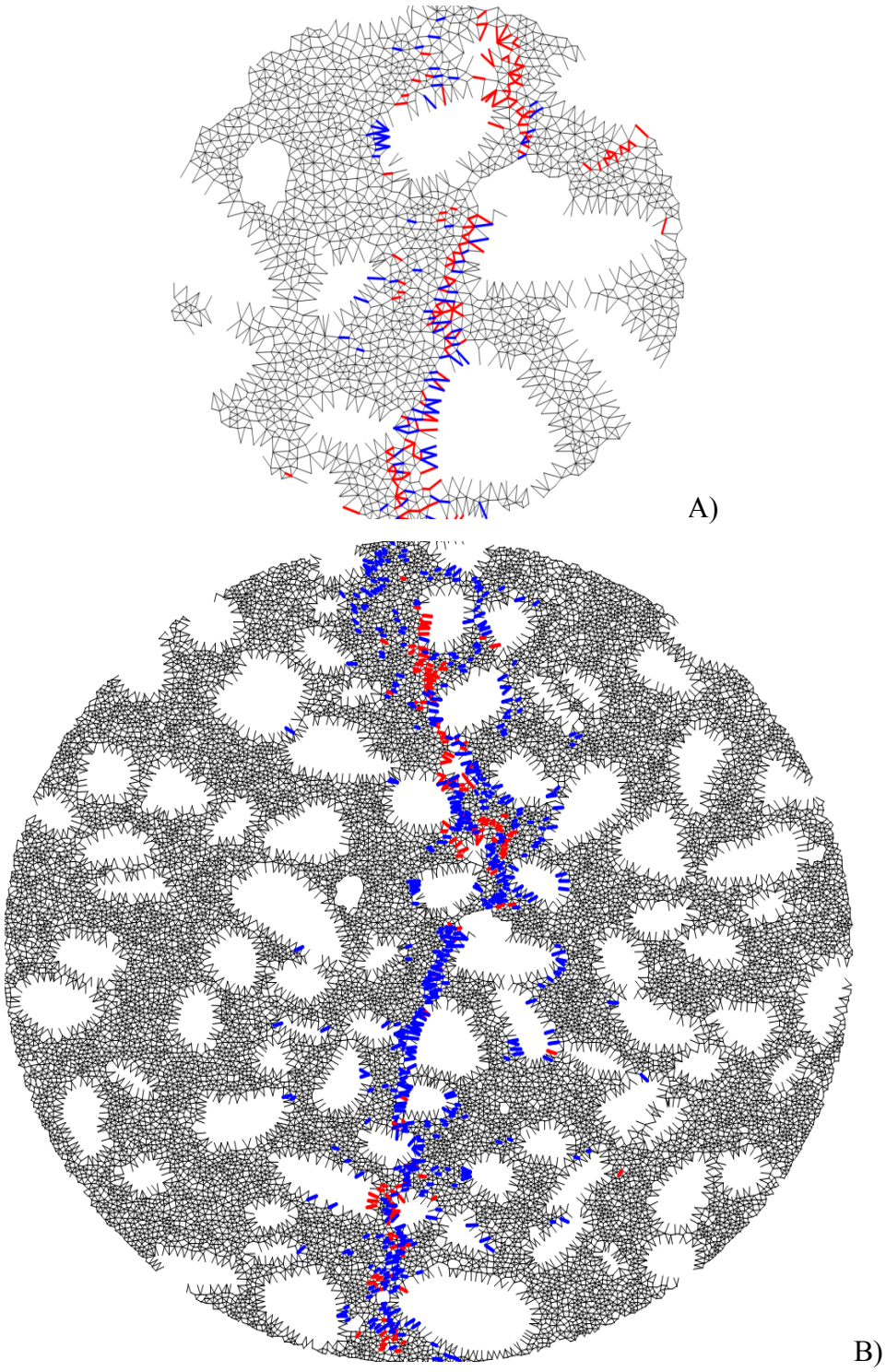

Fig.5.32: DEM results: A) evolution of broken normal contacts up to peak and between peak load and failure for two different specimen diameters *D*: A) *D*=0.05 m, B) *D*=0.15 m (blue marks - broken contacts up to the peak, red colour - broken contacts up to failure, specimen are not properly scaled)

Evolution of coordination number

The evolution of the coordination number (average number of contacts per particle) N for two specimens D=0.05 m and D=0.15 m is demonstrated in Fig.5.33.

The coordination number was slightly smaller for D=0.15 m due to a higher number of particles in the specimen At the deformation beginning, the mean coordination number was N=4.8-4.9 in both the specimens. At the peak, the mean coordination number reduced to N=4.70-4.85 due to micro-cracking (the reduction rate was higher for D=0.05 m). At the deformation end, it decreased to N=4.55-4.57 due to macro-cracking. The change of N was more pronounced after the peak load for the smaller specimen to a stronger fracture process (Fig.5.32).

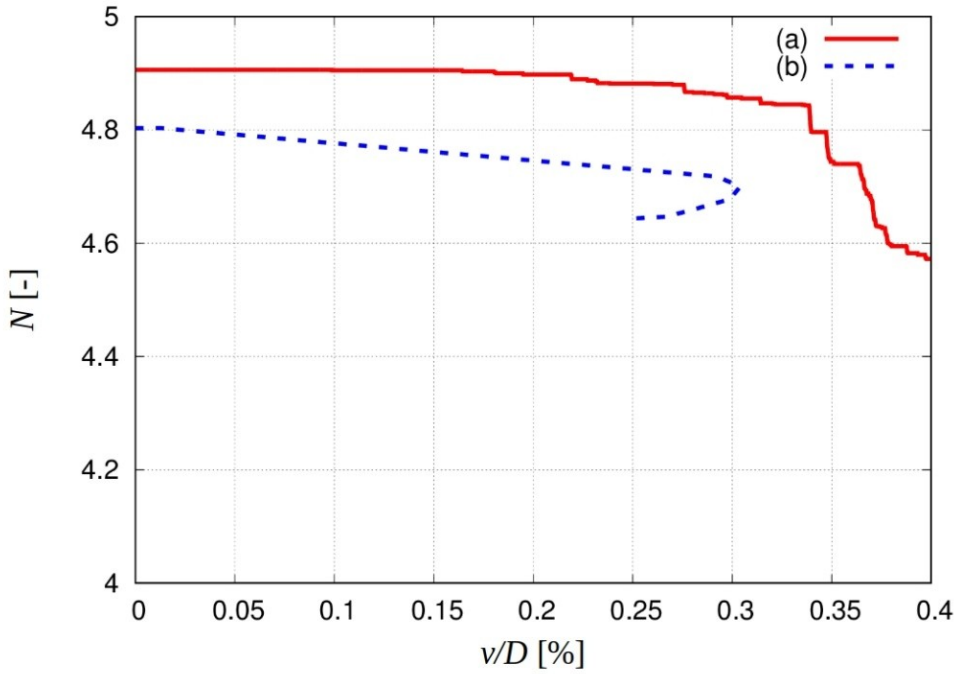

Fig.5.33: 2D DEM results: evolution of coordination number N versus normalized vertical displacement v/D for two different specimen diameters: a) D=0.05 m and b) D=0.15 m

Evolution of inter-particle contact forces

Figures 5.34 demonstrates the distribution of inter-particle normal contact forces F_n for two different specimen diameters D. The normal contact forces were split into the compressive (Fig.5.34I) and tensile forces (Fig.5.34II) and were shown for the peak load (Fig.5.34a) and at the failure (Fig.5.34b). The red/blue lines denote the forces higher than the average force in the

assembly (sum of all forces divided by their number) and the black lines denote the forces lower than the average force to separate strong and weak contacts.

The maximum compressive/tensile forces were equal to 32/7 N at the peak load and 19/6 N at the failure for D=0.05 m and 38/9 N at the peak load and 31/8 N at the failure for D=0.15 m. The mean values were 2.0/1.0 N and 0.5/0.3 N or 1.3/0.5 N and 1.1/0.4 N, respectively.

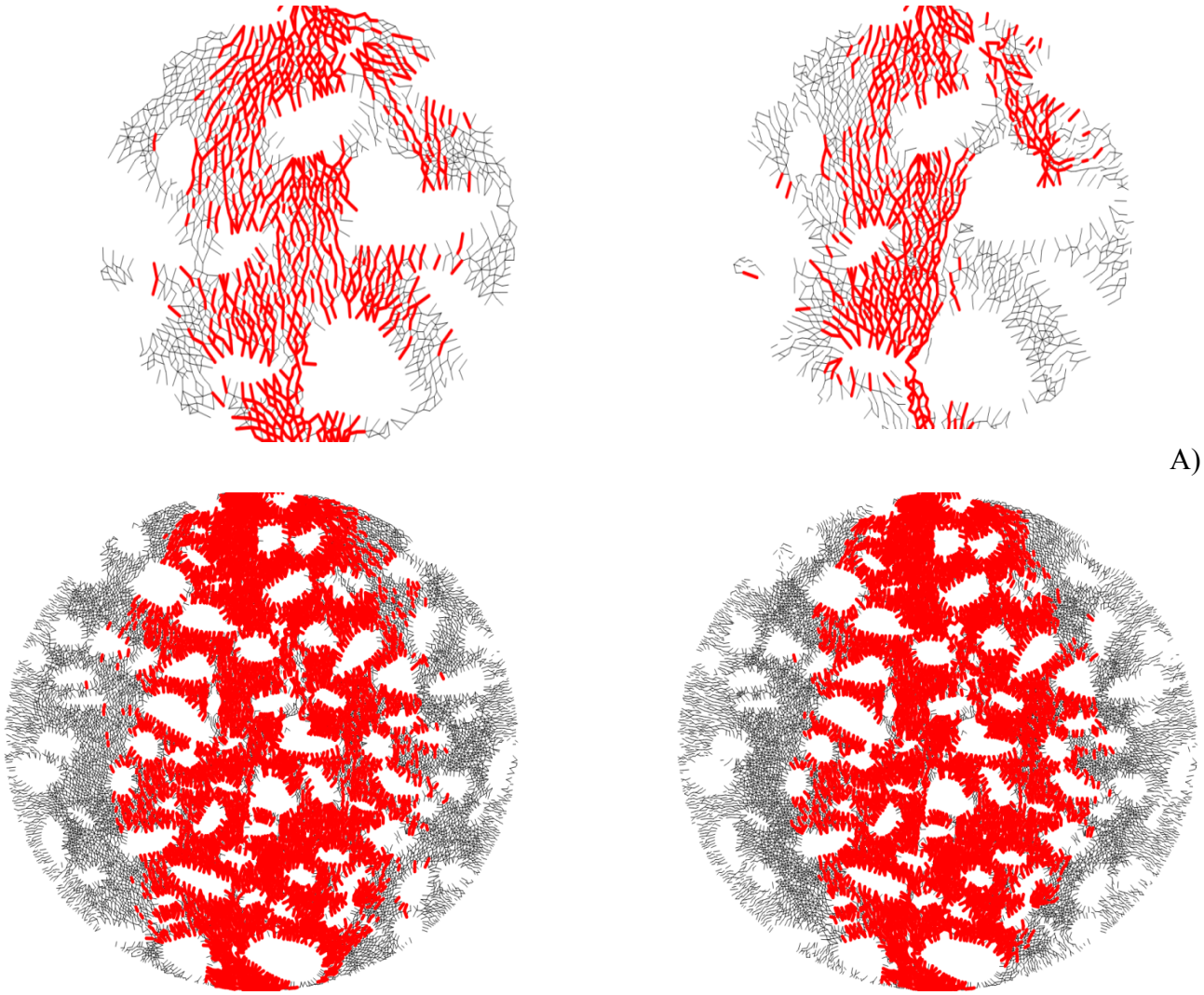

A)

B)

I)

a) b)

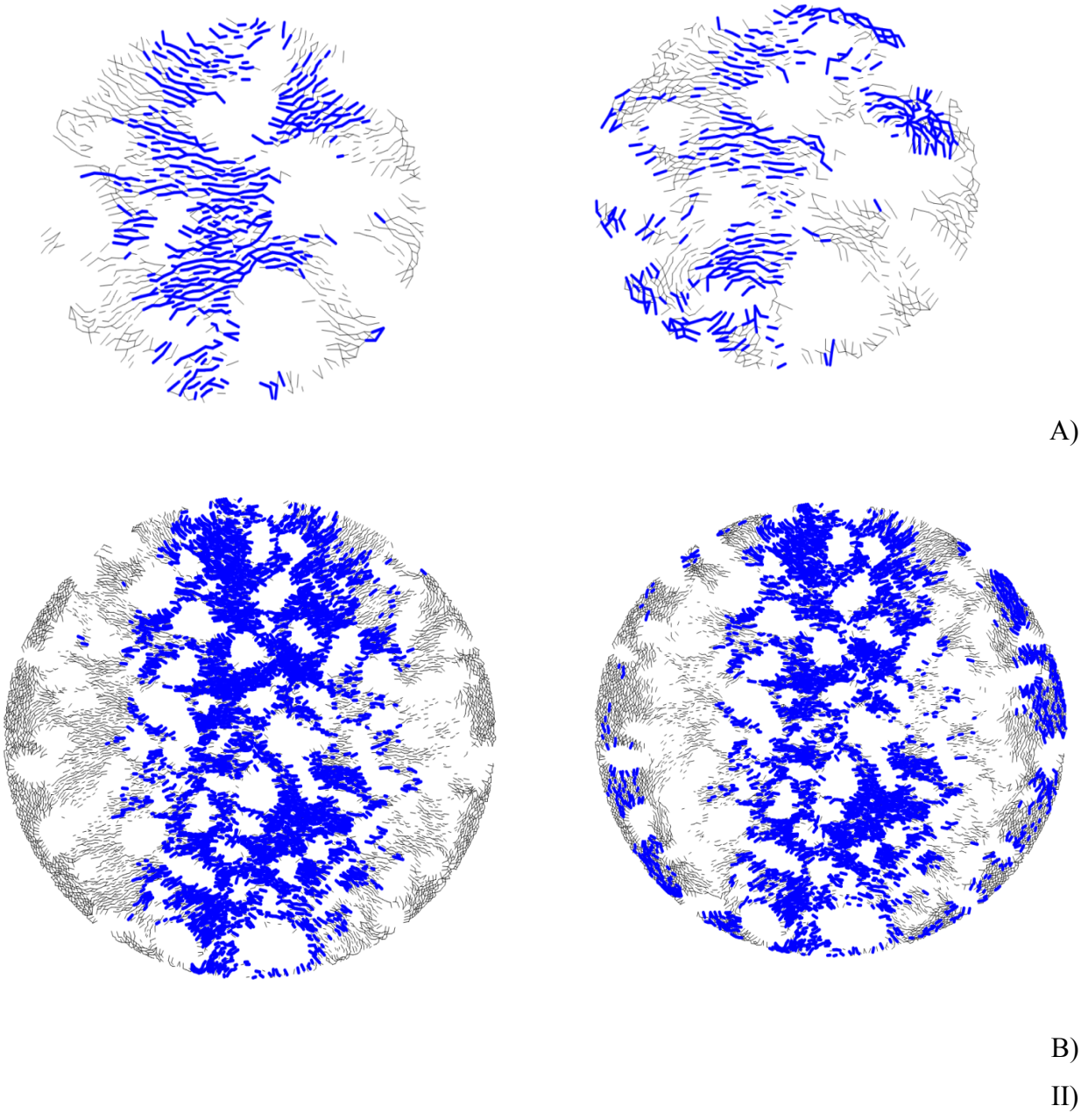

Fig.5.34: 2D DEM results: distribution of inter-particle normal contact forces two different specimen diameters *D*: I) compressive forces, II) tensile forces, A) *D*=0.05 m, B) *D*=0.15 m, a) forces up to the peak load for *v/D*=0.36%/0.30%, b) contacts after the peak load for *v/D*=0.40%/0.25% (red and blue colour - forces above mean value, black colour - forces below mean value)

The force transmission within particulate bodies is via co-existing strong and weak contacts which form the corresponding strong and weak force networks. The external vertical splitting force *P* was transmitted mainly via a network of strong compressive contact forces that formed clear force

chains parallel to *P* (red lines in Fig.5.34). The weak contact forces (black lines in Fig.5.34) were insignificant. Initially, large vertical compressive normal contact forces were created in the specimen mid-region (Fig.5.34). The tensile normal forces were located in a perpendicular (horizontal) direction. In the boundary regions compression obviously dominated over tension. Before the peak of the vertical force, the compression and tensile forces increased, however some single tensile forces started to break due to the contact damage. After the peak load, the tensile forces started to decrease. When a vertical macro-crack already crossed through the specimen, the contact force networks appeared to be sparse and some tensile forces became located mainly along the specimen circumference due to the compression of two separated specimen halves.

The %-number of strong compressive/tensile normal contact forces was 35.2/31.8% (peak load) and 31.4/30.6 (failure) for D=0.05 m. The %-number of strong compressive/tensile normal contact forces was however 31.2/31.8% (peak load) and 30.7/30.5 (failure) for D=0.15 m. Thus, the %-number of strong compressive normal contact forces was higher for the smaller specimen (due to its higher strength). The %-number of strong tensile contact normal forces was similar in both the specimens.

The results of Fig.5.34 are well co-related with Figs.5.31 and 5.32. Large changes in the distribution of contact forces after the peak load are noticeable for D=0.05 m (Fig.5.34A) due to the stronger cracking process (Fig.5.32). They were not visible for D=0.15 m (Fig.5.34B).

Evolution of crack displacements

Figure 5.35 presents the evolution of the average normal and shear displacement along the main central macro-crack exactly at the mid-height for two different specimen diameters: D=0.05 m and D=0.15 m.

The failure had a clear tensile type. i.e. the normal crack displacement always dominated over the tangential crack displacement. The crack displacements clearly increased after the peak load. The normal crack displacement was slightly higher at the peak load for D=0.15 m (0.20 μm versus 0.15 μm versus) and at the failure for D=0.05 m (0.70 μm versus 0.60 μm versus). The tangential crack displacement was a few times smaller than the normal one.

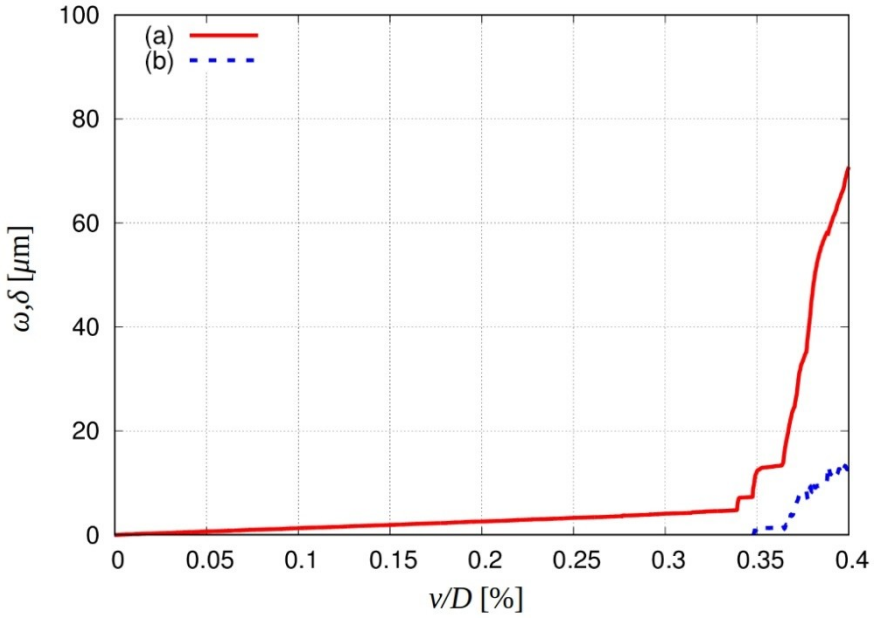

A)

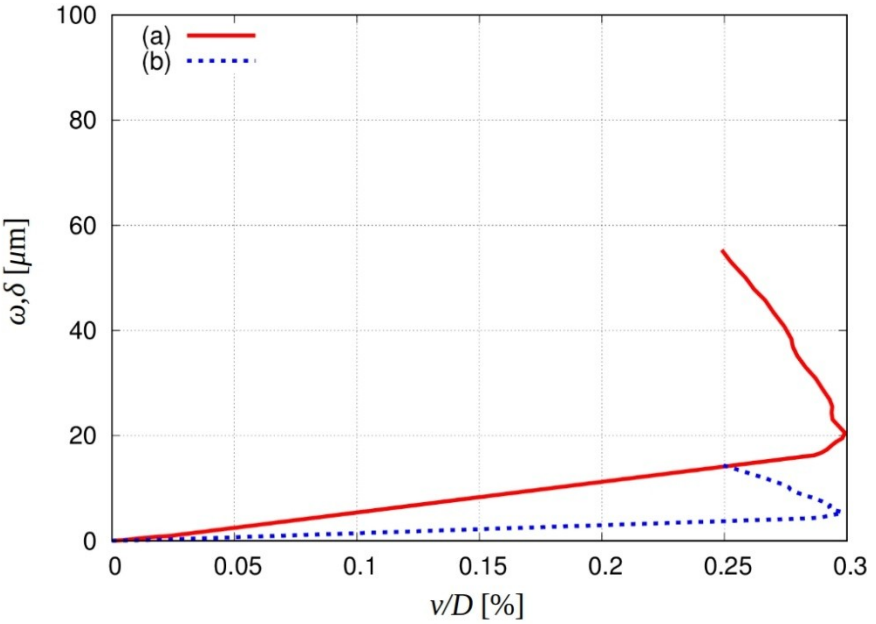

B)

Fig.5.35: DEM results: evolution of crack displacement versus normalized vertical displacement v/D in macro-crack in central specimen region (a) normal displacement w and b) shear displacement δ) for two different specimen diameters: A) D=0.05 m and B) D=0.15 m

Internal energies (Suchorzewski et al. 2019)

Non-fractured state

In a discrete undamaged concrete system there exist initially 2 main internal energies: elastic and dissipated energy. In addition, the numerical dissipation and kinetic energy also take place due to

the application of DEM. The elastic internal energy stored at existing contacts N between aggregate grains E_e, expressed in terms of work of the elastic contact tangential forces F_s on the elastic tangential displacements S_c and the elastic contact normal forces F_n on the elastic penetration depths U (Figs.2a and 2b) was

$$E_e = \sum_1^N \left(\frac{|F_s|^2}{2K_s} + \frac{|F_n|^2}{2K_n}\right). \tag{40}$$

When the tangential force between grains reached the value of F_s^{max} (Fig.2a), the dissipated energy D_p, expressed in terms of work of the tangential (shear) forces on the conjugate sliding displacements S_l (Fig.2a), was determined as (with $F_\mu = F_n \times \tan\mu$)

$$D_p = D_{p'prev} + \Delta D_p \qquad \text{with} \quad \Delta D_p = \sum_i^N F_\mu \Delta S_l \tag{41}$$

The dissipated energy was calculated incrementally at each time step and summed for the time period of the contact of two respective particles. The kinetic energy E_k of grains was caused by their translation and rotation (m - the particle mass, I - the moment of inertia of a particle, v_p - the particle translational velocity and ω_p - the particle rotational velocity)

$$E_k = \sum_1^N \left(\frac{1}{2} m v_p^2 + \frac{1}{2} I \dot{\omega}_p^2\right). \tag{42}$$

In addition, the numerical dissipation D_n, expressed in terms of work of dampened normal and tangential forces (Eq.6) on the conjugate normal and tangential displacements U and S_l (Figs.2a and 2b) was specified as

$$D_n = D_{n'prev} + \Delta D_n \qquad \text{with} \qquad \Delta D_n = \sum_i^N \left(F_{damped}^i \ \Delta U(S_l)\right). \tag{43}$$

The cohesion contact failure energy release E_s was (Fig.2a)

$$E_s = \frac{1}{2}\left(\frac{(F_s^{max})^2}{K_s} - \frac{(F_\mu)^2}{K_s}\right). \tag{44}$$

In general, the total accumulated energy was in the non-fractured specimen

$$E_{(unfract\ )} = E_e + E_k + D_p + D_n + E_s. \tag{45}$$

It was equal to the external boundary work W expended on the particle assembly by the external vertical splitting force P on the vertical specimen top displacement v ($W = W_{prev} + \sum Pdv$).

Fractured state (with normal contact breakage)

When the particle normal contacts started to break during deformation, the broken normal springs were immediately removed from the DEM system (together with the tangential springs). Thus, the existing up to this moment internal elastic energy of removed (broken) contacts (shear and tensile contact energy) had to be added to the total internal energy. The total removed contact failure energy E_{rc} (composed of the shear E_s and tensile E_t contact failure energy) was equal to (Figs.2a and 2b)

$$E_{rc} = E_s + E_t = \frac{1}{2}\frac{(F_s)^2}{K_s} + \frac{1}{2}\frac{(F_n^{min})^2}{K_n}, \tag{46}$$

where F_s is the actual elastic tangential force.

In general, the total accumulated energy E for the fractured specimen was thus equal to

$$E_{(fract\ )} = E_e + E_k + D_n + E_{rc} = W. \tag{47}$$

Energies in two specimens with different diameter

Figure 5.36 shows the evolution of the calculated normalized energy $E/(0.25\pi D^2)$ against the normalized vertical piston displacement v/D for two concrete specimens D=0.05 m and D=0.15 m. The strain increment after the peak load ($\Delta v/D$) was the same in both cases ($\Delta v/D$=0.05%).

The evolution of the elastic internal energy E_e in a normal and tangential direction was similar to the evolution of the mobilized specimen strength (expressed by the splitting tensile stress in Fig.5.36a). The elastic internal energy E_e was obviously significantly higher than the plastic damping D_p due to cohesion. The elastic energy portion due to the tangential force action was obviously smaller than that due to the normal force action in view of the lack of plastic damping in

a normal direction. The kinetic energy E_c was insignificant due to numerical damping and quasi-static numerical tests.

For the normalized vertical top displacement v/D=0.35% corresponding to the peak load for D=0.05 m, (Fig.5.36), the normalized elastic internal energy was equal to E_e^n=97.2% (normal energy – 70.0%, tangential energy – 27.2%), normalized plastic dissipation was almost D_p^n=0.0%, normalized energy of removed cohesive contacts was equal to D_{rc}^n=0.8%, normalized kinetic energy was equal to E_c^n=0.6% and normalized numerical damping was equal to D_n^n=1.4% of the total normalized energy (Fig.5.36A). For v/D=0.4 mm corresponding to the test end (Fig.5.36), the normalized elastic internal energy was E_e^n=45%, normalized plastic dissipation was D_p^n=0.25%, normalized energy of removed cohesive contacts was D_{rc}^n=3.3%, normalized kinetic energy was E_c^n=0.25% and normalized numerical damping was D_n^n=51.2% of the total normalized energy (Fig.5.36A).

In the case of D=0.15 m, for the normalized vertical top displacement v/D=0.30% corresponding to the peak load (Fig.5.36), the normalized elastic internal energy was equal to E_e^n=73% (normal energy – 54%, tangential energy - 19%), normalized plastic dissipation was almost D_p^n=0.0%, normalized energy of removed cohesive contacts was equal to D_{rc}^n=1.2%, normalized kinetic energy was equal to E_c^n=0.15% and normalized numerical damping was equal to D_n^n=25.65% of the total normalized energy (Fig.5.36B). At the failure (v/D=0.25%, Fig.5.36), the normalized elastic internal energy was 54%, normalized plastic dissipation was D_p^n=0.25%, normalized energy of removed cohesive contacts was equal to D_{rc}^n=3.5%, normalized kinetic energy was E_c^n=0.1% and normalized numerical damping was D_n^n=42.15% of the total normalized energy (Fig.5.36B). Due to the snap-back instability, the total internal energy reduced by 25%, the elastic normal internal elastic energy reduced by 52% and the elastic tangential internal energy reduced by 30%. In turn, the plastic dissipation, numerical damping and elastic energy from removed cohesive contacts increased on average by the factor 2.

The total normalized internal energy was higher by 10% at the peak load (1.35 kN/m against 1.25 kN/m) and by 70% at the failure (1.6 kN/m against 0.95 kN/m) in the smaller specimen D=0.05 m (Fig.5.36A) as the result of the higher vertical force P and ductility (Fig.5.36). The contribution of the total normalized elastic energy to the total normalized energy was significantly higher for D=0.05 m before the peak (97% versus 73%) and for D=0.15 m at the failure (54% versus 45%) due to fracture (see *Evolution of broken contacts*). The total normalized elastic energy

E_e^n was thus higher by 40% at the peak load and smaller by 10% at the failure in the smaller concrete specimen (D=0.05 m) due to the different fracture type in both the specimens. The stronger contribution of the total normalized elastic energy at the peak caused the higher strength of the small specimen (with respect to the small fracture impact, see *Evolution of broken contacts*). The contribution of the numerical damping D_n was inverse, i.e. higher for D=0.15 m before the peak load and for D=0.05 m after the peak load.

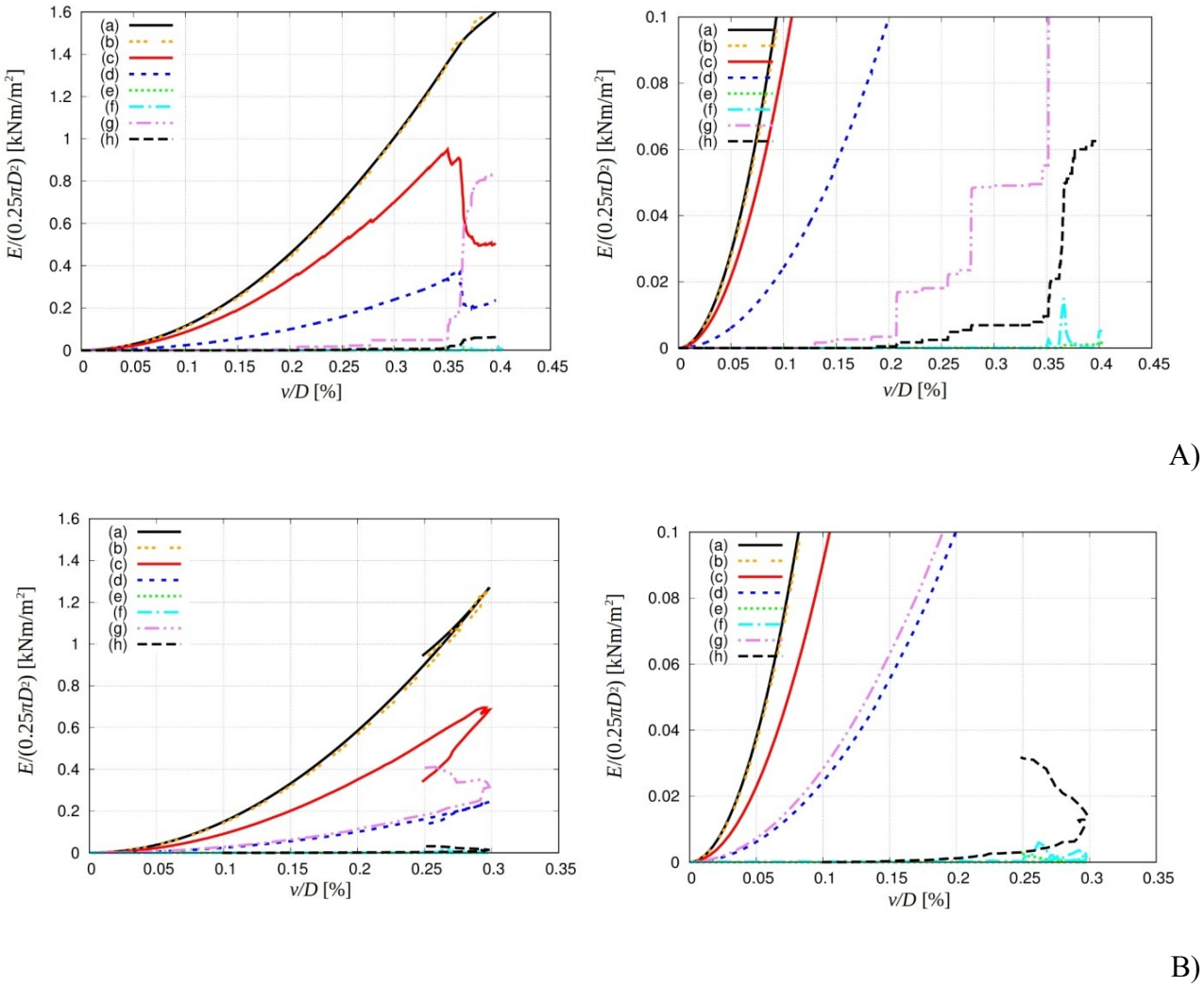

Fig.5.36: Evolution of normalized energy $E/(0.25\pi D^2)$ in 2D concrete specimen versus normalized vertical piston displacement v/D for 2 different specimen diameters D: A) D=0.05 m and B) D=0.15 m based on DEM (d_{cm}^{min}=0.35 mm): a) external work, b) total internal work, c) normal elastic energy, d) tangential elastic energy, e) plastic dissipation, f) kinetic energy, g) numerical damping and h) energy of removed cohesive contacts

Energies' split in two specimens with different diameter

Figures 5.37 and 5.38 show the split of normalized energies into two regions: region in the fractured region (marked in blue in Fig.5.30) and region beyond the fractured region.

For the smaller specimen (D=0.05 m), the total normalized absorbed energy E_{abs}^{n} in the fractured zone was higher than the total normalized released energy E_{rel}^{n} in the remaining unloaded region by the factor 2.5 at the peak load and 1.6 at the failure. For the larger specimen (D=0.15 m), the total normalized absorbed energy E_{abs}^{n} in the fractured zone was however smaller than the total normalized released energy E_{rel}^{n} in the remaining region by 15% at the peak load and larger by 20% at the failure (Figs.5.37 and 5.38).

In the case of D=0.05 m, the increment of the total normalized absorbed energy after the peak load in the fractured zone ΔE_{abs}^{n} was significantly higher by the factor than the increment of the total normalized released energy after the peak load in the remaining unloaded region ΔE_{rel}^{n} ($\Delta E_{abs}^{n} > \Delta E_{rel}^{n}$) (Fig.5.38) that caused a global quasi-brittle behaviour in the post-peak region of the small concrete specimen (Fig.5.29). For D=0.15 m, the increment of the total normalized absorbed energy after the peak load in the fractured zone ΔE_{abs}^{n} was smaller than the increment of the total normalized released energy after the peak load in the remaining region ΔE_{rel}^{n} ($\Delta E_{abs}^{n} < \Delta E_{rel}^{n}$) (Fig.5.38) that contributed to a global very brittle behaviour with the snap-back instability in the post-peak regime (Fig.5.29). The same tendency occurred for the total normalized elastic energy amounts after the peak load (Figs.5.37C and 5.38C). The maximum total normalized absorbed energy in the fractured region was as twice as large for D=0.05 m (Figs.5.37A and 5.38A). Therefore the normalized kinetic energy and normalized numerical damping (both connected with each other) were obviously higher in the fractured region and were again higher for D=0.05 m in this region.

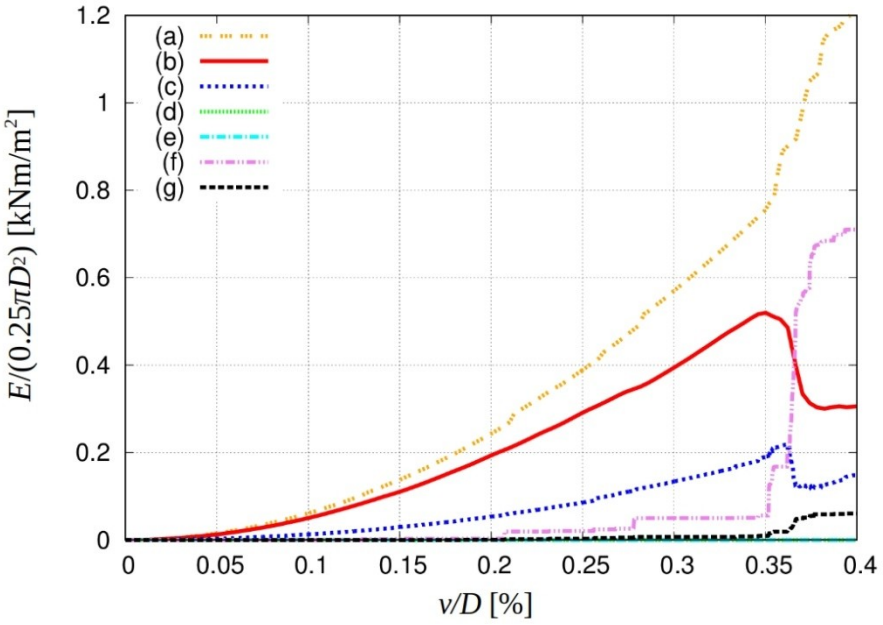

A)

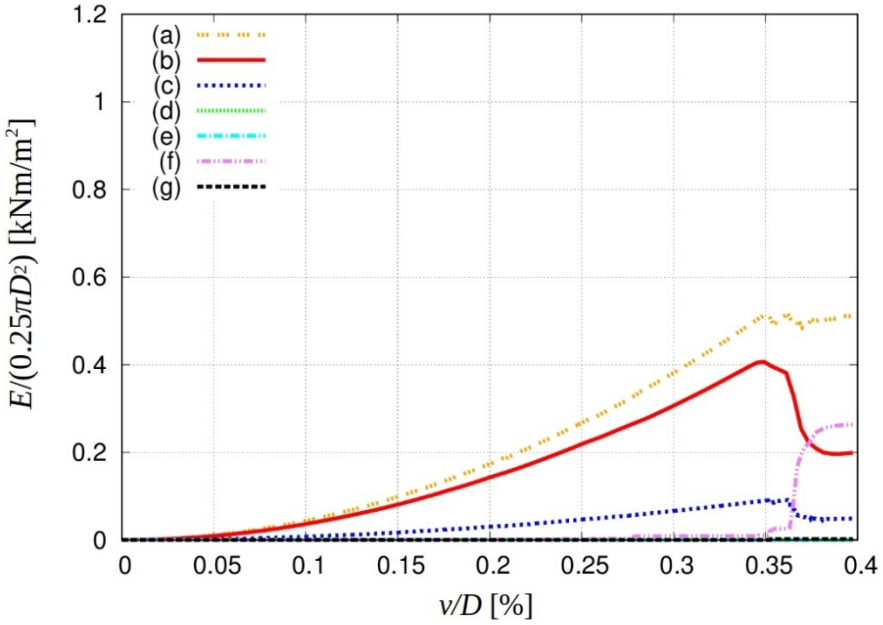

B)

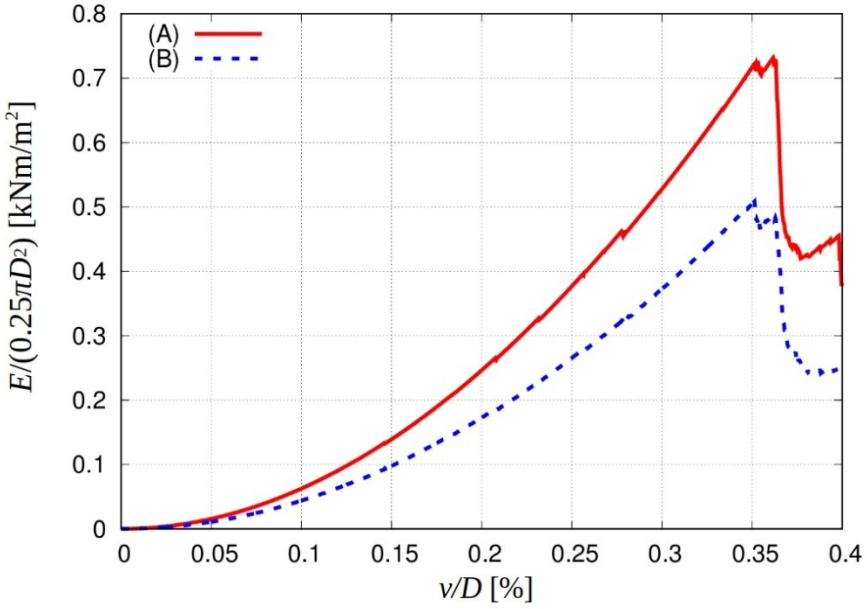

C)

Fig.5.37: Evolution of normalized energy $E/(0.25\pi D^2)$ in concrete specimen with D=0.05 m versus normalized vertical piston displacement v/D using DEM: (A) fractured region, B) remaining unloaded region and C) total elastic energy (a) total internal work, b) normal elastic energy, c) tangential elastic energy, d) plastic dissipation, e) kinetic energy, f) numerical damping, g) energy of removed cohesive contacts)

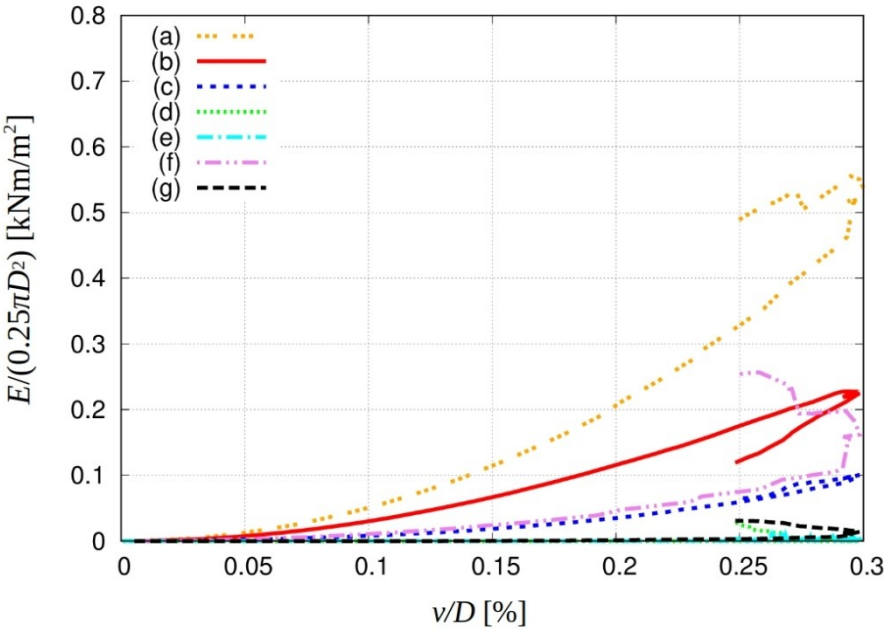

A)

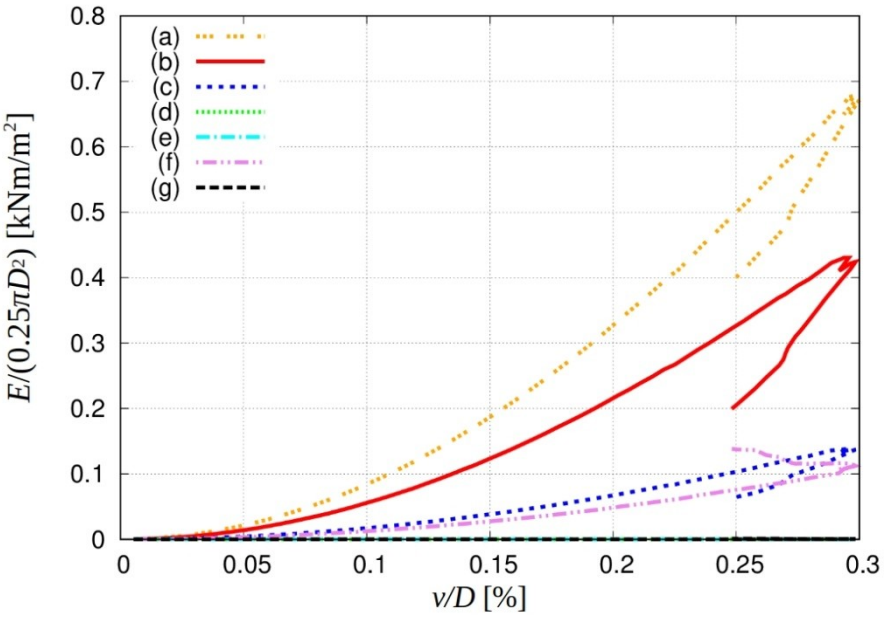

B)

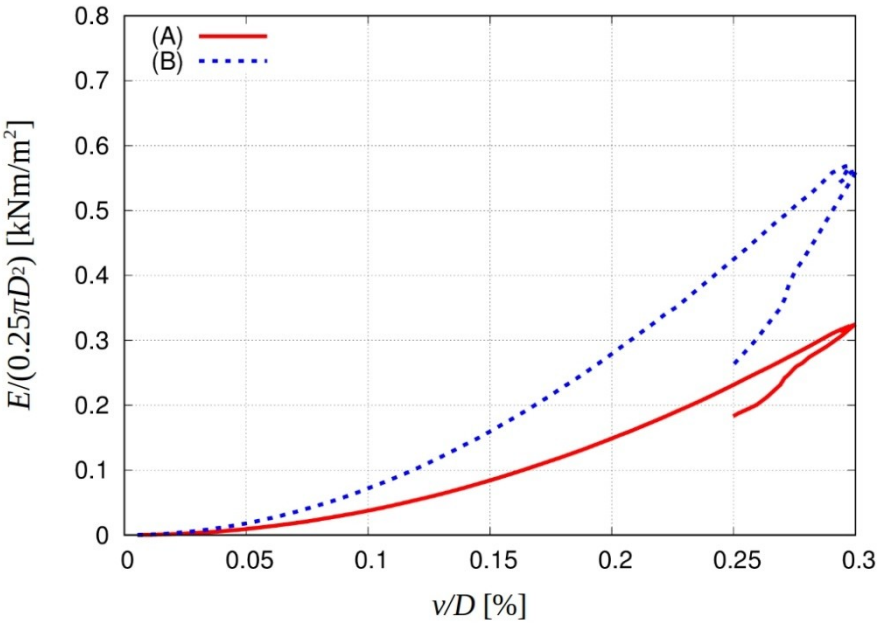

C)

Fig.5.38: Evolution of normalized energy $E/(0.25\pi D^2)$ in concrete specimen with D=0.15 m versus normalized vertical piston displacement v/D using DEM: A) fractured region, B) remaining unloaded region and C) total elastic energy (a) total internal work, b) normal elastic energy, (tangential elastic energy, d) plastic dissipation, e) kinetic energy, f) numerical damping, g) energy of removed cohesive contacts)

5.4 Comparison with size effect experiments from literature

Figure 5.39 presents the cross-section of 4 2D cylindrical concrete specimens with the diameter D=74 mm, D=100 mm, D=150 mm and D=290 mm assumed for DEM calculations. The crack opening was measured between two spheres situated in the specimens mid-height at the distance of 65 mm in a horizontal direction (as in experiment). Note that the exact micro-structure used in experiments could not be reproduced due to the lack of data.

Figure 5.40 compares the DEM results with the experimental ones by Carmona et al. (1998) with respect to the vertical force P against CMOD. The vertical force P was calculated as the sum of vertical inter-particle forces along the horizontal mid-height section (with L equal to the mean particle diameter). The experimental and numerical results are in satisfactory agreement. For two largest specimens (D=150 mm and D=290 mm) the peak vertical force was lower by 10% than in the experiment, whereas for two smallest specimens (D=74 mm and D=100 mm), P_{max} was higher by 15% and 25%. For a better accuracy, the real micro-structure of concrete specimens has to be taken into account in DEM (Skarżyński et al. 2016, Suchorzewski et al. 2018a).

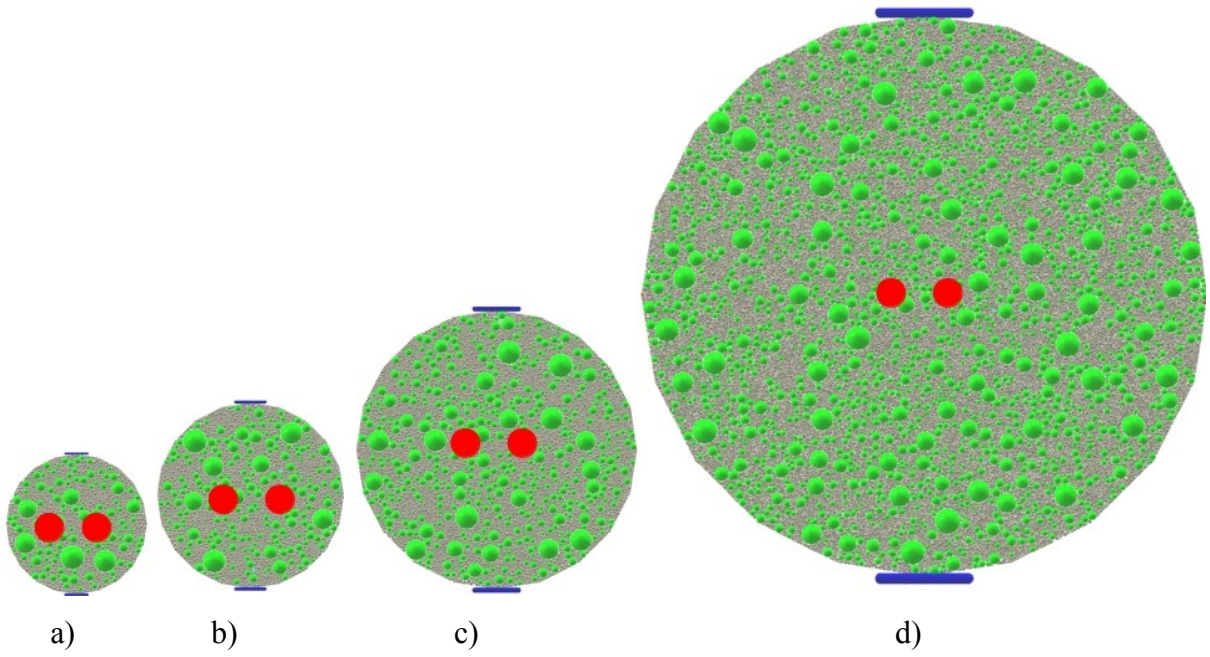

Fig.5.39: Cross-sections of concrete specimens in tests by Carmona et al. (1998) with diameter: a) D=74 mm, b) D=100 mm, c) D=150 mm and d) D=290 mm for DEM calculations (grey colour denotes cement matrix d_a<2 mm, green spheres denote aggregates with ITZ (2 mm<d_a< 12 mm), blue clusters of spheres describe loading plates, red points are points for CMOD measurement at specimen mid-height)

Figure 5.41 describes the numerical size effect due to the specimen strength and specimen brittleness, expressed by the inclination α of the initial softening curve (α=f*(CMOD/D*) to the horizontal in the counter-clockwise direction versus the experimental outcomes. The DEM indicate that the tensile strength increased and brittleness decreased with decreasing specimen diameter. The calculated concrete tensile strength changed by 16% between D=74 mm and D=100 mm, by 3% between D=100 mm and D=150 mm and by and 2.5% between D=150 mm and D=290 mm. The trends of the calculated varying σ versus D and α versus D were similar to the experimental ones except of two smallest specimens. The too low tensile strength in experiments for the smallest specimens was probably caused by boundary effects caused by concrete drying (Vorechovsky 2007). Note that other experiments did not indicate this phenomenon (Section 3.4).

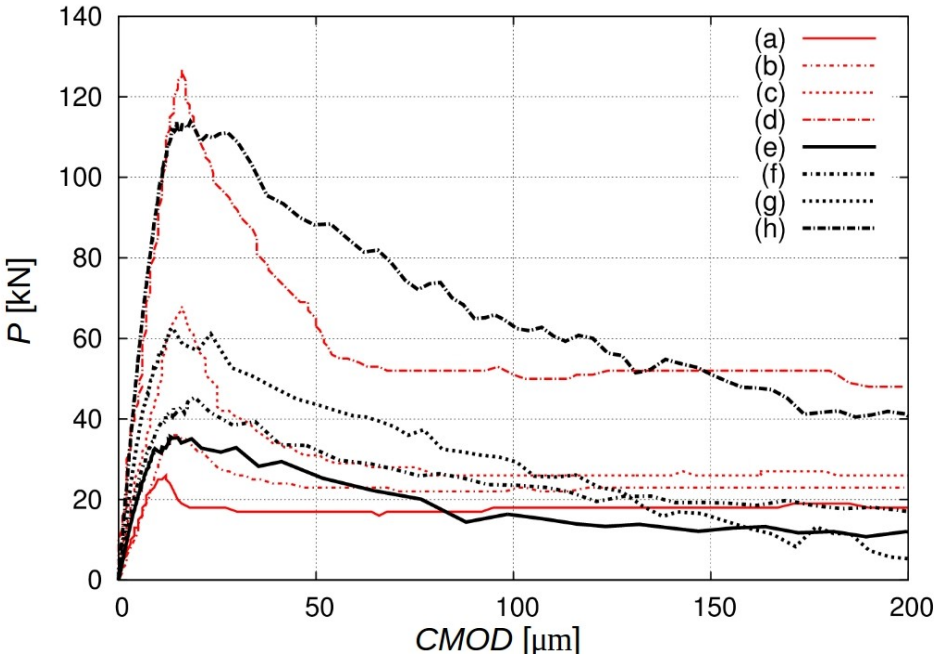

Fig.5.40: Vertical force P against crack mouth opening displacement (CMOD) from experiments by Carmona et al. 1998 (red lines): a) D=74 mm, b) D=100 mm, c) D=150 mm, d) D=290 mm and from DEM (black lines): e) D=74 mm, f) D=100 mm, g) D=150 mm and h) D=290 mm

The deformed concrete specimens are shown in Figure 5.42. The crack was simulated by broken element contacts in the granular assembly (Fig.5.43). For all concrete specimens one almost vertical crack appeared in the specimen's central region. The crack was curved due to the presence of aggregate and always propagated through the cement matrix and ITZs, which were the weakest

phases in specimen. The macro-crack was strongly non-uniform (in particular under the loading plate and at the specimen bottom) and possessed several small branches. Directly under the loading plate, a stiff wedge with two inclined cracks might occur (Figs.5.42a, 5.42b and 5.42d). The macro-cracks were created by bridging the interfacial micro-cracks (Skarżyński et al. 2016, Suchorzewski et al. 2018a). First, broken contacts occurred in ITZs at aggregate particles. Next they developed along aggregate circumferences. Afterwards they connected with each other in the cement matrix by bridging (Skarżyński et al. 2016, Suchorzewski 2018a). There existed many micro-cracks in the central specimen region (Fig.5.4.5).

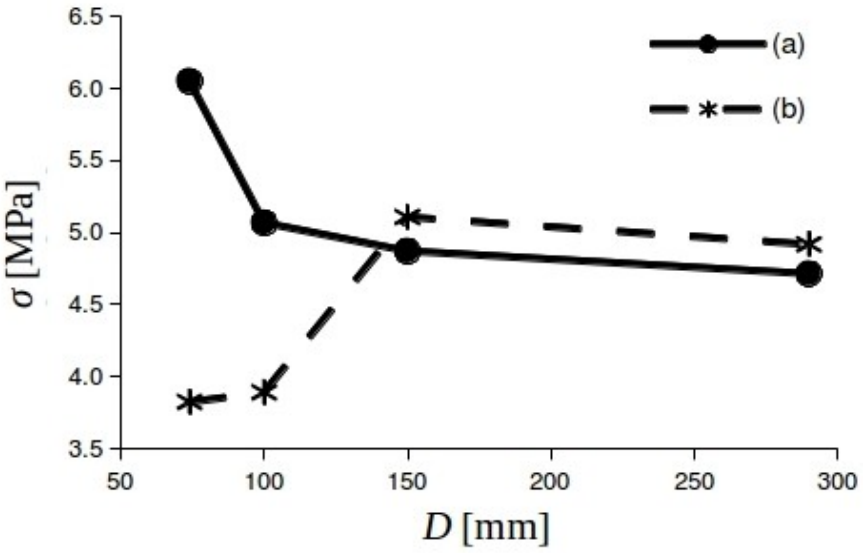

A)

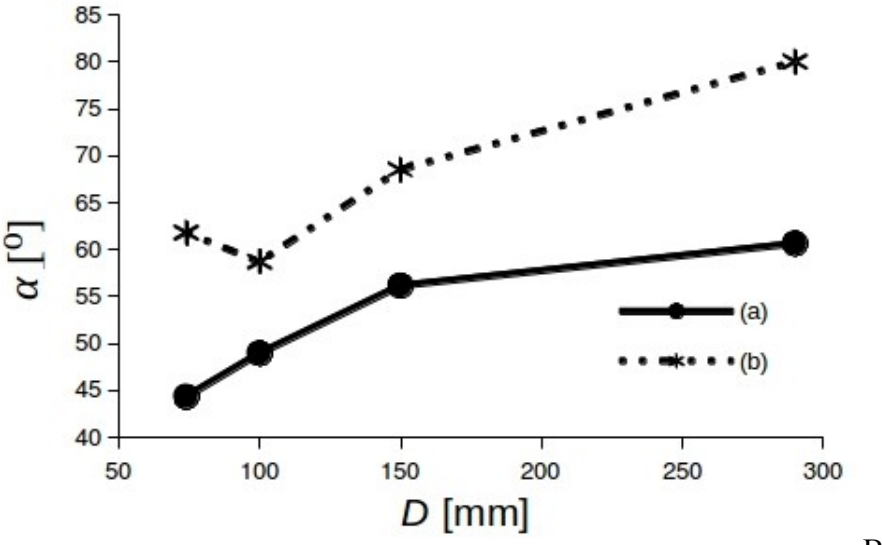

B)

Fig.5.41: Size effect in concrete by DEM (a) versus splitting tensile experiments (b): A) splitting tensile stress σ versus specimen diameter D and B) softening curve inclination to horizontal α versus specimen diameter D

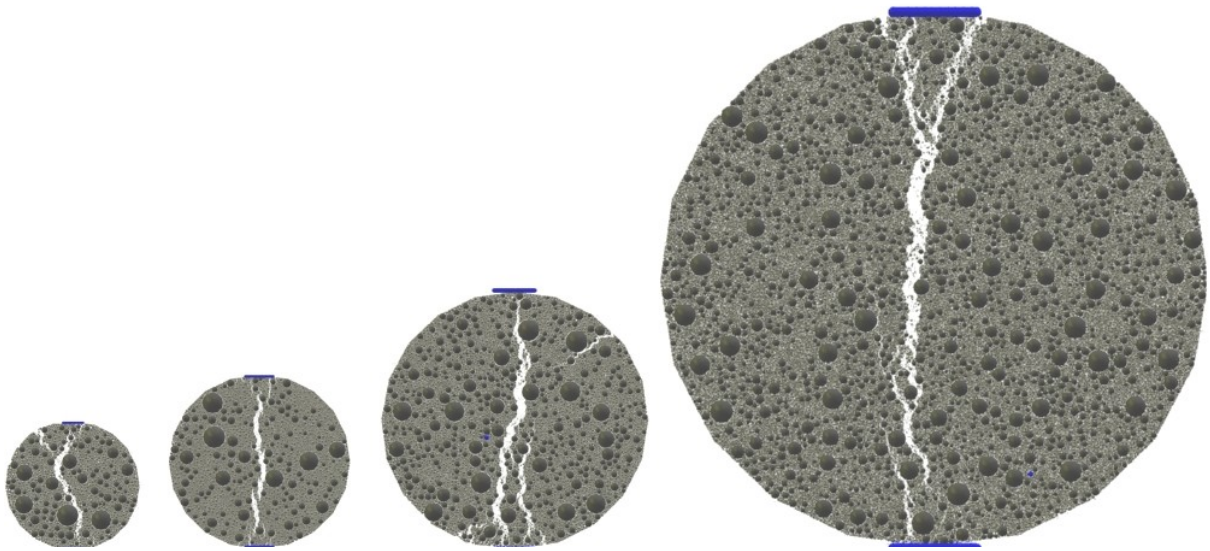

Fig.5.42: Crack patterns from DEM in deformed concrete specimens: a) D=74 mm, b) D=100 mm, c) D=150 mm and d) D=290 mm for CMOD=50 μm (displacements were magnified by factor 40)

Figure 5.44 shows the normal force contact evolution. The red lines in Fig.5.44 correspond to compressive forces and the blue lines to tensile forces. The thickness of lines in Fig.5.44 represents the magnitude of the normal contact force between two particles. The external vertical splitting force was transmitted via a network of contact forces which formed force chains. They carried the majority of the loading and transmitted it on the entire system and were the predominant structure of internal forces at micro-scale. Initially large vertical compressive normal forces were created in the almost entire specimen. In a perpendicular (horizontal) direction tensile normal forces occurred (Fig.5.44a). In the boundary regions compression obviously dominated over tension. Before the peak vertical force, the compression forces increased and some single tensile forces started to disappear due to the contact damage (Fig.5.44b). After the peak force when a vertical macro-crack occurred, the compressive forces concentrated in the specimen mid-region whereas the tensile forces became located mainly along the specimen circumference due to the compression of two separated specimen halves (Fig.5.44c).

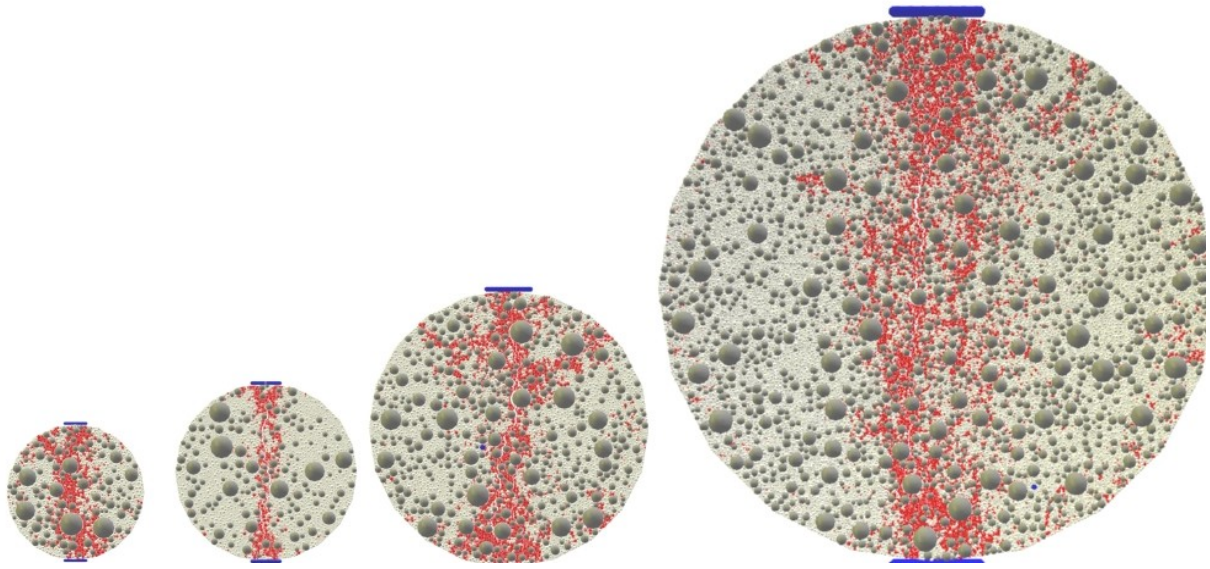

a) b) c) d)

Fig.5.43: Broken contacts (in red) in concrete specimens from DEM: *D*=74 mm (a), *D*=100 mm (b), *D*=150 mm (c) and *D*=290 mm (d) for CMOD=50 μm

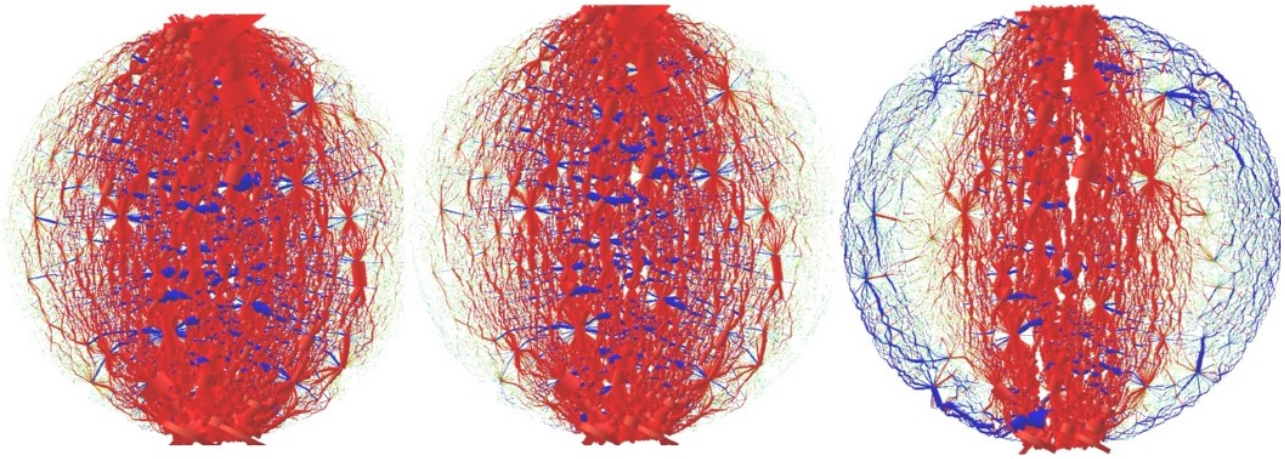

a) b) c)

Fig.5.44: Evolution of contact normal forces (specimen diameter D=150 mm) for crack mouth opening displacement CMOD: a) 10 μm, b) CMOD=20 μm and c) CMOD=50 μm (red lines indicate compressive normal forces and blue lines tensile normal forces, line thickness denotes force magnitude)

5.5 Comparison with own size effect experiments

The laboratory experiments described in Chapter 3.3 were simulated with DEM similarly as in Chapter 5.3). This time a stochastic distribution of aggregates was taken into account due to micro-CT images for three specimen diameters D=74 mm, D=150 mm and D=250 mm (Fig.5.45). The full 3D CT scan was possible before the test solely for the smallest specimen D=74 mm due to size limitations in the micro-CT system.

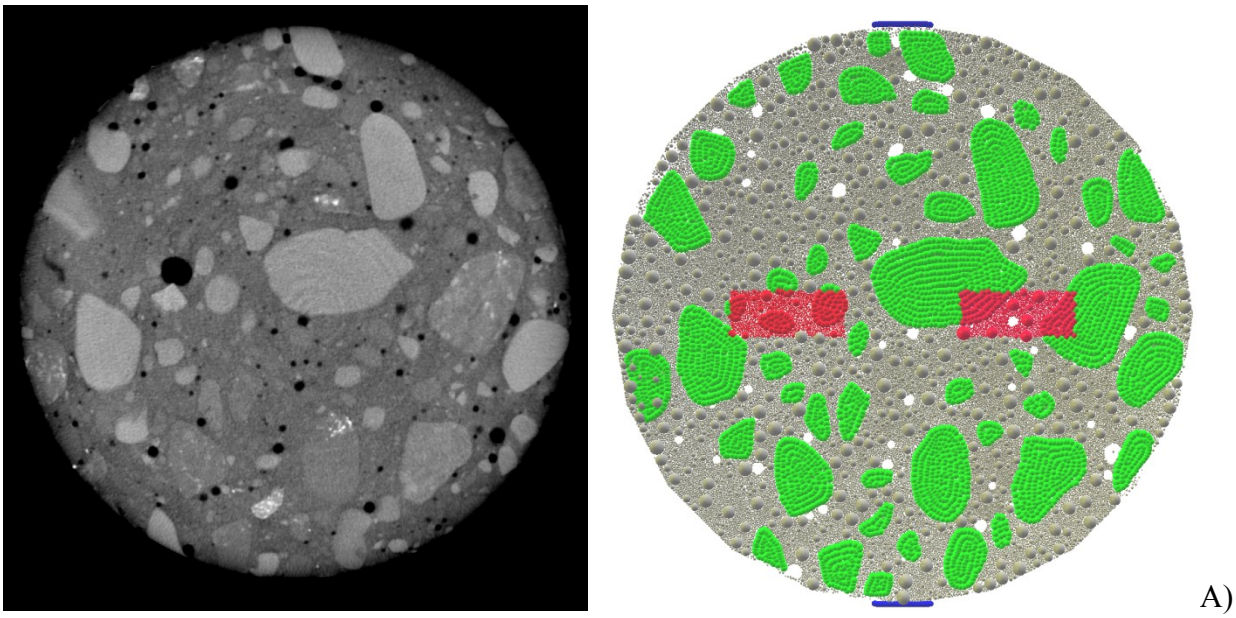

A)

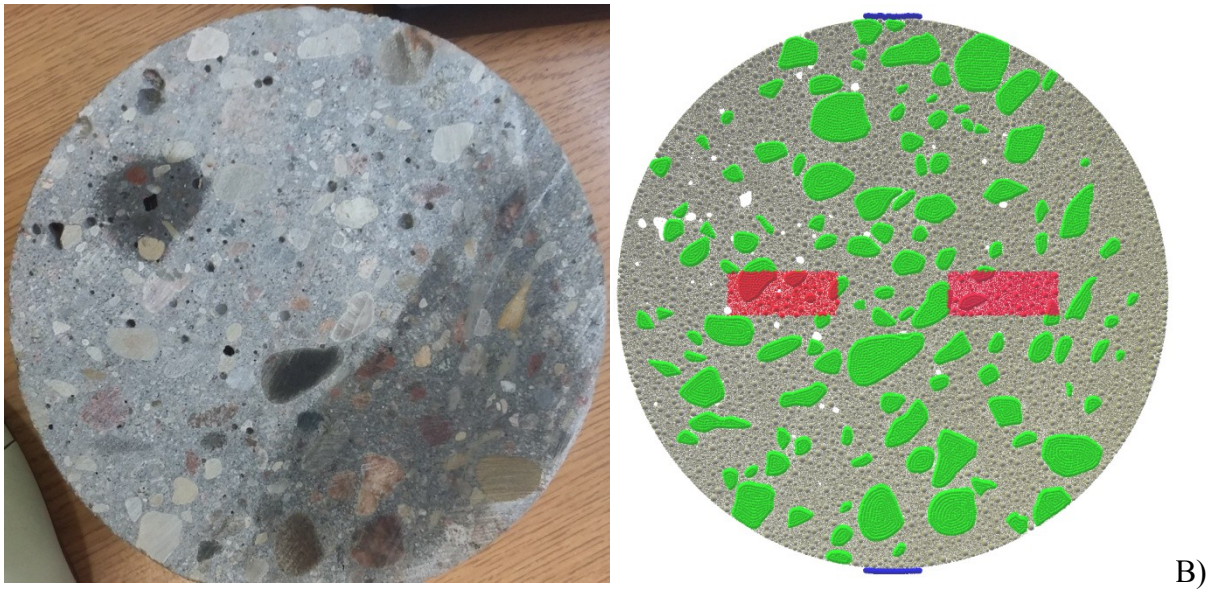

B)

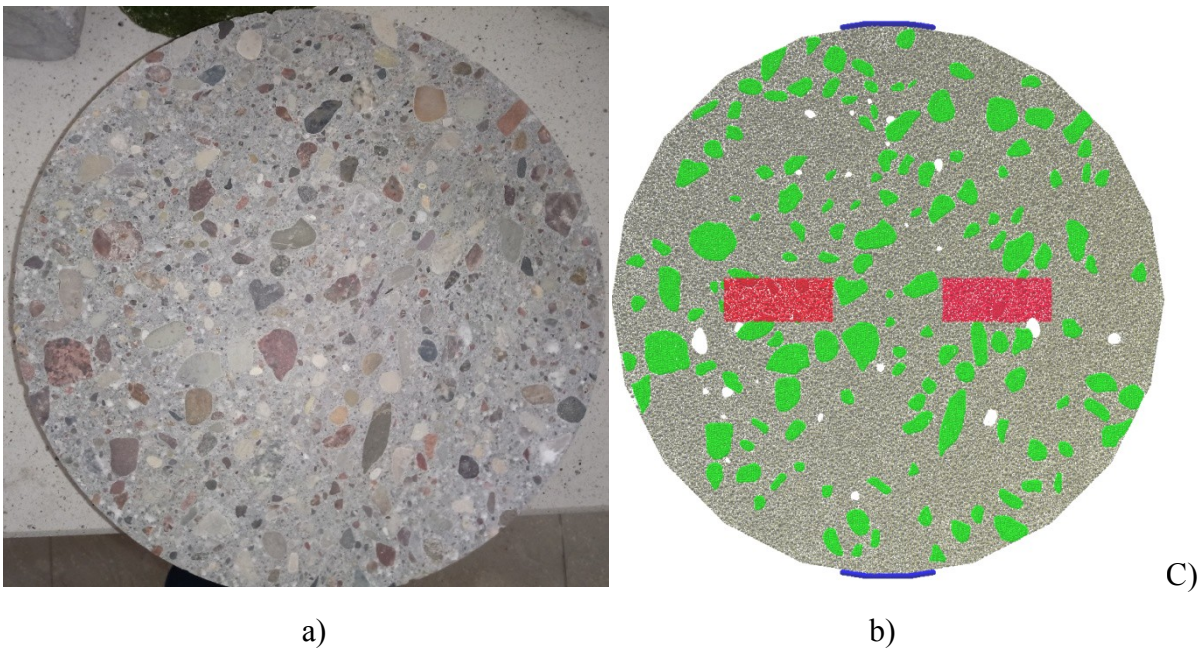

a) b) C)

Fig.5.45: Concrete specimens a) view on front surface and b) DEM model for 3 different specimen diameters D: A) D=74 mm, B) D=150 mm and C) D=250 mm (green particles represent aggregate, grey particles stand for cement matrix and white spots are empty zones representing macro-pores, red squares indicate area for measurement of average CMOD and blue particles are loading strips , note that specimens are not proportionally scaled)

The DEM calculations for concrete splitting were carried out with the following parameters of the cohesion and tensile strength: cement matrix ($E_{c,cm}$=15 GPa, C_{cm}=140 MPa and T_{cm}=22 MPa) and ITZs ($E_{c,ITZ}$=12 GPa, C_{ITZ}=112 MPa and T_{ITZ}=17.6 MPa) based on uniaxial compression test calibration (Fig.5.46). ITZs were again assumed as the weakest phase. The ratio $E_{c,ITZ}/E_{c,cm}$=0.8 was again chosen based on the experiments by Xiao et al. (Xiao 2013). The remaining ratios were also assumed as 0.8: C_{ITZ}/C_{cm}=0.8 and T_{ITZ}/T_{cm}=0.8. The hardboard loading/bearing strips at the top and bottom of the specimen were built of spheres' clusters with the width, proportionally to the diameter D as in experiments. Their diameter was 0.5 mm with the 5-times lower stiffness than the cement matrix (stiffness of a hardboard used in experiments). The deformation was induced by prescribing the vertical top displacement in such a way that the changes of CMOD (crack mouth opening displacement) were approximately linear (as in experiments). CMOD was calculated as a horizontal displacement at the specimen mid-height between mid-points of two regions with the area of A=5×15 mm^2 (D=150 mm), twice as small and twice as large for D=74 mm and D=250 mm. The mid-points were at the distance of 40 mm as in the experiment, for D=150 mm and were proportionally scaled for other diameters. The time step was Δt=10^{-8} s. The calculation time on 8-

core CPU 3.3 GHz varied between 10 days and 2 months depending on the specimen diameter. The calculated mean nominal inertial number I for the maximum vertical load (that quantifies the significance of dynamic effects) was $<10^{-4}$ that always corresponded to a quasi-static regime. The minimum diameter of particles creating the cement matrix was reduced to d_{min}=0.15 mm for all specimens. The 2D concrete specimens under tensile splitting included in total about 42'000, 230'000 and 491'000 spheres for D=74 mm, D=150 mm and D=250 mm respectively. The values of cohesion were calibrated with the aid of the uniaxial compression test wherein random spheres were assumed with the same size as in the concrete mix. The specimens for the compression test were sawed out from the same concrete block like the ones used in splitting tension. The cylindrical specimens had a diameter D=100 mm and the depth of t=100 mm. Therefore, the obtained strength might be directly compared with one measured on cubic specimens 150×150×150 mm^2 (EN 12390-1:2012). The experimental compressive strength was 38 MPa for ε=0.19%. The satisfactory agreement both in stiffness and strength was achieved (Fig.5.5.2).

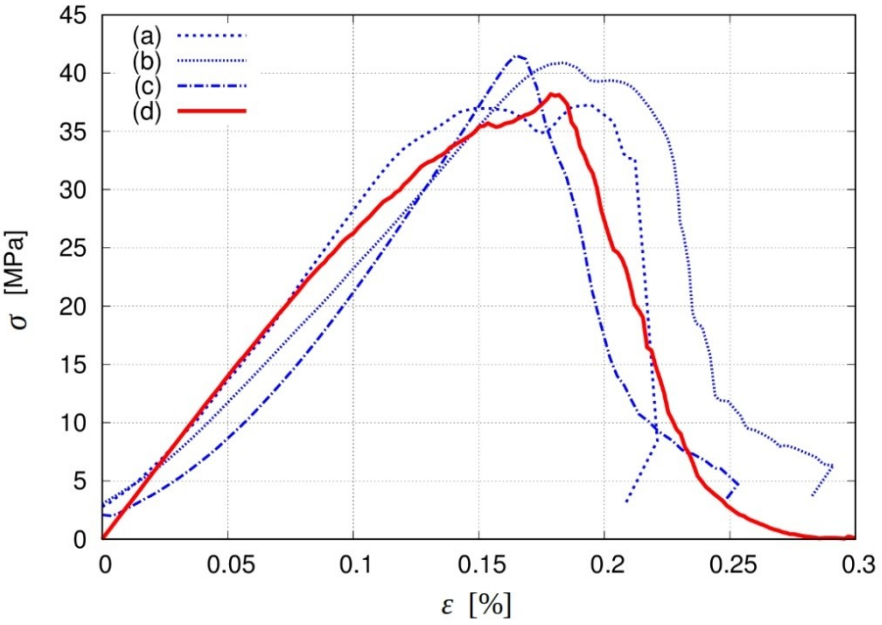

Fig.5.46: Stress-strain curves σ-ε curves in uniaxial compression test: a)-c) experimental curves and d) DEM result

The DEM results for splitting as compared to the experiments are shown in Figs.5.47 and 5.48. Very good agreement was achieved between numerical and experimental results for all specimens diameters with respect to the stress-displacement curve (Fig.5.47) and fracture geometry (Fig.5.51).

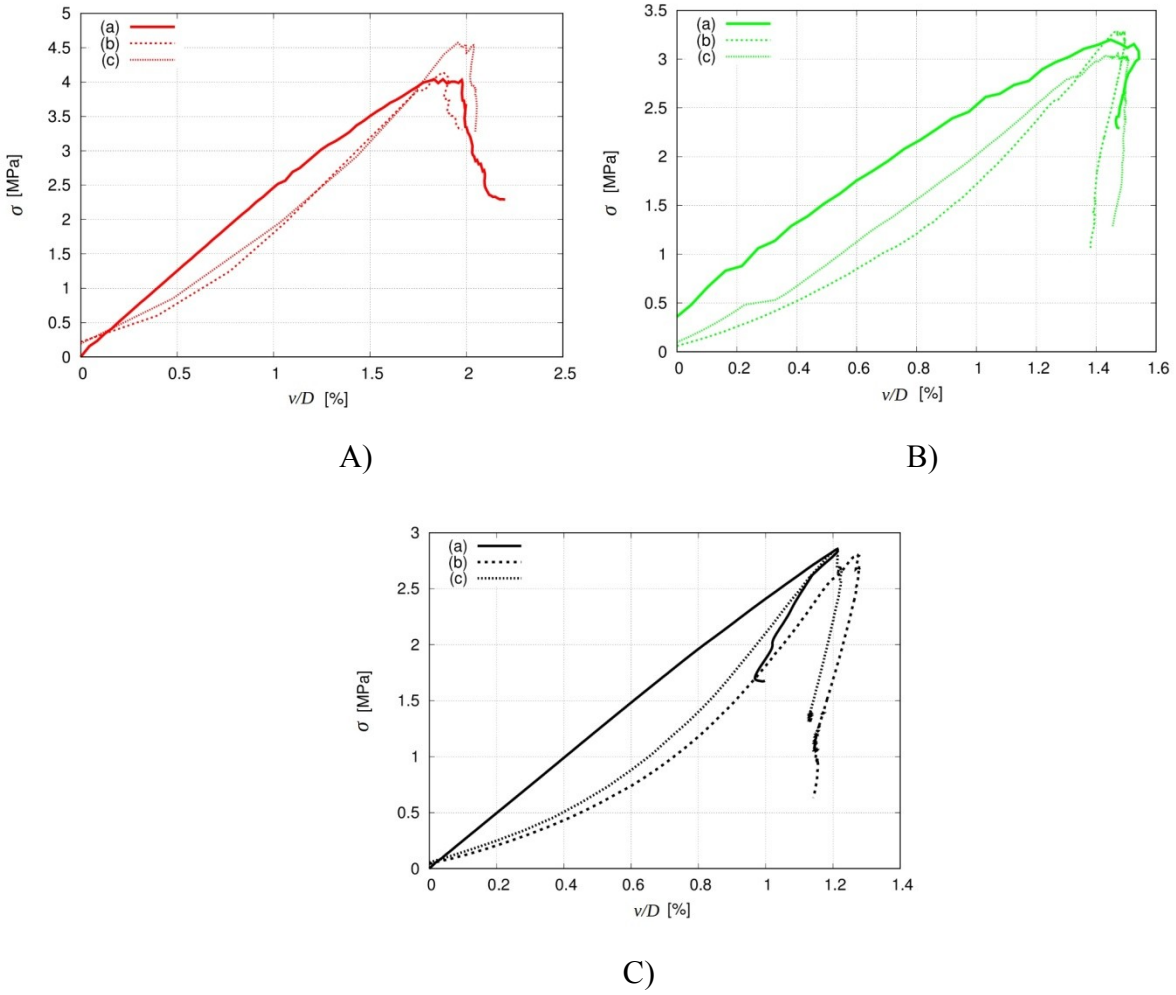

Fig.5.47: Tensile stress σ versus normalized displacement v/D for splitting tension: a) DEM and b)-c) experiments for different specimen diameters (A) D=74 mm, B) D=150 mm and C) D=250 mm)

The calculated maximum tensile splitting stress $\sigma=2P_{max}/(\pi DL)$ decreased with increasing diameter D. For D=74 mm, the calculated tensile splitting strength was f_t=4.0 MPa for v/D=1.8% (Fig.5.47Aa), for D=140 mm, f_t=3.2 MPa for v/D=1.5% (Fig.5.3.3.Ba)) and f_t=2.8 MPa for v/D=1.2% (D=250 mm, Fig.5.47Ca). Apart from the smallest specimen D=74 mm, where the DEM strength was smaller by 4% than the lower experimental result (Fig.5.47Ab), the remaining DEM results were between the experimental curves. For the specimen D=250 mm, the strength obtained with DEM (Fig.5.47Ca) was equal to the higher experimental result (Fig.5.47Cc). The elastic response of the DEM model was similar as in the experiment, however, the initial hardboard compression-hardening response was not well reproduced (since the loading boards in DEM were assumed to be rigid). This behaviour is clearly visible in the case of the largest specimen (Fig.5.47Cb-c) where this effect was most significant due to a very high compression force in the

experiment (above 80 kN). The concrete brittleness decreased with increasing specimen diameter. A clear snap-back mode of failure occurred for specimens D>74 mm, expressed by a simultaneous reduction of the vertical stress σ and vertical piston displacement v after the maximum stress σ_{max}. The calculated rate of softening was similar as in the experiment for the specimens D=74 mm and D=150 mm. For the largest specimen D=250 mm, the calculated softening was higher than in the experiment.

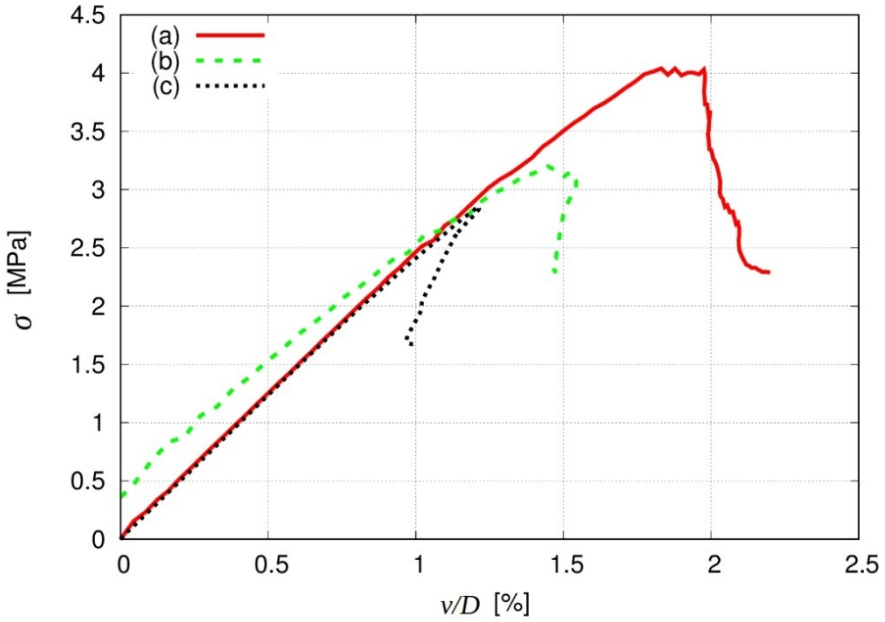

Fig.5.48: Tensile stress σ versus normalized displacement v/D curves for splitting in DEM for specimen diameters D: a) D=74 mm, b) D=150 mm and c) D=250 mm

The clear size effect was obtained in calculations, characterized by the loss of strength and ductility with increasing specimen diameter. The calculated elastic stiffness was similar for all 3 specimens. The curve for D=74 mm (Fig.5.58a) showed a plastic behaviour close to the the peak (for v/D=1.8-2%). The specimen D=250 mm indicated a very brittle behaviour (snap-back) after the peak, changing the displacement direction from positive to negative one (Fig.5.48c).

The damage in DEM may be described by the number of broken contacts n (Fig.5.49). The broken contacts were divided on those broken in ITZz (Fig.5.49a), cement matrix (Fig.5.49b) and the total number of broken contacts (Fig.5.49c). The amount of contacts broken in ITZ up to the peak was equal to 57%, 62% and 68% for D=74 mm, D=150 mm and D=250 mm respectively (Fig.5.49a). For the specimen D=150 mm (Fig.5.49B) in elastic part of the curve the fast creation of the macro-

crack is visible as an increase of broken contacts number (mainly in cement matrix). It is connected with instant crack appearance between the two largest aggregate grains in the specimen centre. After the peak, the increase of broken contacts in the cement matrix was greater than in ITZs by the factor of 5. The normalized total number of broken contacts in peak increased with the specimen diameter and was equal to n/D=17.5 for D=74 mm (Fig.5.49A), n/D=22 for D=150 mm (Fig.5.49B), n/D=28 for D=250 mm (Fig.5.49C). Those specimens were more damaged before the peak and thus had the lower strength.

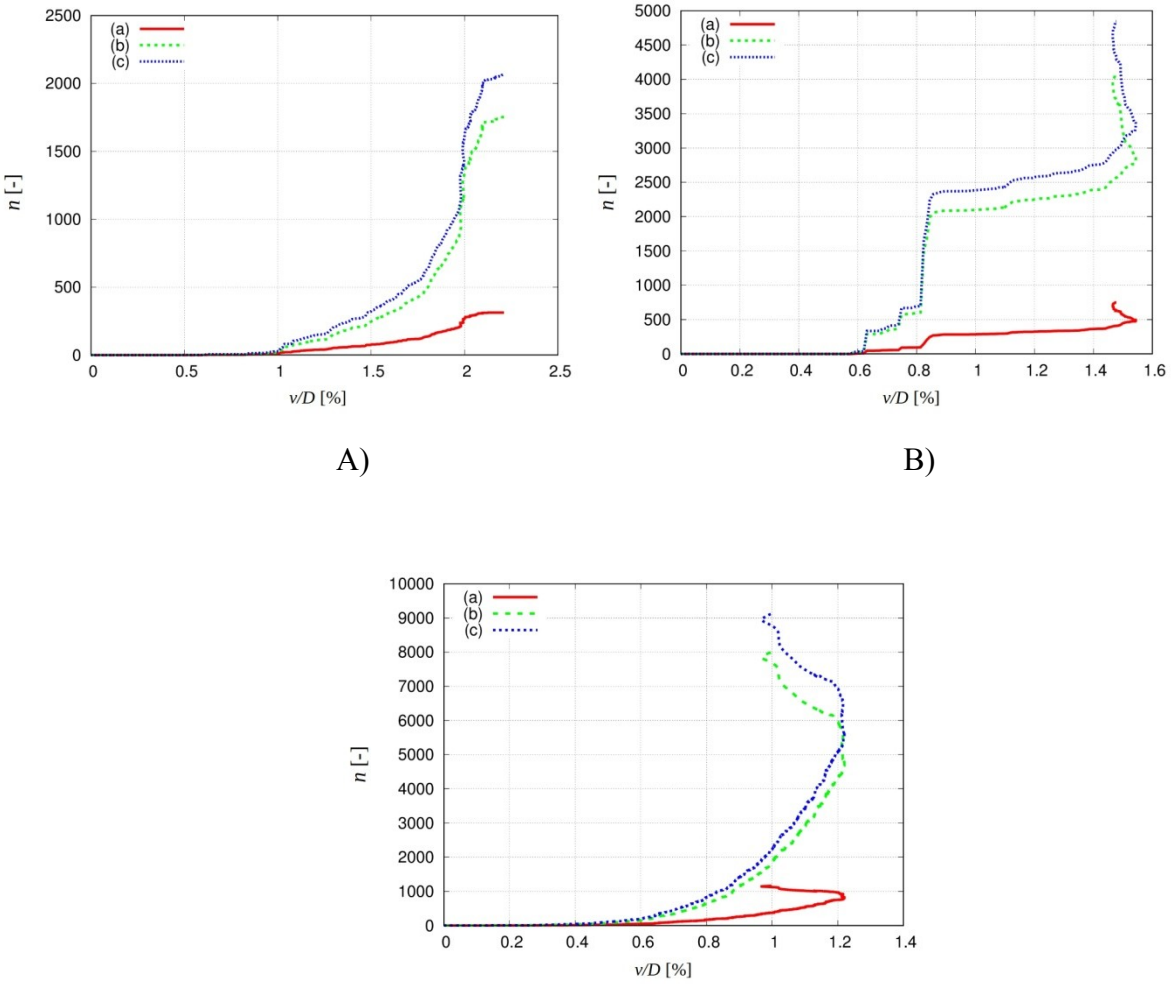

Fig.5.49: Number of broken contacts n against normalized displacement v/D for splitting in DEM: a) ITZ, b) cement matrix, c) all particles for different specimen diameters D (A) D=74 mm, B) D=150 mm, C) D=250 mm)

Figure 5.50 presents the relative number of broken contacts normalised by the number of particles (the so-called coordination number *N*). The coordination number was always slightly smaller for the larger specimen due to a higher number of particles in the specimen. The initial coordination number was similar for all specimens and was equal to about *N*=4.82. In the smallest specimen *D*=74 mm, the coordination number decreased down to *N*=4.7, whereas for the specimen *D*=150 mm and *D*=290 mm to *N*=4.75 and *N*=4.78. From the peak load to the test end, the reduction rate of *N* was higher for the smaller specimen due to more intense fracture.

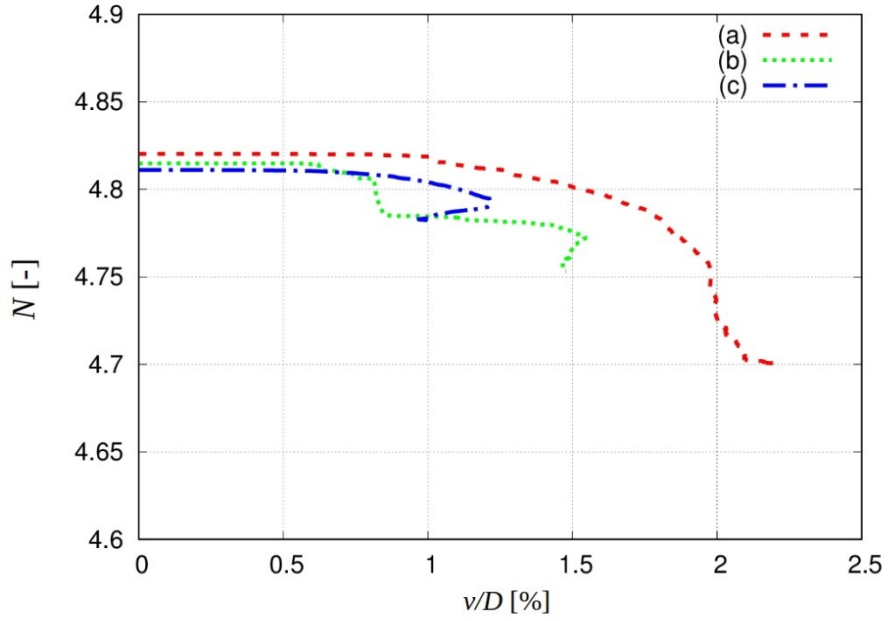

Fig.5.50: Coordination number *N* versus normalized displacement *v*/*D* curves for splitting tension test calculated with DEM in specimens with different diameter *D* (a) *D*=74 mm, b) *D*=150 mm and c) *D*=250 mm)

Finally, the crack morphologies expressed by broken contacts (in red, Fig.51b) and deformed specimens (Fig.51c) were compared with the micro-CT scans of Fig.5.51. For the specimen *D*=250 mm, the image from the digital camera of full specimen height was additionally presented as the specimen was too high for full scanning (2/3 of the total specimen height was solely scanned with micro-CT).

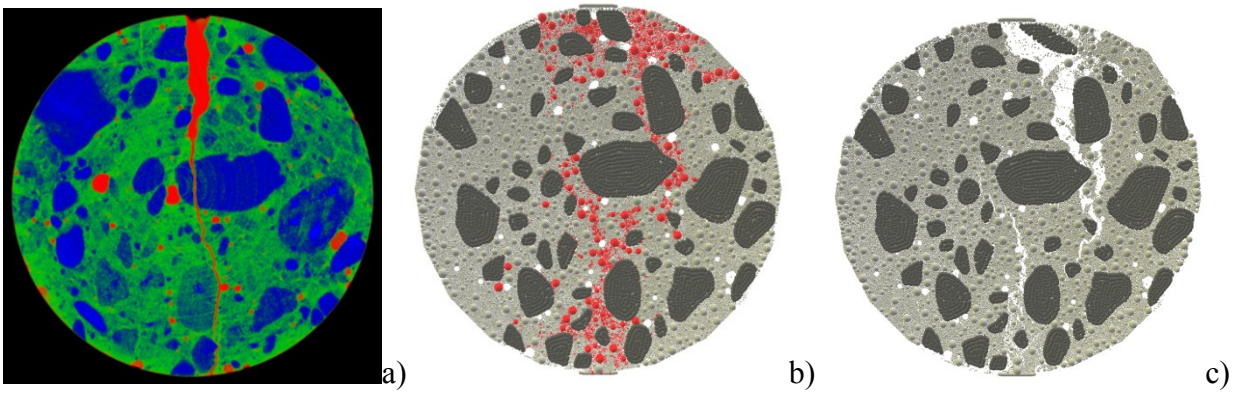

a) b) c)

A)

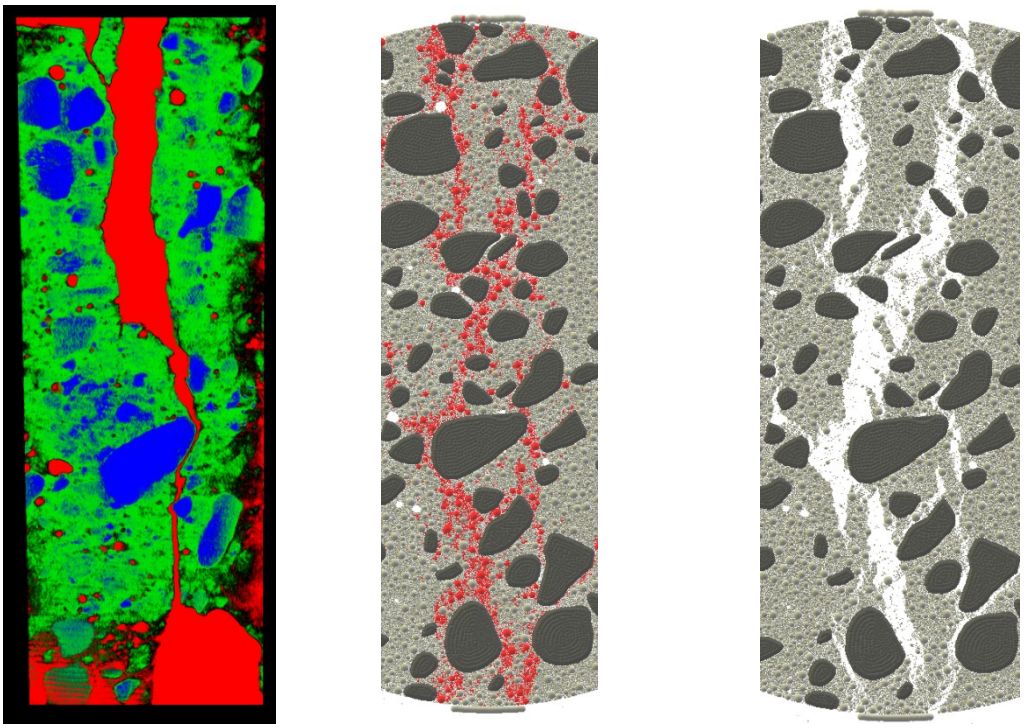

a) b) c)

B)

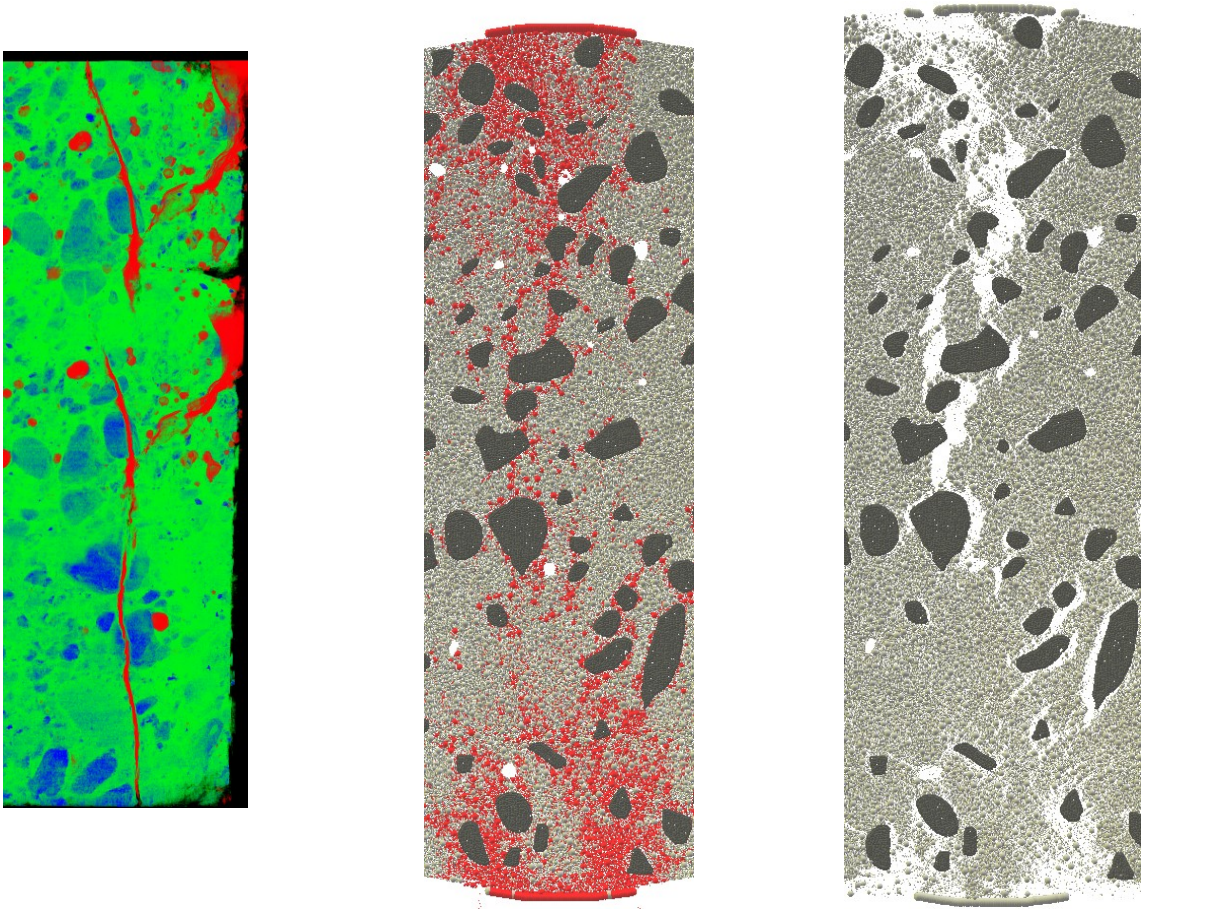

a) b) c)

C)

Fig.5.51: Crack geometry: a) micro-CT images, b) deformed specimens in DEM and c) images of broken contacts (particles with broken contacts were marked with red colour) in DEM for different specimen diameters *D* (A) *D*=74 mm, B) *D*=150 mm and C) *D*=250 mm)

For the specimen *D*=74 mm (Fig.5.51A), the crack propagated close to the same aggregate particles, however, on their opposite sides than in the experiment. The crack propagated near the large aggregate in the specimen's mid-height on the right side instead of breaking it on the left side. The bottom part of the crack was narrow and straight as in the experiment, however, the crack propagated on the left side of a large aggregate, opposite to the experiment wherein it followed the right edge of the aggregate (Fig,5.51Ac). Additionally, the crack was more curved. The large aggregate at the mid-height of the specimen was also broken in the experiment. The top of the specimen was crushed in the experiment that was reproduced in DEM as intensive micro-cracking of the cement matrix under the loading board (Fig.5.51Aa) and wider crack opening. In the small specimen, some fine differences in the aggregate shape and pores' position greatly influenced the

crack pattern. Moreover, the 3D aggregate arrangement influenced the crack shape. To obtain a more realistic crack patterns, the 3D DEM simulations should be carried out. The cracks computed in DEM for D=150 mm were more realistic as compared to the experiment (Fig.5.51B). For D=150 mm, no aggregate breakage occurred in the experiment (Fig.5.51Ba) Note that the crushed peace of specimen fell apart during transportation (Fig.5.51Ba). The same crack's shape was reproduced in DEM as to the crack's branching at the specimen top (Fig.5.51Bb-c). The main crack followed the left side of a large aggregate in the specimen's mid-height, however the another branching appeared at the specimen bottom (Fig.5.51Bc) with a finer crack that propagated at the same side of the aggregate as in the experiment. Finally, the largest specimen D=250 mm was almost symmetrically cracked in DEM while in the experiment it was curved to the right side (Fig.5.51Cc), probably due to a small load eccentricity. The crack was curved to the left at the specimen top, both in the experiment and DEM, forming a wedge connecting the straight part of the crack with the loading strip edge (Fig.5.51Ca-c). The similar behaviour was obtained in the specimen's mid-height wherein the crack in DEM was curved to the left (Fig.5.51Cb-c). Even though, the macro-crack developed along other aggregate particles, it had a very small width in the specimen mid-height and was branched with various micro-cracks at bottom and top both, as in the experiment and DEM (Fig.5.51Ca-c). The intense cracking at the top and bottom (the wedges) was obtained in the model as a multiple micro cracking in the cement matrix.

The macroscopic DEM results: strength (Fig.5.52) and angle α between the horizontal axis and softening curve (Fig.5.53) from the experiments (Section 3) were directly compared directly with DEM simulation results. The strength reduction was very similar in the experiment and DEM for the specimens D=150 mm and D=250 mm. The size effect on brittleness (defined as the angle α between horizontal axis and the softening part of the curve) was stronger in DEM than in the experiment. For the smallest specimen, the softening angle in DEM was equal to the mean angle in experiment (α=78°) whereas for the specimens D=150 mm and D=250 mm was equal to α=95° and α=106° in the experiments and α=102° and α=120° in the numerical calculations (the difference 7%-13%).

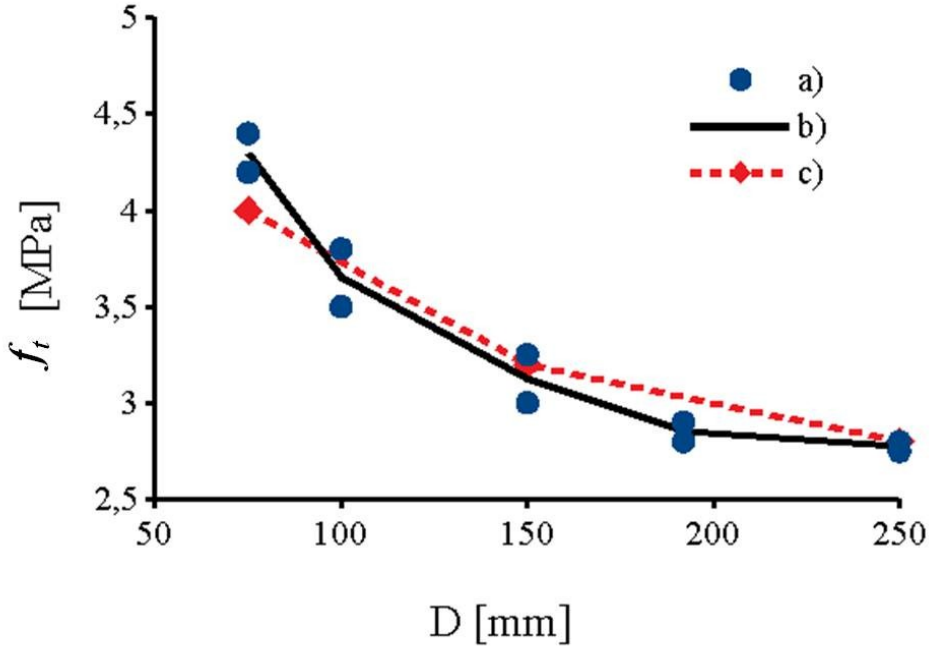

Fig.5.52: Comparison of experimental and numerical results of tensile splitting strength *ft* against specimen diameter *D* for: a) each specimen (dots), b) mean value trend (continuous line) and c) DEM result (dashed line)

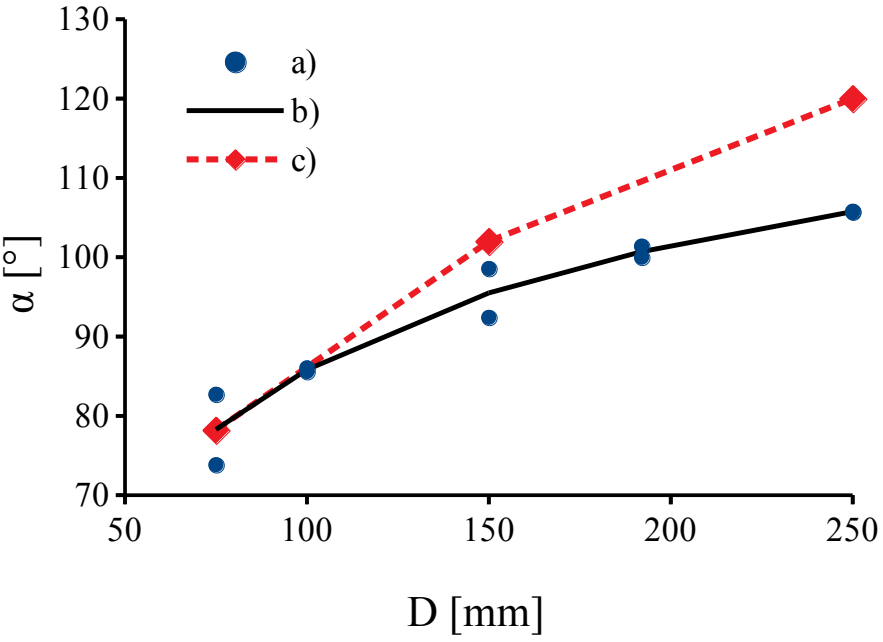

Fig.5.53: Softening parameter α versus specimen diameter *D* for each specimen in tensile splitting experiment (dots), b) mean value trend (continuous line) and c) DEM result (dashed line)

Chapter 6

Conclusions

Some interesting conclusions may be offered from the experimental and numerical research works on concrete fracture at the meso-scale:

Experiments

- The size effect on strength and brittleness of concrete occurred in tensile splitting test due to fracture and non-uniformity of the vertical tensile stress caused by a formation of compressive wedges at the loading/supporting regions. The strength and ductility of concrete diminished with increasing specimen diamter. In experiments under the CMOD control mode, a snap-back phenomenon occurred.

- The type of a loading/supporting strip strongly affected the concrete behaviour during tensile splitting. The splitting tensile strength was smaller by 10%, CMOD corresponding to the strength was smaller by 20% and displacement corresponding to the strength was smaller by 300% when the steel loading/supporting cylinders were used. A clear compressive wedge took place when plywood loading/supporting boards were used.

- ITZs had a different width and porosity depending on aggregate roughness that determines the strength and brittleness of concrete. The width increased with growing aggregate roughness. ITZs usually did not surround all aggregate particles but covered solely 80-90% of the aggregate circumference. The ITZ porosity decreased towards the cement matrix. ITZs acted as attractors for a macro-crack.

- The cracks in concrete occurred through bridging of interfacial micro-cracks. The macro-cracks propagated also sometimes through weak aggregate particles. The crack branching also happened.

- The width of the fracture process zone (strain localization) was about 3.4 mm ($0.28\times d_a^{max}$).

- X-ray micro-CT is a powerful tool to quantitatively measure the internal damage in concrete.

DEM analyses (uniaxial compression and tension)

- The DEM model demonstrated its accuracy and applicability for concrete in terms of its elasticity and fracture properties. It realistically followed fracture including the occurrence of micro-cracks during their onset, formation and propagation (including phenomena of crack bridging, crack branching and inter-locking). The amount, shape and location of cracks were strongly affected by the shape of aggregate, its location and strength of ITZs.

- The calculated concrete strength increased with increasing ratio $C_{ITZ}/C_{cm,}$ and minimum cement particle diameter (tension) and decreasing number of ITZs. The ductility became larger mainly with decreasing ratio C_{ITZ}/C_{cm} (tension) and decreasing minimum cement particle diameter (compression). The crack number increased with increasing amount of ITZs. The cracks were more curved when the larger number of ITZs was assumed in DEM. The concrete ductility increased in 3D computations. The rate of breakage was significantly higher in ITZs than in the cement matrix. The tensile inter-granular fracture dominated.

- The calculated concrete strength was larger by 10% for spheres than for clusters of spheres due to stress concentrations for the real aggregate with sharp edges that contributed to the smaller strength and faster cracking. More straight cracks occurred when spheres were used. The number of broken contacts was higher and more uniform for spheres. It was also higher in 3D than in 2D simulations.

- The discrete macro-cracks were curved due to a stochastic distribution of aggregate particles including ITZs. They were created by bridging the interfacial micro-cracks (in calculations and in experiments). They possessed many small branches. The micro-cracking also occurred far beyond the crack tip. The external vertical load was transmitted via a network of normal contact forces which formed force chains. The compressive normal contact forces connected to the tangential contact forces developed along macro-cracks due to aggregate inter-locking.

DEM analyses (splitting tension)

- The experimental size effect was realistically reproduced in numerical calculations at the aggregate level, i.e. the concrete strength and ductility decreased with increasing concrete specimen diameter. The calculated decreasing strength approached an asymptote with increasing cylindrical specimen diameter within the considered specimen size range.

- DEM proved its capability to model concrete fracture in detail by taking the snap-back instability into account. The agreement of calculated stress-displacement results and crack shapes with experimental ones was satisfactory. The decrease of the strength of ITZs and minimum particle diameter in the mortar caused the reduction of both the splitting tensile strength and material brittleness.

- The external vertical splitting force was transmitted via a network of normal contact forces which formed clear force chains. Some compressive forces appeared also along the macro-crack edge due to aggregate inter-locking.

- For the force line contact, the total number of broken normal contacts was always lower by about 10% than for the force surface contact. The rate of the normal contact breakage was higher in ITZs before the peak load and in the cement matrix after the peak load. Nearly 30-40% (cement matrix) and 90% (ITZs) of normal contacts were damaged before the peak load due to micro-cracking. Due to cracking, the coordination number reduced from 4.75-4.80 down to 4.57-4.59.

- The calculated maximum tensile normal stress along the central vertical line was very similar as the measured one and as the theoretical one according to the elastic theory. The calculated maximum compressive normal stress was smaller at the boundaries for plywood boards than for steel cylinders.

- The shear crack displacement dominated over the normal crack opening before fracture and during fracture the normal crack displacements were obviously higher due to a tensile dominating failure. The particle rotations occurred after the bond breakage. The maximum rotations were very small (0.7°).

- Due to the snap-back instability, the total internal energy reduced by 15%, the elastic normal internal energy reduced by 60% and the elastic tangential internal energy reduced by 20%. The plastic dissipation, numerical damping and elastic energy from removed cohesive contacts increased by the factor 2.5, 2 and 2.5, respectively.

- The continuous micro-cracking process started in the central vertical region at a very early deformation stage, i.e. far before the peak load. It consisted of two/three intensity regimes depending upon the specimen size. Initially, it evolved with the moderate intensity before the peak load for both the specimens and later with the pronounced intensity for the smaller specimen or with the pronounced and following moderate intensity for the larger specimen. The pronounced micro-cracking process

mainly started in the smaller specimen slightly before the peak load and in the larger specimen clearly before the peak load.

- The snap-back behaviour occurred after the peak load in the larger specimen since the specimen was already strongly fractured and relatively fewer contacts were needed in the post-peak regime to fully damage the specimen in contrast to the smaller specimen. The specimen failure had a clear tensile type. i.e. the normal crack displacement always dominated strongly over the tangential crack displacement. At the peak, a clear macro-crack already developed in the larger specimen with the height equal to the half of the specimen diameter. For the smaller specimen, there existed many micro-cracks at the peak load. The width of FPZ was about 1/3 of the maximum aggregate diameter.

- The higher strength of the smaller specimen was caused by the contribution of the normalized elastic energy that was greatly higher at the peak load than for the larger specimen due to the much lower fracture process intensity, expressed by a lower relative number of broken contacts with respect to the specimen diameter. The greatest total normalized internal energy absorbed in the fractured region was higher at the peak load by 30% in the smaller specimen. The greatest total normalized internal energy released in the region beyond the fracture zone was higher at the peak load by 30% for the larger specimen.

- The load was carried in the specimens by strong compressive normal contact forces. The %-number of strong compressive/tensile normal contact forces was higher at the peak load for the smaller specimen due to its higher strength and low fracture intensity. After the peak, their drop was by far higher for the smaller specimen due to the high fracture intensity.

APPENDIX 1

Experimental study of shear strength and failure mechanisms in RC beams scaled along height or length

(published in the paper by Suchorzewski, J., Korol, E., Tejchman, J. i Mróz, Z. Experimental study of shear strength and failure mechanisms in RC beams scaled along height or length. *Engineering Structures*, 157, 203-223, 2018).

A1.1 Introduction

The extensive experimental studies and analytical formulae were presented in order to specify the dependence of the critical stress value on the size factor for plain and reinforced concrete beams subjected to bending, tension or compression (e.g. Bažant et al. (1994), Carpintieri (1989), Bažant et al. (1998), Duan et al. (2004), Bažant et al. (2007), Hoover&Bažant (2014), Korol et al. (2013), Korol&Tejchman (2014a)). The evolution of a post-critical softening modulus was also observed but regrettably not systematically documented. A transition from the snap-through response in the post-critical phase under load control for small size elements to snap-back response for large size elements observed in tests and predicted numerically (Korol&Tejchman(2014a), Korol et al. (2014b), Korol et al. (2015)) indicates the growth of brittleness of elements with growing size factor.Most tests were conducted for geometrically similar beams of varying size and reinforcement ratio (Korol et al. (2015), Kani (1967), Walraven (1978), Bažant et al. (1991), Yang et al. (2003), Reineck et al. (2003), Lubell et al. (2004), Tan et al. (2005), Zhang and Tan (2007), Belgin&Sener (2008)). However, only several papers were devoted to the analysis of the size effect in beams for an independent variation of height and length (e.g. Słowik&Smarzewski (2013)). This class of the variation of geometric parameters is typical in the engineering design and requires a separate study. The objective of the present paper is to identify experimentally differing failure mechanisms in reinforced concrete beams subjected to four-point bending for a separate variation of the depth and length at the constant thickness. Special attention was paid to a description of a shear fracture process (inherently related to the size effect) by specifying the width of strain localization zones by means of the digital image correlation (DIC) technique and measuring crack opening and slip displacements. The commonly used code procedures using strut-and-tie models proposed in the literature were used to calculate theoretical ultimate shear strengths in order to compare them with experimental outcomes. In addition, crack widths and deflections were compared with code formulae.

A1.2 Specimens geometry

The beams of the series '1' were scaled along the effective height D in the proportion 1:2:4 with the constant effective span length l_{eff}=2700 mm. The beams were denoted as S1D18a108, S1D36a108 and S1D72a108, where the symbol *S1* denotes the series '1', D - the effective beam depth in [cm] and a - the shear zone length in [cm]. Note that the beam S1D36a108 (D=360 mm) had the same dimensions as the concrete beam (denoted as SL40) used in the size effect experiments by Korol (Krol et al. 2010) and was twice as high as the beam S1D18a108 (D=180 mm) and twice as small as the beam S1D72a108 (D=720 mm). Thus, the shear zone length a and bending zone length b (distance between two concentrated forces *V)* were constant a=1080 mm and b=540 mm, respectively (Fig.A1.1A, Tab.A1.1). The shear span parameter $\eta_a=a/D$ was 1.5, 3 and 6, the length parameter $\eta_l=l_{eff}/D$=3.75, 7.5 and 15 and the bending span parameter $\eta_b=b/D$ was 0.75, 1.5 and 3. Each beam height h included 3 identical concrete specimens in order to verify the result repeatability (indicated as: S1D18A108_1 - S1D18a108_3, S1D36a108_1 - S1D36a108_3 and S1D72a108_1 - S1D72a108_3).

The beams of the series '2' had the same height (D=360 mm) but varying effective span length l_{eff} and shear span a (the latter scaled in the proportion 1:2:3) (Fig.A1.1B, Tab.A1.2). The beams were denoted as S2D36a36 (a=360 mm), S2D36a72 (a=720 mm) and S2D36A108 (a=1080 mm) with the length parameter $\eta_l=l_{eff}/D$=3.5, 5.5 and 7.5, shear span parameter $\eta_a=a/D$=1.0, 2.0 and 3.0 and bending span parameter $\eta_b=b/D$=1.5. The longest beam from the series 2 (S2D36a108) had the same dimensions as the beam from the series '1' denoted as S1D36a108. The beam S2D36a36 was as twice as short as the beam S2D36a72 and the beam S2D36a108 was as twice as long as the beam S2D36a72. Each beam included 2 identical specimens only (instead of 3) in order to reduce the costs of the beams' production (denoted as: S2D36a36_1 and S2D36a36_2, S2D36a72_1 and S2D36A72_2 and S2D36a108_1 and S2D36a36_2).

In total 15 beams (series '1': 9 beams and series '2': 6 beams) were subjected to four-point bending. The ratio of the shear span a to the effective height D varied from $\eta_a=a/D$=1 up to η_a=6, thus different failure modes were expected to be developed (Zhang&Tan 2007b, Belgin&Sener 2008). The ratio of the bending span b to the effective height D varied from $\eta_b=b/D$=0.75 up to η_b=3 (series '1') and η_b=1.5 (series '2').

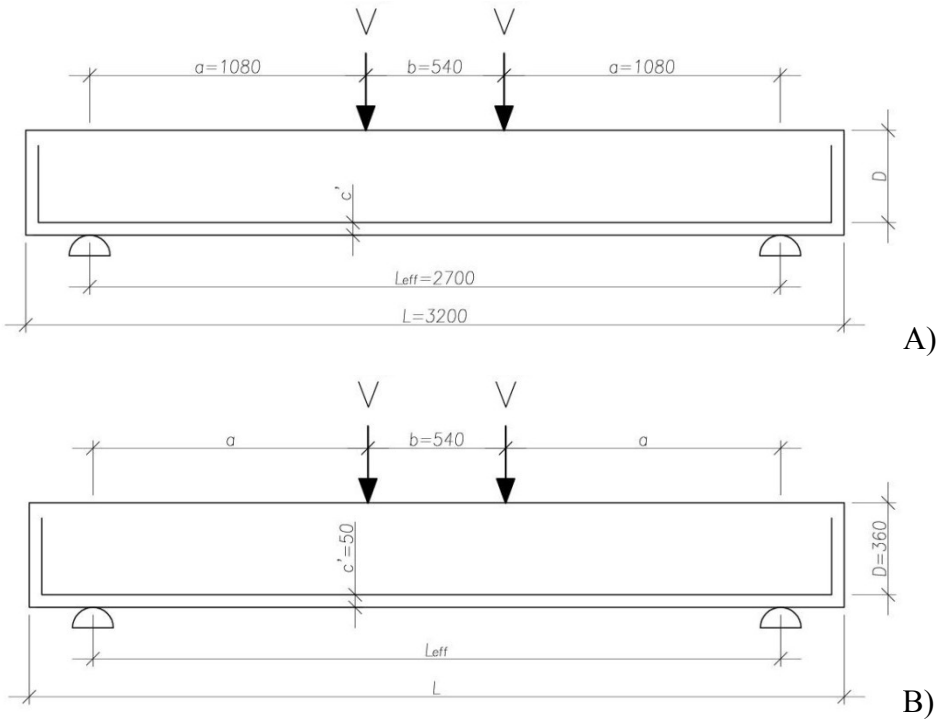

Fig.A1.1: Experimental reinforced concrete beams under four-point bending: A) loading scheme for series '1' (l_{eff}=2700 mm, a=1080 mm, b=540 mm) with varying D, B) loading scheme for series '2' (D=360 mm, b=540 mm) with varying a and $l_{eff.}$ (D - effective beam height, l_{eff} - distance between beam supports, l - total beam length, V - vertical concentrated force applied, a - shear zone span, b - bending zone span, dimensions are in [mm])

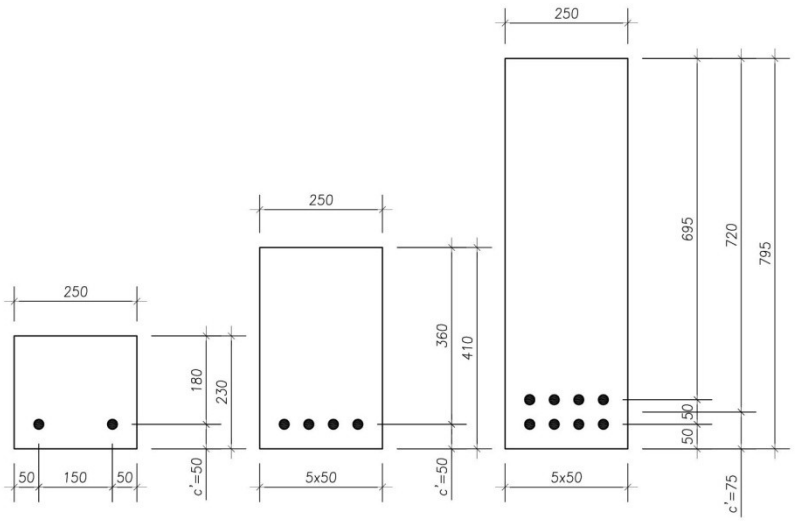

a) b) c)

Fig.A1.2: Experimental cross-section of: a) beam S1D18a108 (D=180 mm), b) beams: S1D36a108, S2D36a36, S2D36a72, S2D36a108 (D=360 mm) and c) beam S1D72a108 (D=720 mm) (dimensions are in [mm])

Tab.A1.1: Dimensions of RC beams in test series '1'

Beam dimension	**Beam S1D18a108**	**Beam S1D36a108**	**Beam S1D72a108**
***D* [mm]**	180	360	720
l_{eff} [mm]	2700	2700	2700
***a* [mm]**	1080	1080	1080
***b* [mm]**	540	540	540
$\eta_l=l_{eff}/D$	15	7.5	3.75
$\eta_a=a/D$	6	3	1.5
$\eta_b=b/D$	3	1.5	0.75
$\eta_c=c'/D$	0.28	0.14	0.10

Tab.A1.2: Dimensions of RC beams in test series '2'

Beam dimension	**Beam S2D36a36**	**Beam S2D36a72**	**Beam S2D36a108**
***D* [mm]**	360	360	360
l_{eff} [mm]	1260	1980	2700
***a* [mm]**	360	720	1080
***b* [mm]**	540	540	540
$\eta_l=l_{eff}/D$	3.5	5.5	7.5
$\eta_a=a/D$	1	2	3

$\eta_b=b/D$	1.5	1.5	1.5
$\eta_c=c'/D$	0.14	0.14	0.14

The reinforcement of all beams consisted of ribbed bars of the diameter ϕ=20 mm with the mean yielding stress of 560 MPa (class B500) and the modulus of elasticity of 205 GPa. The longitudinal reinforcement ratio was designed as ρ_l=1.4%. Each beam size required a different number of bars depending on the effective depth D. The beams of D=18 cm and D=36 cm had 2 and 4 bars in one layer, respectively whereas the beam of D=72 cm had two layers with 4 bars i.e. 8 bars in total (Fig.A1.2). In order to avoid the anchorage zone failure and slip between reinforcement and concrete, hooked steel bars were used (Fig.A1.1) with the anchorage length of 130 mm, 310 mm or 670 mm, depending on the beam height.

Tab.A1.3: Concrete mixture recipe

Material	**Weight or volume in dry state**
Portland cement: CEM II/A-V 42.5R	340 kg
Aggregate:	
sand 0-2 mm	775 kg
gravel 2-8 mm	750 kg
gravel 8-16 mm	400 kg
Water	140 l

The specimens from the series '1' and series '2' were casted separately, however the concrete recipe was similar (Tab.A1.3). The maximum aggregate diameter was d_{max}=16 mm and the water to cement ratio was 0.41. The accompanying tests were performed, including uniaxial compression on 6 cubes (150×150×150 mm^3), splitting tension and elastic compression on 3 cylinders (φ=150 mm and L=150 mm). The measured average compressive strength on cubes f_{cm} was 59.26 MPa (series '1', standard deviation of 2.37 MPa) and 63.81 MPa (series '2', standard deviation of 2.09 MPa) (the mean value $\bar{f}_{cm} = 61.5$ MPa). Thus the corresponding concrete class was C45/55. The average characteristic splitting tensile strength was 2.81 MPa (series '1', standard deviation of 0.52 MPa) and 3.61 MPa (series '2', standard deviation of 0.76 MPa) (the average value was 3.21 MPa). The

measured average elastic modulus was E=33.1 GPa (series '1', standard deviation of 2.36 GPa) and E=35.3 GPa (series '2', standard deviation of 3.02 GPa).

A1.3 Test procedure

The tests were performed under displacement-controlled conditions. Steel loading plates were always used in order to avoid local concrete crushing. Their area was always the same, i.e. 100×250 mm^2 (l_a×t). The area of support (bearing) plates (l_b×t) had also the same size. During the test, the vertical force and displacements were measured. The true deflection at the mid-span and support displacement were registered by means of linear variable displacement transducers (LVDT's). The steel strains were traced with strain gauges placed on reinforcement bars at the beam mid-span.

The back side of beams was intended for 2D displacement measurements of localized zones using the non-invasive Digital Image Correlation (DIC) technique (Skarżyński&Tejchman (2013b), Skarżyński et al. (2011), Bhardi&Inoue (2005), Rechenmacher&Finno (2004), Słonimski et al. (2007)). The ability of DIC method to measure the width of a localized zone on the concrete surface was confirmed in laboratory tests by Skarzynski et al. (Skarżyński&Tejchman 2013b) The localized zones were registered above a small notch in the concrete cover (below the reinforcement) at the beam mid-span (the notch length was 20 mm). The digital camera Nikon D800 with the image resolution of 36 MPix was used. The image captured area on the concrete surface of size 75 mm (height) and 50 mm (width). The images were taken every 30 seconds. The pixel number per mm was about 90 pix/mm. On the opposite side of beams above the notch tip the digital microscope DG-3X with a lens with the magnification up to 1000× was used to trace a crack propagation.

The front side of the beam was prepared to track cracks and to measure their width with a simple microscope. A detailed description including crack opening ω and slip displacements δ were calculated based on measurements with a digital extensometer of DEMEC type with base of 100 mm. The measuring mesh consisting of equilateral triangles which covered the area where a critical diagonal crack was expected to appear. The number of triangles varied between particular series depending on the beam size. During test the elongation of triangle sides (AB, AC and BC) was measured and the crack trajectory was registered. The crack normal (opening) displacement ω and crack tangential (shear) displacement δ were calculated using a simplified formula by Sato et al. (Sato et al. 2004). The increments of lengths of triangle sides AB and AC (Fig.A1.3) can be expressed as follows:

$$l_1^{'} - l_1 = \Delta l_1 = \delta \cos\theta_1 + \omega \sin\theta_1 , \tag{A1.1}$$

and

$$l_2^{'} - l_2 = \Delta l_2 = \delta \cos\theta_2 + \omega \sin\theta_2 , \tag{A1.2}$$

where: l_i=|AB| – the initial triangle side length, l_i'=|AB'| – the deformed triangle side length and θ_i - the angle between the crack and triangle side. Equations 2 and 3 allowed for determining the crack displacements δ and ω:

$$\delta = \frac{(l_1^{'} - l_1)\sin\theta_2 - (l_2^{'} - l_2)\sin\theta_1}{\cos\theta_1 \sin\theta_2 - \cos\theta_2 \sin\theta_1} \tag{A1.3}$$

and

$$\omega = \frac{(l_1^{'} - l_1)\cos\theta_2 - (l_2^{'} - l_2)\cos\theta_1}{\cos\theta_2 \sin\theta_1 - \cos\theta_1 \sin\theta_2} . \tag{A1.4}$$

The varying angles θ_1 and θ_2 were measured during post-processing analyses of images taken during tests. Since the angle differences inside all equilateral triangles during deformation were negligible, therefore for the simplicity of calculations these internal angles were assumed to be constant (60^o).

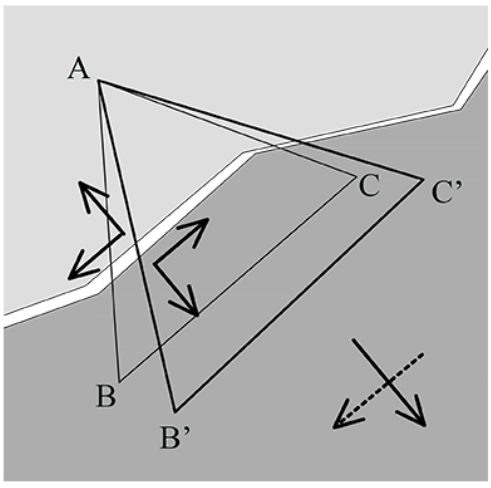

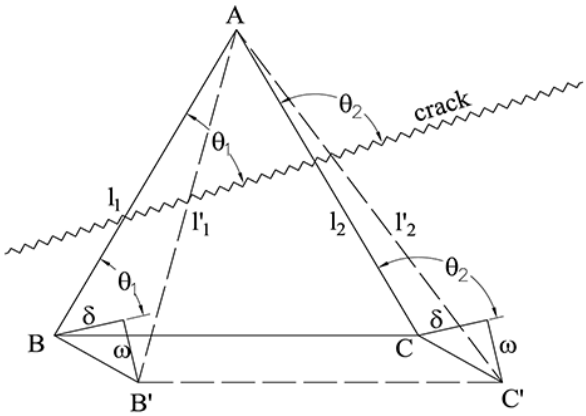

positive crack sliding direction

positive crack opening direction

Fig.A1.3: Calculation method of crack opening and sliding displacements based on grid of equilateral triangles on concrete surface (ABC - initial triangle location, AB'C' - - displaced triangle location) (Sato et al. 2004)

A1.4. Experimental results

Failure modes and nominal strength

Series '1': varying effective depth *D* and bending zone span *b* at constant shear zone span *a*

The varying effective depth D=0.18, 0.36 and 0.72 m and constant shear span a=1.08 m contributed to the variation of the parameter η_a from 1.5 through 3.0 up to 6.0, the parameter η_b from 0.75 up to 3 and the parameter η_l from 3.75 up to 15. It was experimentally observed that these parameters had a great effect on the beam failure mode and ultimate load.

The smallest beams S1D18a108 with η_a=6.0 (η_b=3, η_l=15) reached their limit state in the flexural failure mechanism developing in the central beam zone, inducing concrete cracking and longitudinal reinforcement yielding combined with concrete crushing in the upper beam portion. This failure mode was preceded by growth and opening of bending cracks leading to localized failure combined with a significant increase of the beam deflection. The total averaged ultimate vertical force acting on the beams was $P_{max}=2V_{max}$=120.74 kN (Fig.A1.4a) while the normalized average deflection u/D corresponding to the failure onset was 12.3%. This failure mode and the related scale effect was analyzed in numerous papers (Bažant&Planas (1998), Korol et al. (2013), Korol&Tejchman 2014), Korol et al. (2015)). The effective stress σ_{eff} used for the expression of beam strength was the elastic stress value at the external beam layer $\sigma_{eff}=(3P_{max}/tD)a/D$.

The medium high beams S1D36a108 for η_a=3 (η_b=1.5, η_l=7.5) failed in shear with dominant normal diagonal crack displacements (so-called diagonal shear-tension failure (Sato et al. 2004) and this type of failure was sudden and brittle. The mean total ultimate vertical force was $P_{max}=2V_{max}$=242.47 kN (Fig.A1.4b) while the normalized average deflection u/D corresponding to the ultimate force was 1.71%. The highest beams S1D72a108 with η_a=1.5 (η_b=0.75, η_l=3.75) failed in shear with significant both tangential and normal diagonal crack displacements (so-called diagonal shear-compression failure (Sato et al. 2004)) and with a huge increase of the ultimate shear strength supported by an internal arch action (Fig.A1.4c). This failure mode was also sudden and brittle. The mean total ultimate vertical force was $P_{max}=2V_{max}$=1029.70 kN (Fig.A1.4c) while the normalized average deflection u/D corresponding to P_{max} was 1.0%. The vertical-force-deflection

diagrams were similar for beams with the similar geometry (Fig.A1.4). All curves after first cracking changed their slope and behave almost linearly up to the yield plateau and/or up to the peak force (for the beams S1D36a108 and S1D72a108, the yield plateau was not reached). The post-peak softening was not observed due to a sudden loss of the beam stability during failure.

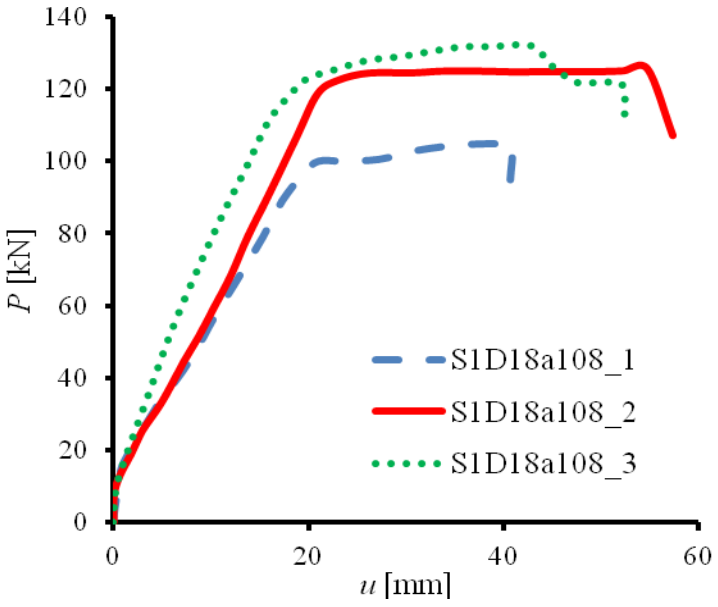

a)

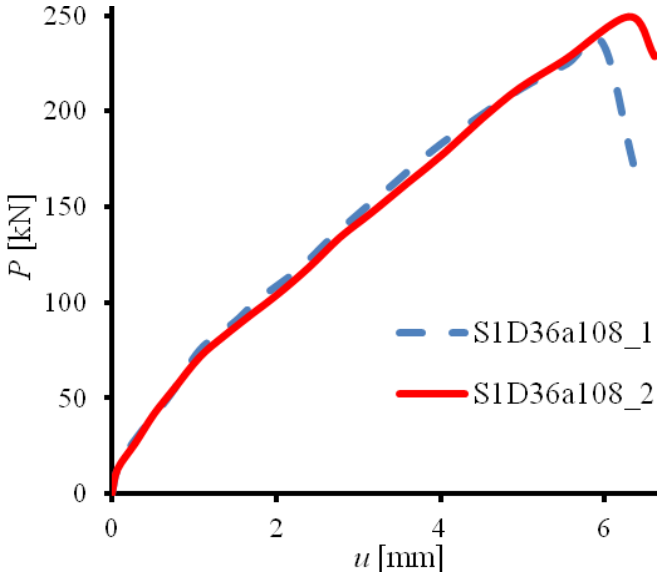

b)

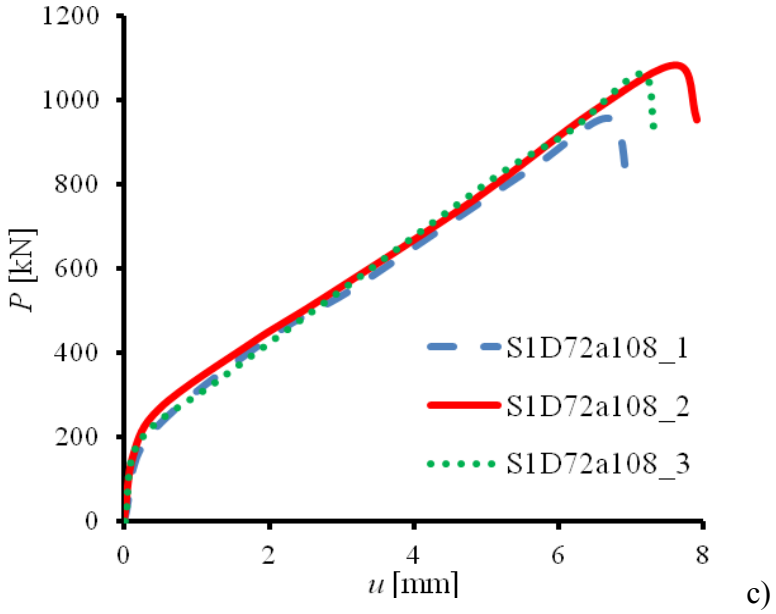

Fig.A1.4: Experimental force - deflection diagrams P=f(u) for RC beams (series '1' with l_{eff}=1080 mm and b=540 mm): a) S1D18a108 (D=180 mm, η_a=6), b) S1D36a108 (D=360 mm, η_a=3) and c) S1D72a108 (D=720 mm, η_a=1.5, P=2V)

Series '2': varying shear zone span a at constant effective depth D and bending zone span b

The varying shear span a=0.36 m, 0.72 m and 1.08 m and constant beam depth D=0.36 m provided the varying shear span parameter η_a from 1.0 through 2.0 up to 3.0 and constant bending span parameter η_b=1.5, (η_l=3.5-7.5). The effect of the varying shear span on the nominal strength and failure mode was very strong (Tab.A5). The longest beam S2D36a108 with η_a=3.0 failed due to diagonal shear failure with the dominant tension by reaching the mean ultimate vertical force P_{max}=2V_{max}=229.42 kN (Fig.A1.5a). The corresponding normalized deflection u/D was 1.65%. The shortest beams S2D36a36 with η_a=1.0 (η_l=3.5) failed due to the shear failure combined with the dominant compression. The mean total ultimate vertical force was P_{max}=1330.48 kN (Fig.A1.5c) while the corresponding normalized deflection was 1.83%. The failure was characterized by a high shear strength and relatively low deflection. The shear span parameter η_a=2 in the beam S2D36a72 (η_l=5.5) (Fig.A1.5b) turned out to be a transitional limit value between high beams and low beams where the failure changed its mode. The first beam S2D36a72_1 failed in shear with dominant normal diagonal crack displacements and the second one S2D36a72_2 failed in shear with significant both normal and tangential diagonal crack displacements. Due to a varying failure mode, the ultimate vertical forces and corresponding deflections strongly varied (Fig.A1.5). The beam S2D36a72_1 reached P_{max}=320.17 kN and u/D=1.86% whereas the beam S2D36a72_2:

P_{max}=439.43 kN and u/D=3% . The difference in the ultimate force was 35% while in the deflection was 60%. The force-deflection diagrams were nearly linear up to the peak force and had similar shapes (Fig.A1.5). The post-peak softening was not registered because of the sudden failure.

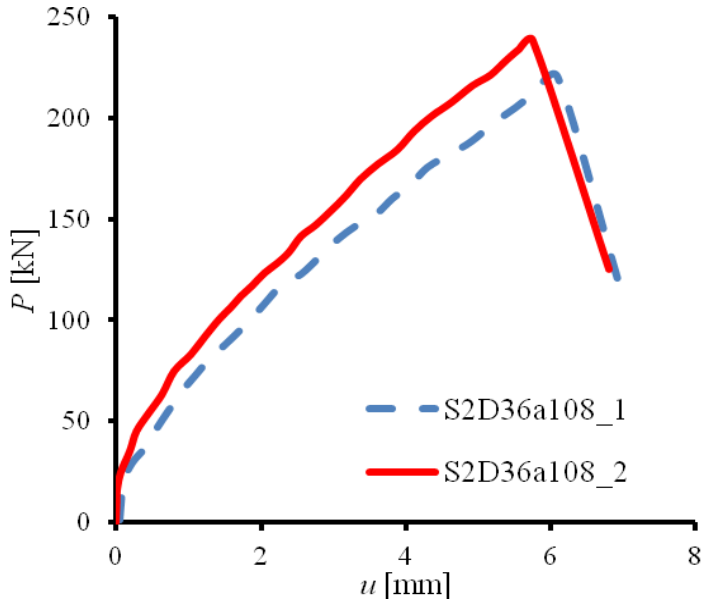

a)

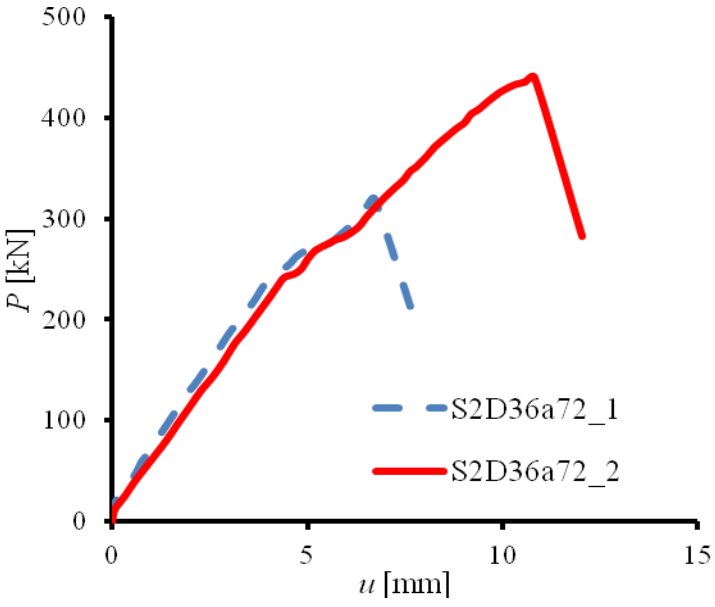

b)

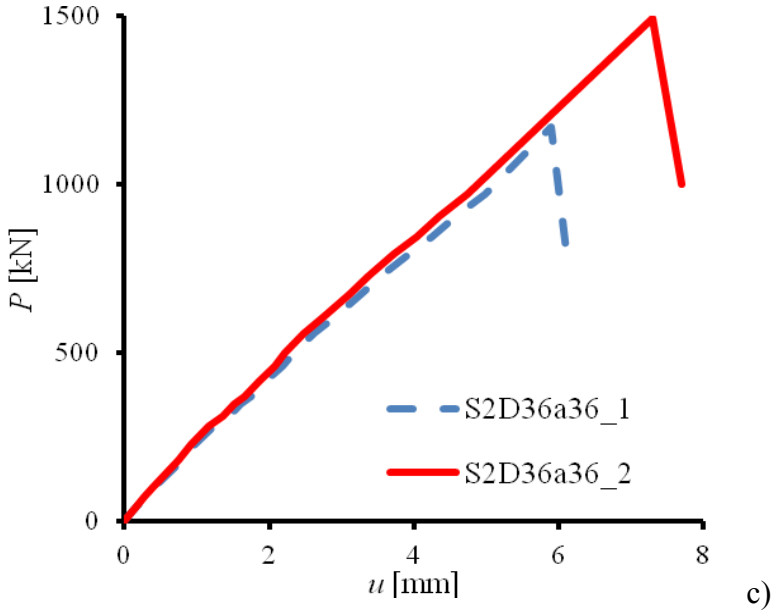

Fig.A1.5: Experimental vertical force - deflection diagrams P=f(u) for RC beams (series '2' with D=360 mm and b=540 mm): a) S2D36a108 (η_a=6), b) S2D36a72 (η_a=3) and c) S2D36a36 (η_a=1) (P=2V)

The effective ultimate shear stress representing beam strength was assumed as its mean cross-sectional value $\tau_c=V_{max}/(tD)$. In the series '1' (l_{eff}=2700 mm, a=1080 mm) its mean value was τ_c=1.34 MPa, τ_c=1.35 MPa and τ_c=2.86 MPa for the beam S1D18a108 (D=180 mm, η_a=6, η_b=3), S1D36a108 (D=360 mm, η_a=3, η_b=1.5) and S1D72a108 (D=720 mm, η_a=1.5, η_b=0.75), respectively (Tab.A1.4, Fig.A1.6). Thus the effective failure stress τ_c increased with increasing depth D due to a different failure mode but decreased with increasing span ratio η_a (Figs.A1.6A-6B). In the series '2' (η_b=1.5, D=360 mm), the measured shear strength $\tau_c=V_{max}/(tD)$ decreased with increasing shear span a and effective length l_{eff} from τ_c=7.39 MPa (η_a=1, η_l=3.5) to τ_c=2.11 MPa (η_a=2, η_l=5.5) and next down to τ_c=1.31 MPa (η_a=3, η_l=7.5) (Tab.A1.4, Figs.A1.6A). Thus with the decrease of η_a from 3 down to 1.5 (η_l=7.5-3.75), the shear strength increased 2.2 times but with the decrease of η_a from 3 down to 1 (η_l=7.5-3.5), the shear strength increased 6 times. Figure A1.5C presents the shear strength evolution for increasing parameter η_a based on own experimental data (Fig.A1.6Ca) and compared with results obtained by Słowik and Smarzewski (2012) (Fig.A1.6Cb) wherein the beams were scaled along their length. Both experimental data show good agreement.

Tab.A1.4: Experimental results providing failure load P_{max} and shear failure stress $\tau_c=V_{max}/(tD)$ for two failure modes with RC beams of series '1' and series '2' (Y – flexural mechanism with reinforcement yielding, T – shear-tension failure in concrete with dominant normal diagonal crack opening displacements, C – shear-compression failure in concrete with combined significant tangential and normal crack displacements, t=0.25 m)

Beam description	**Beam '1'** P_{max} **[kN]**	**Beam '2'** P_{max} **[kN]**	**Beam '3'** P_{max} **[kN]**	**Mean value** P_{max} **[kN]**	$\tau_c=V_{max}/(tD)$ **[MPa]**	**Failure mode***
S1D18a108 η_a=6.0, η_b=3.0, η_c=0.28	104.88	125.52	131.83	120.74	**1.34**	Y
S1D36a108 η_a=3.0, η_b=1.5, η_c=0.14	*	235.70	249.24	242.47	**1.35**	T
S1D72a108 η_a=1.5, η_b=0.75, η_c=0.10	953.86	1075.32	1059.91	1029.70	**2.86**	C
S2D36a36 η_a=1.0, η_b=1.5, η_c=0.14	1170.12	1490.83	-	1330.48	**7.39**	C
S2D36a72 η_a=2.0, η_b=1.5, η_c=0.14	320.17	439.43	-	379.80	**2.11**	C/T
S2D36a108 η_a=3.0, η_b=1.5, η_c=0.14	220.32	238.51	-	229.42	**1.31**	T

*result's lack due to measuring system failure

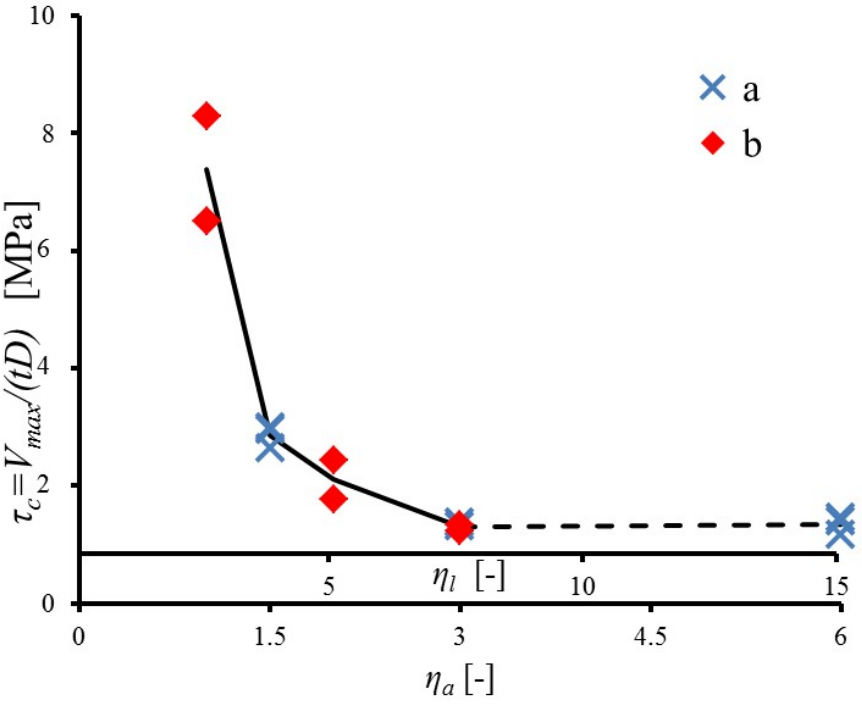

A)

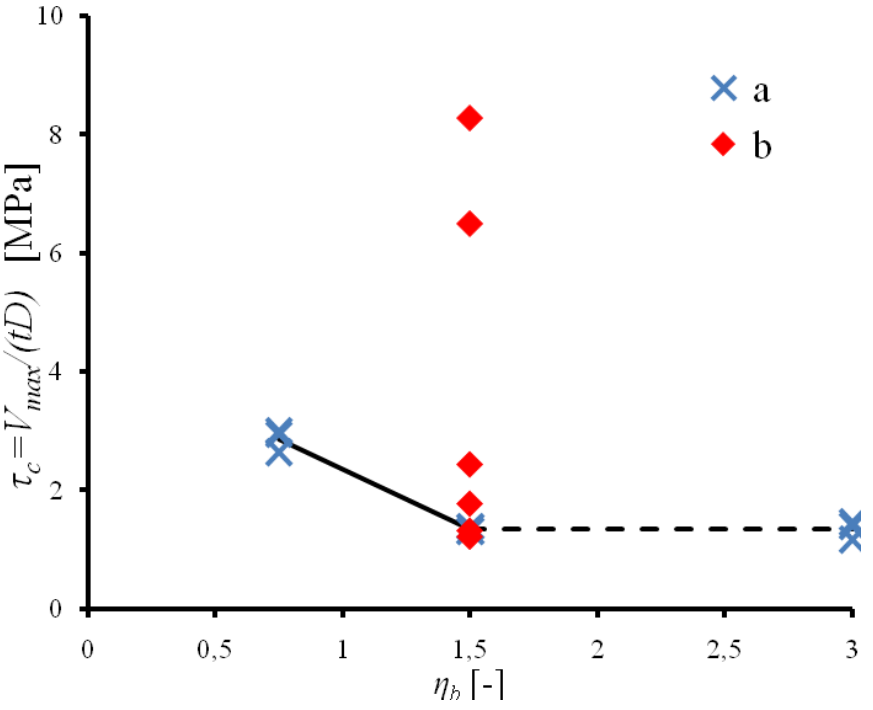

B)

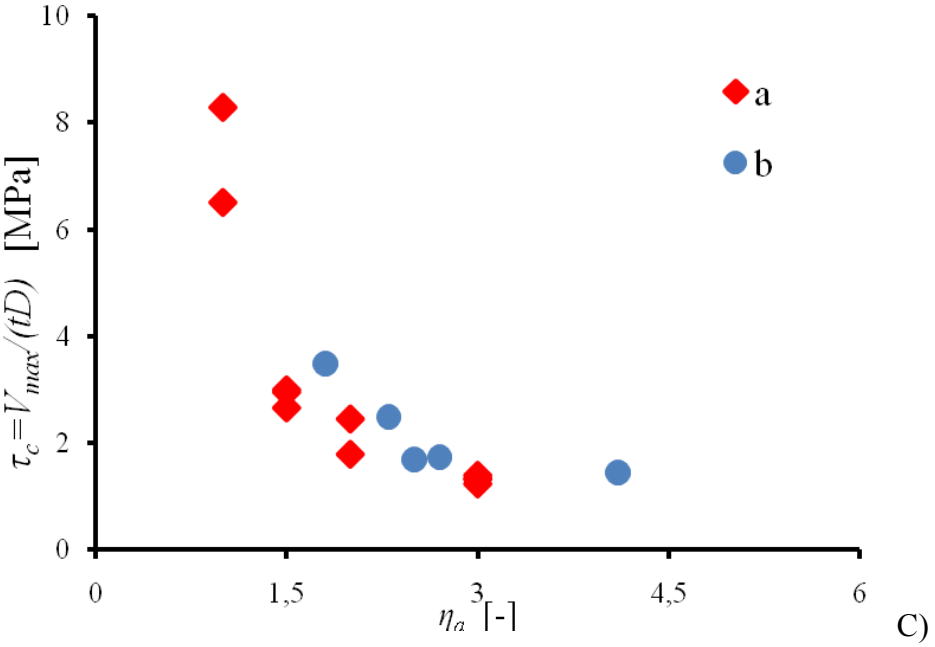

Fig.A1.6: Experimental results presenting evolution of shear strength: A) for varying length parameter $\eta_l = l/D$ and shear span parameter $\eta_a = a/D$, B) for varying bending span parameter $\eta_b = b/D$ (a) series '1' with varying effective depth D and bending span b at constant shear span a and b) series '2' for varying η_a with constant effective depth D and bending span b) and C) as compared with experiments by Slowik and Smarzewski (2012) for different η_a (a) our experiments and b) experiments by Słowik and Smarzewski (2012) (note that beams for η_a=6 failed in flexural mechanism).

A1.5 Failure mechanisms and crack patterns

Figure A1.7 presents the typical evolution of cracks for 3 different failure modes with increasing load. The failure modes were determined based on DEMEC measurements (see section A1.8). The crack evolution was similar for all the specimens up to 50% of the ultimate load value. First, the vertical flexural cracks appeared in the beam mid-span region (8-12% of the failure force) wherein the bending moment was constant. Later inclined cracks formed in the shear zone due to shear stress action close to both supports. A further evolution of the crack pattern was different: the low beams (η_a=6, η_l=15) failed in bending by reinforcement yielding (Fig.A1.7A) and the high beams ($\eta_l \leq$7.5) failed in brittle diagonal shear (Figs.A1.7B and A1.7C). The shape and location of the critical diagonal crack from the nearest support depended upon the failure type.

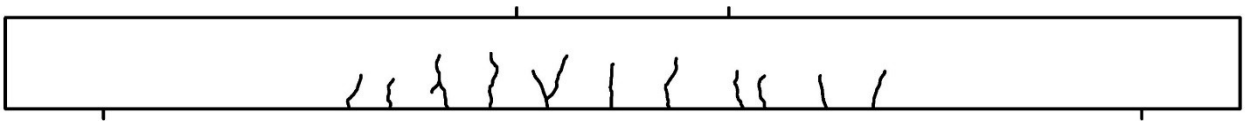

a)

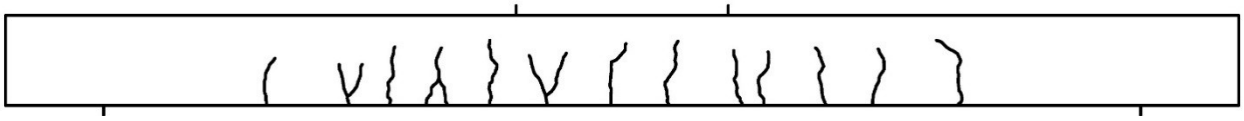

b)

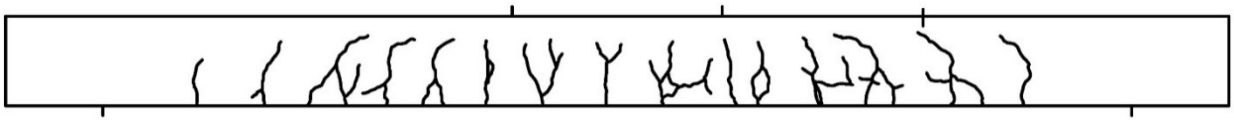

c)

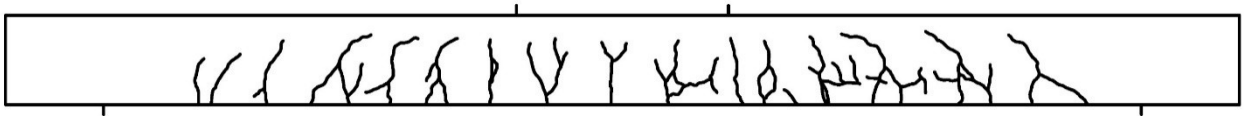

d)

A)

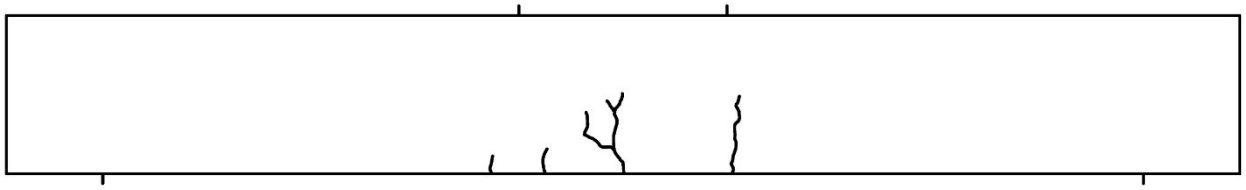

a)

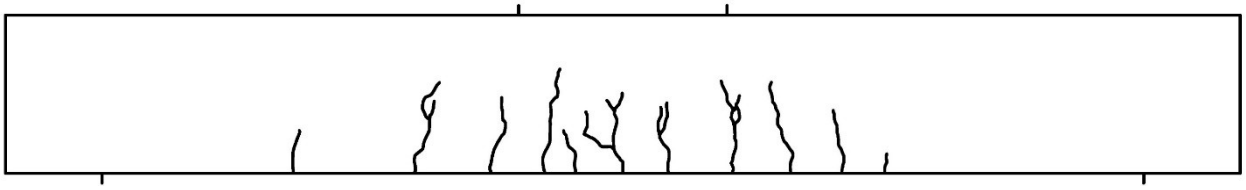

b)

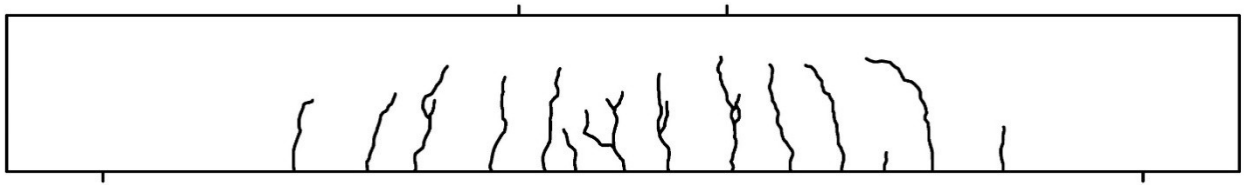

c)

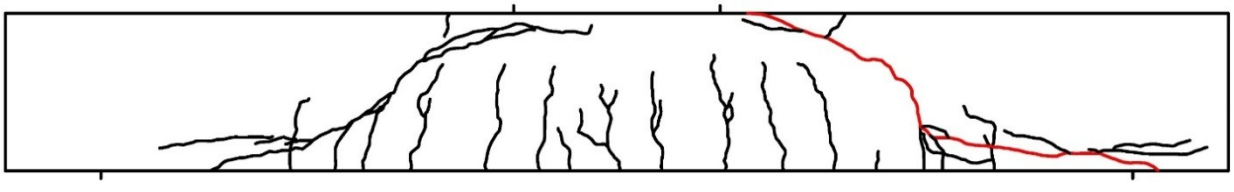

d)

B)

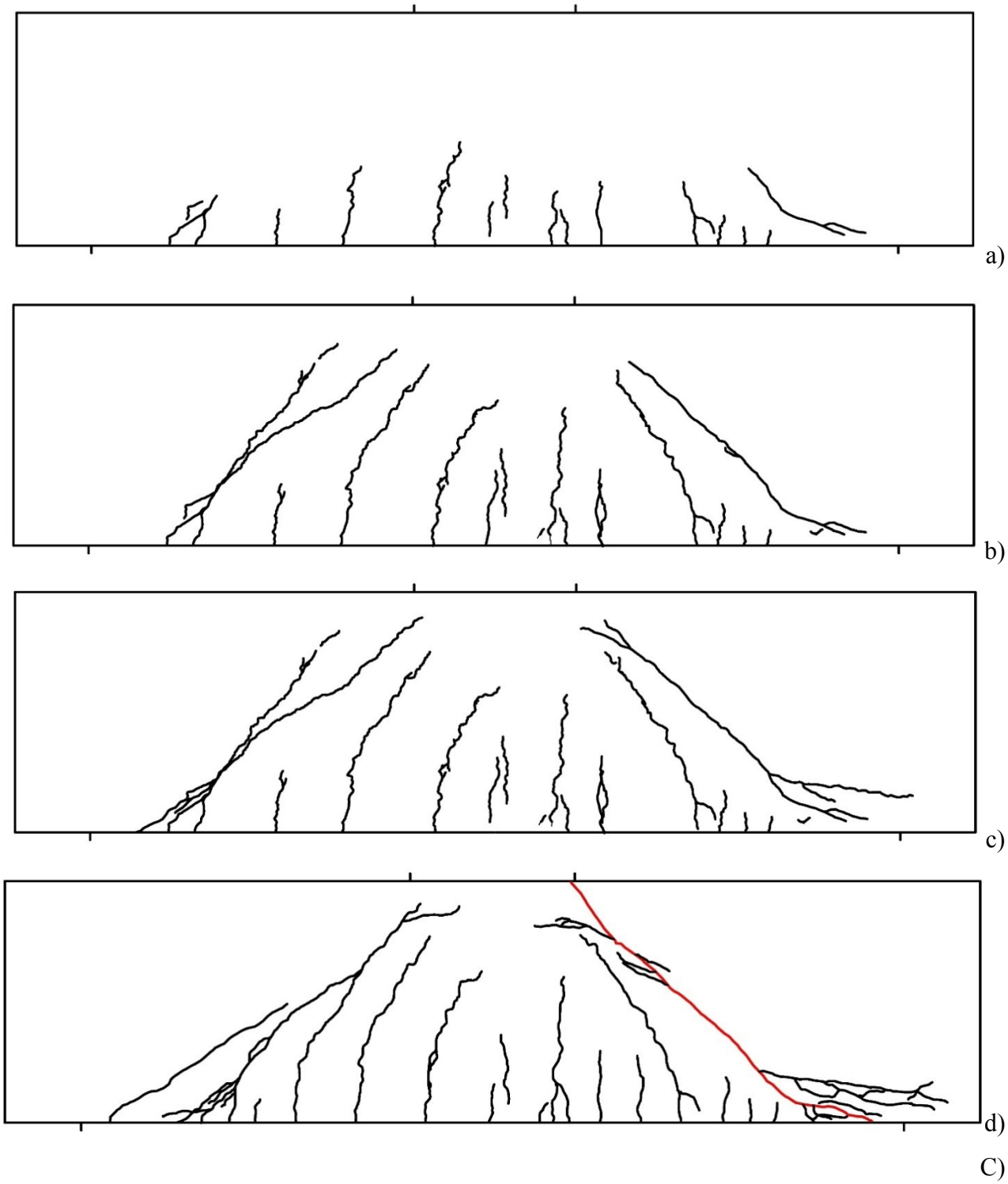

Fig.A1.7: Typical crack pattern evolution for different failure modes in RC beams: A) beam mechanism with reinforcement yielding (S1D18a108, η_a=6), B) shear failure in concrete with dominant normal diagonal crack displacement (S1D36a108, η_a=3) and C) shear failure in concrete with dominant tangential diagonal crack displacement (S1D72a108, η_a=1.5) for increasing vertical force P (a) 25%, b) 50%, c) 70% and d) 100% of failure force P_{max})

Figure A1.8 presents the final crack pattern (at the failure) for RC beams with the different ratio $\eta_a=a/D$. In the beam S1D18a108 (a/D=6) (Fig.A1.8a), the vertical cracks stabilized after reaching 12% of the beam height for 80% of the peak force P_{max}. Next the crack width in the bending span domain b continuously increased. The critical diagonal crack for low beams (η_a=3, Fig.A1.8b) initiated near the mid-point of the shear span a and after reaching the ⅓ of the beam height turned to the direction of the vertical force point with the angle between 16.8° and 19.4°, whereas in the bottom part, where the crack propagated through reinforcement, the angle varied between 42.2° and 43.6°. The distance between the critical diagonal crack and beam support d_c related to the shear span a varied between d_c/a=0.5 (η_a=3) for low beams up to as d_c/a=0 for high beams (η_a=1). The dominant inclined crack propagated towards a beam compression zone and support, reaching at the failure first the beam top and next the beam bottom. The formation of a critical diagonal crack for high beams (η_a=1 and η_a=1.5) (Figs.A1.8c and A1.8f) was sudden. Shortly after the appearance, the critical diagonal crack stabilized at the 65% of the beam height. The further growth towards a compression zone was very slow and stable. Just before the failure a new diagonal crack appeared in concrete by connecting the support and vertical force point. The crack evolution for the beam S2D36a72_1 (Fig.A1.8d) was similar to the one for low beams with the ratio a/D=3 (Fig.A1.8b) while the second beam S2D36a72_2 (Fig.A1.8e) had a crack pattern typical for high beams. For η_a=2-3 the critical diagonal cracks (Figs.A1.8b and A1.8e) were strongly curved to the horizontal in the compressive region opposite to the cases with η_a<2 where they were almost straight (Figs.A1.8c and A1.8f). In general, the crack geometries were approximately in agreement with the direction of compressive principal stresses.

Crack inclination and heights

The mean failure diagonal crack inclination to the horizontal changed from 30° up to 42° for η_a=1-3 (Fig.A1.9).The critical diagonal crack ($\eta_a\leq$3) was significantly steeper for the smaller ratio of η_a and η_l (Fig.A1.10). The average number of main cracks decreased with decreasing shear span ratio a/D and changed from 4 cracks in the beam S1D18a108 up to 8 for the beam S1D72a108. The crack spacing increased from 14 cm (beams S1D18a108 and S1D36a108) up to 20 cm for the highest beam S1A108D72. In the beam series '2' it was constant - 12.5 cm. The crack width w was the largest for the beam S1D18a108 due to steel yielding (w=0.35 mm) and the smallest for the highest beam S1D72a108 (w=0.20 mm).

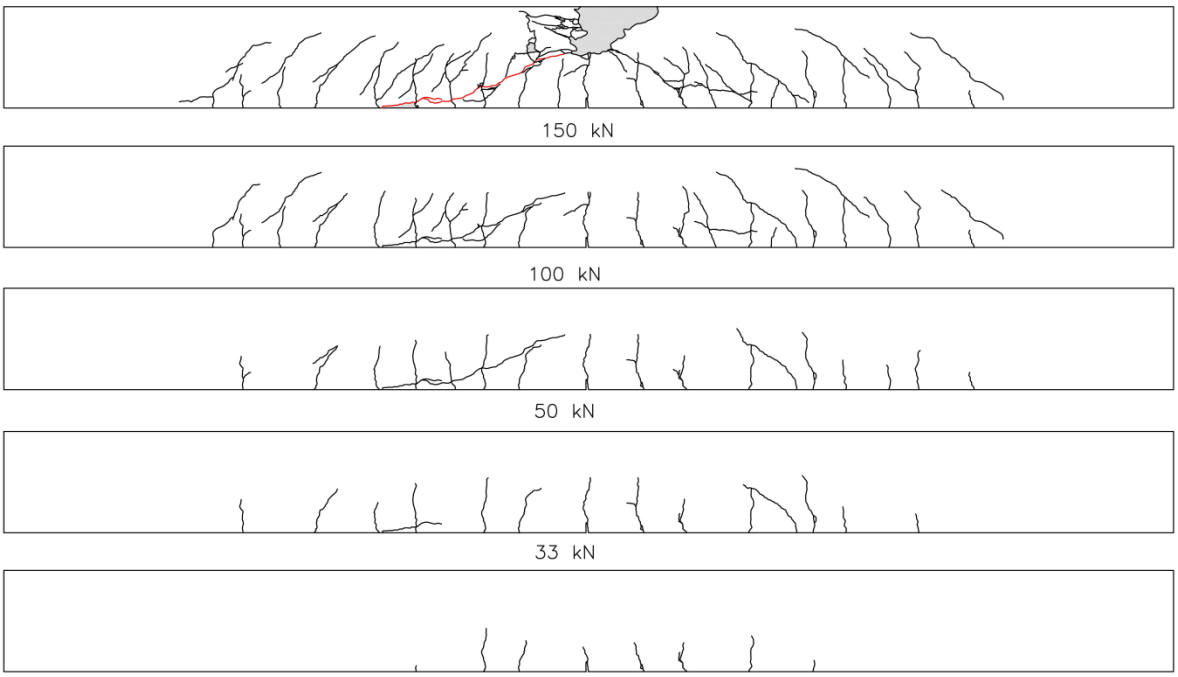

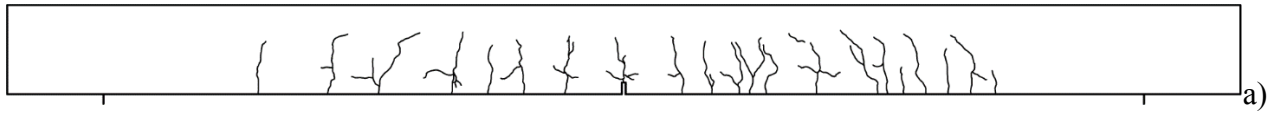
a)

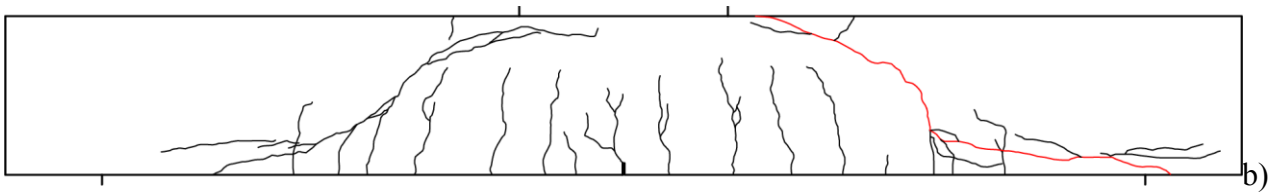
b)

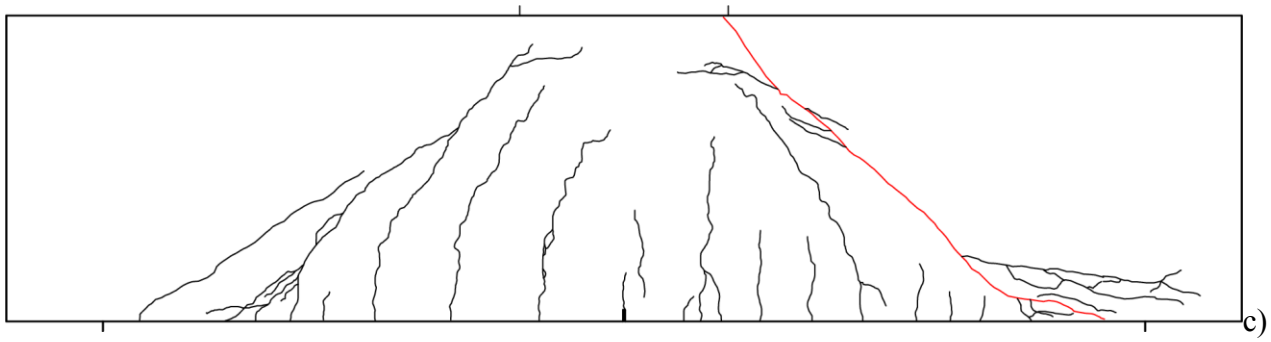
c)

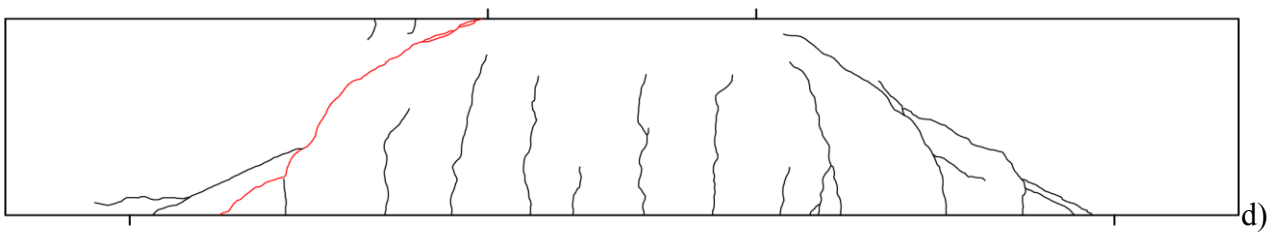
d)

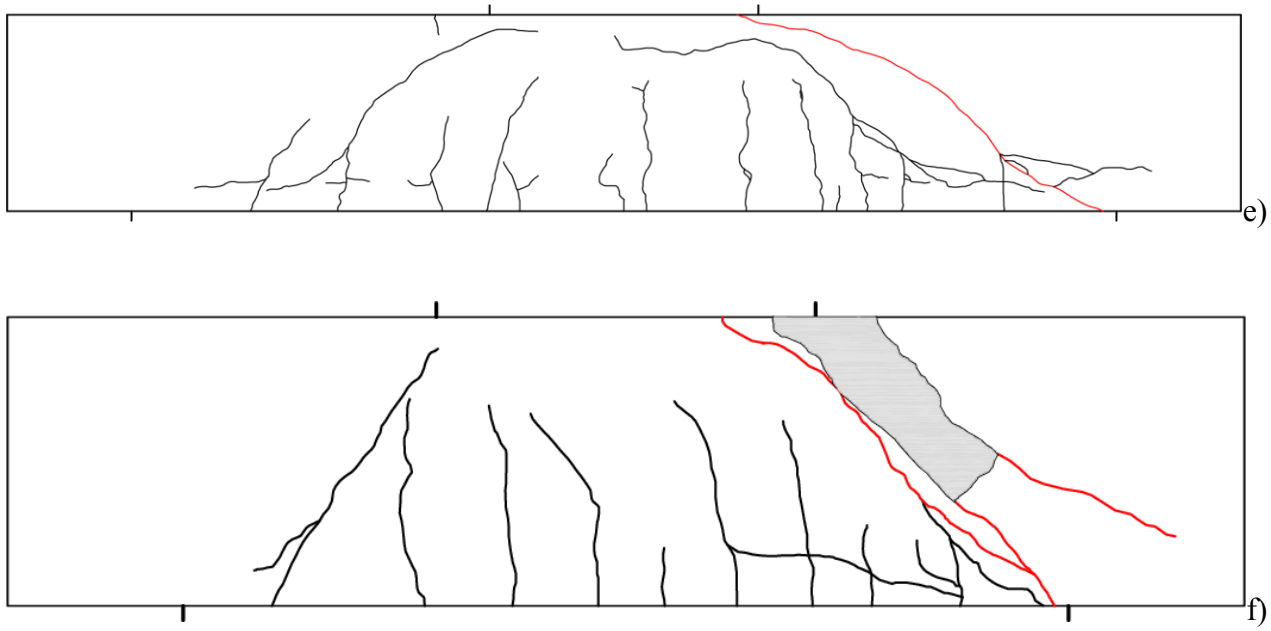

Fig.A1.8: Crack pattern at failure typical for each beam geometry depending upon ratio *a/D* for different failure mode: a) reinforcement yielding (S1D18a108, η_a=6), b) shear failure in concrete with dominant normal diagonal crack displacement (S1D36a108, η_a=3), c) shear failure in concrete with dominant tangential diagonal crack displacement (S1D72a108, η_a=1.5), d) shear failure in concrete with dominant normal diagonal crack displacement (S2D36a72_1, η_a=2), e) shear failure in concrete with dominant tangential diagonal crack displacement (S2D36a72_2, η_a=2) and f) shear failure in concrete with dominant tangential diagonal crack displacement (S2D36a36, η_a=1) (critical diagonal crack is marked in red, beams are not proportionally scaled).

The DIC method was applied to visualize localized zones based on displacements which precede macro-cracks. Digital Image Correlation (DIC) technique. DIC is a well-known velocity measuring non-invasive procedure, originally developed for fluid mechanics and used for the analysis of displacements in tests on soil and rock models (Bhandari&Inoue 2005, Rechenmacher&Finno 2004, Słonimski et al. 2007, White et al. 2003, Skarżyński&Tejchman 2013, Skarżyński et al. 2013, Skarżyński et al. 2011). It operates by tracking spatial variations of brightness within an image (divided into a mesh of patches) by comparing successive images so that displacement data can be extracted from sequences of images, and strains then calculated from gradients of measured displacements. The capability of DIC for measuring the shape and width of fracture process zones in concrete was confirmed in the experimental research results (Skarżyński&Tejchman 2013,

Skarżyński et al. 2013, Skarżyński et al. 2011). The surface on the opposite side of the beam was observed with a digital microscope DG-3x.

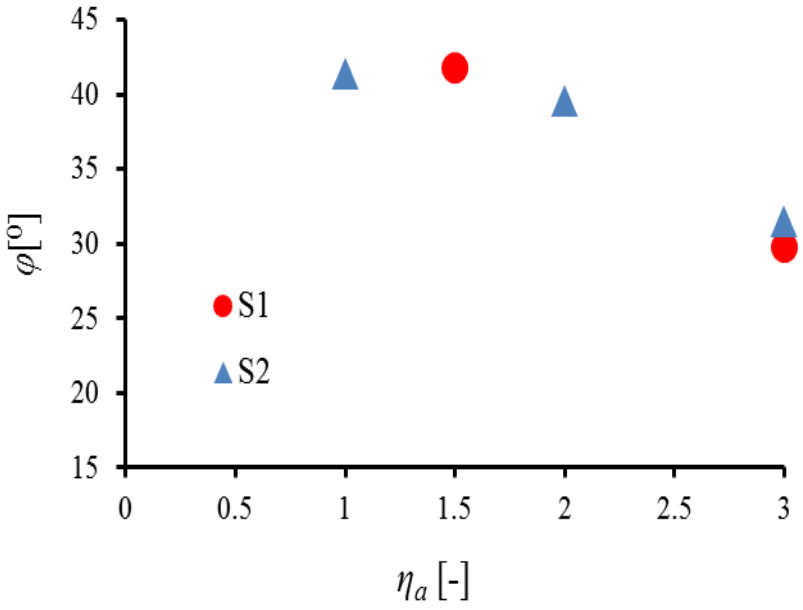

Fig.A1.9: Diagonal failure crack inclination to horizontal φ in RC beams for experiment series '1' (S1, triangular markers) and '2' (S2, diamond markers) versus ratio $\eta_a=a/D$=1-3 *(a* - shear domain span, *D* - effective height)

Figure A1.11 shows the evolution of a vertical (flexural) localized zone with increasing vertical force for the beam S1D18a108_2 (3 cm above the beam bottom) which failed in bending (η_l=15, η_a=6). The localized zone appeared at around 2% of the failure force. Later, at 3.75% of the failure load, two localized zones could be observed. Next both the zones were connected and created a branching (at 5% of the failure force). The right localized zone reached the top border of the image frame for 11.3% of the failure force.

For P=15 kN (12.5% of P_{max}) the macro-crack appeared along the left localized zone (Fig.A1.2). The width of the flexural localized zone was 2.4 mm (based on DIC).

The evolution of the horizontal normal strain ε_{xx} for the high beam S2D36a36 (η_l=3.5, η_a=1) which failed in shear is demonstrated in Fig.A1.13 again in the bending region **(**10 mm above the beam bottom**)**. First, the localized zone was noticed at the 5% of the failure force reaching 75% of the DIC frame height. For the 6.5% of failure force, the localized zone was visible over the entire

height of the frame. The maximum horizontal strain increased linearly with the vertical force growth. The maximum horizontals strains for the 17% (Fig.A1.13c) of the failure force were 2 times higher than at 3% (Fig.A1.13d) of the failure force. Figure A1.13g shows the evolution of cumulative horizontal displacement in the image area for different force levels. A jump in the distribution of horizontal displacement increments indicated the crack presence. This width of the flexural localized zone was again 2.4 mm (based on DIC).

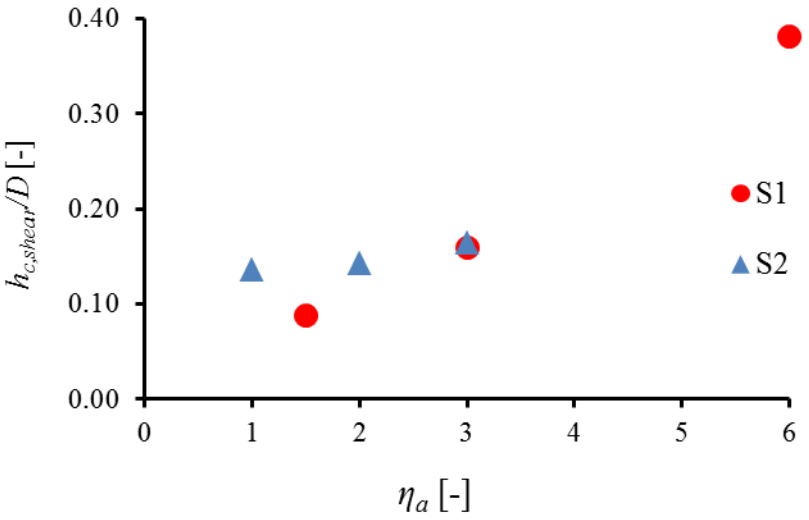

a)

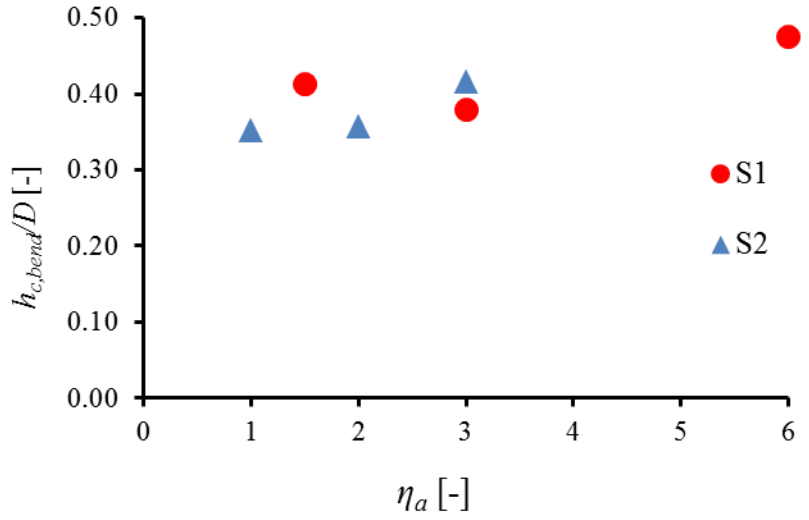

b)

Fig.A1.10: Experimental normalized mean height of compressive zone h_c/h in RC beams for series '1' (S1; marked with dots) and '2' (S2, marked with triangles) in shear zone (a) and bending zone (b) versus $\eta_a=a/D$ (a - shear span, D - effective height)

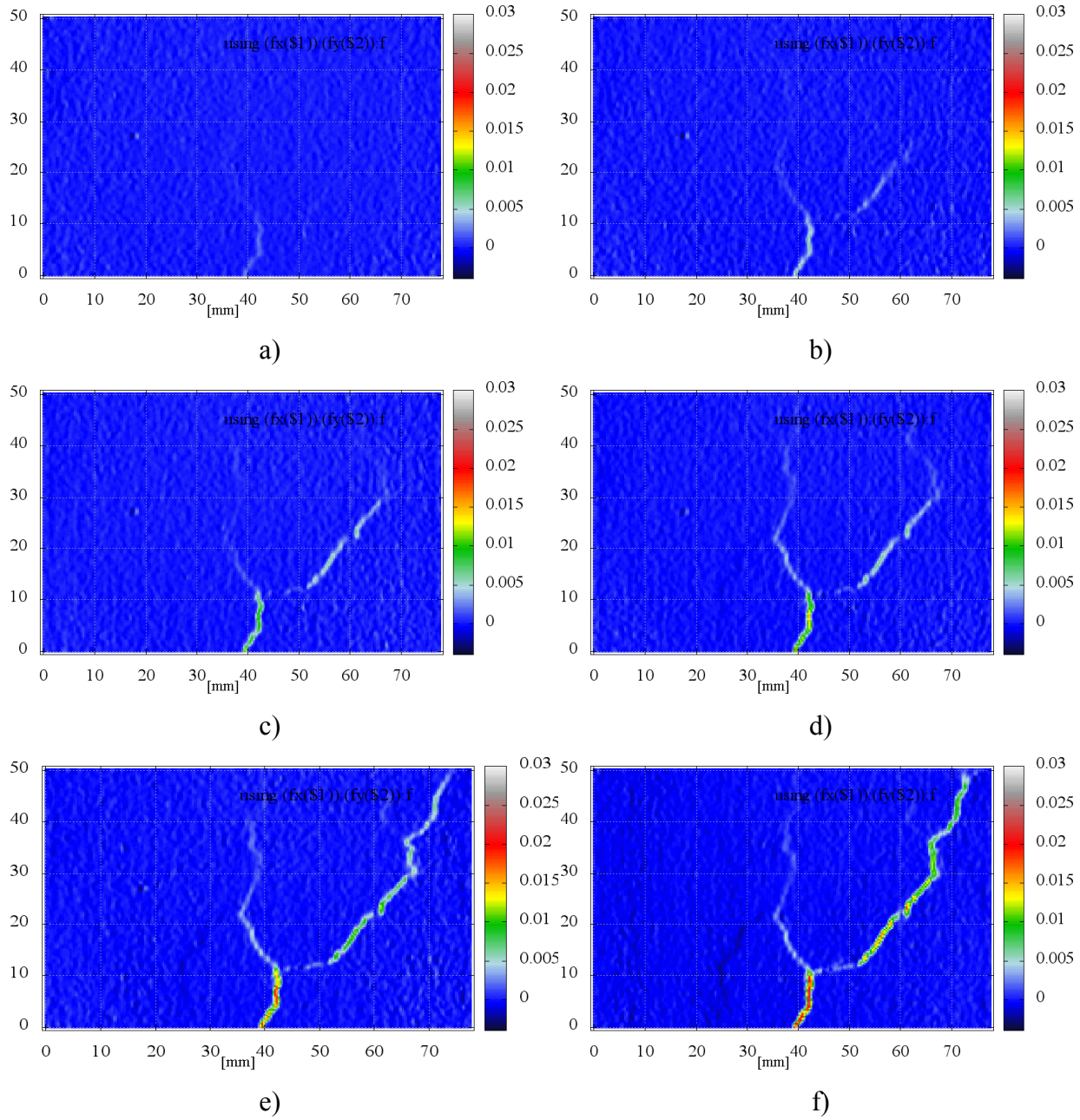

Fig.A1.11: Horizontal normal strain maps ε_{xx} for beam S1D18a108_2 failed in bending ($\eta_a=a/D=6$) (vertical and horizontal axes denote coordinates in [mm] and colour scale strain intensity) for increasing vertical force P: a) 2%, b) 3.75%, c) 5%, d) 6.5%, e) 8.2%, f) 11.3% of failure force P_{max} (strains are shown for mid-span, 3 cm above beam bottom)

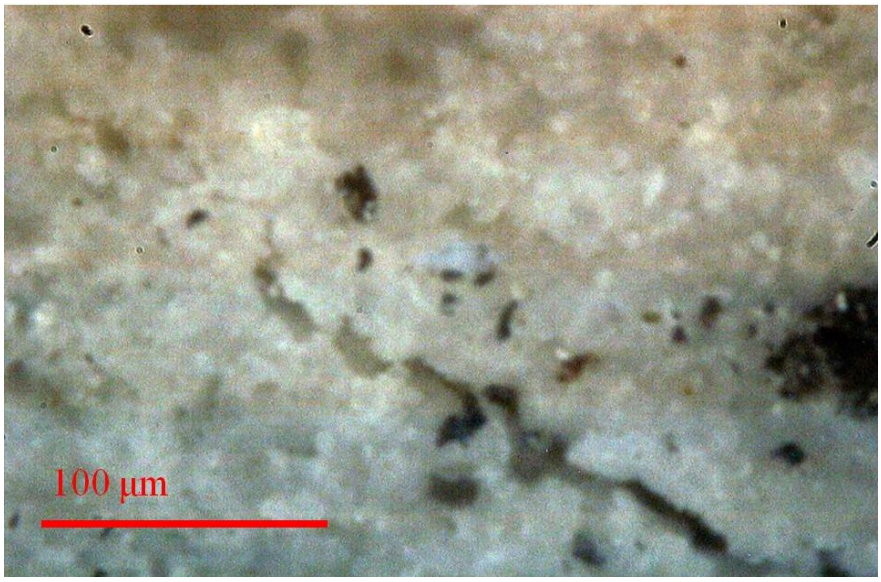

Fig.A1.12: Macro-crack on beam surface S1D18a108-2, image taken by microscope DG-3X with magnification 1000× for 15 kN at same height as DIC image of Fig.A1.11 (crack width w_c≈0.009 mm)

The DEMEC triangle measurements enabled us to accurately determine the crack normal (opening) and crack tangential (shear) displacement (Eqs.A1.3 and A1.4, Section A1.3). Figure A1.14 shows the location of triangles in DEMEC measurements for RC beams. Figures A1.15 and A1.16 present the crack displacement evolutions for each beam size for two locations: bottom (reinforcement) and top (shear-compression zone). All measured crack displacements in 4 beams S1D36a108 (a/D=3), S1D72a108 (a/D=1.5), S2D36a72 (a/D=2) and S2D36a36 (a/D=1) are shown in Fig.A1.16. The measurement accuracy of crack displacements was 0.001 mm.

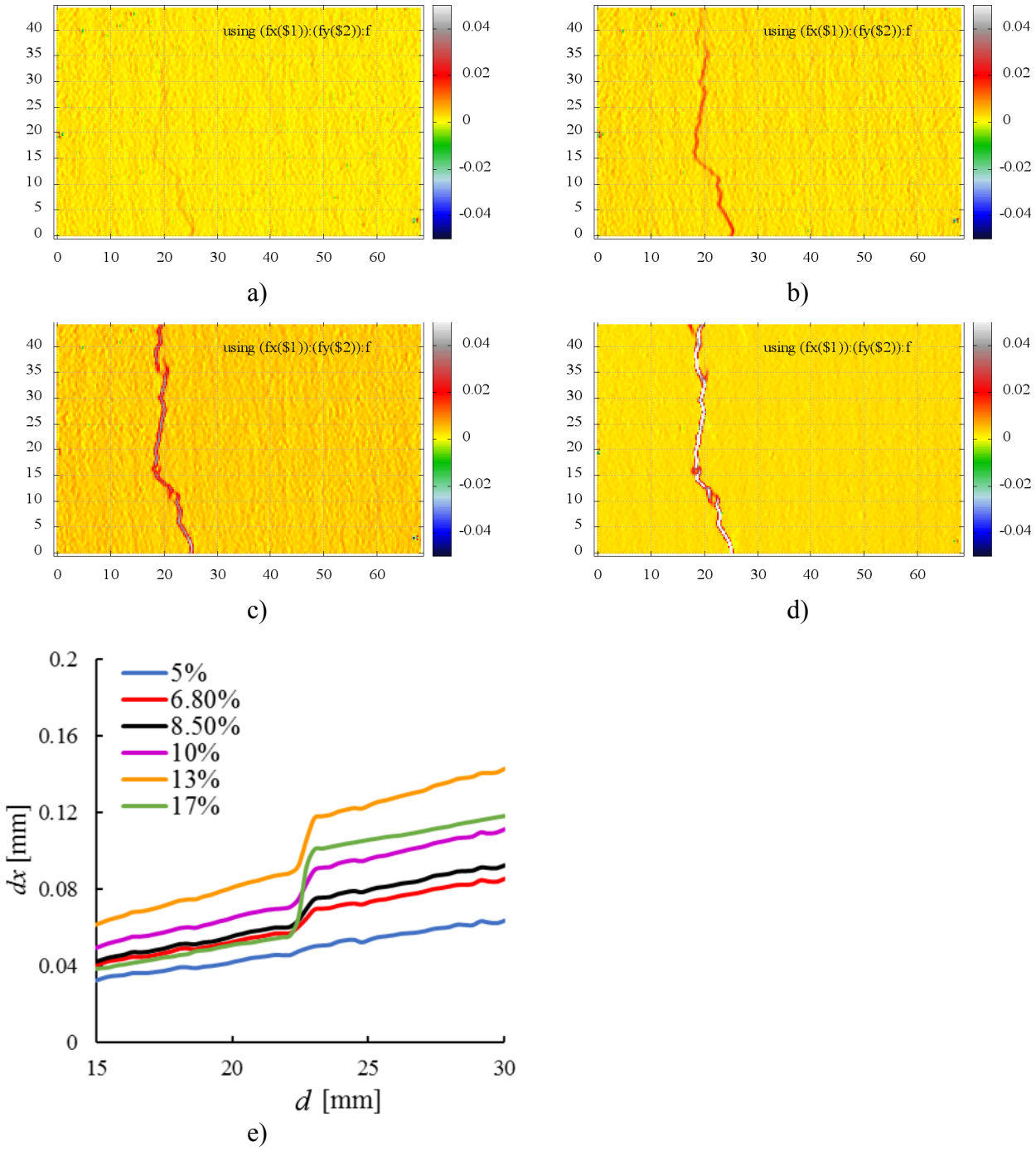

Fig.A1.13: Horizontal normal strain maps ε_{xx} for beam S2D36a36_1 (η_a=1) for increasing vertical force: a) 5%, b) 6.8%, c) 13%, d) 17% of failure force P_{max} (strains are shown in mid-span - 10 cm above beam bottom), e) evolution of cumulative horizontal displacement *dx* along image frame width *d* for different force levels - 10 mm above beam bottom (vertical and horizontal axes denote coordinates in [mm] and colour scale strain intensity)

a)

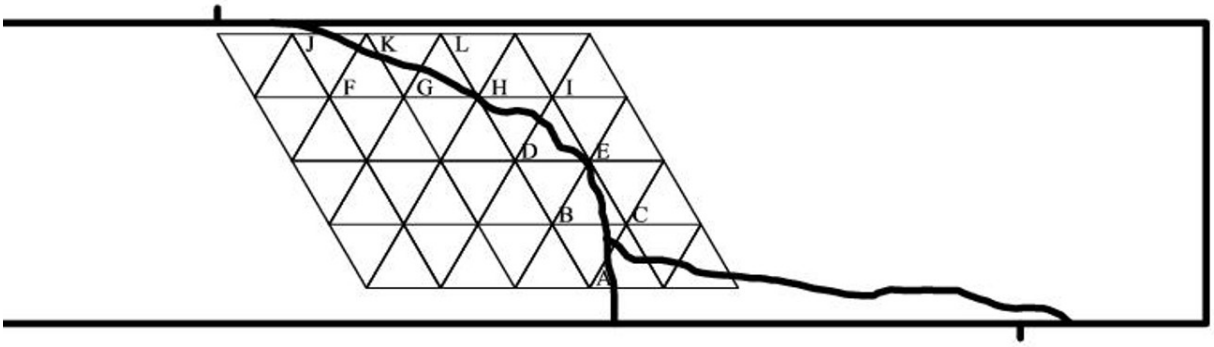

b)

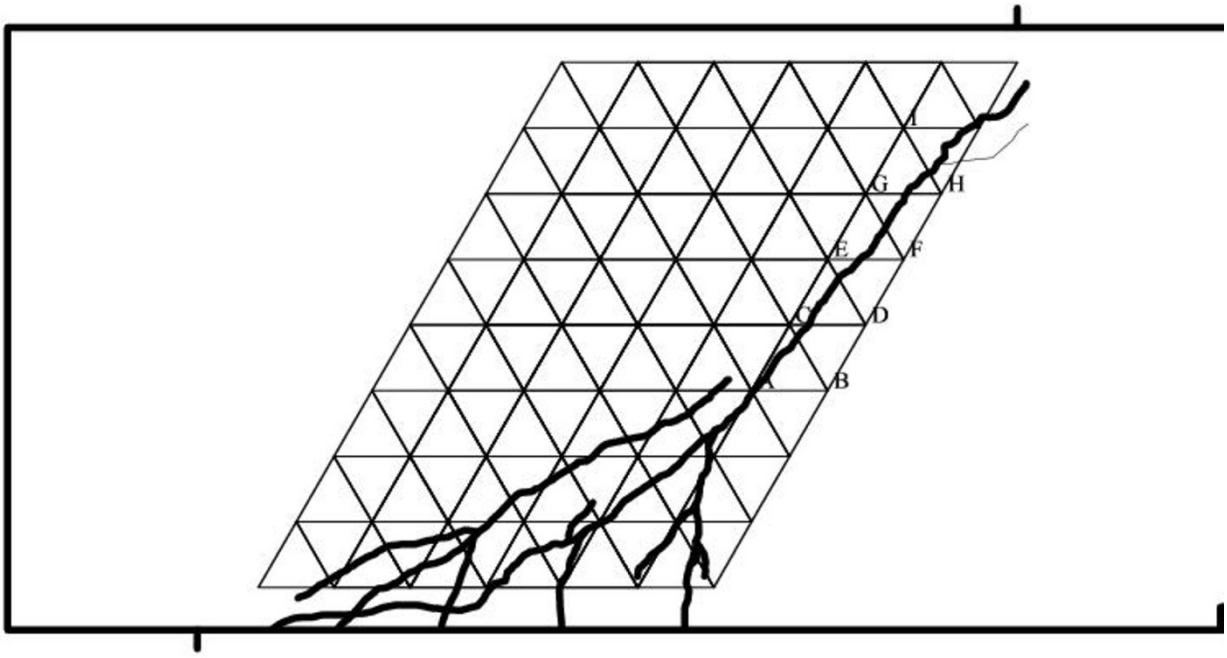

c)

A)

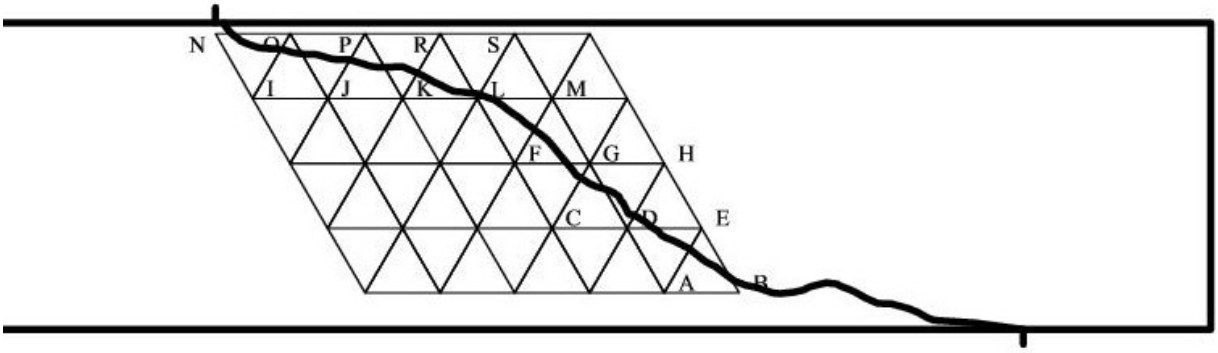

a)

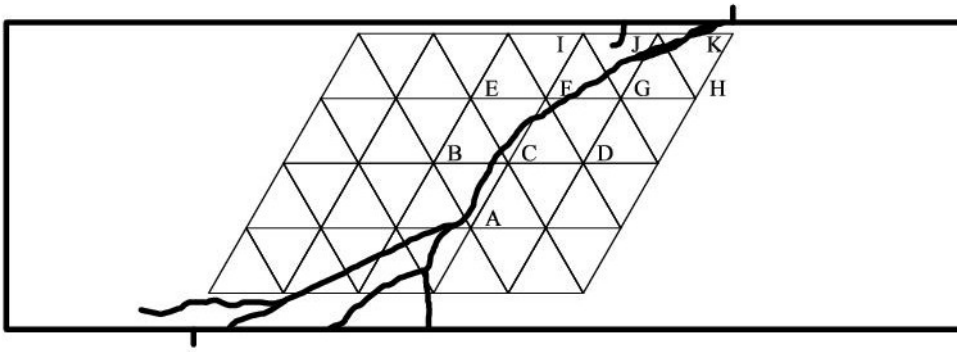

b)

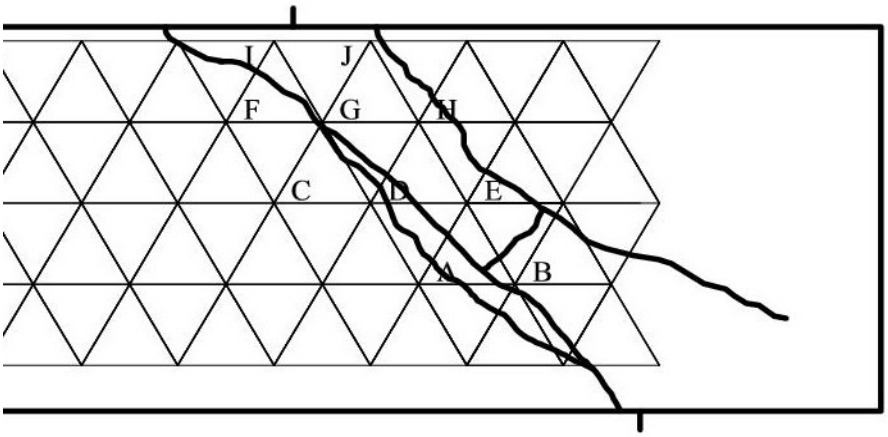

c)

B)

Fig.A1.14: Location of triangles for DEMEC measurements in RC beams: A) series '1': a) S1D18a108 (D=180 mm, η_a=6), b) S1D36a108 (D=360 mm, η_a=3), c) S1D72a108 (D=720 mm, η_a=1.5) and B) series '2': a) S2D36a108 (a=1080 mm, η_a=3) b) S2D36a72 (a=720 mm, a/D=2), c) S2D36a36 (a=360 mm, η_a=1) (main cracks are marked by thick solid lines)

In the beam S1D18a108 (D=180 mm, η_a=6, mean P_{max}=120 kN) which failed in bending by reinforcement yielding (Fig.A1.15Aa), an insignificant tangential crack displacement was observed (δ<0.02 mm) whereas the normal crack opening constantly grew with increasing vertical force P (from P=35 kN) up to ω=0.14 mm (bottom) and ω=0.12 mm (top) (Fg.1.15A).

In the beam S1D36a108 (D=360 mm, η_a=3, mean P_{max}=242 kN) which failed in shear (Fig. A1.15Ab), a slightly larger tangential diagonal crack displacement was observed at the bottom (δ=0.04 mm) (Fig.1.15Ba). This tangential crack displacement occurred as a straight flexural crack changed into an inclined shear crack (P=150 kN). The maximum normal crack displacement was significantly larger (ω=0.27 mm). At the beam top region, a small tangential crack displacement continuously increased from the test initiation up to δ=0.003 mm (Fig.A1.15Bb). The small normal crack displacement, ω=0.017 mm, was negative in this zone due to compression (the crack reached the triangle location just before failure). Summing up the tangential crack displacement was insignificant along the entire diagonal shear crack.

In the beam S1D72A108 (D=720 mm, η_a=1.5, mean P_{max}=1029 kN) which also failed in shear (Fig.A1.15Ac), the failure diagonal crack development was initiated later (P=400 kN) with a proportional normal ω and tangential displacement δ at the beam bottom (Fig.1.15Ca). The maximum crack displacements were: δ=0.10 mm and ω=0.30 mm. At the beam top region, the failure crack was preceded by a tangential crack displacement up to δ=0.1 mm without a normal crack displacement (Fig.A1.15Cb). The normal crack displacement appeared when the diagonal failure crack was created. The maximum crack displacements were: δ=0.58 mm and ω=0.25 mm. Thus the tangential crack displacement was higher than the normal one along the diagonal shear crack in the compressive beam region.

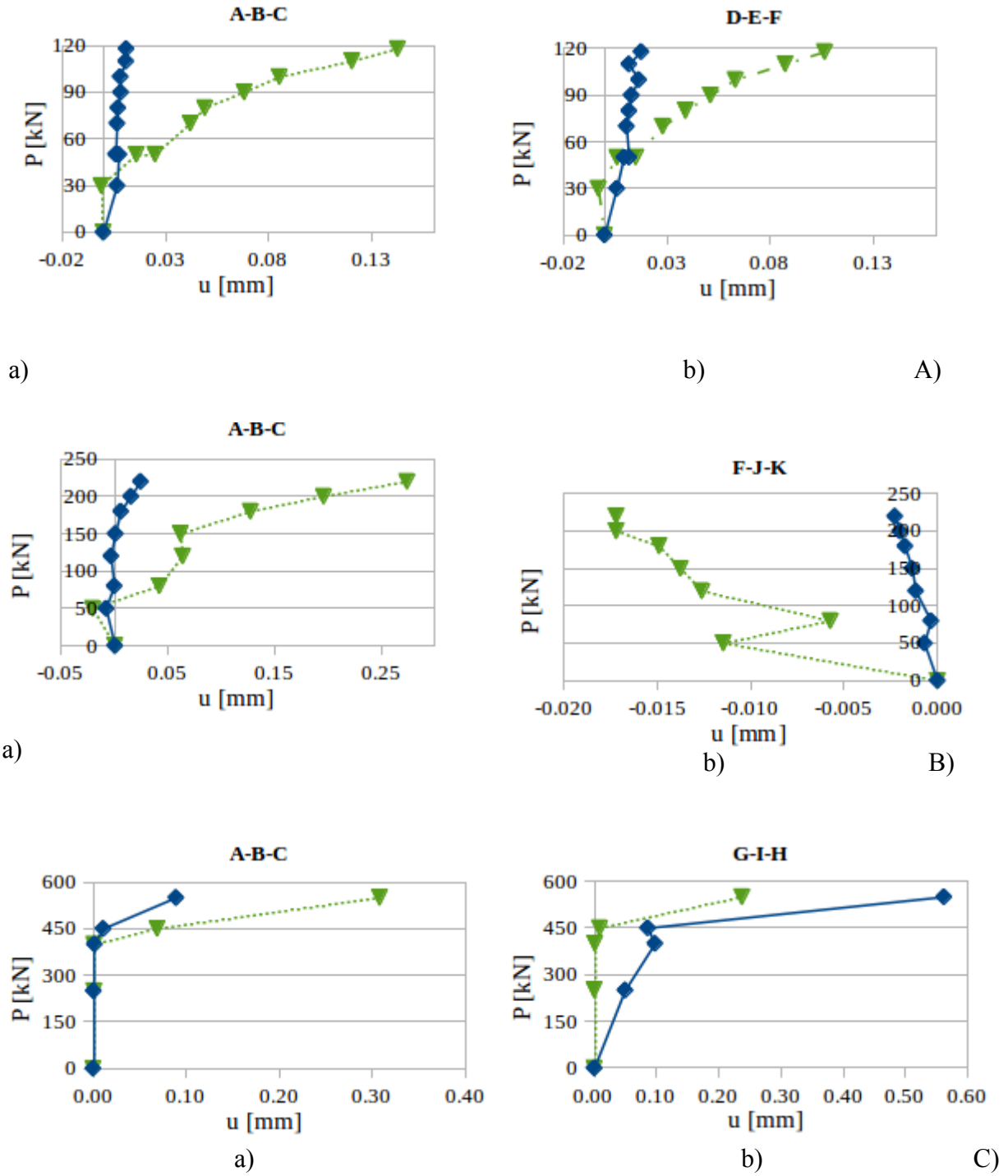

Fig.A1.15: Experimental force – normal and tangential crack displacements in RC beams (series '1'): A) S1D18a108 (D=180 mm, η_a=6) (Fig.A1.14Aa), B) S1D36a108 (D=360 mm, η_a=3) (Fig.A1.14Ab) and C) S1D72a108 (D=720 mm, η_a=1.5) (Fig.A1.14Ac) for: a) bottom triangle in reinforcement anchorage zone and b) in compression-shear zone (continuous blue lines denote tangential displacement δ and dashed green lines denote normal displacement ω, sections are shown in Fig.A1.14)

The beam S2D36a108 (D=360 mm, η_a=3, mean P_{max}=229 kN, Fig.A1.16Ba) exhibited the same behaviour as the beam from the series '1' (S1D36a108, a/D=3) with a clear normal diagonal crack displacement at the bottom (ω=0.11 mm) and a small tangential crack displacement along the entire crack (δ=0.02 mm) (Fig.1.16A).

In the beam S2D36A72 (D=360 mm, η_a=2, mean P_{max}=379 kN, Fig.A1.16Bb), the normal crack displacement again strongly dominated (Fig.A1.16B). At the bottom, the normal crack first opened (ω=0.16 mm) due to bending and later closed (down to ω=0.05 mm) when the diagonal shear crack crossed the reinforcement (Fig.A1.16Ba). In the beam top region, a negative (compressive) normal crack displacement increased with the force P up to P=250 kN (ω=-0.04 mm)). Later when the crack crossed the triangle, this normal crack displacement changed into a significant positive (tensile) one (ω=0.20 mm) (Fig.A1.16Bb). The maximum tangential crack displacement was insignificant there δ=0.02 mm.

The behaviour of the diagonal shear crack in the most slender beam S2D36a36 (D=360 mm, η_a=1, mean P_{max}=1330 kN, Fig.A1.16Bc) was similar as this in the beam S1D72a108 (η_a=1.5) (Fig.A1.16C). At the bottom the normal and tangential diagonal crack displacements increased from the test beginning (Fig.A1.16Ca). The maximum crack displacements were: δ=0.15 mm and ω=0.38 mm. At the beam top region, they also immediately increased (Fig.A1.16Cb). The maximum crack displacements were there: δ=0.08 mm and ω=0.10 mm.

Summing up, the limit load P_l in experiments depended on two non-dimensional geometric parameters $\eta_a=a/D$ and $\eta_b=b/D$ and the scale parameter D, thus $P_l = P_l(\eta_a, \eta_b, D)$. The length parameter $\eta_l = l_{eff} / D = 2\eta_a + \eta_b$ was affected then by η_a and η_b. Depending upon $\eta_a=a/D$, two failure mechanisms occurred, namely the flexural mechanism in the central beam zone and the shear mechanism developed through a combined shear-tension or shear-compression mode in exterior beam zones. Two shear failure modes were distinguished depending on the dominance of tension or compression acting on the progressive shear crack interface.

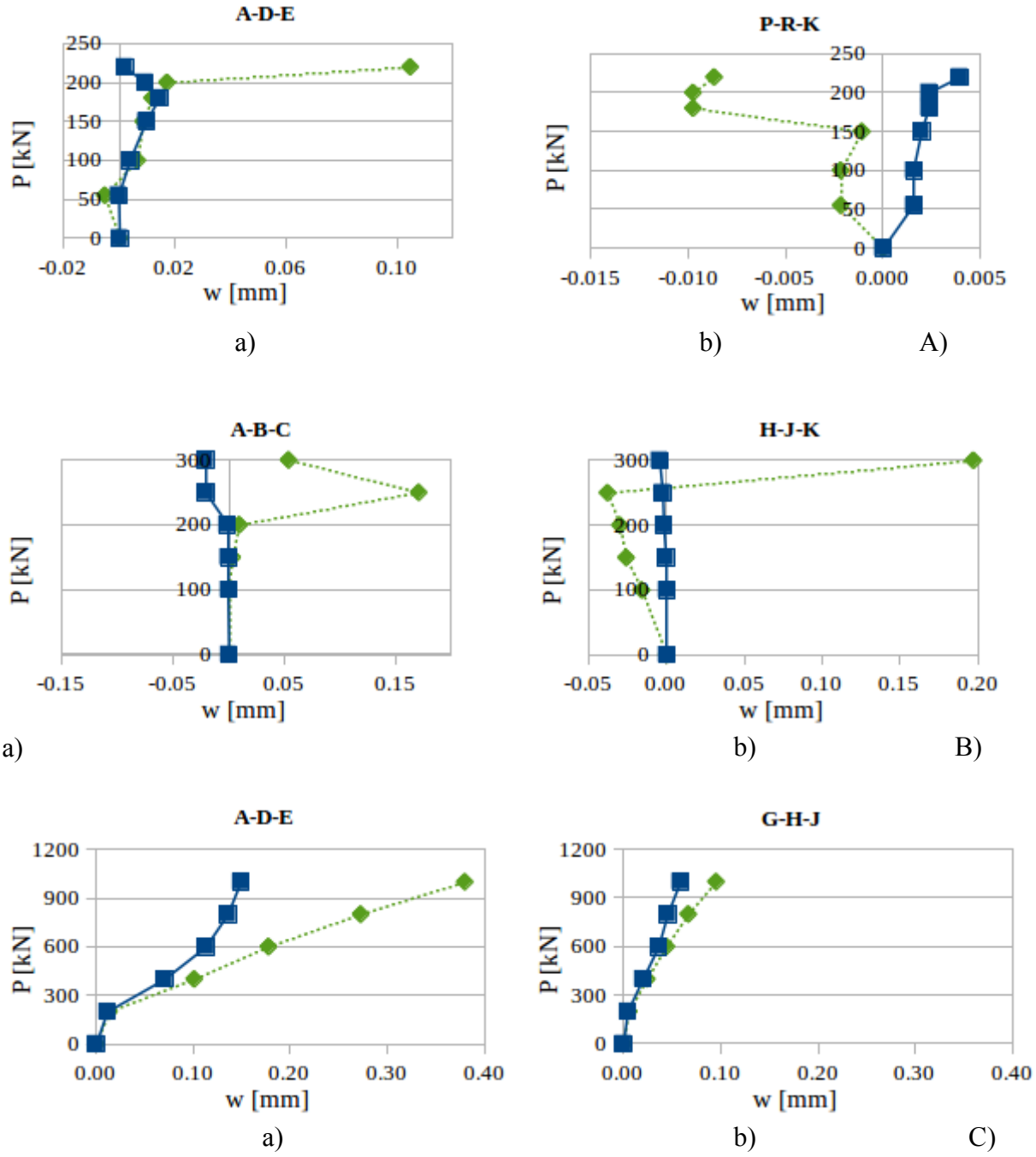

Fig.A1.16: Experimental force – normal and tangential crack displacements in RC beams (series '2'): A) S2D36a108 (a=1080 mm, η_a=3) (Fig.A1.14Ba), B) S2D36a72 (a=720 mm, η_a=2) (Fig.A1.14Bb) and C) S2D36a36 (a=360 mm, η_a=1) (Fig.A1.14Bc) for: a) bottom triangle in reinforcement anchorage zone and b) in compression-shear zone (continuous blue lines denote tangential displacement δ and dashed green lines denote normal displacement ω, sections are shown in Fig.A1.14)

A1.6. Analytical calculation

Initially the experimentally measured beam shear strengths were compared with the analytical values based on EC (EN 1992-1-1 (2008)) and ACI 318-14 (2014) and proposed by Zhang and Tan (2007).

EN 1992-1-1 (2008)

The characteristic shear strength of RC beams without shear reinforcement was calculated as

$$V_{Rd,c} = [C_{Rd,c}k(100\rho_l f_c)^{\frac{1}{3}}]tD \geq \left(0.035k^{\frac{3}{2}}f_c^{\frac{1}{2}}\right)tD \quad \text{(A1.5)}$$

with

$$k = 1 + \sqrt{200/D}, \quad \text{(A1.6)}$$

where $C_{Rd,c}$ is the recommended empirical coefficient derived from experiments (the characteristic value of $C_{Rd,c}$=0.18), ρ_l denotes the longitudinal reinforcement ratio (ρ_l=1.4%) and f_c is the uniaxial (cylinder) compressive strength of concrete (f_c=49 MPa=0.8 $\bar{f}_{cm}$), t=0.25 m and D in [mm]).

ACI 318-14 (2014)

The shear strength of high RC beams was calculated by applying a simple strut-and-tie model (Fig.A1.17). With the angle θ between the strut and tie ($\tan\theta_s=D/a$) and compressive force in the strut F_{us}, the ultimate vertical force V_n was computed from the strut compressive force:

$$V_n=F_{us}sin\theta_s \quad \text{(A1.7)}$$

with

$$F_{us}=f_{ce}A_{cs}=f_{ce}w_s t=0.85\beta f_c w_s t, \quad \text{(A1.8)}$$

wherein f_{ce} - the effective strut compressive strength, $A_{cs}=w_s\times t$ - the cross-sectional area at the end of the strut (t=0.25 m), w_s- the strut width of diagonal strut, f_c – the cylinder compressive strength (f_c=49 MPa) and β - the efficiency factor (β=0.6). The width of the strut w_s was related to l_c and l_b and calculated as

$$w_s=l_c\cos\theta_s + l_b\sin\theta_s \quad \text{with} \quad \tan\theta_s=D/a \quad \text{(A1.9)}$$

and l_c=2c' (η_a=1 and 2) for one reinforcement layer and l_c=2c'+50 mm (η_a=1.5) for two reinforcement layers with c'=(h-D) (l_a=100 mm - the width of the loading plate, l_b=100 mm - the width of the bearing plate).

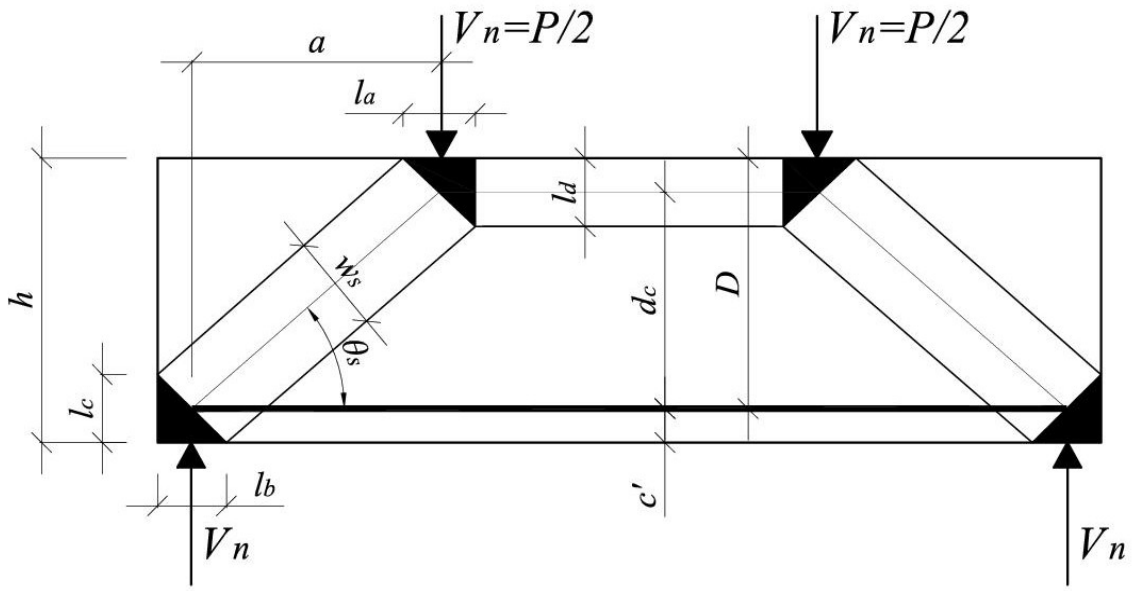

Fig.A1.17: Strut-and-tie model for deep beams under 4-point bending (θ_s - strut inclination angle to horizontal, w_s – width of diagonal strut (w_s=$l_c$cosθ_s + $l_b$sinθ_s, l_a=100 mm – width of loading plate, l_b=100 mm - width of supporting plate, l_c=l_d=2c', tanθ_s=d_c/a, d_c=h-c'-0.5l_d,=(D-c)/a, c'=h-D) (Zhang and Tan 2007)

The inclination angle of the diagonal compressive strut was: θ_s=26.6^o (η_a=2), θ_s=33.7^o (2 reinforcement layers)/θ_s=35.5^o (1 reinforcement layer) (η_a=1.5) and θ_s=45.0^o (η_a=1), for the deep beams S2D36A72, S1D72A108 and S2D36A36, respectively. The width of the strut was thus (Eq.A1.9): w_s=134.2 mm for η_a=2, w_s=180.3 mm (2 reinforcement layers)/w_s=139.5 mm (1 reinforcement layer) for η_a=1.5 and w_s=141.4 mm for η_a=1 (with l_a=l_b=100 mm).

In the experiments, the average width of the compression strut between the loading and bearing plates versus the shear ratio was: w_s=94 mm (η_a=2), w_s=166 mm (η_a=1.5) mm and w_s=126 mm (η_a=1) (Figs.A1.7 and A1.8). The diagonal strut width was measured as the distance between the critical diagonal crack and nearest diagonal crack in the beam mid-height. The measured values of w_s were smaller by 30% (η_a=2), 5% (η_a=1.5) and 10% (η_a=1) than the theoretical ones. The measured inclination angles of the diagonal strut were about θ_s=40^o for η_a=1-2 (Fig.8) and were

significantly higher than the theoretical values for η_a=1.5-2 (θ_s=33.7^o and θ_s=26.6^o) and smaller than the theoretical values for η_a=1 (θ_s=45.0^o).

Zhang and Tan (2007) proposed the modification of a strut-and-tie model (Fig.A1.17) by taking into account the Mohr-Coulomb failure condition in a tension-compression stress state and a contribution of the bottom reinforcement to the strut compression. The ultimate force V_n in RC beams without web reinforcement may be determined from the formula (Zhang&Tan 2007)

$$V_n \left[\frac{4\sin\theta_s\cos\theta_s}{f_t A_c}+\frac{\sin\theta_s}{f_c A_{str}}\right]=1, \tag{A1.10}$$

where $A_c=d_c\times t$ is the effective cross-sectional area of high beams ($d_c=D$-0.5l_d), $A_{str}=w_s\times t$ is the cross-sectional area of the strut, θ_s is angle between the strut and tie ($\tan\theta_s=d_c/a=(D-c')/a$) (Fig.A1.17), f_c denotes the cylinder compressive strength and f_t is the maximum tensile strength of the bottom nodal zone which can be calculated as the sum of two components:

$$f_t=\frac{4A_s f_y\sin^2\theta_s}{A_c}+0.31\sqrt{f_c}\left(\frac{\varepsilon_{cr}}{\varepsilon_1}\right)^{0.4}, \tag{A1.11}$$

The first component in Eq.A1.11 results from the main longitudinal reinforcement (f_y - yield stress in reinforcement) and the second component from the cracked concrete tensile strength (ε_{cr} - the concrete strain during cracking taken as 0.00008, ε_1 - the principal tensile strain of the concrete strut ($\varepsilon_1=\varepsilon_s+(\varepsilon_s+\varepsilon_2)ctg^2\theta_s$, ε_s and ε_2 - the tensile strain of longitudinal reinforcement and peak compressive strain of the concrete strut at crushing). The width of the compressive strut w_s was assumed according to ACI 318-14 (2004) (Eq.A1.9). The inclination angle of the diagonal compressive strut ($\tan\theta_s=d_c/a$) was: θ_s=24.77^o (η_a=2), θ_s=31.86^o (η_a=1.5) and θ_s=43.08^o (η_a=1).

Alternative strut-and-tie models

The ACI-model (Eqs.A1.7-A1.8) may be modified to analytically specify the size effect. The strut width was simply calculated as $w_s=l_c/\cos\theta$ (Fig.A1.17), thus the support plate length equalled $l_b=l_c$ $\tan\theta_s$. The inclination angle θ_s was expressed by the relationship

$$\tan\theta_s=\frac{D-c'}{a}=\frac{D}{a}\left(1-\frac{c'}{D}\right)=(1-\eta_c)\frac{1}{\eta_a}. \tag{A1.12}$$

The ultimate force V_n can now be related to two scale parameters η_a and η_c, thus

$$V_n = F_{us}\sin\theta_s = f_{ce} w_s t \sin\theta_s = 1.7\cdot 0.6 f_c \frac{c't}{\cos\theta_s} \times \sin\theta_s = 1.02 f_c\, c't \tan\theta_s = \\ = 1.02 f_c\, c't \frac{1}{\eta_a}(1-\eta_c) \tag{A1.13}$$

and the related ultimate shear strength was

$$\tau_c = \frac{V_n}{tD} = 1.02 f_c' \eta_c (1-\eta_c)\frac{1}{\eta_a}. \tag{A1.14}$$

Assuming the lower bound approach, we can neglect the contribution of the reinforcement force component in the axial compressive strength of the concrete strut in Eq.A1.10. Then the following alternative expression for V_n is obtained

$$V_n\left[\frac{4\cos\theta_s \sin\theta_s}{A_c f_t} + \frac{1}{\sin\theta_s A_{str} f_c}\right] = 1, \tag{A1.15}$$

where $A_c f_t = 4 A_s f_y \sin^2\theta_s$ as it follows from Eq.A1.11 when the effect of the second term representing the concrete tensile strength is neglected. Similarly, $A_{str} = w\times t = l_c/\cos\theta_s = 2c't/\cos\theta_s$ and $\tan\theta_s = (1-\eta_c)/\eta_a$ (Eq.A1.12). The following expressions for V_n and τ_c were now obtained:

$$V_n = \tau_c A_c \qquad \text{and} \qquad \tau_c = \frac{1-\eta_c}{\eta_a}\frac{\rho_l f_y}{1+\frac{1}{2\eta_c}\frac{\rho_l f_y}{f_c}}. \tag{A1.16}$$

Comparing Eqs.A1.14 and A1.16 it is seen that the critical stress value depends on two geometric parameters η_a and η_c. In Eq.A1.12 only the concrete compressive strength is present but in Eq.A1.16 both concrete and reinforcement strengths affect the critical shear stress.

Similarly, starting from Eq.A1.15 and neglecting the concrete tensile strength in Eq.A1.11, we can express τ_c as follows

$$\tau_c = \frac{1-\eta_c}{\eta_a} \frac{\rho_l f_y \left[\eta^2{}_a + (1-\eta_c)^2 \right]}{\eta^2{}_a + (1-\eta_c)^2 + \frac{1}{2\eta_c} \frac{\rho_l f_y}{f_c} (1-\eta_c)^2}. \tag{A1.17}$$

The residual flexural force $V_{res,flex}$ was calculated from the equilibrium of the compression zone force $F_c = f_c h_c t$ (where the height of the compression zone is $h_c = \rho_l D \frac{f_y}{f_c}$) and tensile force of reinforcement $F_s = \rho_l f_y D t$ (by assuming the full concrete cracking in the tensile zone)

$$V_{\max,flex} = \rho_l f_y D t \frac{1}{\eta_a} [1 - \frac{\rho_l f_y}{f_c}]. \tag{A1.18}$$

A1.7. Comparison between experimental and theoretical results

The results of the shear strength $\tau_c = V_{max}/(tD)$ (V_{max}=0.5P_{max}) for all theoretical models as compared to the experimental values are presented in Table A1.5.and in Fig.A1.18.

Analytical formulae by Eq.A1.7-A1.11 (Tab.A1.5, Fig.A1.18A)

According to the strut-and-tie model in ACI 318-14 (Eq.A1.7-A1.8) and the strut-and-tie model (STM) by Zhang and Tan (2007) (Eqs.A1.10 and A1.11), the ultimate shear strength was solely calculated for 3 deep beams: S1D72A108 (η_a=1.5, η_l=3.75), S2D36A72 (η_a=2, η_l=5.5) and S2D36A36 (η_a=1, η_l=3.5). These models are solely valid for structural elements wherein the strut inclination angle θ_s ranges from 25^o to 65^o (ACI 318-14 (2004)).

EC underestimated the vertical load (strength) of all beams except of slender beams with η_a=3 and 6 (Fig.A1.18A). ACI/STM overestimated (for η_a=1.5-2) and underestimated (for η_a=1) the shear strength of high beams (Tab.A1.5, Fig.A1.18A). The result difference was +100%/+60% (η_a=2), +20%/+40% (η_a=1.5) and -5%/-25% (η_a=1). STM indicated a size effect (strength decreased with increasing η_a) Thus, the absolute value of the difference diminished with decreasing η_a (the difference was smaller for ACI for η_a=1-1.5 and for STM for η_a=2. The highest difference was for the beams with dominant normal crack displacements (η_a=2-3). A better agreement was achieved for η_a=1.5 (ACI/STM) if one reinforcement layer was taken into account in calculations (Tab.A1.5).

Alternative formulae by Eq.A1.14, A1.16 and A1.17 (Tab.A1.5, Fig.A1.18B)

The alternative formulae realistically capture the size effect. With the modified ACI formula (Eq.A1.14), a more realistic result of τ_c was achieved for η_a=1.5-2, however for η_a=1, the result of τ_c was less realistic as compared to Eqs.A1.7-A1.9 (the strength was lower by 25% than the experimental result). It may be seen that Eq.A1.16 fits well the test data, except for $\eta_a = 1$ where the experimental value of τ_c is much higher (by 75%). On the other hand, Eq.A1.17 provided a higher assessment of the shear strength than Eq.A1.16.

The discrepancies between the experimental and theoretical results are caused by the following factors: 1) different strut widths and strut inclinations for all high beams(η_a=1-2, η_l=3.5-5.5),
2) different shape of the compressive strut for η_a=2 (Fig.A1.7e),
3) varying strut width along the beam height in experiments (Fig.A1.7),
4) lack of the reinforcement yielding in experiments and
5) different width of the compressive strut and upper compressive horizontal zone.

In the experiments, the mean strut width was smaller (η_a=1-2), the strut inclination to the horizontal was lower (η_a=1-1.5) or higher (η_a=2) and the strut shape was more parabolic (η_a=2) comparing to theoretical value obtained with ACI standard formulas (Eq.A1.9). In addition, the strut width varied along the beam height in experiments (Fig.A1.6), the steel reinforcement did not yield and the width of the compressive strut was different than the width of the upper compressive horizontal zone.

Crack width and deflection

Figure A1.19 presents the maximum experimental flexural crack widths w in the beam mid-regions for the mean maximum vertical forces P_{max}^{exp} of Tab.A1.5 as compared to EC2 (EN 1992-1-1 (2008)) and ACI (ACI 224R-01). For P_{max} and the beam series '1' the standard flexural crack spacing l_s were 182 mm, 148 mm and 142 mm (EC2) and 222 mm, 140 mm and 127 mm (ACI) whereas the experimental ones were different: 218 mm, 140 mm and 137 mm with increasing η_a from 1.5 up to 6 (Fig.A1.20a). In the series '2' (D=360 mm), the standard values of l_s for P_{max} were 148 mm (EC2) and 140 mm (ACI) versus the experimental ones were between 96 mm (η_a=1) and 137 mm (η_a=2-3) (Fig.A1.20b). Thus, the standard values of the flexural crack widths w were the most realistic for the beams with η_a>1.5.

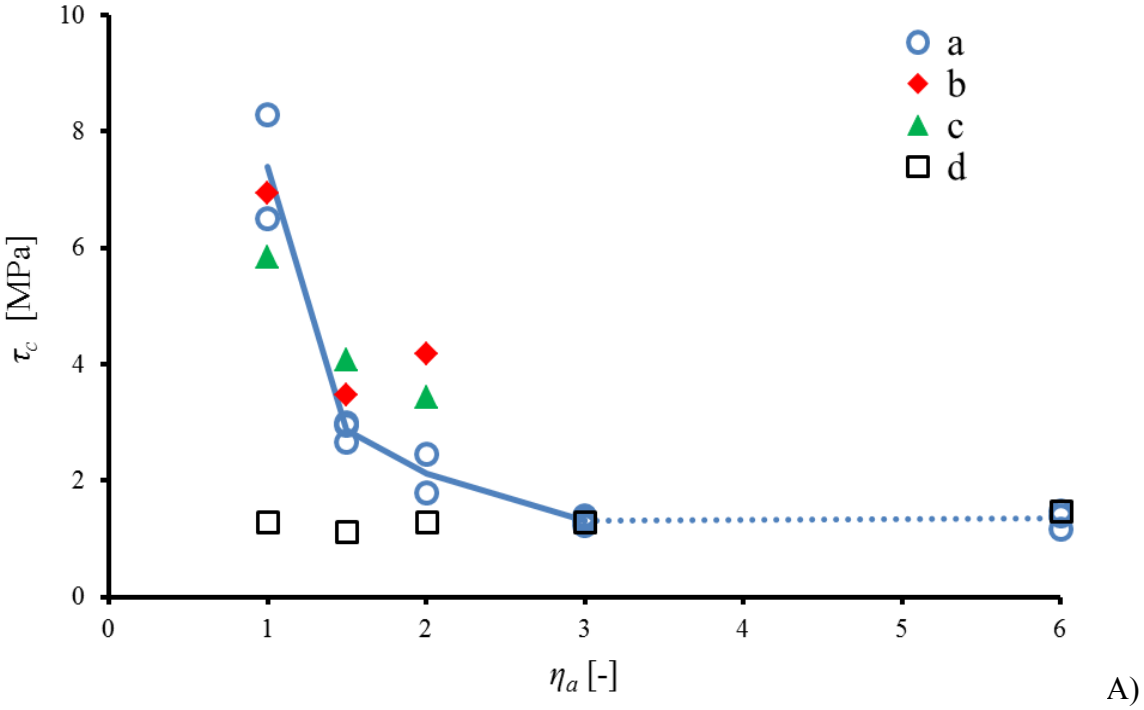

A)

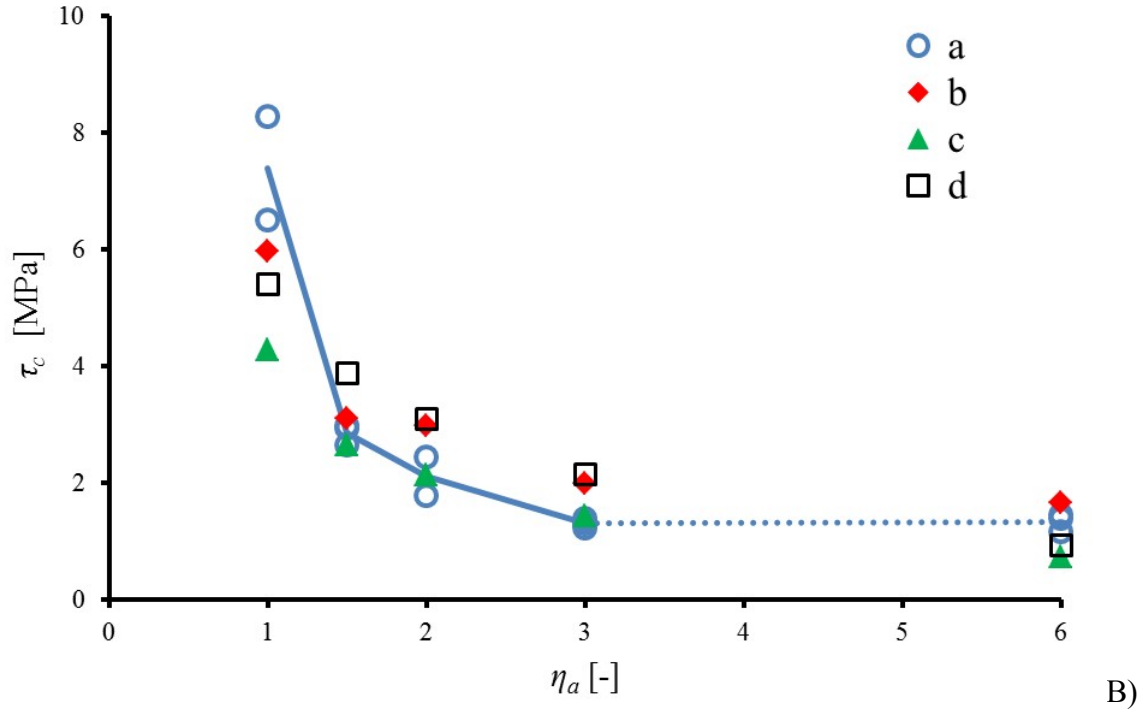

B)

Fig.A1.18: Shear strength $\tau_c=V_{max}/(tD)$ ($V_{max}=0.5P_{max}$) for varying shear span parameter $\eta_a=a/D$ in experiments (a) and in analytical solutions: A) codes ((b) ACI (Eqs.A1.7-A1.9), c) STM (c) (Eqs.A1.10 and A1.11) and d) EC2 (Eqs.A1.5 and A1.6)) and B) alternative formulae (b) alternative ACI (Eq.A1.14), c) alternative STM (Eq.A1.16) and alternative STM (Eq.A1.17) (note that beams for η_a=6 failed in flexural mechanism)

Tab.A1.5: Shear strengths $\tau_c=V_{max}/(tD)$ ($V_{max}=0.5P_{max}$) for RC beams according to EC2 (Eqs.A1.5 and A1.6), ACI 318 (Eqs.A1.7-A1.9), STM (Eqs.A1.13 and A1.14), alternative ACI (Eq.A1.12), alternative STM (Eq.A1.16), alternative STM (Eq.A1.17) and Eq.A1.18 as compared to experimental values (Y - reinforcement yielding, T – diagonal shear-tension failure with dominant normal diagonal crack displacements, C – diagonal shear-compression failure with significant both tangential and normal diagonal crack displacements, (*) - calculated for beams with one reinforcement layer if η_a=1.5). Note values for η_a>2 (Eqs.A1.12, A1.16 and A1.17) were calculated for inclination angles θ greater than limit angle for ACI and STM

Beam	***a*** **[mm]**	***D*** **[mm]**	**Failure mode**	τ_c^{exp} **[MPa] (exp.)** **Tab.A1.4**	τ_c^{ACI} **[MPa]** **Eq.A1.7-A1.9**	τ_c^{STM} **[MPa]** **Eq. A1.10-A1.11**	τ_c^{EC} **[MPa]** **Eqs. A1.5-A1.6**	τ_c^{ACI} **(alternative)** **[MPa]** **Eq.A1.14**	τ_c^{STM} **(alternative)** **[MPa]** **Eq.A1.16**	τ_c^{STM} **(alternative)** **[MPa]** **Eq.A1.17**	τ_c^{flex} **[MPa]** **Eq. A1.18**
S2D36a36 (η_a=1, η_c=0.14)	360	360	C	**7.39**	6.94	5.83	1.29	5.98	4.28	5.42	6.59
S1D72a108 (η_a=1.5, η_c=0.10 (0.14*))	1080	720	C	**2.86**	3.47 (2.67*)	4.07 (3.87*)	1.13	3.11 (2.15*)	2.65 (2.26*)	3.90	4.39
S2D36a72 (η_a=2, η_c=0.14)	720	360	C/T	**2.11**	4.17	3.43	1.29	2.99	2.14	3.10	3.29
S1D36a108 (η_a=3, η_c=0.14)	1080	360	T	**1.35**			1.29	1.99	1.43	2.16	2.20
S2D36a108 (η_a=3, η_c=0.14)	1080	360	T	**1.31**			1.29	1.99	1.43	2.16	2.20
S1D18a108 (η_a=6, η_c=0.28)	1080	180	Y	**1.34**			1.47	1.67	0.73	0.94	1.10

Finally, the beam deflections were calculated by EC2 (EN 1992-1-1 (2008)) and ACI (ACI 435R-95) and compared with the mean experimental values for P_{max}^{exp} (Fig.A1.21). The creep effects were neglected. For the high shear span ratio a/D=3-6 the experimental beam deflections for P_{max}^{exp} were underestimated by about 10-20%**.** For the small shear span ratio ($\eta_a \leq 2$), the standard deflections were underestimated by the factor 3. For the beams S2D36a36 (η_a=1), S1D72a108 (η_a=1.5) and S2D72a36 (η_a=2), the standard formulae provided the deflection values of u=2.19 mm, u=2.66 mm and u=2.90 mm (EC2) and u=2.20 mm, u=2.58 mm and u=2.76 mm (ACI) whereas in the experiments they were higher and equal on average to 6.90 mm (Fig.A1.8c), 7.23 mm (Fig.A1.7c) and 6.84 mm (Fig.A1.8b), respectively.

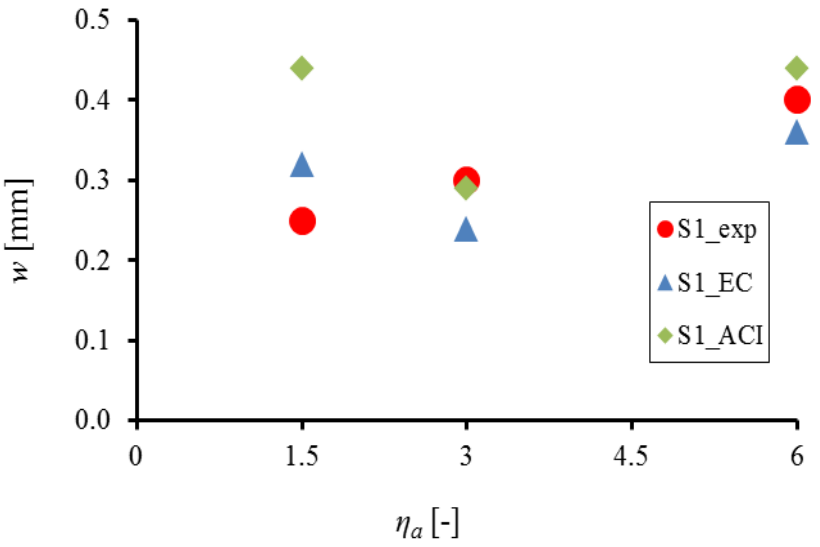

a)

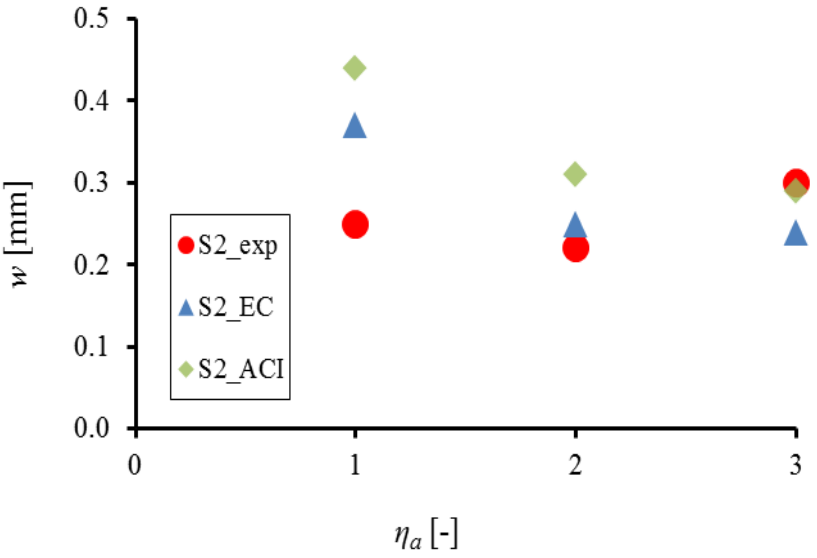

b)

Fig.A1.19: Experimental (circles) and analytical flexural crack widths w by EC2 (triangles) and ACI (diamonds) versus $\eta_a=a/D$ for P_{max} in RC beams: a) series '1' (S1) and b) series '2' (S2)

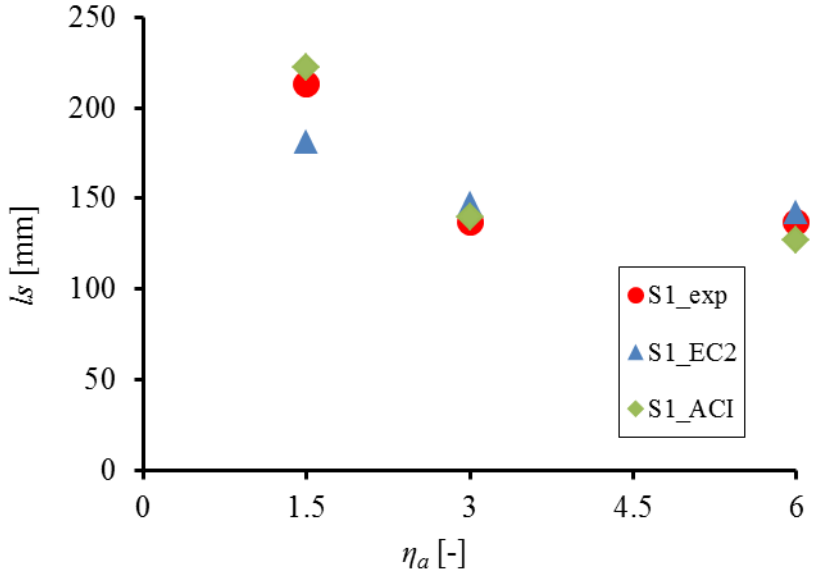

a)

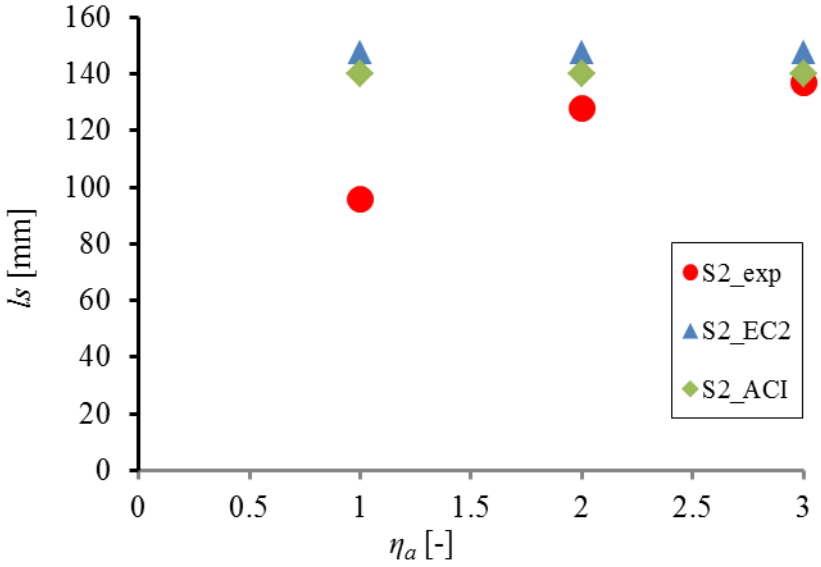

b)

Fig.A1.20: Experimental (circles) and analytical flexural crack spacing l_s by EC2 (triangles) and ACI (diamonds) versus $\eta_a=a/D$ for P_{max} in RC beams: a) series '1' (S1) and b) series '2' (S2)

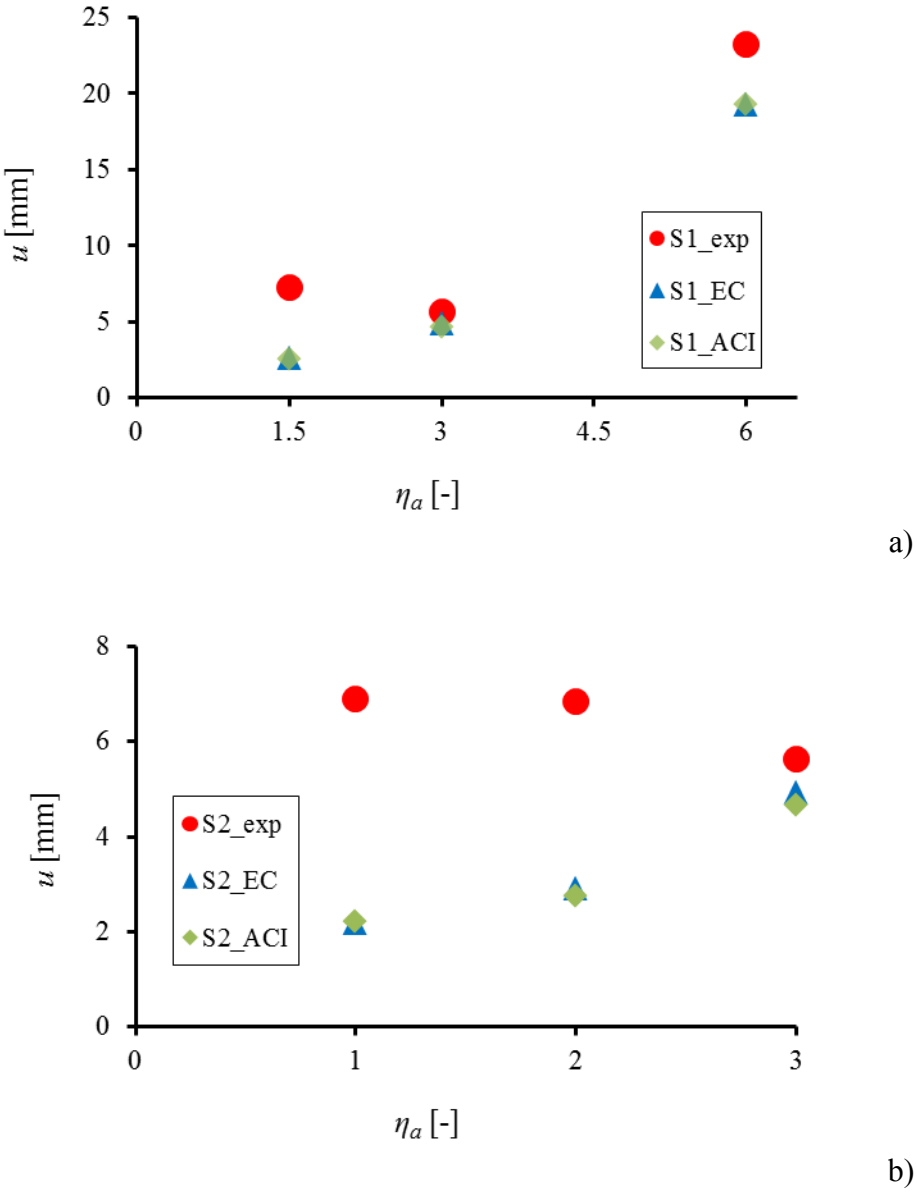

Fig.A1.21: Beam deflections u in experiments (circles) and calculated according to EC2 (triangles) and ACI (diamonds) (without creep) versus $\eta_a=a/D$ for P_{max}: a) series '1' (S1) and b) series '2' (S2)

A1.7 Conclusions

The following basic conclusions may be derived from our novel size effect experiments on RC beams being scaled along either the depth or length with the size parameters $\eta_a=a/D$=1-6, η_b=0.75-3 and $\eta_l=l_{eff}/D$=3.5-15:

- The shear strength of beams evidently decreased with increasing both parameters $\eta_a=a/D$ and $\eta_l=l_{eff}/D$. It also decreased with increasing parameter η_b from 0.75 up to 1.5 in beams with varying effective depth and constant effective length. The shear strength's increase was extremely large (250%) in the range of η_a=1.0 (η_l=3.5) and η_a=1.5 (η_l=3.75) in series '2' with constant effective depth D.

- Two different failure modes were observed in RC beams: plastic flexural expressed by reinforcement yielding for a/D=6 (η_l=15, η_b=3) and brittle shear in concrete with dominant normal diagonal crack displacements (so-called shear-tension failure) for η_a=2-3 (η_l=5.5-7.5, η_b=1.5) or with simultaneous significant normal and tangential diagonal crack displacements (so-called shear-compression failure) for η_a=1-2 (η_l=3.5-5.5, η_b=0.75-1.5). The distance between the critical diagonal crack and beam support d_c related to the shear span a varied between d_c/a=0.5 for low beams (η_a=3) up to d_c/a=0 for high beams (η_a=1).

- For high beams, the strut-and-tie models following ACI and Zhang and Tan overestimated the shear strength for η_a=1.5-2 (by 20%-100%) and underestimated for η_a=1 (by 5%-25%). The difference between experimental and the theoretical results by ACI and Zhang and Tan increased with decreasing η_a. The alternative formulae based on the modification of ACI/STM significantly improved the theoretical results in the range of η_a=1.5-2 but at the same time significantly worsen the results for η_a=1.

- The discrepancies between the experimental and theoretical results were caused by the different strut widths and strut inclinations for all high beams with η_a=1-2 and different shapes of compressive struts for the beams with η_a=2. In addition, the strut width varied along the beam height in all experiments for η_a=1-3. The evident disadvantage of strut-tie models is the fact that they do not distinguish between 2 different failure modes in shear (diagonal tension and shear compression) which affect the beam strength to a different grade.

- The standards EC2 and ACI realistically determined the flexural crack widths and beam deflections solely for the beams with η_a=2-6 with respect to cracks widths and with η_a=3-6 with respect to deflections. For η_a=1 the standard crack widths were higher by the factor 1.5-1.8 and the standard deflections were smaller by the factor 3.

APPENDIX 2

Experimental investigations of shear strength and failure mechanisms in RC beams with stirrups scaled along height or length

(published in the paper by Korol, E., Suchorzewski, J., Tejchman, J. i Mróz, Z. Experimental investigations of shear strength and failure mechanisms in RC beams with stirrups scaled along height or length, submitted to *Engineering Structures,* 2019).

A2.1 Introduction

The extensive experimental studies of a size effect were performed for plain and reinforced concrete (RC) beams that were geometrically similar. In the case in RC beams without shear reinforcement, a strong size effect was experimentally observed wherein diagonal shear-tensile fracture occurred (Walraven (1978), Bažant et al. (1991), Kim&Park (1994), Tan&Lu (1999), Angelakos et al. (2001), Yang (2003), Reineck et al. et al. (2003), Lubell et al.(2004), Tan et al. (2005), Korol et al. (2014a)). It was predominantly of the energetic type. The experimental diagonal failure cracks had in experimental tests similar paths and relative lengths at the maximum load independently of the beam size. The size effect was also observed in RC beams with shear reinforcement (Walraven (1994), Tan et al. (2005), Zhang and Tan (2007a, 2007b)). In these experiments, a diagonal shear-tensile fracture (Walraven 1994), Tan et al. (2005), Zhang and Tan (2007b)) or crushing of a compressive zone (Zhang and Tan 2007b) took place in concrete. Thus the use of stirrups did not suppress the size effect provided the longitudinal and vertical reinforcement yielding did not occur. However, only a few papers were devoted to a size effect in RC beams without and with vertical reinforcement scaled along height or length (e.g. RC beams without shear reinforcement (Korol et al. 2014a) and RC beams with shear reinforcement (Zhang and Tan 2007b). The effect of the varying reinforcement ratio on the failure mode in RC beams was experimentally shown by Carpinteri et al. (2011). The observed failure mode changed from longitudinal reinforcement yielding, through diagonal tension to compressive zone crushing with increasing reinforcement ratio.

The objective of the present paper is to identify experimentally different failure mechanisms in reinforced concrete beams including vertical (shear) reinforcement for a separate variation of the depth and length. Special attention was paid to a description of a fracture process by measuring the critical crack opening and slip displacements. The commonly used code procedures using strut-and-tie models proposed in the literature were applied to calculate theoretical shear strengths in order to

compare them with experimental outcomes. In addition, crack widths and deflections were compared with code formulae. The current RC beams, in contrast to those in (Suchorzewski et al. 2018c), were equipped with both longitudinal and shear (transverse) reinforcement. The geometry of beams in the current study was similar to those in (Suchorzewski et al. 2018c – see Appendix 1) for comparative purpose. The shear strength of beams without shear reinforcement in our previous investigations (Suchorzewski et al. 2018c – see Appendix 1) evidently decreased with the increasing ratio of the shear span to the beam depth $\eta_a = a/D$ (η_a=1-6) and the ratio of the effective beam length to the beam depth η_l (η_l=3.5-15). The failure modes changed with the varying parameter η_a. The beams were damaged due to reinforcement yielding (η_a=6), diagonal tension (a critical diagonal crack has a dominant normal opening displacement) (η_a=2-3) or shear (a critical diagonal crack has a dominant tangential opening displacement) (η_a=1-2). None of the verified analytical models (EC2 1992-1-1, ACI 318-14 and Zhang and Tan (2007)) was able to estimate the strength of tested beams with a satisfactory accuracy. For high beams, the strut-and-tie models following ACI 318-14 and Zhang and Tan (2007) overestimated the shear strength by 20%-100% for η_a=1.5-2 (20-100% for (ACI 318-14 and 40%-66% for Zhang and Tan (2007)) and underestimated it by 5%-20% for η_a=1 (5% for ACI 318-14 and 20% for Zhang and Tan (2007)). Thus the difference between experimental and the theoretical results by ACI 318-14 and Zhang and Tan (2007) increased with decreasing η_a. The own alternative formulae based on the modification of the formulae Zhang and Tan (2007), ACI 318-14 significantly improved the theoretical results in the range of η_a=1.5–2 but not accurately for η=1. The discrepancies between the experimental and theoretical results were caused by: a) the varying strut widths and strut inclinations for all high beams with η_a=1-2 and b) the different shapes of compressive struts for the beams with η_a=2 in the experiments. The evident disadvantage of strut-tie models was the fact that they were not able to distinguish between two different failure modes in shear (diagonal tension and shear compression) which affected the beam strength to a different grade. The experimental results concerning strength, brittleness and fracture were however realistically described in FE calculations using a coupled elasto-plastic-damage model with non-local-softening for concrete (Marzec et al. 2019).

A2.2 Specimens geometry

The beams of the series '3' had the same effective depth (D=360 mm) and varying span length l_{eff} and shear span a (the latter scaled in the proportion 1:1.5:3). The beams were denoted as S3D36a2016, S3D36a108 and S3D36a54, where the symbol *S3* denotes the series '3', D - the effective beam depth in [cm] and a - the shear zone length in [cm]. Note that the beam S3D36a108

(D=360 mm) had the same dimensions as and beams S1D36a108, S2D36a108 in series without stirrups and the concrete beam (denoted as SL40) used in the size effect experiments by Korol and Tejchman (Korol and Tejchman 2014) and was twice as short as the beam S3D36a216 (D=180 mm) and twice as long as the beam S3D36a54. Thus, the effective depth D and bending zone length b (distance between two concentrated forces V) were constant D=360 mm and b=540 mm, respectively (Fig.A2.1A, Tab.A2.1). The shear span parameter $\eta_a=a/D$ was 1.5, 3 and 6. Each beam length l_{eff} included 2 identical concrete specimens in order to verify the result repeatability (indicated as: S3D36a216_1 – S3D36a216_3, S3D36a108_1 – S3D36a108_3 and S3D36a54_1 – S3D36a54_3).

The beams of the series '4' had different thickness than all previous beams equal to t=150 mm due to limitations of the loading device. The beams in series '4' various effective depth D in the proportion 1:2:4 with the constant effective span length l_{eff} =2700 mm. (Fig.A2.1B, Tab.A2.2). The beams were denoted as S4D18a108 (D=180 mm), S4D36a108 (D=360 mm) and S4D72a108 (D=720 mm). The beam from S4D36a108 had the same dimensions as the beam from the series '3' denoted as S3D36a108 and beams S1D36a108, S2D36a108 in series without stirrups. The beam S4D18a108 was as twice as low as the beam S4D36a108 and the beam S4D72a108 was as twice as high as the beam S4D36a108. Each beam included 2 identical specimens (denoted as: S4D18a108_1 and S4D18a108_2, S4D72a108_1 and S4D36a108_2 and S4D72a108_1 and S4D72a108_2).

The reinforcement of all beams consisted of ribbed bars of the diameter ϕ=25 mm and ϕ=10 mm with the mean yielding stress of 560 MPa (class B500) and the modulus of elasticity of 205 GPa. The longitudinal reinforcement ratio was designed as ρ_l=4.2% to eliminate possibility of steel yielding due to presence of stirrups. The transverse reinforcement ratio was always equal to ρ_s=0.4% and was formed with double-sheared stirrups with diameter of ϕ=8 mm made out of the same steel as longitudinal reinforcement. Each beam size required a different number of bars depending on the effective depth D. The beams of D=18 cm had 2 bars in two layers, D=36 cm 2 bars in two layers and one more bar in third layer, whereas the beam of D=72 cm had 6 layers with 2 bars i.e. 12 bars in total (Fig.A2.1C). In order to avoid the anchorage zone failure and slip between reinforcement and concrete, hooked steel bars were used (Fig.A2.1) with the anchorage length of 130 mm, 310 mm or 670 mm, depending on the beam height.

The specimens from the series ‘3’ and series ‘4’ were casted separately, however the concrete recipe was similar as in previous series (see Tab.A1.3).

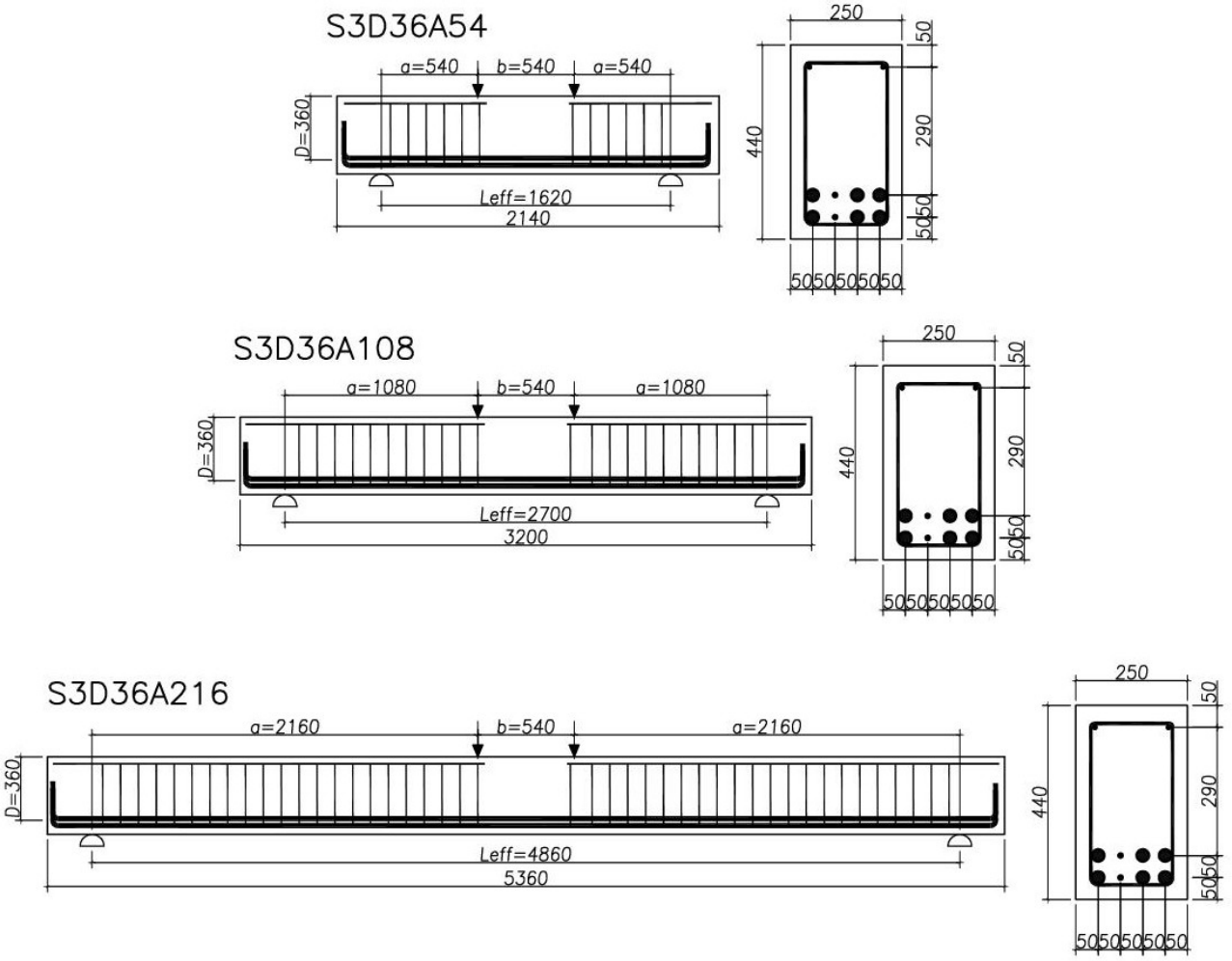

A)

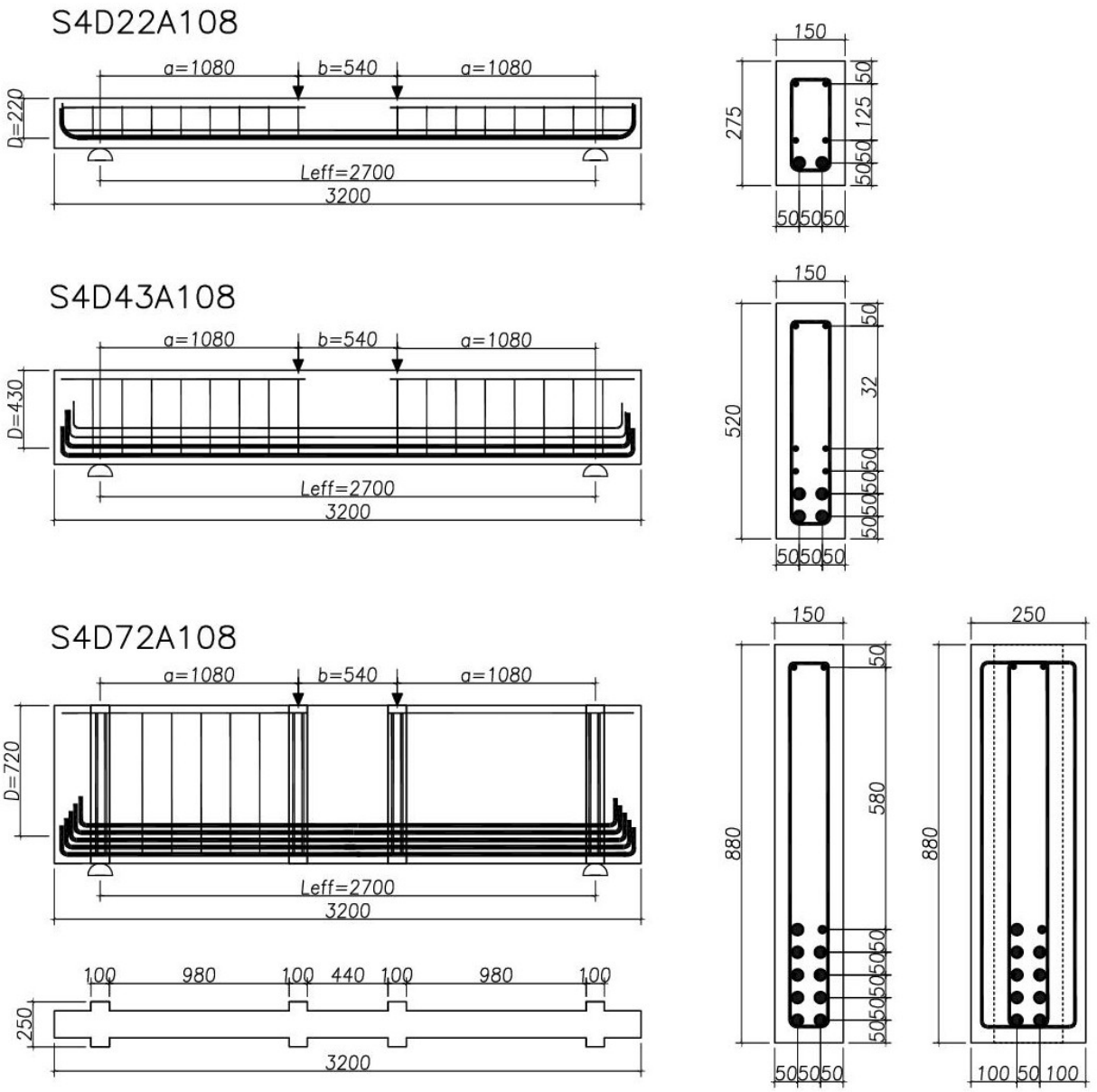

B)

Fig.A2.1: Experimental reinforced concrete beams under four-point bending: A) loading scheme for series '3' (D=360 mm, b=540 mm) with varying a and l_{eff} with varying a and $l_{eff,}$ B) loading scheme for series '4' (l_{eff}=2700 mm, a=1080 mm, b=540 mm) with varying D (D - effective beam height, l_{eff} - distance between beam supports, l - total beam length, V - vertical concentrated force applied, a - shear zone span, b - bending zone span, dimensions are in [mm])

Tab.A2.1: Dimensions of reinforced concrete beams in series 3

Beam dimension	Beam S3D36A54	Beam S3D36A108	Beam S3D36A216
***D* [mm]**	360	360	360
***H* [mm]**	440	440	440
l_{eff} **[mm]**	1620	2700	4860
***a* [mm]**	540	1080	2160
***b* [mm]**	540	540	540
$\eta_a=a/D$	1.5	3	6
$\eta_l=l_{eff}/D$	4.5	7.5	13.5
$\eta_b=b/D$	1.5	1.5	1.5
$\eta_c=c'/D$	0.22	0.22	0.22

Tab.A2.2: Dimensions of reinforced concrete beams in series 4

Beam dimension	Beam S4D22A108	Beam S4D43A108	Beam S4D72A108
***D* [mm]**	220	430	720
***H* [mm]**	275	520	870
l_{eff} **[mm]**	2700	2700	2700
***a* [mm]**	1080	1080	1080
***b* [mm]**	540	540	540
$\eta_a=a/D$	5	2.5	1.5
$\eta_l=l_{eff}/D$	12	6.3	3.75

$\eta_b=b/D$	2.5	1.25	0.75
$\eta_c=c'/D$	0.43	0.38	0.22

A2.3 Test procedure

The test procedure was analogical to the one described in Section A1.3.

A2.4. Experimental results

Series '3': varying shear span *a* for constant effective depth *D* and bending zone span *b*

The constant effective depth D=0.36 m and varying shear span a=540, 1080 and 2160 mm contributed to the change of the parameter η_a from 1.5 through 3.0 up to 6.0 (Tabs.A2.1-2). The parameter η_b was 1.5 and the parameter η_l varied from 4.5 up to 13.4.

The longest beams S3D36A216 with η_a=6.0 (η_b=1.5, η_l=13.5) failed due to concrete crushing in the constant bending moment zone since both flexural and shear reinforcement were sufficient to resist the critical bending and shear stresses. The total averaged ultimate vertical force acting on the beams was $P_{max}=2V_{max}$=474.6 kN. The average deflection u corresponding to the failure onset was 35.4 mm while its normalized values u/D and u/L_{eff} were u/D=9.8% and u/L_{eff}=3‰. All beams had similar normalized load-deflection paths including the registered post-peak brittleness resulting from the compressive concrete behaviour in the softening regime (Fig.A2.2A). In contrast, the slender beams with the same parameter η_a=6.0 but without shear reinforcement and lower reinforcement ratio failed due to steel yielding.

The beams S3D36A108 with η_a=3 constituted a transitional geometry between two different failure mechanisms. The beam S3D36A108_1 failed in shear-compression for $P_{max}=2V_{max}$=802 kN and u=12.0 mm (u/D=3.3% and u/L_{eff}=4.4‰) and the beam S3D36A108_3 was damaged due to concrete crushing in the constant bending moment zone for $P_{max}=2V_{max}$=954 kN with u=20.1 mm (u/D=5.6% and u/L_{eff}=7.4‰). The beam S3D36A108_2 (made of weaker concrete) lost its load bearing capacity also due to concrete crushing for $P_{max}=2V_{max}$=601 kN and u=16.7 mm (u/D=4.6% and u/L_{eff}=6.2‰). The beams S3D36A108_2 and S3D36A108_3 which failed due to concrete crushing had the relatively higher normalized deflection u/D for P_{max} than the beam S3D36A108_1 that was damaged in shear-compression. Moreover, the beams S3D36A108_2 and S3D36A108_3 showed more ductility after reaching P_{max} in contrast to the beam S3D36A108_1 (Fig.A2.2B). The normalized load-deflection diagrams in Fig.2.2B indicated the similar curve shapes corresponding

to the beams S3D36A108_2 and S3D36A108_3 that failed in the same failure mode in spite of weaker concrete. The beams from our previous study without transverse reinforcement which had a similar geometry but no shear reinforcement failed in diagonal tension.

All deep beams S3D36A54 with η_a=1.5 failed in shear-compression with a significant increase of the shear strength supported by an internal arch action (Fig.A2.2C). The beam S3D36A54_2 (casted together with S3D36A108_2) which was made of weaker concrete, reached $P_{max}=2V_{max}$=1165 kN with the corresponding deflection u=7.7 mm (u/D=2.1% and u/L_{eff}=4.8‰). In the beam S3D36A54_1, the failure force was $P_{max}=2V_{max}$=1574 kN with u=6.8 mm (u/D=1.9% and u/L_{eff}=4.2‰) while in the beam S3D36S54_3, $P_{max}=2V_{max}$=1271 kN with u=5.2 mm (u/D=1.4% and u/L_{eff}=3.2‰). The beams S3D36A54_1 and S3D36A54_3 had the similar load-deflection curves that demonstrated a very stiff beam response connected with the high vertical load and small deflection (Fig.A2.2C). The beam S3D36A54_2 possessed the relatively low ultimate force and high deflection as compared to S3D36A54_1 and S3D36A54_3 (due to weaker concrete). The post-peak behaviour was brittle (all beams lost their capacity in a sudden failure).

Series '4': varying effective depth *D* and bending zone span *b* at constant shear zone span *a*

The varying effective depth D=0.22, 0.43 and 0.72 m and constant shear span a=1.08 m contributed to the change of the parameter η_a from 5 through 2.5 down to 1.5, the parameter η_b from 2.5 down to 0.75 and the parameter η_l from 12 down to 3.75 (Tab.A2.2). The effect of the varying parameter η_a on beams' strength, ductility and failure modes was very strong.

The lowest beams S4D22A108 with η_a=5.0 failed due to concrete crushing in the constant bending moment zone similarly to the beams S3D36A218 with η_a=6.0 in the series '3'. The average ultimate vertical force achieved by the beams S4D22A108 was $P_{max}=2V_{max}$=207.4 kN with the corresponding average deflection u=19.1 mm. The load-displacement curves (Fig.A2.3A) had similar shapes and all of them showed the post-peak structural quasi-brittle behaviour. The average normalized deflection was u/D=7.8% and u/L_{eff}=7.1‰.

For the medium-high beam (η_a=2.5), two beams S4D43A108_1 and S4D43A108_2 lost the load bearing capacity in shear-compression with the average P_{max}=751 kN for u=13.5 mm (u/D=3.1% and u/L_{eff}=5.2‰). However, the third beam S4D36A108_3 failed due to concrete crushing in the constant bending moment zone for P_{max}=732 kN with u=14.3 mm (u/D=3.3% and u/L_{eff}=5.3‰). The force-deflection curves (Fig.A2.3B) had the similar shapes up to the peak force, later the post-peak

behaviour was different. The beams S4D36A108_1 and S4D36A108_2 failed in a brittle way and the beam S4D36A108_3 n a quasi-brittle way.

The highest beams S4D72A108 were first designed as plain beams with the rectangular cross-section ('trial beams'). The highest 'trial' beams denoted as S4D72A108_T1 and S4D72A108_T2 (with η_a=1.5) failed due to local concrete crushing at the supporting plate for P_{max}=1375 kN and u=8.62 mm. For this reason, the beam S4D72A108_T3 was strengthened by increasing its thickness locally at supports. It failed under shear-compression conditions for P_{max}=1423 kN and u=8.7 mm (u/D=1.2% and u/L_{eff}=3.2‰). The beams S4D72A108_1 and S4D72A108_2 had however 4 symmetric pilasters at all loading/supporting points (Fig.A2.1). Those beams also failed in shear-compression for the similar load, i.e. P_{max}=1418 kN for u=9.6 mm (u/D=1.3% and u/L_{eff}=3.5‰). The entire force-deflection curves of the beams S4D72A108_1, S4D72A108_2 and S4D72A108_T3 (Fig.A2.3C) were of a similar shape.

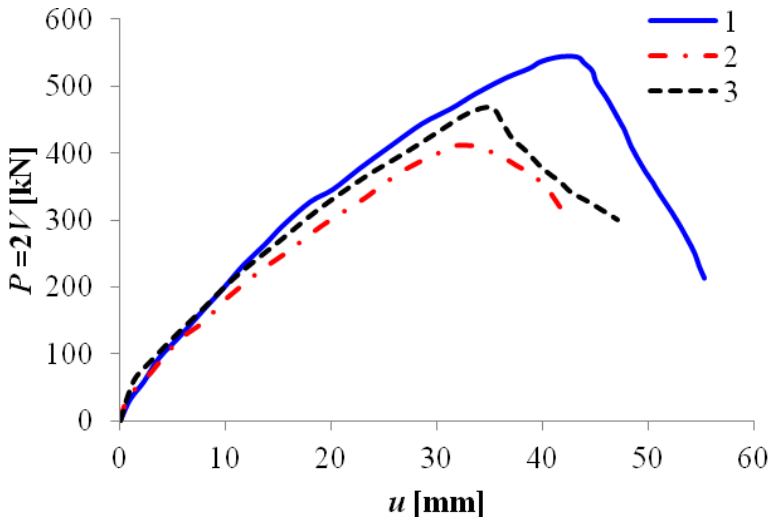

A)

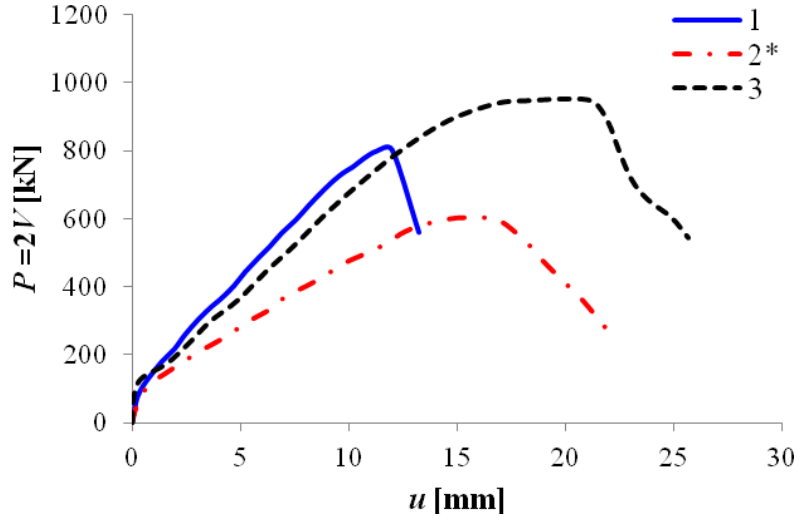

B)

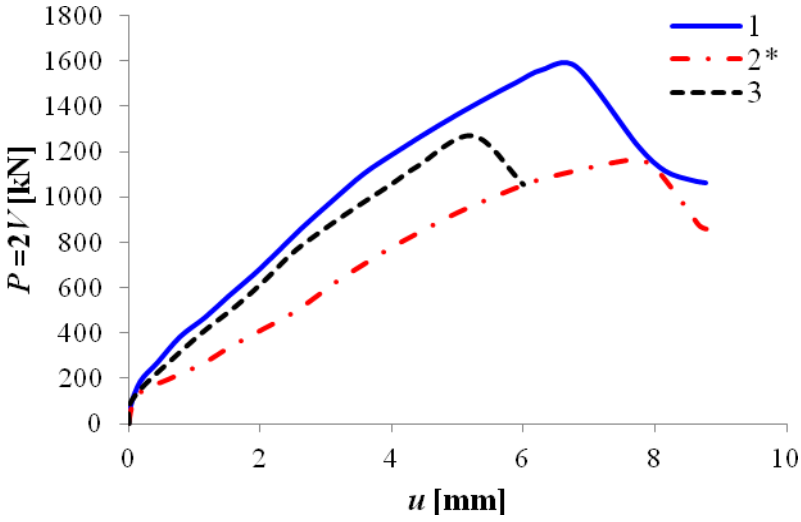

C)

Fig.A2.2: Experimental normalized vertical force-deflection P=f(u) curves of RC beams with stirrups (series '3') of Fig.A2.1: A) S3D36A216 with η_a=6.0, B) S3D36A108) with η_a=3.0 and C) S3D36A54 with η_a=1.5 (* - beams made of weaker concrete)

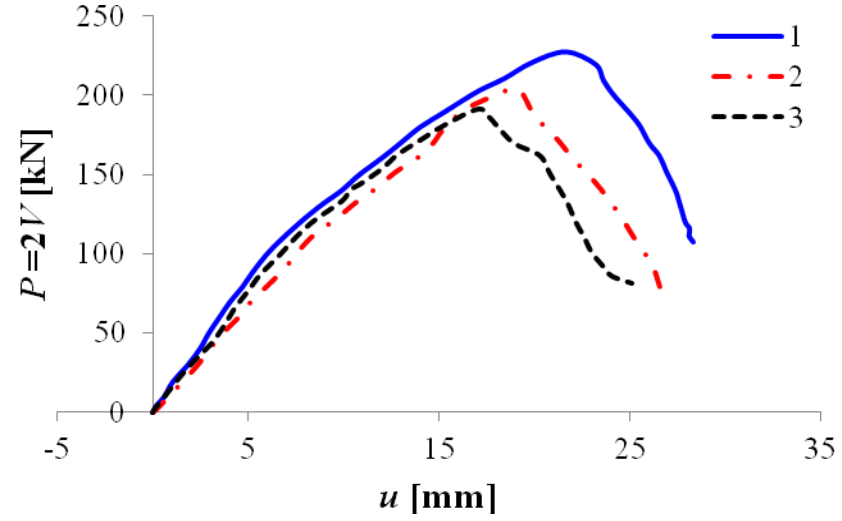

a)

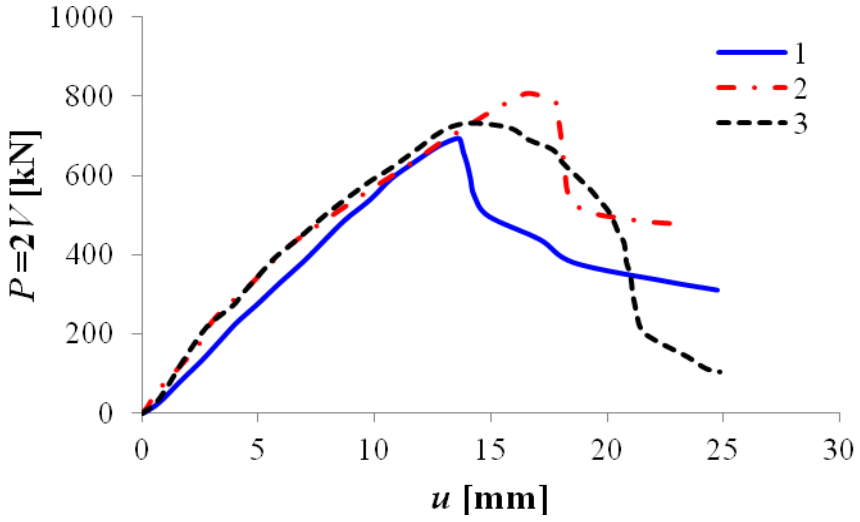

b)

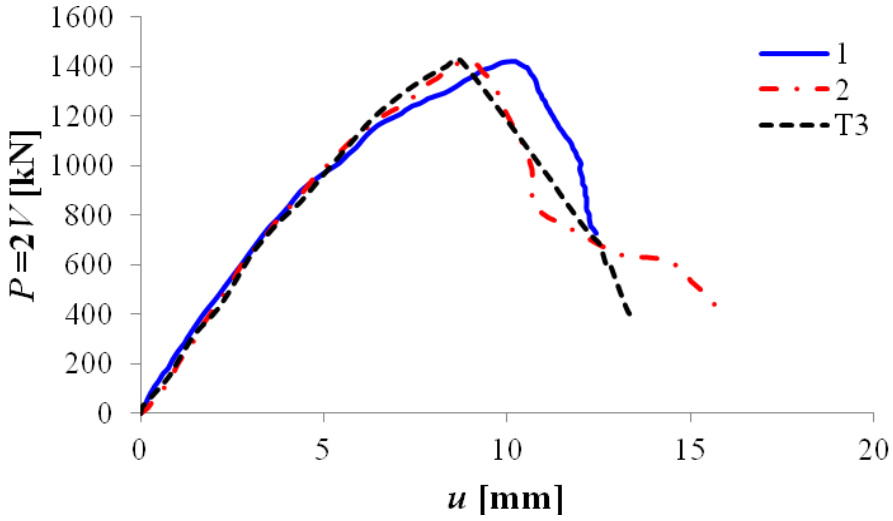

c)

Fig.A2.3: Experimental normalized vertical force-deflection P=f(u) curves of RC beams with stirrups (series '4') of Fig.A2.1: A) S4D22A108 with ηa=6.0, B) S4D43A108 with ηa=3.0 and C) S4D72A108 with ηa=1.5

Figure A2.4 compares the experimental results from Series '3' and '4', expressed as a function of the parameters $\eta_a=a/D$ and $\eta_b=b/D$. The normalized ultimate shear stress in both the series was related to the uniaxial compression strength f_c as $V_{max}/(tDf_c)$ due to the different concrete class. It apparently decreased with increasing parameter η_a. The increasing beam depth D (with the constant a) had a slightly weaker effect on the ultimate shear stress reduction than the decreasing shear span a (with the constant D).

Tab.A2.3: Experimental failure force $P_{max}=2V_{max}$ and shear failure stress $v=V_{max}/(tD)$ for two failure modes with RC beams including stirrups of series '3' and series '4' (C - crushing of concrete in compression zone, SC – shear-compression)

Beam description	**Beam '1'** P_{max} **[kN]**	**Beam '2'** P_{max} **[kN]**	**Beam '3'** P_{max} **[kN]**	**Mean value** P_{max}**[kN]**	$v=V_{max}/(tD)$ **[MPa]**	**Failure mode**
S3D36A216 η_a=6.0, η_b=1.5	544	411	469	475	2.64	C
S3D36A108 η_a=3.0, η_b=1.5	802	601	954	878*	4.88*	SC/C
S3D36A54 η_a=1.5, η_b=1.5	1574	1165	1271	1423*	7.43*	SC
S4D22A108 η_a=5.0, η_b=2.5	227.4	203.6	191.2	207.4	3.17	C
S4D43A108 η_a=2.5, η_b=1.5	694	807.5	731.8	744.4	5.76	SC/C

S4D72A108 η_a=1.5, η_b=0.75	1420	1416	1423	1420	6.52	SC

*average value without beam '2' of weaker concrete

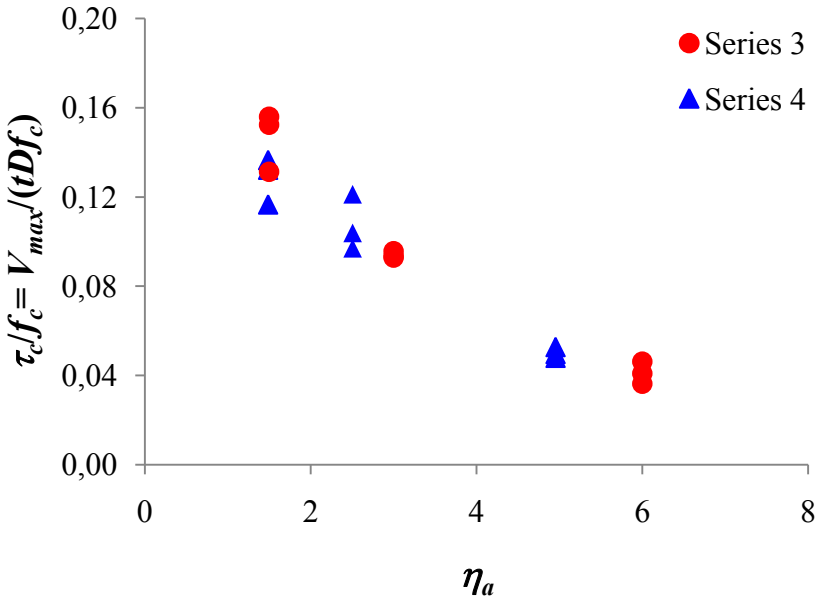

a)

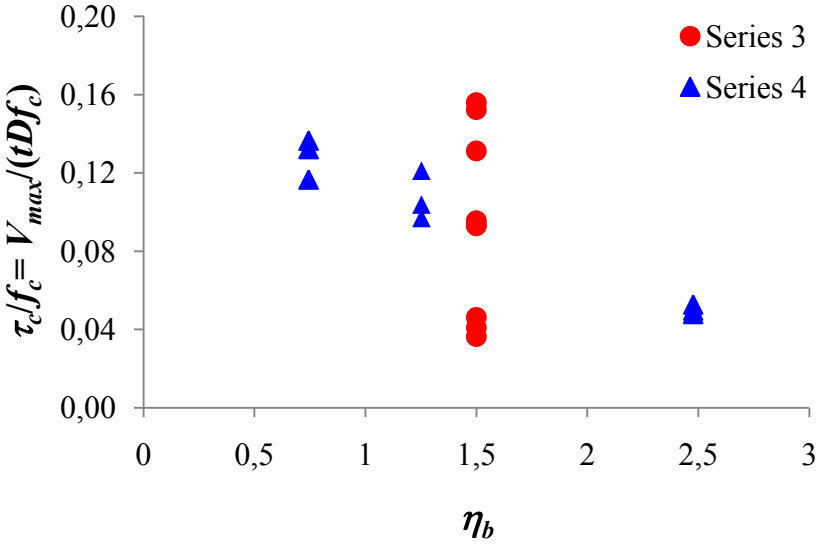

b)

Fig.A2.4: Experimental normalized ultimate shear stress τ_c/f_c in series '3' and '4' for varying parameters $\eta_a=a/D$ (a) and $\eta_b=b/D$ (b) (f_c - uniaxial compression strength of concrete)

Figure A2.5 presents the comparative results from current and previous experiments on the RC beams without shear reinforcement (Series '1' and '2'). The series 1 had the varying beam depth D=180 mm, 360 mm and 720 mm and the constant shear span a=1080 mm with the corresponding parameter η_a=6, 3 and 1.5. The series 2 had the constant beam depth D=360 mm and the varying shear span a=360, 720 and 1080 mm with the corresponding parameter η_a=a/D=1, 2 and 3. The presence of stirrups obviously increased the beam strength in particular for the lower parameter η_a; the shear strength increased by 130% (η_a=3.0) and 300% (η_a=1.5). Their presence also strongly affected the failure mode. The slender beams without stirrups (η_a=6 in the series '1') failed due to steel yielding whereas the slender beams with stirrups (η_a=6 in the series '3') failed due to concrete crushing. The beams of a transitional geometry without stirrups in the series '1' (with η_a=2.5) failed in diagonal tension whereas the beams in the series '4' with η_a=3.0 failed due to shear-compression/concrete crushing. The deep beams with η_a=1.5 in both the series '1' and series '4' behaved similarly and failed under shear-compression conditions. The beams with the varying shear span a without stirrups in the series '2' and with stirrups in the series '3' had also a similar trend for the parameter $\eta_a \leq 3$ (Fig.A2.5b). The ultimate shear stress of the beams with the varying depth D in the series '1' and series '4' had also a similar trend when $\eta_a \leq 3$ (Fig.A2.5a). The increase of the ultimate shear stress of the beams with η_a=1 as compared to η_a=2 in the series '2' was significantly stronger than between η_a=2 and η_a=3 (series '2') or between η_a=1.5 and η_a=3 (series '3'). Thus the ultimate shear stress did not proportionally change with η_a. The shear reinforcement in the beams with the varying shear span had the same effect as in the beams with the varying beam depth. The stirrups in the series '3' increased the ultimate shear stress and changed the beam failure mode of the beams with η_a=3 as compared to the series '2'.

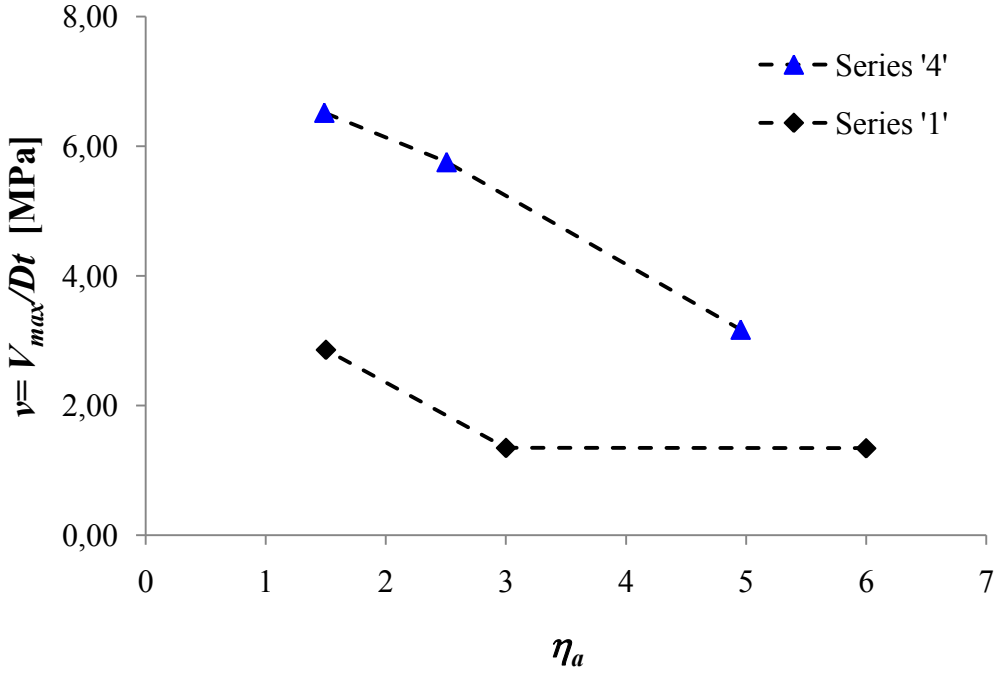

a)

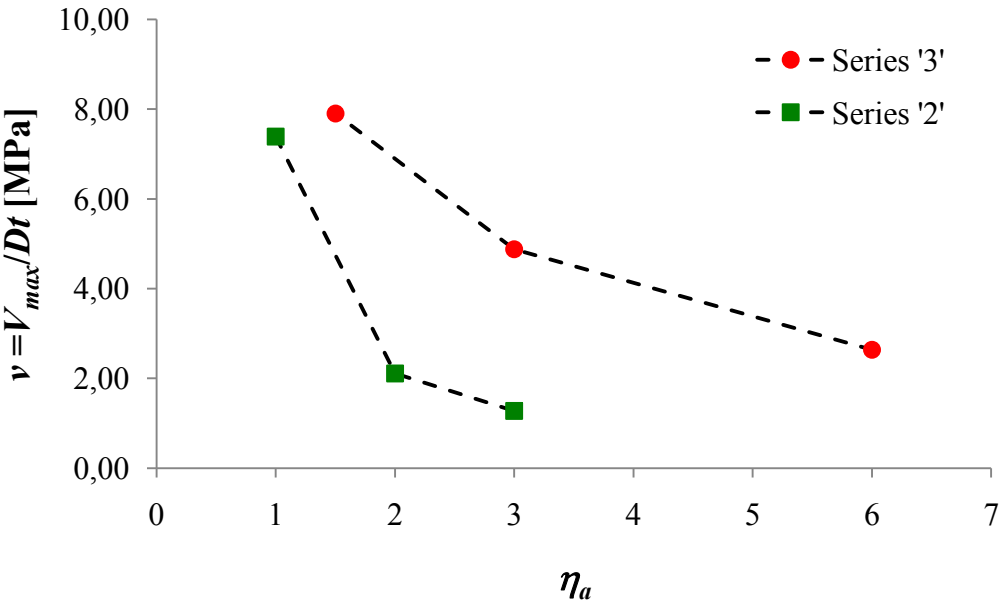

b)

Fig.A2.5: Average ultimate shear stress in beams with shear reinforcement (series '3' and series '4') and without shear reinforcement (series '1' and series '2') with varying parameter $\eta_a=a/D$ (D - effective depth and a - shear span)

Tab.A2.4: Experimental and theoretical shear strengths/ultimate stresses according to various analytical models of Section 4 (v_C^{Exp} – experimental average shear stress of beams failing due to concrete crushing, v_{SC}^{Exp} – experimental average shear strength of beams failing due to shear-compression)

Beam	η_a	Failure mode	ν_C^{Exp}	ν_{SC}^{Exp}	ν^{EC} (Eq.6)	ν^{Fl} (Eq.17)	ν^{STM} (Eq.8)	ν^{MSTM} (Eq.12)	ν^{CSTM} (Eq.16)
S3D36A216	6	C	2.64	-	2.03	2.86	-	-	-
S3D36A108	3	C/SC	5.30	4.46	2.03	5.72	4.52	5.91	3.63
S3D36A54	1.5	SC	-	7.90	2.03	-	8.22	10.43	8.43
S4D22A108	5	C	3.14	-	2.11	3.38	-	-	-
S4D43A108	2.5	C/SC	5.67	5.82	2.11	6.84	4.97	6.78	4.65
S4D72A108	1.5	SC	-	6.52	2.11	-	6.83	10.11	5.19

A2.5 Failure mechanisms and crack patterns

The simultaneous proportional scaling of the RC beams along two dimensions (length and height) did not change the parameter $\eta_a=a/D$, hence a failure mode (assuming the constant reinforcement ratio) remained the same as it was demonstrated in experiments by Korol and Tejchman (Korol&Tejchman 2014). In contrast, the separate scaling of RC beams along one direction only (i.e. length or height) modified the parameter $\eta_a=a/D$ that affected the failure mode. The other parameters that affected the failure mode were the flexural ρ_l and shear ρ_s reinforcement ratios. The sketches in Fig.A2.6 illustrate the changes of the failure mode with the varying geometry parameter η_a and reinforcement ratios ρ_l and ρ_s. The slender beams with η_a>4 and without shear reinforcement (sketch 'a' in Fig.8) failed due to steel yielding (symbol 'Y'). With decreasing parameter η_a, the failure mode changed from diagonal tension (symbol 'DT') for beams with a transitional geometry η_a (sketch 'e') to shear-compression (symbol 'SC') for deep beams (sketch 'i'). When the main reinforcement ratio increased (the steel yielding was eliminated), the slender beams failed in diagonal tension (sketch 'b') and the beams of a transitional geometry were damaged by either diagonal tension or shear-compression failure (sketch 'f') while the deep beams influenced by an arch action failed in shear-compression (sketch 'j'). Adding of a sufficient amount of shear reinforcement ρ_s in slender beams (to suppress the shear failure) contributed to concrete crushing

(symbol 'CC') in the constant bending moment zone (sketches 'c' and 'd'). The 'CC' failure occurred before the main and shear reinforcement strength were achieved. The beams of a transitional geometry with shear reinforcement (sketches 'g' and 'h') were damaged due to shear-compression or concrete crushing. The further increase of the shear reinforcement ratio might change the failure mode in deep beams from shear-compression (sketch 'k') to the damage of the support's zone (sketch 'l'). The support zone failure in deep beams (symbol 'N') was due to insufficient nodal zone strength which was weaker than both the strut and tie strength i.e. both failure type 'Y' and 'SC' could not occur (the CCT node at the support is always weaker than the CCC node at loading point).

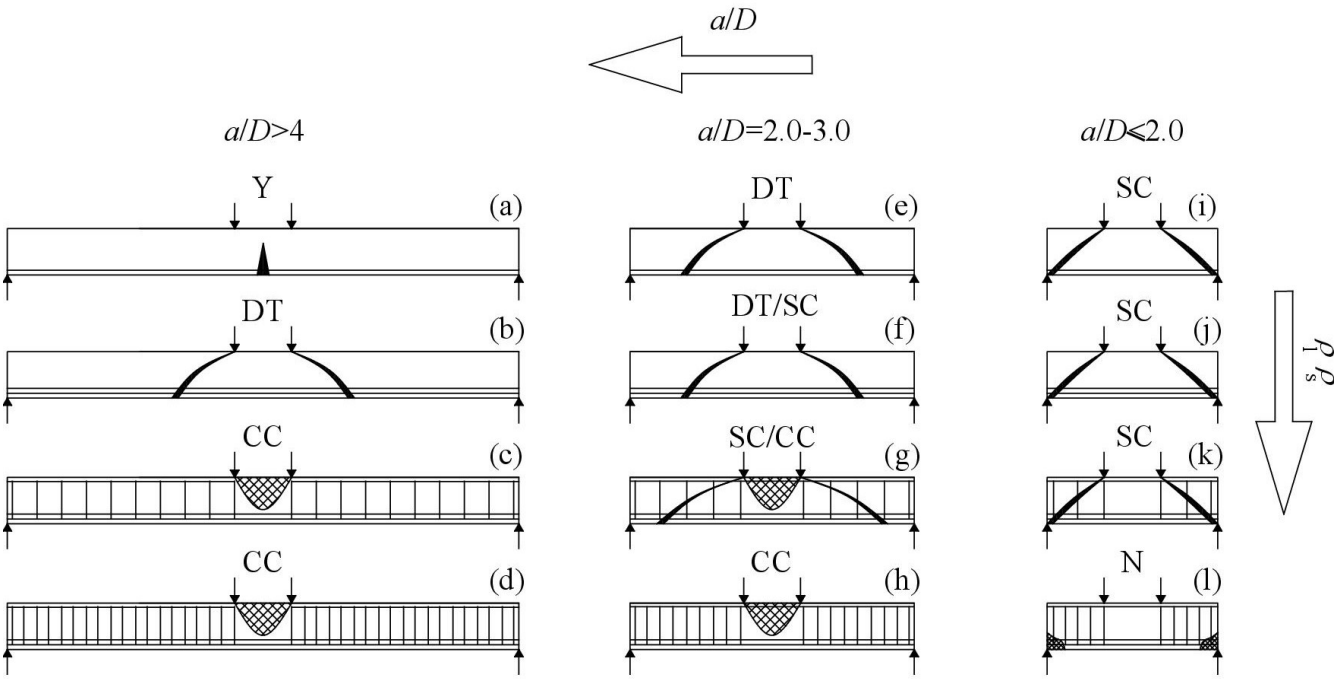

Fig.A2.6: Sketches of failure modes of RC beams with/without stirrups of varying geometry and reinforcement ratio (Y - reinforcement yielding, DT - diagonal tension, SC - shear-compression, CC - concrete crushing and N –support zone crushing)

The evolution of the cracking process of the beam S3D36A216 with concrete crushing in the compression zone is shown in Fig.A2.7. First, for about 13% of P_{max}, some vertical flexural cracks appeared in the constant bending moment zone *b* and gradually developed into the compression zone direction up to 52% of the beam total height *H* (h^b_{cr}=0.52×*H*). The inclined cracks initiated in the shear zones *a* for 30% of P_{max} and stopped to grow after reaching approximately the beam height of h^a_{cr}=0.66×*H*. The flexural and shear cracks never crossed the upper beam edge. The

average crack spacing (measured above the reinforcement) was s=98 mm. The cracks extended up to the width of w=0.4 mm in the bending zone b and w=0.15 mm in the shear zone a leading to a significant beam deflection. The concrete crushing started with a nearly horizontal crack which developed between two loading points close to the upper beam edge. The subsequent cracks were more curved and propagated towards the beam bottom. The cracks coincided with a trajectory of principal tensile stresses. Finally, the sudden failure took place after a significant part of the concrete surface separated at the beam mid-span region.

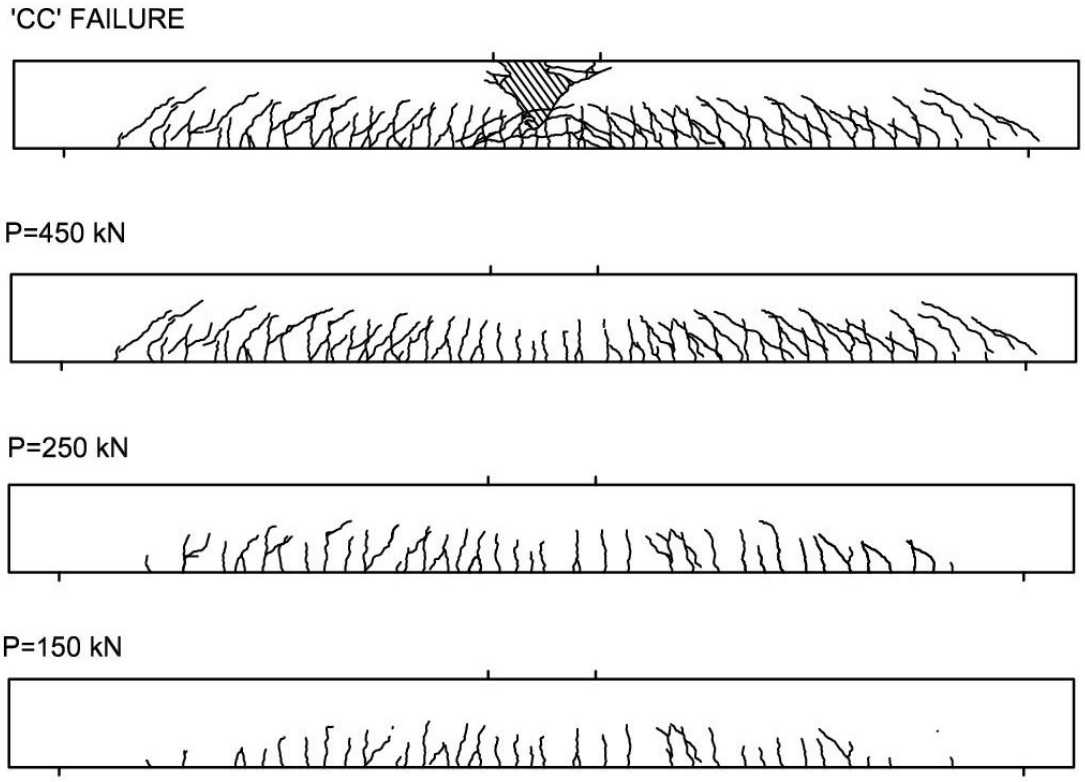

Fig.A2.7: Crack pattern evolution in RC beam S3D36A216_3 failing due to concrete crushing in constant bending moment zone

Figure A2.8 presents the crack evolution with increasing vertical load P in the beam S3D36A108_1 that failed in a shear-compression failure mode. All beams S3D36A108 cracked similarly except of the final loading stage. First, the vertical cracks appeared in the bending zone b at 8% of P_{max} and next developed finally up to h^b_{cr}=0.52×H. Next, the inclined cracks started to grow for 17% of P_{max} and the cracked section in the shear zones a was higher than in the bending zone h^a_{cr}=0.79×H. Afterwards, the beams S3D36A108_2 and S3D36A108_3 failed due to concrete crushing in the constant bending moment zone (in the same way as the beams S3D36A216). In contrast,

S3D36A108_1 failed in shear-compression with a critical diagonal crack that appeared for 43% of P_{max} and was affected by both tangential (shear) and normal (opening) crack displacements. Eventually, in the front of the critical crack tip, local concrete crushing occurred and afterwards the crack intersected the beam upper edge that caused the sudden beam failure. The critical crack inclination to the horizontal was 35° and its normalized distance to the support was d_c/a=0.39. The average crack distance in the beams S3D36A108 was s=11 mm (measured above the longitudinal reinforcement level) and was similar as in all 3 beams independently of the failure mechanism. The maximum width of vertical cracks in the constant bending moment zone was w=0.15 mm in all beams. The inclined cracks were wider than the vertical ones and had the width of w=0.3 mm (except of the critical one). The critical crack in the beam S3D36A108_1 had the width of w=1.0 mm before the failure. As compared to the longer beams S3D36A216, the shorter beams S3D36A108 had the narrower vertical cracks and wider inclined cracks. The cracked section height in the bending zone h^b_{cr} was the same in the beams S3D36A108 and S3D36A216 whereas in the shear zone the shorter beams had the cracked section by 33% higher. The average crack distance differed by 14% as compared to the longer beams.

The subsequent cracking stages preceding the shear-compression failure mode of a strut in the beams S3D36A54 can be seen in Fig.A2.9. The initial vertical cracks appeared for 6% of P_{max} in the constant bending zone *b*. Next, for 28% of P_{max}, the inclined cracks developed and the last one (the nearest one to the support) turned out to be the critical one. The inclination of the critical crack to the horizontal was 44°. The crack initiated from the corner of the supporting plate. The cracked section height before the failure was h^b_{cr}=0.52×H in the bending zone and h^a_{cr}=0.87×H in the shear zone. When the critical crack reached the loading plate, a few new cracks appeared parallel to the critical one. Afterwards, concrete between those parallel cracks was crushed and separated from the remaining beam part. The maximum width of the vertical cracks was similar in all deep beams S3D36A54 w=0.15 mm while the width of the inclined cracks (except of the critical one) was w=0.4 mm. The critical crack had the width of w=1.2 mm before the failure. The crack distance was s=110 mm and was similar as in the beams S3D36A108.

Figure A2.10 presents the final crack pattern for RC beams of the series '3' with a different failure mode due to the varying $\eta_a=a/D$. In all beams, the flexural cracks in the bending zone *b* had the same average height independently of η_a, whereas the inclined cracks in the shear zones developed higher for the lower parameter η_a. The crack spacing was slightly lower in the longest beams by ca.

10% as compared to the other beams. The width of flexural cracks was larger in the longest beams and the inclined cracks were the widest in the shortest beams.

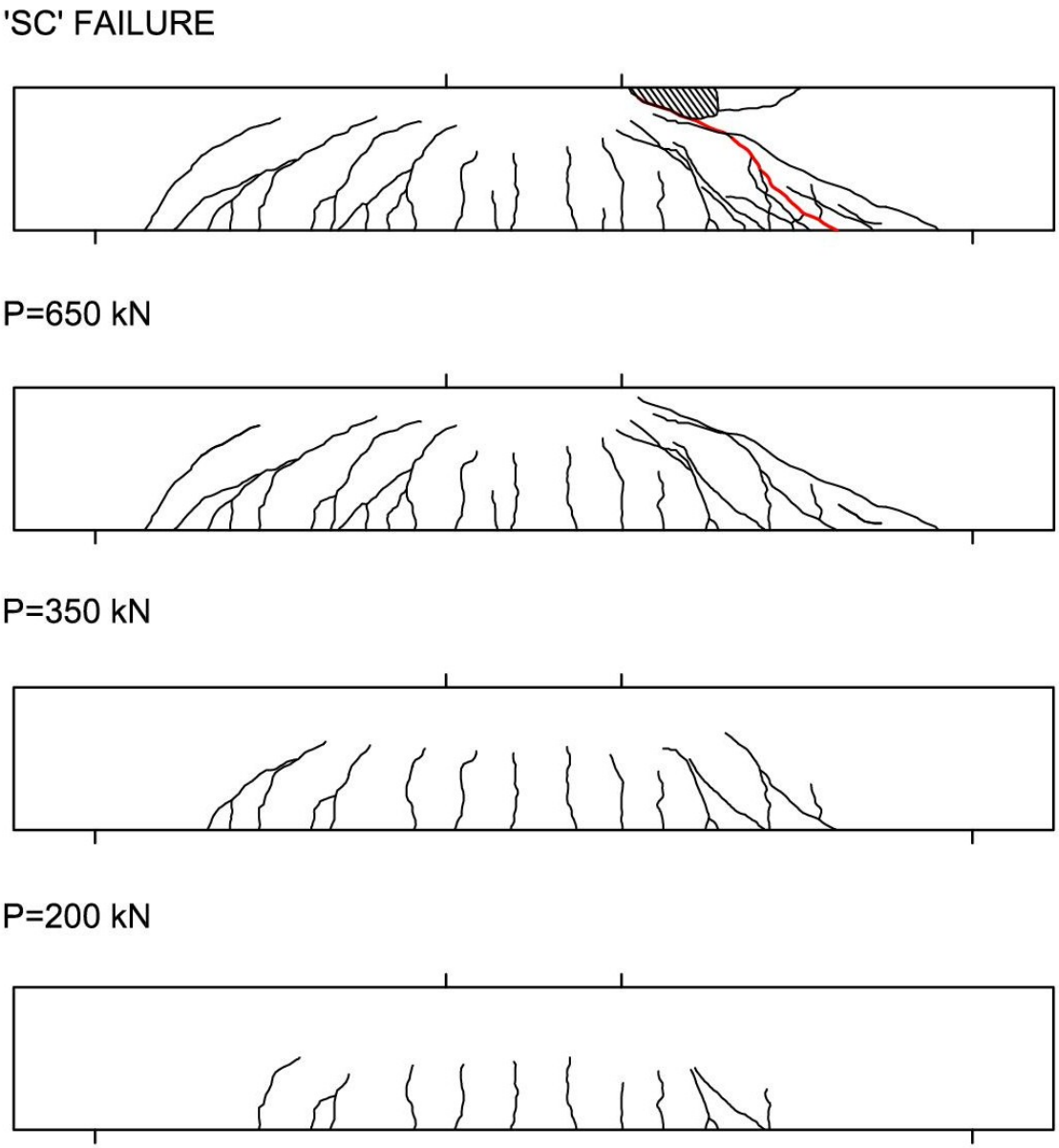

Fig.A2.8: Crack pattern evolution in RC beam S3D36A108_1 during shear-compression failure (critical diagonal crack is in red)

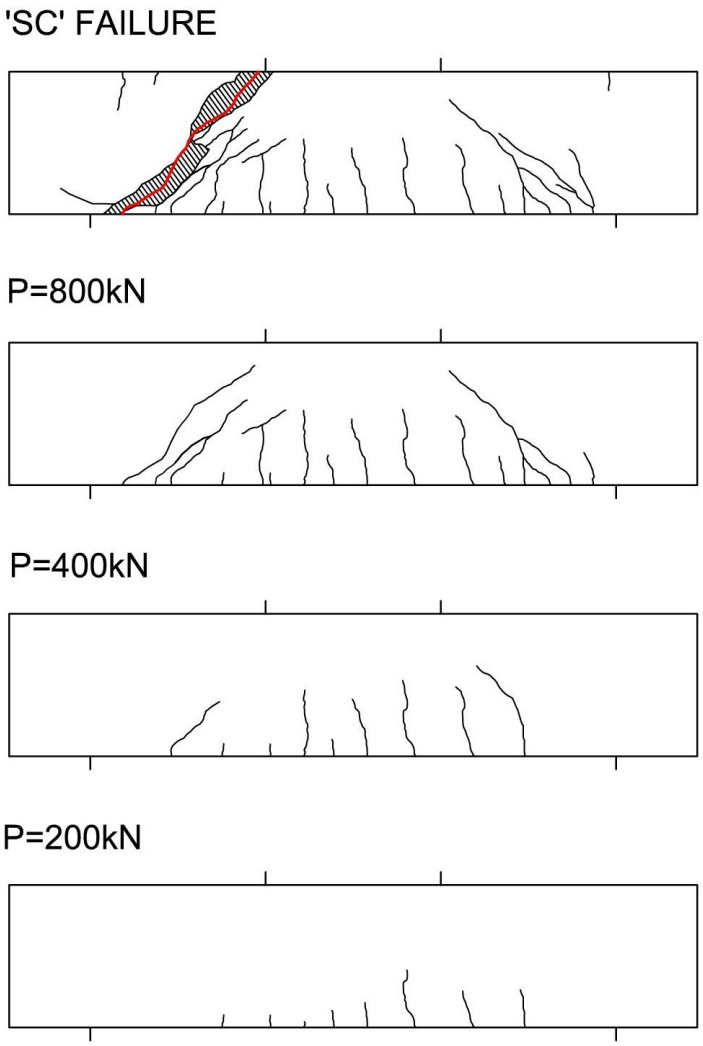

Fig.A2.9: Crack pattern evolution in RC beam S3D36A54_1 during shear-compression failure (critical diagonal crack is in red)

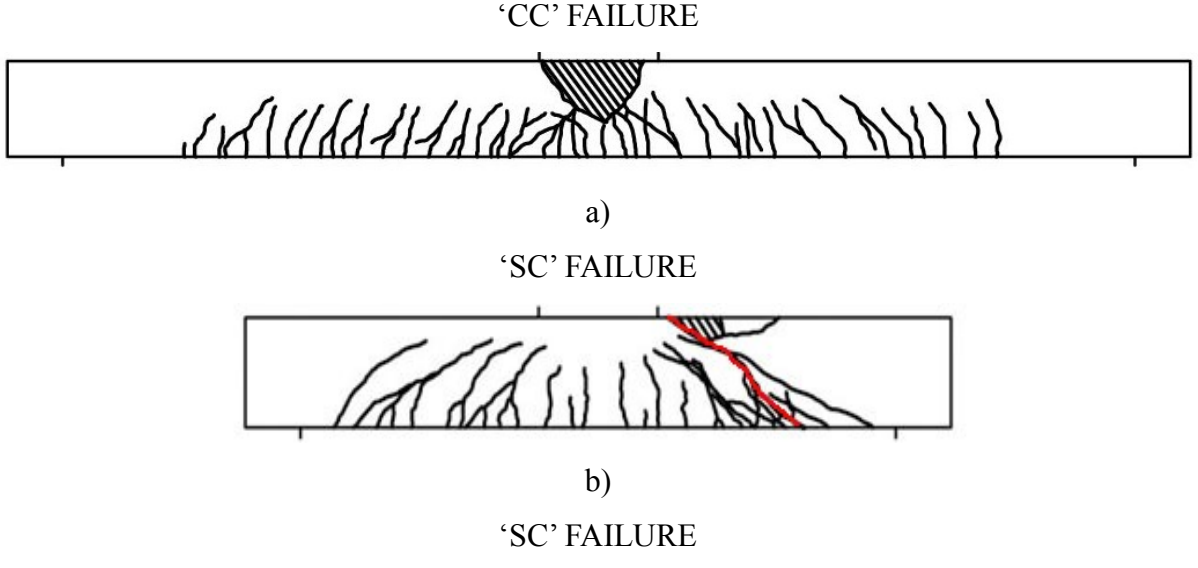

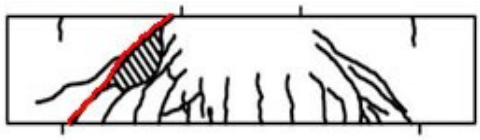

c)

Fig.A2.10: Crack pattern at failure in RC beams of series '3': a) concrete crushing in beam S3D36A216_1 with η_a=6, b) shear-compression failure in beam S3D36A108_1 with η_a=6 and c) shear-compression strut failure in beam S3D36A54 with η_a=1.5 (critical diagonal crack is in red)

Figure A2.11 includes the final crack patterns for RC beams in the series '4' that failed in a different mode due to the varying parameter η_a=*a/D*. The average crack spacing in the lowest beams was about 50% lower than in other beams in the series '4'. The flexural cracks in the bending zone *b* were always shorter than the inclined cracks in the shear zone *a*. The higher the beam and lower η_a, the more pronounced was the difference between the height of vertical and inclined cracks in the bending and shear zone. The width of cracks was also affected by the beam depth *D* (and η_a) as in the series '3'. The flexural cracks were wider in the lower beams (i.e. for the higher parameter η_a). In contrast, the shear cracks were wider in higher beams (i.e. for the lower parameter η_a).

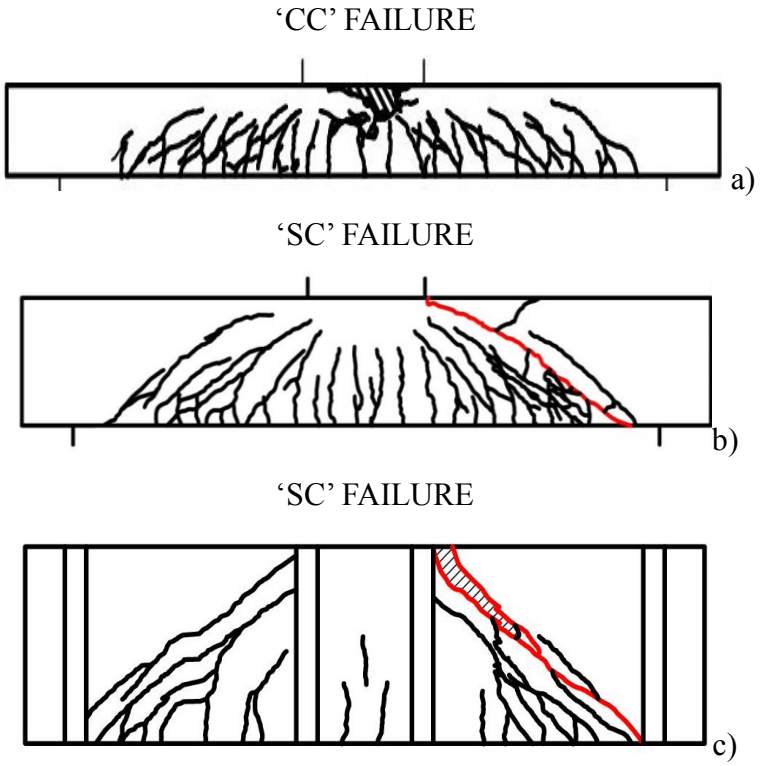

Fig.A2.11: Crack pattern at failure in RC beams (series '4'): a) concrete crushing in beam S4D22A108_1 for η_a=5, b) shear-compression failure in beam S4D43A108_2 for η_a=2.5 and c)

shear-compression failure in beam S4D72A108_2 with pilasters for η_a=1.5 (critical diagonal crack is in red)

Crack inclination and heights

Figure A2.12A compares the normalized height of the compressive zone in the pure bending b and shear zone a. The height of the compressive zone was calculated as a difference between the measured cracked section height and the beam total height (h^b_c=H-h^b_{cr} or h^a_c=H-h^a_{cr}). The height of the compressive zone in the pure bending part was independent of a and η_a (D was constant). Whereas, the height of the compressive zone in the shear span was proportionally increasing with o a and η_a. Figure A2.12B compares the average normalized compressive zone height in the series '4' that was separately measured in the bending *b* and shear zone *a*. Similarly to the series '3', the compressive zone height in the pure bending area h^b_c was proportional to the beam depth *D* and independent of η_a. On the other hand, the compressive zone height in the shear span h^a_c was proportionally increasing with η_a.

DIC – digital image correlation

The digital image correlation method (DIC), was described in A1.5.

Figure A2.13 shows the evolution of an exemplary vertical (flexural) localized zone at the beam mid-span with the increasing vertical force for the beam S3D36A108_2 that failed in bending (η_a=3). The localized zone was enforced by a small notch. The localized zone appeared at around 3% of the failure force. The localized zone reached the top of the image frame for 9% of the failure force.

In order to calculate the width of a localized zone w_{lz}, the calculated displacements were fitted first by the error function ERF (Skarżyński et al. 2011, Skarżyński&Tejchman 2013a):

$$ERF(x) = \frac{2}{\sqrt{x}} \int_0^x e^{-t^2} dt \,. \tag{A2.1}$$

The halved error function evaluated at $\frac{x}{s\sqrt{2}}$ for the positive x-values gives the probability that the measurement under the influence of normally distributed errors with the standard deviation *s* has a distance smaller than *x* from the mean value. The fitting function parameter *s* in Eq.A2.1 was used to

determine the width of a localized zone w_c. Based on experimental results regarding concrete beams (Skarżyński et al. 2011), the width w_{lz} might be calculated from the equation $w_{lz}=4s$. Thus, 95% of the values of the normal distribution function area were within the distance of $2s$ in both the directions from the mean value. The measured width of the localized zone at 10 mm above the bottom beam was w_c=3.13 mm (Fig.A2.14) lying between 2 mm≅d_{50} (d_{50} - the mean aggregate diameter) and 4 mm≅0.25d_{max} (d_{max} - the maximum aggregate diameter). Later a discrete macro-crack was created.

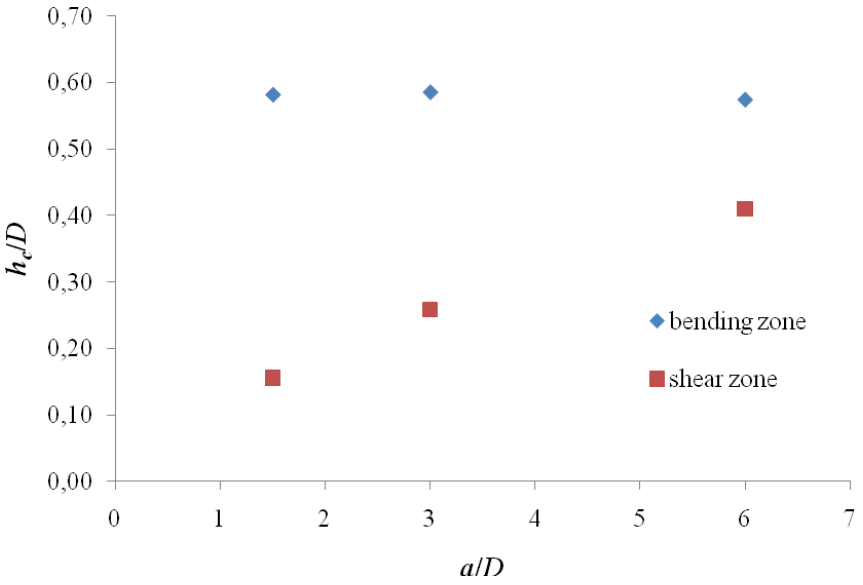

A)

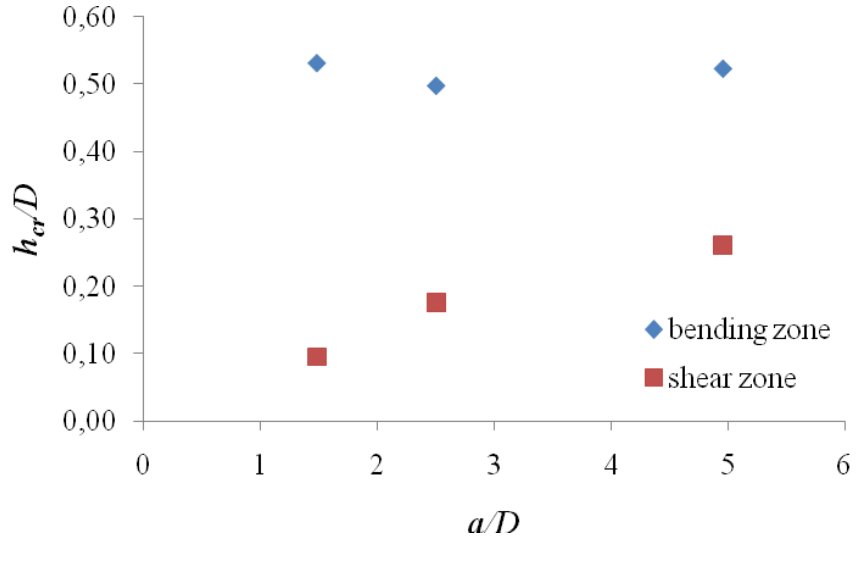

B)

Fig.A2.12: Average normalized compressive zone height h_c/D in RC beams with A) constant depth D and varying shear zone a (series '3') and B) varying depth D and constant shear zone a (series '4')

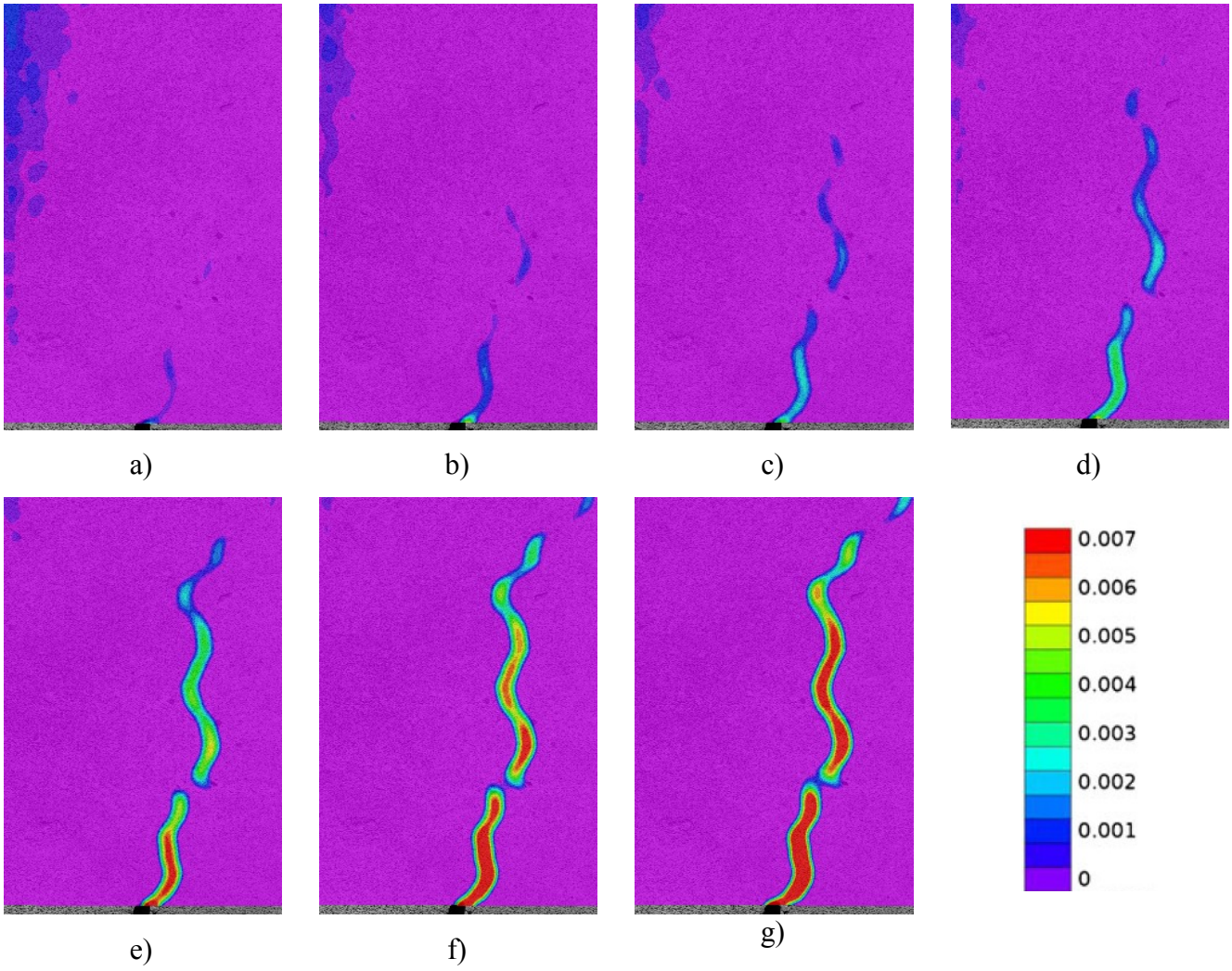

Fig.A2.13: Horizontal normal strain maps ε_{xx} for beam S3D36A108_2 failed in bending ($\eta_a=a/D=6$) (colour scale denotes strain intensity) for increasing vertical force P: a) 3%, b) 4%, c) 5%, d) 6%, e) 7%, f) 8% and g) 9% of failure force P_{max} (strains are shown for beam mid-span)

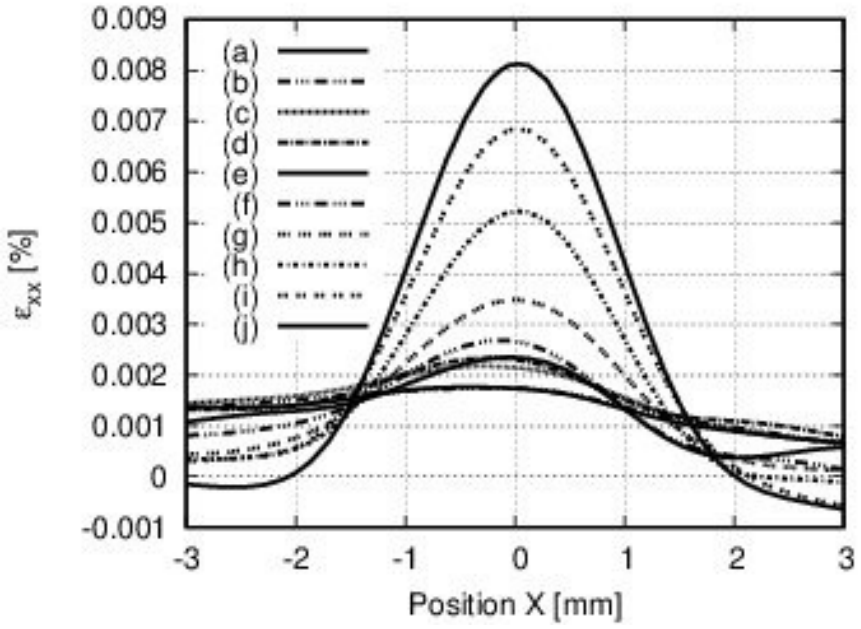

Fig.A2.14: DIC measurements: evolution of horizontal strain ε_{xx} for different load levels (10 mm above beam bottom)

DEMEC crack displacement measurements

The DEMEC triangle measurements enabled us to determine the normal (opening) and tangential (shear) crack displacements (Eqs.A1.1-4). Figure A2.15 shows the triangle location in DEMEC measurements for RC beams. Figures A2.16 and A2.17 present the measured crack displacement evolutions for each beam size at two locations: 1) the beam mid-height and 2) the top of the shear-compression crack. The measured strains are shown in Figs.A2.17 for the RC beams of the series '3'.

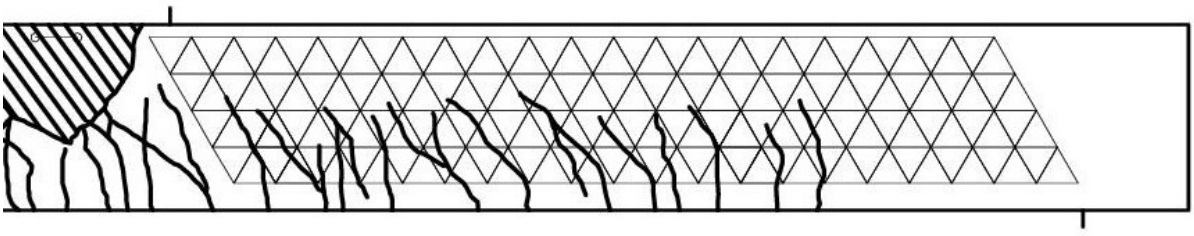

a)

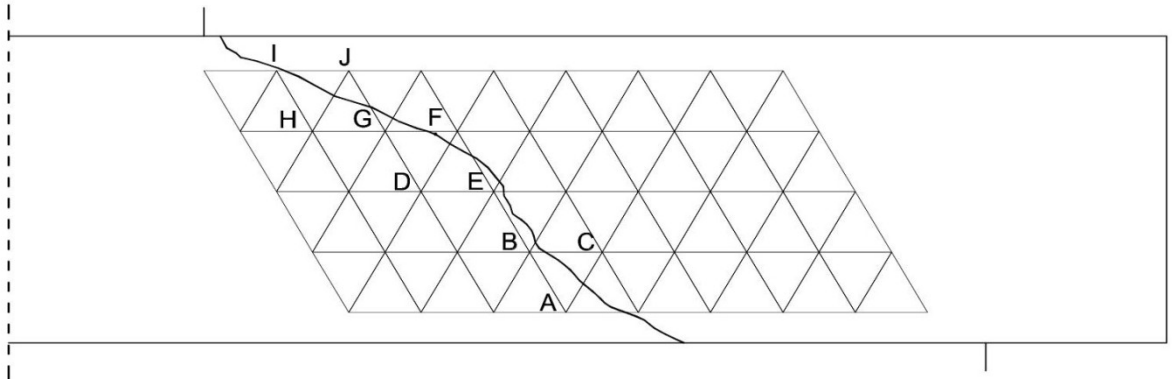

b)

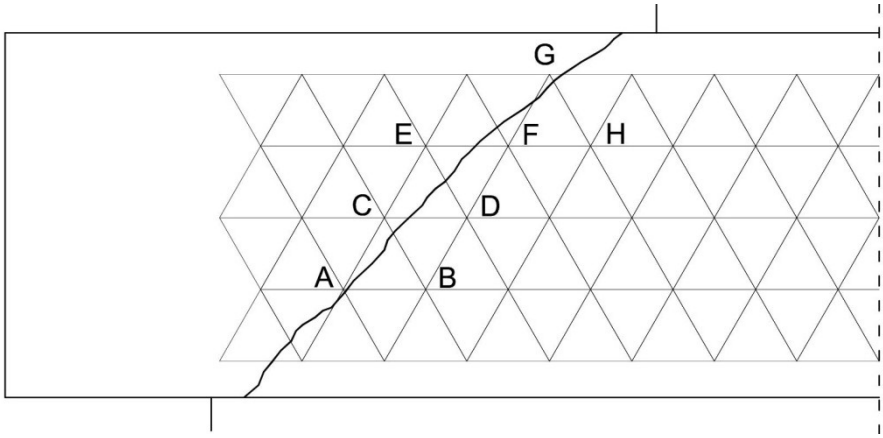

c) A)

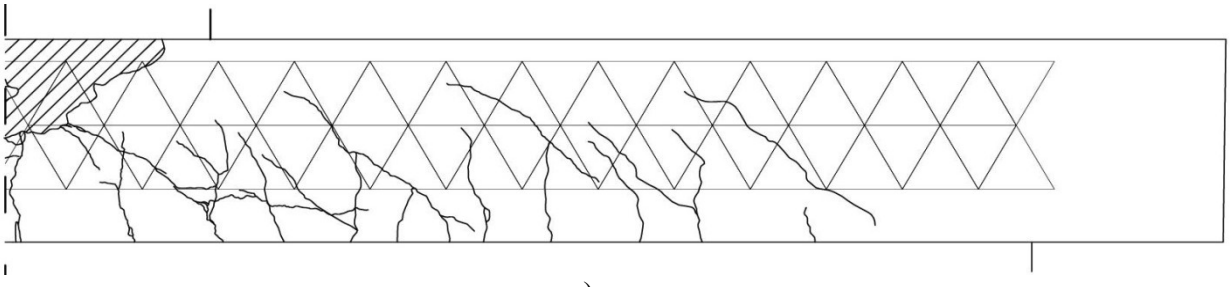

a)

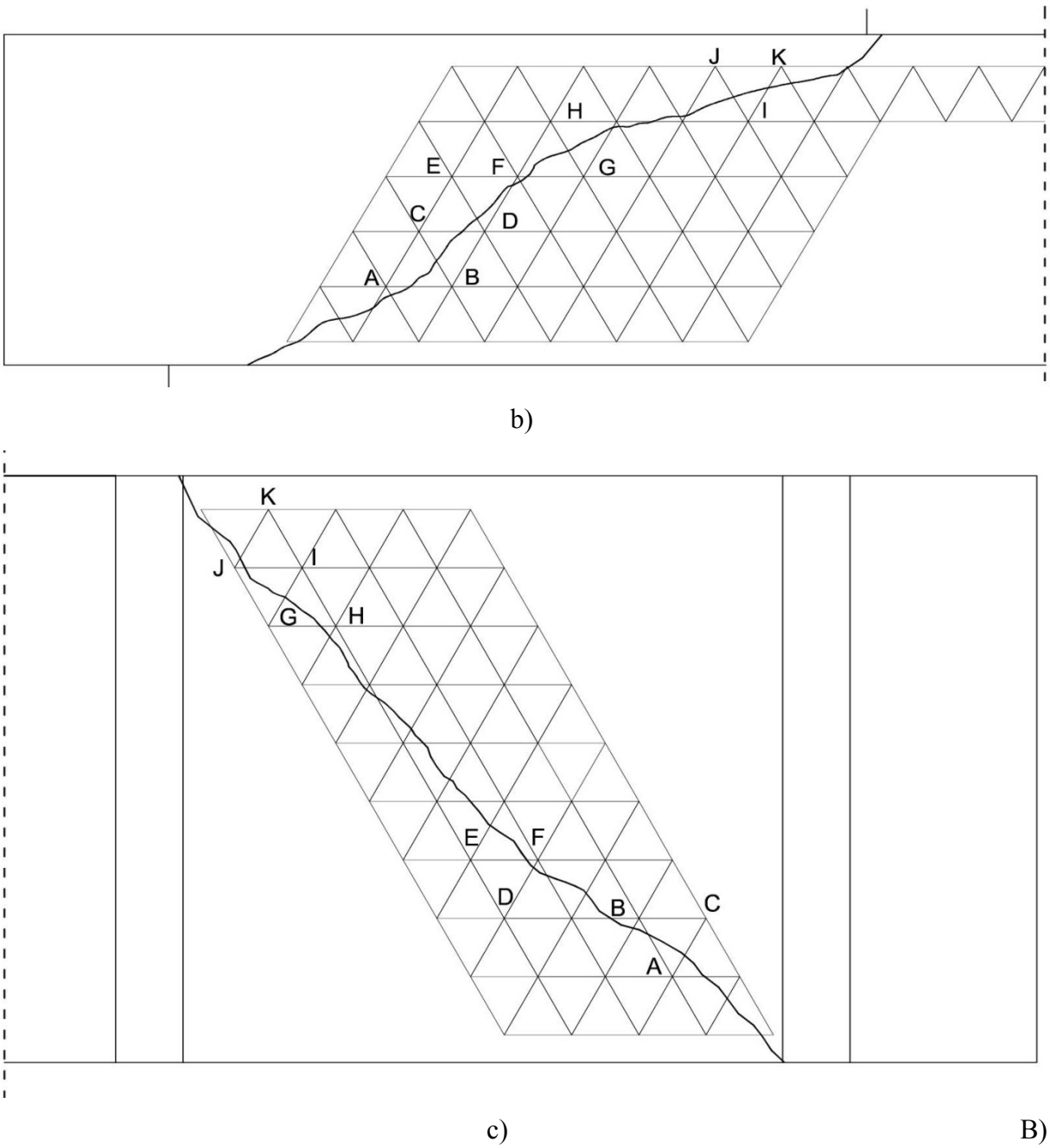

Fig.A2.15: Location of triangles for DEMEC measurements in RC beams in series '3' (A): a) S3D36A216 (a=216 mm, η_a=6), b) S3D36A108 (a=108 mm, η_a=3), c) S3D36A54 (a=54 mm, η_a=1.5) and in series '4' (B): a) S4D22A108 (D=220 mm, η_a=6), b) S4D43A108 (D=430 mm, η_a=3), c) S4D72A108 (D=720 mm, η_a=1.5) (main cracks are marked by thick solid lines)

In the beam S3D36a216 (η_a=6) that failed due to concrete crushing in the compression zone (Fig.A2.16A), the horizontal displacements along the beam length 5 cm below the beam top were the largest in the central (bending) zone. The maximum measured horizontal displacement in the beam mid-point was 0.43 mm. In the beam S3D36a108 (η_a=3) which failed in shear-compression or

concrete crushing (Fig.A2.16B), the tangential diagonal crack displacement was slightly smaller than the normal crack opening at the beam mid-height (Fig.A2.16Ba). The maximum normal crack displacement was there ω=0.5 mm. At the beam top region, the tangential crack displacement continuously increased from the beginning of loading up to δ=0.18 mm (Fig.A2.16Bb). The normal crack displacement, ω=0.1 mm, was negative in this zone due to compression (the crack reached the triangle location just before failure). In the beam S3D36a54 (η_a=1.5) which also failed in shear (Fig.A2.16C), the diagonal crack development started later (for P=400 kN) with the proportional normal ω and tangential displacements δ at the beam mid-height (Fig.A2.16Ca). The maximum crack displacements were: δ=0.08 mm and ω=0.10 mm. At the beam top region, the failure crack was preceded by the increasing tangential crack displacement up to δ=0.18 mm and negative normal crack displacement up to ω=0.13 (Fig.A2.16Cb). Thus the tangential crack displacement was higher than the normal one along the diagonal shear crack in the compressive beam region.

The differences in failure modes were well visible based on the horizontal displacements at the beam top (Fig.A2.17). In the beam S3D36a108_2 which failed in the bending zone due to concrete crushing, the displacement was the largest in the beam mid-point (Fig.A2.17A), whereas in the beam S3D36a108_3 which failed in shear compression it was the largest under the loading plates (Fig.A2.17B). The maximum displacement was greater in the beam failing in bending - 0.43 mm while for the beam failing in shear it was 0.25 mm. The beam S4D18a108 (η_a=6) exhibited the same behaviour as the beam from the series '3' (S3D36a216, η_a=6) with a clear increase of horizontal displacements in the bending zone (Fig.A2.18A). The maximum measured horizontal displacement in the beam mid-region was ω=0.20 mm.

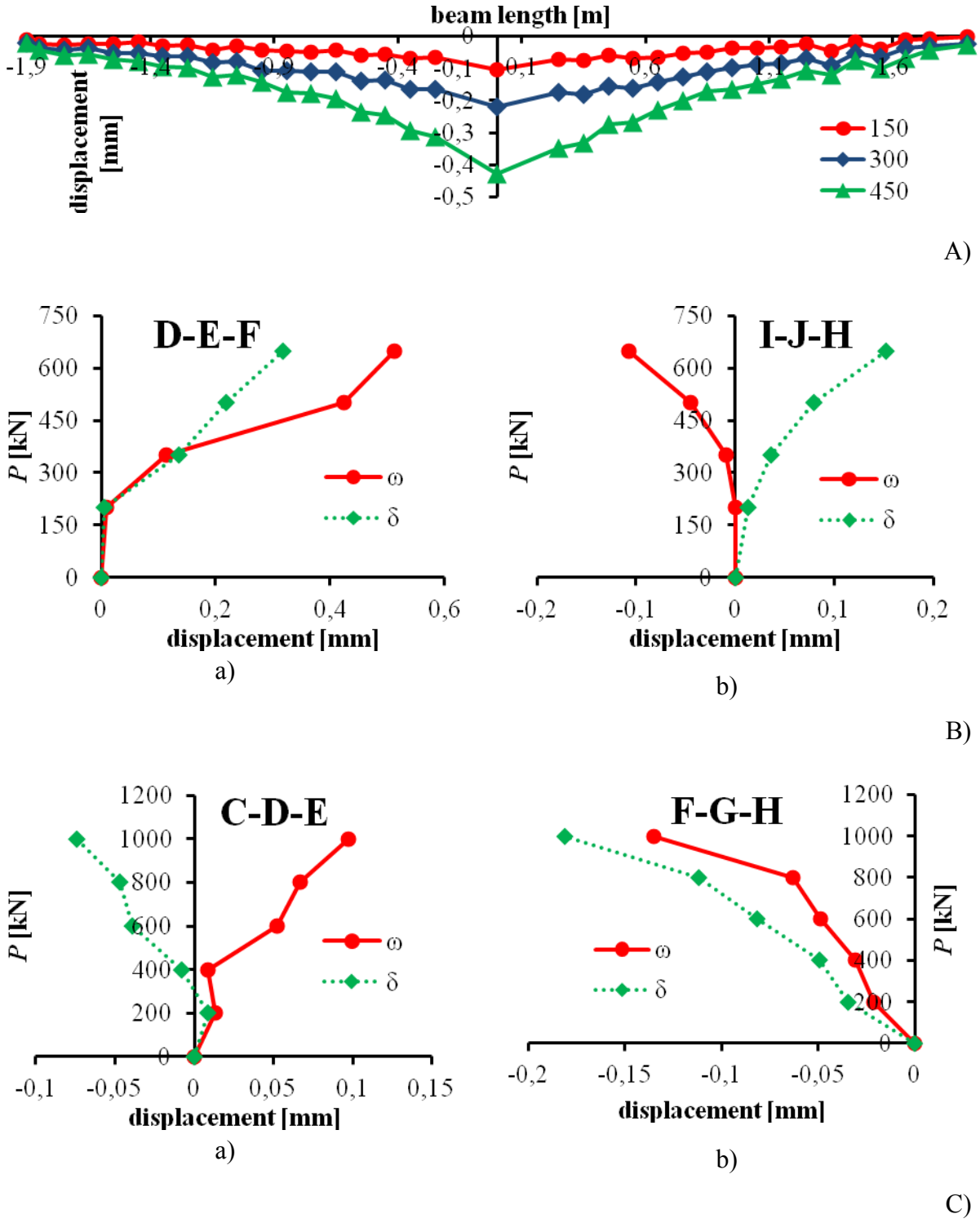

Fig.A2.16: Experimental relationships between normal/tangential crack displacements and vertical force P in RC beams (series '3'): A) S3D36A216 (a=216 mm, η_a=6) (Fig.A2.15Aa), B) S3D36A108 (a=108 mm, η_a=3) (Fig.A2.15Ab) and C) S3D36A54 (a=54 mm, η_a=1.5) (Fig.A2.15Ac) for: a) shear zone mid-height and b) compression-shear zone top (continuous red

lines with dots denote normal displacement ω and dashed green lines with diamonds denote tangential displacement δ, sections are shown in Fig.A2.15)

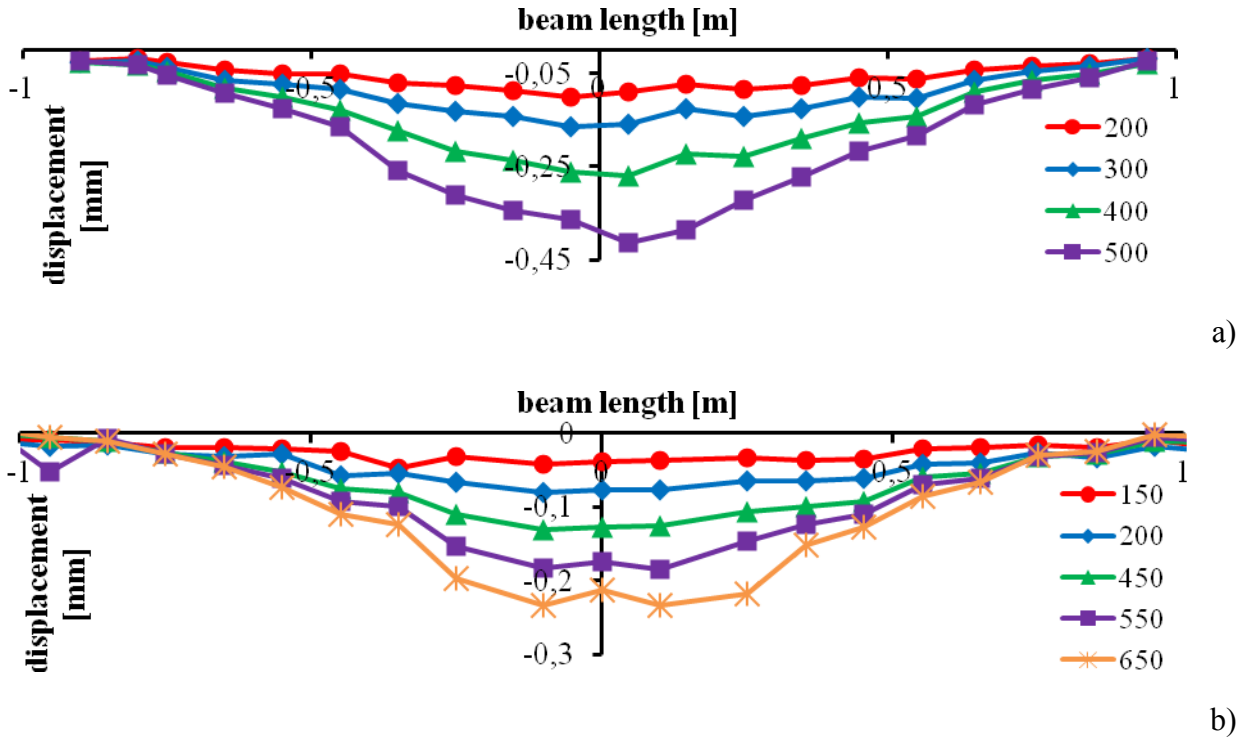

Fig.A2.17: Horizontal normal displacements along RC beam length measured 5 cm below beam top directly before failure for various load level: a) beam S3D36a108_2 (failed by concrete crushing) and b) beam S3D36a108_3 (failed in shear)

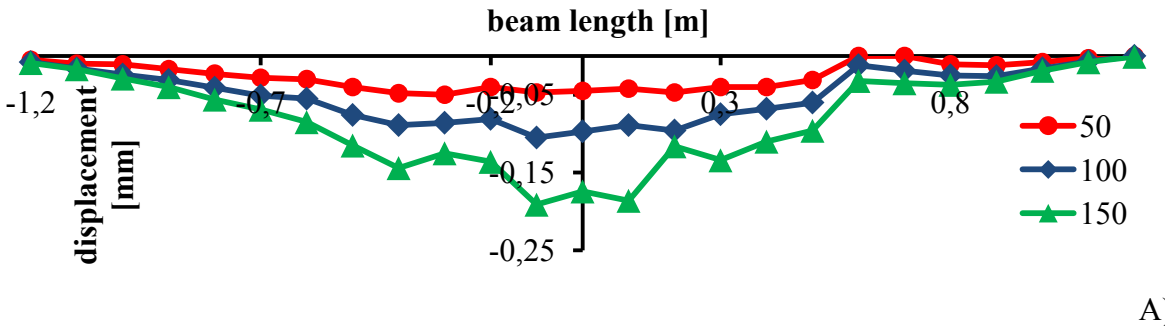

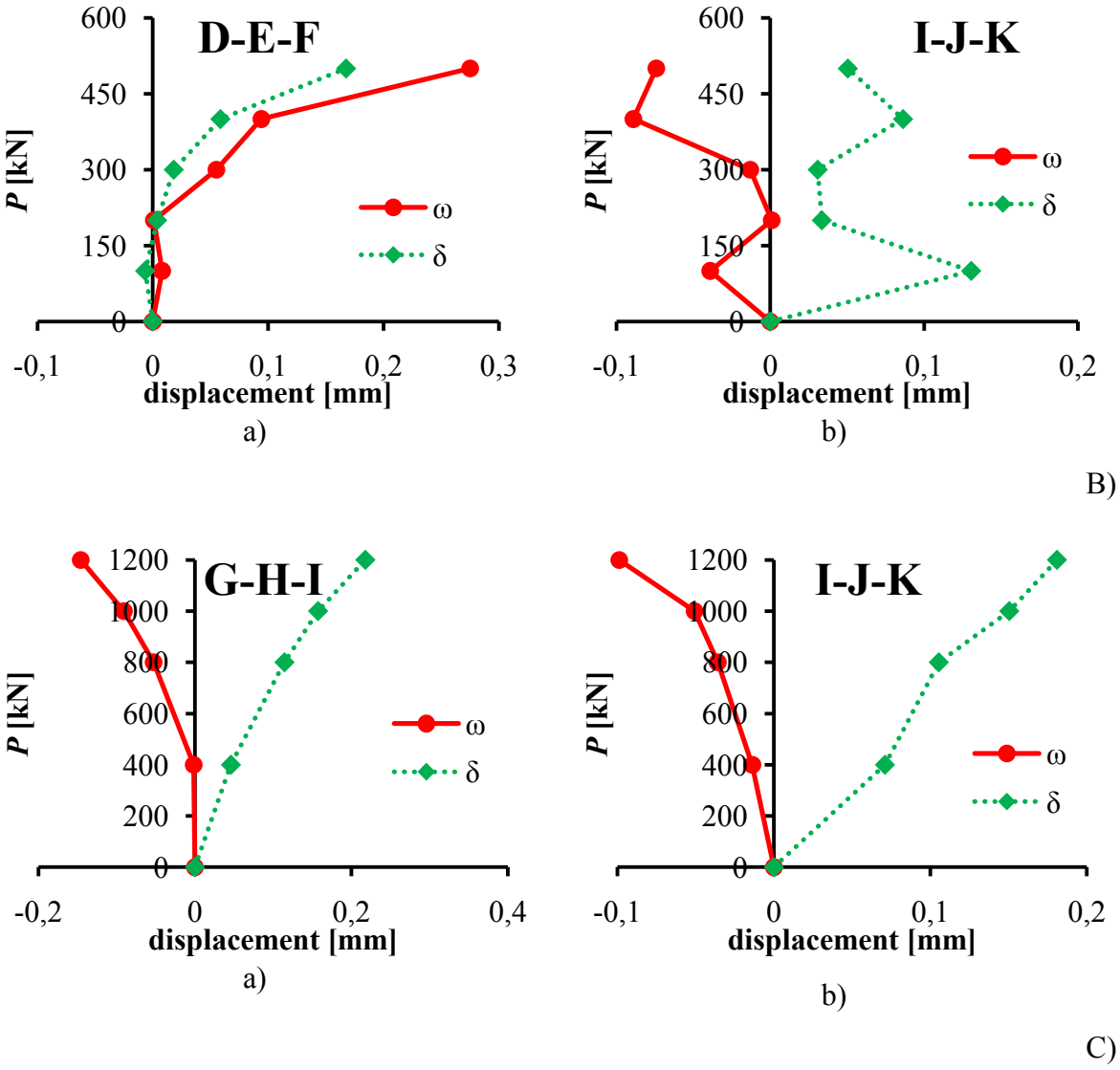

Fig.A2.18: Experimental relationships between normal/tangential crack displacements and vertical force in RC beams (series '4'): A) S4D22A108 (D=180 mm, η_a=6) (Fig.A2.15Ba), B) S4D43A108 (D=360 mm, η_a=3) (Fig.A2.15Bb) and C) S4D72A108 (D=720 mm, η_a=1.5) (Fig.A2.15Bc) for: a) shear zone mid-height and b) compression-shear zone top (continuous red lines with dots denote normal displacement ω and dashed green lines with diamonds denote tangential displacement δ)

A2.6. Analytical calculation

Shear strength

The experimental shear strengths of RC beams with stirrups were compared with the analytical predictions based on the truss analogy proposed in Eurocode (EN 1992-1-1 (2008)), the strut-and-tie model (STM) in ACI (ACI 318-14 (2014)), the modifief strut-and-tie model (MSTM) proposed

by Zhang and Tan (2007) and the cracking strut-and-tie model (CSTM) derived by Chen et al. (2018).

EN 1992-1-1 (2008)

The shear strength of RC beams with stirrups is calculated based on the variable inclination truss analogy. The shear resistance for non-prestressed members should be taken to be less than:

$$V_{Rd,s} = \frac{A_{sw}}{s} z f_{ywd} \cot\theta \text{ (shear reinforcement yielding)} \quad \text{(A2.2)}$$

or

$$V_{Rd,max} = \frac{t\, z\, v_1 f_{cd}}{(\cot\theta + \tan\theta)} \text{ (concrete crushing)}, \quad \text{(A2.3)}$$

where the recommended strut inclination is $1 \leq \cot\theta \leq 2.5$, A_{sw} - the cross-section area of one stirrup, f_{ywd} - the yield strength of stirrups, s denotes the stirrup spacing, f_{cd} - the design concrete compressive strength, v_1 - the empirical coefficient of the cracked concrete shear strength (v_1=0.6 for the characteristic concrete strength f_{ck}<60 MPa) and z - the internal lever arm ($z \cong 0.9D$ for bending).

ACI 318-14 (2014)

The shear strength of deep RC beams according to ACI is calculated by applying a simple strut-and-tie model with the strut inclination angle θ_s defined as $\tan\theta_s = D/a$. (Fig.A1.18). The shear strength of beams is governed by the minimum from the strut compressive strength F_{ns}, the tie tensile strength F_{nt} and the compressive strength of the nodal zone F_{nn}. Generally in deep beams, the strut is the weakest component and the resultant ultimate vertical force V_n and corresponding shear strength $\tau_c = V_n/A_c$ are calculated as

$$V_n = F_{ns} \sin\theta_s = (f_{ce} A_{cs}) \sin\theta_s \quad \text{(A2.4)}$$

and

$$\tau_c = (f_{ce} A_{cs}) \sin\theta_s / A_c, \quad \text{(A2.5)}$$

where f_{ce} - the effective strut compressive strength and $A_{cs} = w_s t$ - the cross-sectional area at the strut end, $A_c = tD$ – the effective cross-sectional area of a beam. The strut width w_s depends on the supporting plate geometry and longitudinal reinforcement arrangement:

$$w_s = l_c \cos\theta_s + l_b \sin\theta_s. \tag{A2.6}$$

where l_b - the supporting plate length and l_c - the height of the CCT node depending on the concrete cover and number of reinforcement layers. The presence of stirrups is taken into account by modifying the effective compressive strength of concrete in the strut $f_{ce}=0.85\beta_s f'_c$ with $\beta_s=0.75$ (in the beams without transverse reinforcement $\beta_s=0.6$). To analytically specify the size effect, Eq.A2.5 can be transformed (by substituting $l_b=l_c \mathrm{tg}\theta_s$) as

$$\tau_c = 2 f_{ce} \eta_c / \eta_a = 1.7 \beta_s f'_c \, \eta_c / \eta_a. \tag{A2.7}$$

The shear strength in Eq.A2.7 is affected by two size parameters η_a and η_c (the shear strength increases with decreasing η_a and increasing η_c) and one material parameter f_{ce} that takes into account the concrete strength and presence of stirrups. The nominal strength of the nodal zone was calculated as $F_{nn}=f_{ce}A_{nz}$ with $f_{ce}=0.85f_c'\beta_n$ ($\beta_n=0.8$ for the CCT node and $\beta_n=1.0$ for the CCC node) wherein A_{nz} - the node face area perpendicular to the strut direction.

Zhang and Tan (2007)

Zhang and Tan (2007) improved a strut-and-tie model by taking into account the Mohr-Coulomb failure condition in a tension-compression stress state and a contribution of the bottom reinforcement to the strut compression. The ultimate force V_n in RC beams may be determined from the formula:

$$V_n \left[\frac{4\sin\theta_s \cos\theta_s}{f_t A_c} + \frac{\sin\theta_s}{f_c A_{str}}\right] = 1, \tag{A2.8}$$

where $A_c=d_c t$ is the effective cross-sectional area of a beam ($d_c=D-0.5l_d$), $A_{str}=w_s t$ is the cross-sectional area of the strut. The width of strut w_s is calculated in the same way as in ACI but with a slightly modified strut inclination angle θ_s defined as $\tan\theta_s=d_c/a$. The maximum tensile strength f_t of the bottom nodal zone is calculated as the sum of three components:

$$f_t = \frac{4A_s f_y \sin^2\theta_s}{A_c} + \frac{f_{ywd} A_{sw} \sin(\theta_s+\theta_w)}{A_c / \sin\theta_s} + 0.31\sqrt{f_c}\left(\frac{\varepsilon_{cr}}{\varepsilon_1}\right)^{0.4}. \tag{A2.9}$$

The first component in Eq.A2.9 results from the main longitudinal reinforcement action, the second part takes into account the effect of shear reinforcement (θ_w - the inclined angle of shear reinforcement with respect to horizontal line) and the third component considers the cracked concrete tensile strength (ε_{cr} - the concrete strain during cracking taken as 0.00008, ε_1 - the principal tensile strain of the concrete strut ($\varepsilon_1=\varepsilon_s+(\varepsilon_s+\varepsilon_2)ctg2\theta_s$, ε_s and ε_2 - the tensile strain of longitudinal reinforcement and peak compressive strain of the concrete strut at crushing). The tensile strain ε_s depends on the compressive zone height and is calculated in an iterative procedure. Thus, the ultimate force resulting from Eq.2.8 (or the corresponding shear strength) cannot be expressed in a straightforward manner by the size parameters η_a , η_b and η_c as it in the case of Eq.A2.7. The ultimate force in Eq.A2.8 depends on six geometric parameters (D, t, c', A_s, A_{sw}, θ_s, and l_d) and five material parameters (f_y, f_{ywd}, f_c, ε_{cr}, and ε_1).

Chen et al. (2018)

The strut-and-tie model formulated by Chen et al. (2018) assumes the strut of the width w_s consisting of a the cracked and un-cracked part that transfer the following ultimate forces (Fig.A2.19):

$$F_{si} = \sigma_{ci} w_{si} t = \kappa_c \beta_{si} f_c' w_{si} t \,, \tag{A2.10}$$

$$F_{sc} = \sigma_{cc} w_{sc} t = \beta_{sc} f_c' w_{sc} t \,. \tag{A2.11}$$

The non-cracked part of the width w_{si} and cracked part of the width w_{sc} have the effective compressive strengths $\sigma_{si}=\kappa_c\beta_{si}f'_c$ and $\sigma_{sc}=\beta_{sc}f'_c$, respectively ($f'_c$ is the cylindrical concrete compressive strength, $\kappa_c=1-f'_c/250$ and $\beta_{si}=0.85$). The strut efficiency coefficient β_{sc} takes into account the aggregate interlocking, dowel action of longitudinal bars and shear reinforcement strength. The value of β_{sc} is found through an iterative procedure with the initial value of $\beta_{sc}=0.85$. The ultimate force of deep beams is obtained as the sum of F_{si} and F_{sc}:

$$V_n = (F_{si} + F_{sc}) \sin\theta_s \,, \tag{A2.12}$$

where the strut angle $\tan\theta_s=(D-c/2)/a$ is the function of the effective beam depth D, shear span a and nodal CCC zone height c (Fig.A2.19). The compression zone depth c can be found using the linear flexural theory (the concrete compressive strength in the compression zone at the mid-span does not reach its ultimate strength). The solution of equation $c^2+2n\rho Dc-2n\rho D^2=0$ (with $n=E_s/E_c$) derived from the equilibrium condition of a plane section provides the compression zone height c.

The ultimate force (or corresponding shear strength) in Eq.A2.12 cannot be presented as an explicit function of the size parameters η_a , η_b and η_c due to an iterative procedure used to determine the strut efficiency coefficient β_{sc} .The ultimate shear strength of deep beams in Eq.A2.12 depends on ten geometric parameters (D, t, b, c, l_{bt}, θ_s, α, ρ, ρv and ϕ_s) and five material parameters (κ_c, β_{si}, f'_c, E_s and E_c).

Flexural strength

The ultimate flexural strength of beams with $\eta_a \geq 2.5$ failing due to concrete crushing in the compression zone was estimated from the equilibrium conditions in the beam section. Assuming a simplified rectangular stress distribution in the compression zone, the lever arm is $z=D(1-0.5\xi_{eff,lim})$ with $\xi_{eff,lim}=0.8\times0.0035/(0.0035+E_c/E_s)$. The ultimate vertical force reads as follows:

$$V_{n,flex} = \frac{\alpha f_c t D^2 \mu_{eff,lim}}{a} \tag{A2.13}$$

with $\mu_{eff,lim}=\xi_{eff,lim}(1-0.5\xi_{eff,lim})$ and $\alpha=0.85$.

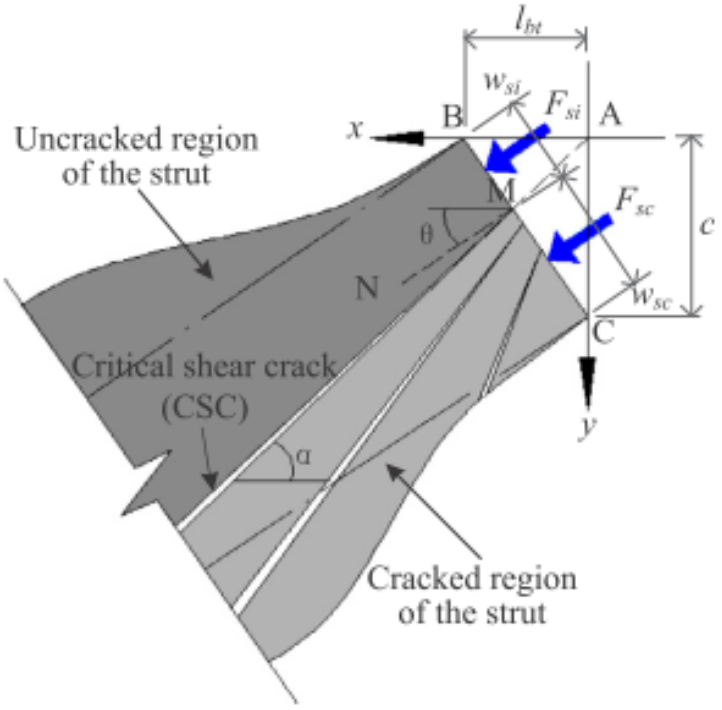

Fig.A2.19: Strut with diagonal cracks at CCC node (Chen et al. 2018)

A2.6. Comparison between experimental and theoretical results

The shear strengths $\tau_c=V_{max}/(tD)$ ($V_{max}=0.5P_{max}$) or ultimate stresses (in the case of flexural failure) predicted by the analytical models from Section 4 were compared to the experimental results in (Tab.A2.5 and Fig.A2.20). The calculations were performed with the mean concrete compressive strength f_{cm}=58 MPa and f_{cm}=56 MPa in the series '3' and '4' and the guaranteed steel yielding strength $f_{ym}=f_{ywm}$=560 MPa. For the beams of a transitional geometry (beam S3D36A108 with η_a=3.0 and S4D43A108 with η_a=2.5), the shear strength was calculated using both the beam theory and strut-and-tie models (even though it is required that $\eta_a\leq$2.0 by ACI (ACI 318-14 (2014)) and $\eta_a\leq$2.5 by Chen (Chen et al. 2018). The experimental and theoretical strut widths w_s and strut inclination angles θ_s are compared in Tab.A2.5. In Tab.A2.6 the average experimental inclined cracks spacing s_I^{EXP} (distance between the inclined cracks measured perpendicularly to the critical shear crack direction just above reinforcement) was also shown.

According to the simple strut-and-tie model (STM) from ACI 318-14 (Eq.A2.5), the predicted shear strengths of deep beams with η_a=1.5 were very close to experimental results in both the series '3' and '4' (higher solely by 5%) (Tab.A2.5 and Fig.A2.20). With respect to the beams with a transitional geometry, the predicted shear strength was the same as the experimentally obtained value for η_a=3 with the shear-compression failure mode. The analytical solution provided for η_a=2.5 the lower shear strength by 15% as compared to the experimental beams that failed due to shear-compression (Tab.A2.5 and Fig.A2.20). The calculated beam strength resulting from the nodal zone strength was in all beams by 7% (CCT node) and 33% (CCC node) higher than the theoretical strut nominal strength (for the beam S4D72A108 the difference further increased up to 80% and 130% accordingly with the pilaster thickness of 250 mm). The measured ultimate vertical forces of beams with η_a=2.5-3.0 were by 1-8% lower than estimated based on the CCT node strengths. In contrast, the high beams with η_a=1.5 were stronger by 11-12% with respect to the theoretical beam strengths resulting from the CCT node failure.

Referring to the model by Zhang and Tan (2007) (Eq.A2.12) (MSTM), the calculated shear strengths of beams with η_a between 1.5 and 3.0 were generally higher than the experimental results by 10-55%. Note that MSTM was successfully verified by Zhang and Tan (2007) against the deep beams with η_a=1.1, that indicated this model had the limited applicability. Based on the cracking strut-and-tie model (CSTM) by Chen et al. (2018), the estimated shear strength related to the experimental results v^{STM}/v^{Exp} varied between 0.80-1.07 for the beams with η_a=1.5-2.5. The highest

difference of 32% was obtained for the beam with η_a=3.0 that was however beyond the model application range. The CSTM predicted the lowest ultimate shear strength (for $\eta_a \leq 3.0$) among all analysed strut-and-tie models. The shear stresses of the beams with η_a=3.0-6.0 failing due to concrete crushing were estimated with the 8%-error using a simple equilibrium condition of plane section (Eq.A2.13). However, the beams' strength with η_a=2.5 was overestimated by 20%. The formula recommended by EC2 (EN 1992-1-1 (2008)) obviously strongly underestimated the ultimate shear strength of all beams failing in shear-compression (for η_a=2.5-3.0, the difference was exceeded by 100%).

The theoretical strut width w_s was obviously 2.5-4 times wider than the experimental crack spacing s_I^{EXP} (Tab.A2.6) since, in the idealized truss model, the single strut represented the several real struts between cracks. The theoretical inclination of the strut θ_s in STM (ACI 318-14) was always lower than the critical shear crack inclination θ_S^{EXP} by 20-50% for η_a=2.5-3.0 and 10-25% for η_a=1.5. MSTM (Zhang and Tan 2007) and CSTM (Chen et al. 2018) further reduced the strut inclination that were by 40-60% and 30-40% lower than the critical shear crack inclination for η_a=2.5-3.0 and η_a=1.5, respectively. This observation confirms the presented STMs should not be used for the beams with η_a=2.5-3.0 due to an incorrect assumption of a single strut connecting a loading and bearing plate. In the case of the beams with η_a=1.5 the simple ACI model provided an acceptable difference between the calculated strut inclination and critical shear crack inclination.

In summary, the best prediction of the shear strength was obtained with the simple strut-and-tie model following ACI (ACI 318-14) (5%-error for η_a=1.5, 15%-error for η_a=2.5 and 1%-error for η_a=3.0). In the RC beams without stirrups (see Appendix 1), ACI (ACI 318-14) offered however very incorrect results for η_a=1.5-2.0 (error of 20-100%) and realistic results for η_a=1 (error of 5%). STMs are very sensitive to a different number of reinforcement layers. The increasing number of layers affects the height of the support nodal zone (CCT node), the strut width and its inclination. Generally, the more reinforcement layers, the higher is the beam strength even with the same reinforcement ratio.

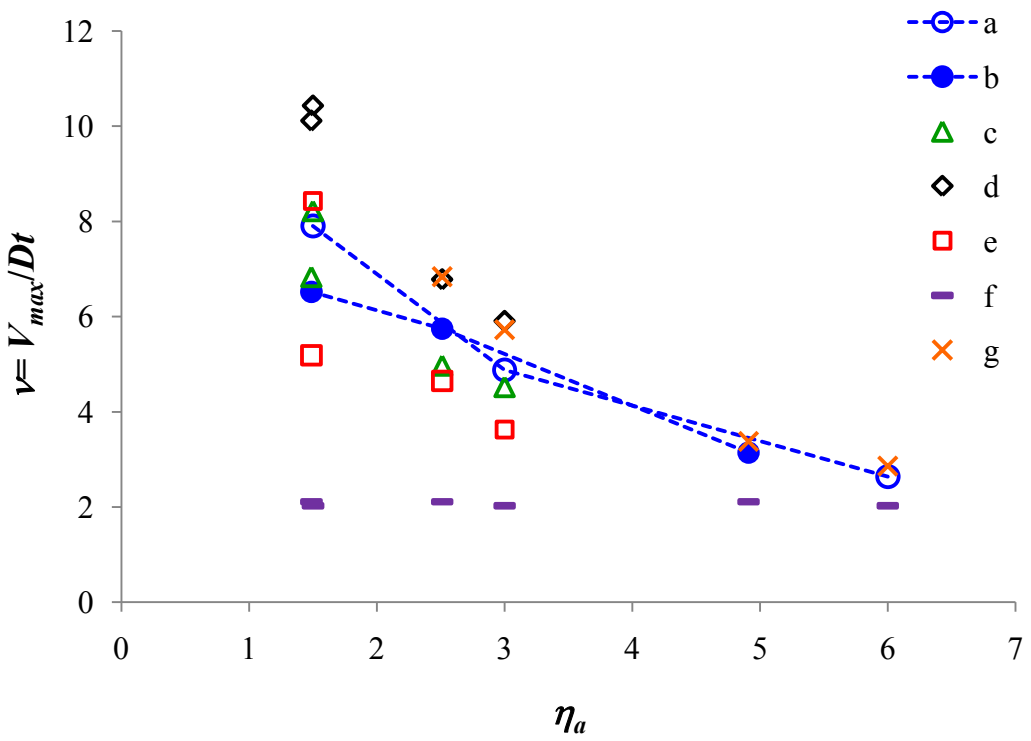

Fig.A2.20: Average experimental ultimate shear stress $\nu=V_{max}/(tD)$ in series '3' (a) and series '4' (b) as compared to analytical solutions based on: c) STM (Eq.A2.5), d) MSTM (Eqs.A2.8), e) CSTM (Eqs.A2.12), f) EC2 (Eqs.A2.2 and A2.3) and g) equilibrium condition in vertical cross-section (Eq.A2.13)

Tab.A2.5: Experimental and theoretical shear strengths/ultimate stresses according to various analytical models of Section 4 (ν_C^{Exp} – experimental average shear stress of beams failing due to concrete crushing, ν_{SC}^{Exp} – experimental average shear strength of beams failing due to shear-compression)

Beam	η_a	Failure mode	ν_C^{Exp}	ν_{SC}^{Exp}	ν^{EC} (Eq.6)	ν^{Fl} (Eq.17)	ν^{STM} (Eq.8)	ν^{MSTM} (Eq.12)	ν^{CSTM} (Eq.16)
S3D36A216	6	C	2.64	-	2.03	2.86	-	-	-
S3D36A108	3	C/SC	5.30	4.46	2.03	5.72	4.52	5.91	3.63
S3D36A54	1.5	SC	-	7.90	2.03	-	8.22	10.43	8.43
S4D22A108	5	C	3.14	-	2.11	3.38	-	-	-
S4D43A108	2.5	C/SC	5.67	5.82	2.11	6.84	4.97	6.78	4.65

S4D72A108	1.5	SC	-	6.52	2.11	-	6.83	10.11	5.19

Tab.A2.6: Experimental inclined crack spacing s_I^{EXP} and critical shear crack inclination θ_S^{EXP} compared to theoretical strut width w_s and strut inclination angle θ_s following STM by ACI (ACI 318-14), MSTM by Zhang and Tan (2007) and CSTM by Chen et al. (2018)

Beam	s_I^{EXP} [mm]	θ_S^{EXP} [°]	w_s^{STM} [mm]	θ_s^{STM} [°]	w_s^{MSTM} [mm]	θ_s^{MSTM} [°]	w_s^{CSTM} [mm]	θ_s^{CSTM} [°]
S3D36A54, η_a=1.5	67	45	180	34	178	28	205	27
S3D36A108, η_a=3.0	68	36	174	18	179	14	199	14
S4D72A108, η_a=1.5	78	39	311	34	319	28	365	27
S4D43A108, η_a=2.5	62	28	202	22	199	17	221	17

Crack width and deflection

Comparing the flexural crack spacing, the distances between cracks were l_s=131.9 mm and l_s=101.0 mm for the beams of the series '3' (D=360 mm) following EC2 (EN 1992-1-1 (2008)) and ACI (ACI 224R-01), whereas the experimental ones varied between 98 mm and 114 mm (Fig.A2.21a). In the series 4, the theoretical values of cracks spacing according to code provisions for V_{max} were 125.2 mm, 118.2 mm and 124.7 mm (EC2) and 84.5 mm, 67.5 mm and 83.4 mm (ACI) while the experimental ones were 79 mm, 118 mm and 124 mm for η_a=1.5, 2.5 and 5.0, respectively (Fig.A2.21b).

Moreover, the beam deflections were calculated (by neglecting creep) with the formulas by EC2 (EN 1992-1-1 (2008)) and ACI (ACI 435R-95)and compared with the average experimental values (Fig.A2.22). For all tested beams, the experimental mid-length deflections for V_{max} were underestimated by about 15-70% as compared to the values obtained with the design codes formulae. For the beams S3D36a54 (η_a=1.5), S3D36a108 (η_a=3.0) and S3D36a216 (η_a=6.0), the standard formulae provided the deflections of u=27.71 mm, u=7.53 mm and u=2.45 mm (EC2) and

u=27.20 mm, u=7.54 mm and u=2.45 mm (ACI) whereas in the experiments they were significantly higher and equal on average to 36.5 mm 16.2 mm and 6.6 mm, respectively. The discrepancies always increased with decreasing η_a.

Figure A2.23 presents the maximum experimental flexural crack widths in the beam mid-regions for the average ultimate vertical forces V_{max} of Tab.A2.3 as compared to EC2 (EN 1992-1-1 (2008)) and ACI (ACI 224R-01),. For the series '4' and for the series '3', the measured crack widths were in good agreement with the standard values for η_a=6.0 (Fig.A2.22), and as twice as small for the series '3' with η_a=1.5-3.0 (Fig.A2.23a).

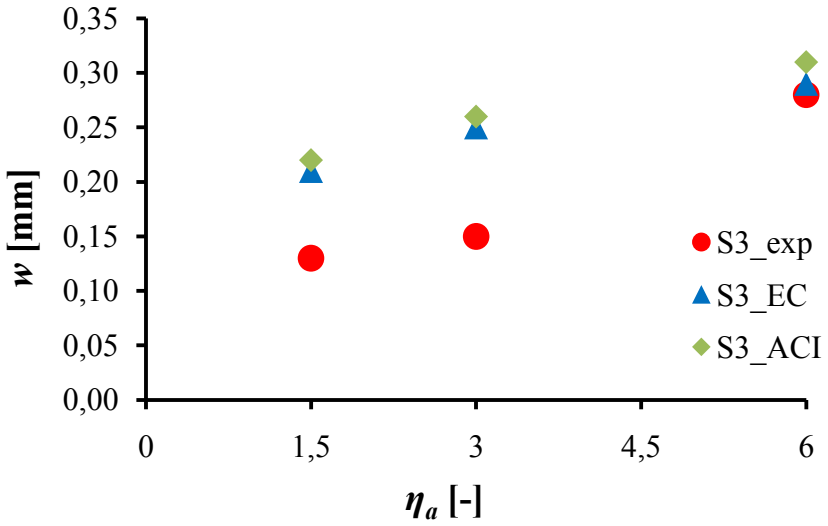

a)

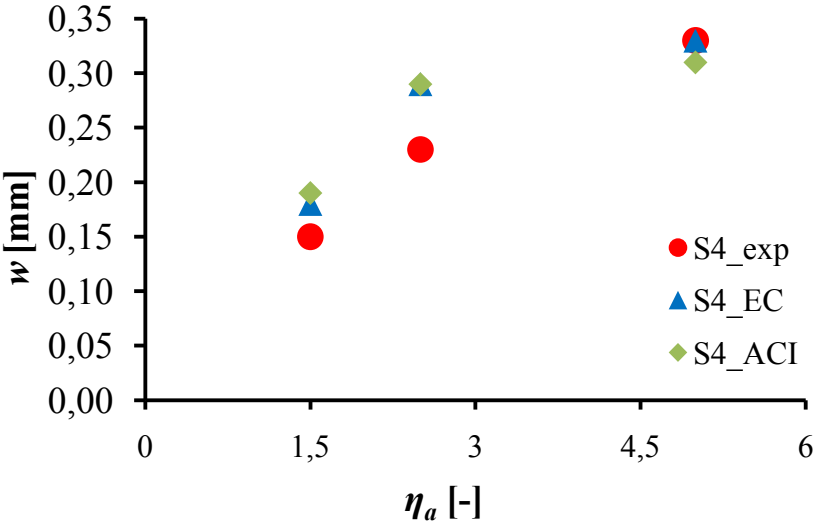

b)

Fig.A2.12: Experimental (circles) and analytical flexural crack widths w by EC2 (EN 1992-1-1 (2008)) (triangles) and ACI (ACI 224R-01 (2000)) (diamonds) versus η_a for P_{max} in RC beams: a) series '3' (S3) and b) series '4' (S4)

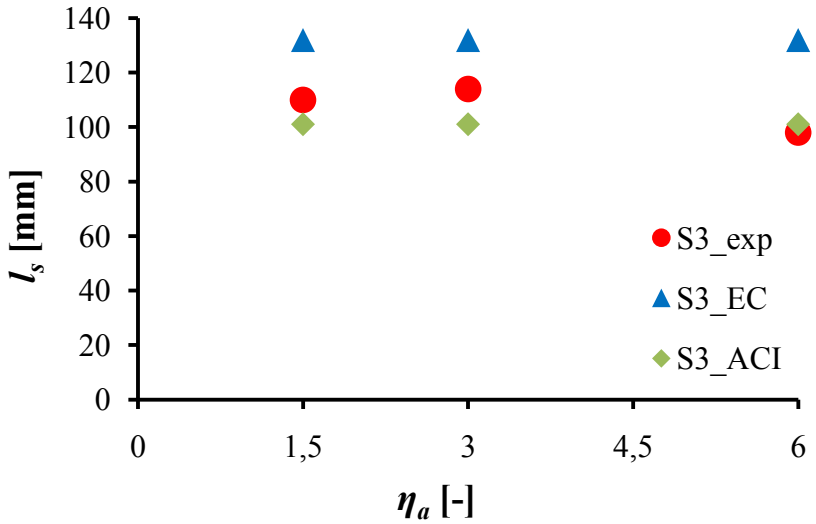

a)

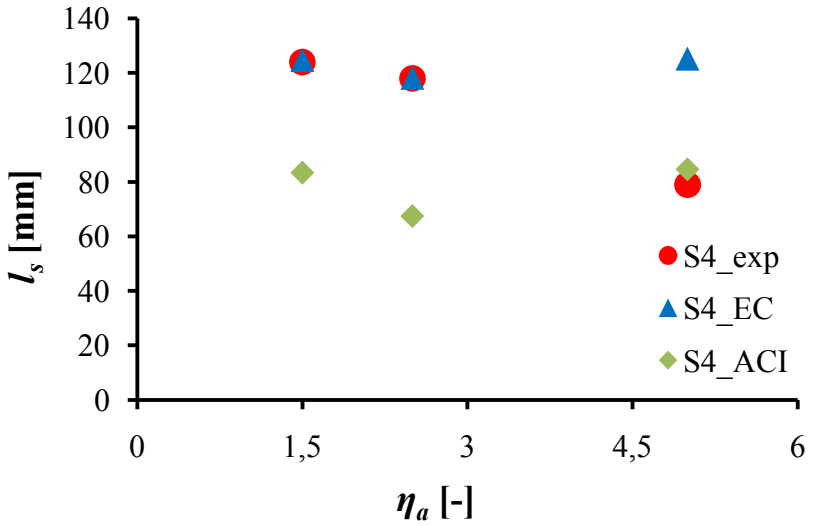

b)

Fig.A2.22: Experimental (circles) and analytical flexural crack spacing l_s by EC2 (EN 1992-1-1 (2008)) (triangles) and ACI (ACI 224R-01 (2000)) (diamonds) versus $\eta_a=a/D$ for P_{max}: a) series '3' (S3) and b) series '4' (S4)

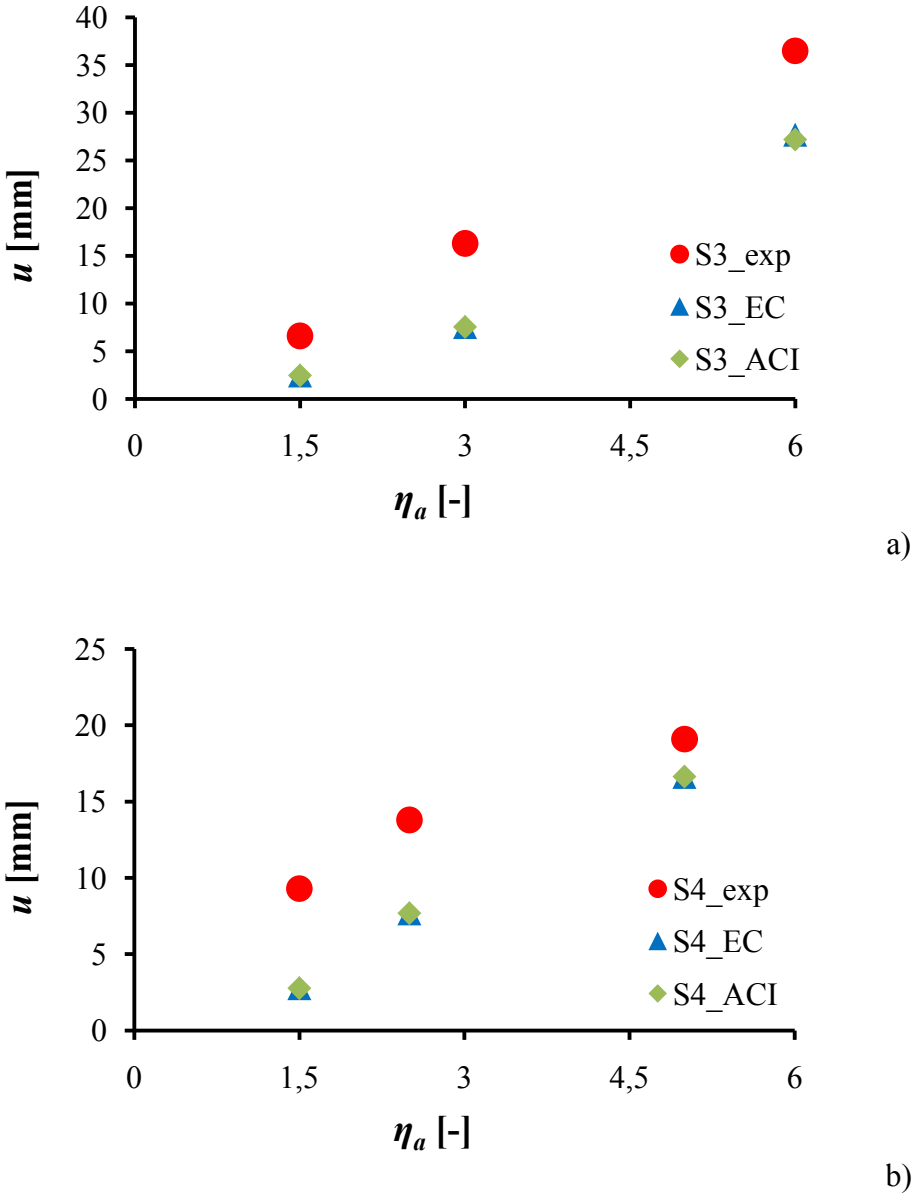

Fig.A2.23: Beam deflections u in experiments (circles) and according to EC2 (EN 1992-1-1 (2008)) (triangles) and ACI (ACI 224R-01 (2000)) (diamonds) versus η_a for P_{max} in RC beams: a) series '3' (S3) and b) series '4' (S4)

A2.7 Conclusions

The following basic conclusions may be offered from our novel size effect experiments on RC beams with both longitudinal and transverse reinforcement being scaled along either the depth or length:

- The shear strength of beams evidently decreased with increasing parameter $\eta_a=a/D$. It also decreased with increasing parameter η_b from 0.75 to 2.5 in beams with the varying effective depth and constant effective length.

- Two different basic failure modes were observed in RC beams with longitudinal and shear reinforcement. First, the concrete crushing in compressive zone occurred in slender beams for η_a=5-6 with a global quasi-brittle post-peak behaviour. As the reinforcement remained elastic, the compressive zone enlarged transversely and interacted with the cracked tensile zone in the final failure stage. Second, the brittle shear-compression failure was registered in beams for η_a=1.5-3.0 where the critical diagonal crack developed with normal and tangential displacements of similar values. In the RC beams without stirrups (Appendix 1), the reinforcement yielding occurred in beams for η_a=6, diagonal tension failure in beams for η_a=2-3 and shear-compression failure in beams for η_a=1-2. The presence of stirrups increased the beam strength by 130% for η_a=1.5 (stirrups did not affect the failure mode) and 280% for η_a=3.0 (stirrups changed the failure mode). The strength of nodal zones according to ACI was sufficient to prevent local concrete crushing at supports in contrast to the experiments with the highest beams wherein it was not high enough and the support zone failure was observed.

- A decrease of η_a due to the varying shear span a with the constant beam depth D had a slightly stronger effect on the beam shear strength than a decrease of η_a due to the varying D with a=const.

- The distance between the critical diagonal crack and beam support d_c related to the shear span a varied between d_c/a=0.5 for beams with η_a=2.5-3 up to as d_c/a=0 for deep beams with η_a=1.5 (similarly as in RC beams without shear reinforcement (Appendix 1)). The inclination of the critical diagonal shear crack to the horizontal was 28°-45° for η_a=1.5-3 (this inclination was similar (30°-42°) in RC beams without stirrups for η_a=1-3 (Appendix 1)).

- The best prediction of the shear strength of deep beams with a/D=1.5 was obtained with the simple strut-and-tie model following ACI (ACI 318-14) (5%-error). The shear strength of beams of a transitional geometry a/D=2.5-3.0 were also satisfactorily described with the same model (error of 1-15%). The strut-and-tie model proposed by Chen (Chen et al. 2018) underestimated the shear strength of most beams (except of the beam S3D36A54) by ca. 20%. The modified strut-and-tie model by Zhang and Tan (2007) overestimated on the other hand the shear strength of all RC beams

with η_a=1.5-3. Thus, the ACI model, in spite of several simplifications assumed, proved to be the most realistic for RC beams with and without shear reinforcement that failed in shear-compression.

- The measured crack widths were in agreement with the standard values for the series '4' and for the series '3' if η_a=6.0, and were as twice as small for the series '3' if η_a=1.5-3.0. The measured beams' deflections were higher by the factor 1.1-3.4 than the code values. In RC beams without stirrups (Appendix 1), the standards realistically determined the flexural crack widths and beam deflections solely for the beams with η_a=2–6 with respect to cracks widths and with η_a=3-6 with respect to deflections (the standard crack widths were higher by the factor 1.5 for η_a=1 and the standard deflections were underestimated by the factor 3 for $\eta_a \leq 2$).

- The size effect formula should be related to a specific failure mode dependent on both strength and geometric parameters. The specification of the failure mode is therefore fundamental in assessing the dependence of the limit load on design or redesign variables.

Bibliography

[1] Angelakos, D., Bentz, E.C., Collins, M.P. Effect of concrete strength and minimum stirrups on shear strength of large members, *ACI Strucural Journal* 98(3) (2001), 290-300.

[2] Baghini, A., Bažant, Z.P., Zhou, Y., Gouirand, O. Carner, F.C. Microplane model M5f for multiaxial behavior and fracture of fiber reinforced concrete. *Journal of Engineering Mechanics* 133 (1) (2007), 66-75.

[3] Bažant, Z.P., Planas, J. *Fracture and size effect in concrete and other quasi-brittle materials.* CRC Press LLC (1998).

[4] Bažant, Z.P. Size effect in blunt fracture: concrete, rock, metal. *Journal of Engineering Mechanics* 110 (1984), 518-535.

[5] Bažant, ZP. Pfeifer, P. Determination of fracture energy from size and brittleness number. *ACI Materials Journa*l 84 (1987a), 463-480.

[6] Bažant, Z.P., Pijaudier-Cabot, G., Pan, J.Y. Ductility, snapback, size effect and redistribution in softening beams and frames. *ASCE J. of Structural Engrg*. 113(12) (1987b), 2348-2364.

[7] Bažant, Z.P., Kazemi M.T. Size effect on diagonal shear failure of beams without stirrups. *ACI Structural Journal* 88(3) (1991), 268-76.

[8] Bažant, Z.P., Kazemi, M.T., Hasegawa, T., Mazars, J. Size Effect in Brazilian Split-Cylinder Tests: Measurements and Fructure Analysis. *ACI Material Journal* (1991), 325-332.

[9] Bažant Z.P. Size effect in blunt fracture concrete, rock, metal. *Journal of Engineering Mechanics* ASCE 110 (1994), 518–35.

[10] Bažant, Z.P, Planas, J. Fracture and size effect in concrete and other quasibrittle materials. CRC Press LCC, Boca Raton, 1998.

[11] Bažant, Z.P, Becq-Giraudon, E. Statistical prediction of fracture parameters of concrete and implications for choice of testing standard. *Cement and Concrete Research* 32 (2002), 529–556.

[12] Bažant, Z.P., Yavari, A. Is the cause of size effect on structural strength fractal or energetic-statistical?. *Engineering Fracture Mechanics* 72 (2005), 1–31.

[13] Bažant, Z.P., Pang, S.D., Vorechovsky, M., Novak, D. Energetic-statistical size effect simulated by S6FEM with stratified sampling and crack band model. *International Journal for Numerical Methods in Engineering* 71(11) (2007), 1297-1320.

[14] Bažant, Z.P., Yavari, A. Response to A. Carpinteri, B. Chiaia, P. Cornetti and S. Puzz's Comments on "Is the cause of size effect on structural strength fractal or energetic-statistical?". *Engineering Fracture Mechanics* 74 (2007a), 2897-2910.

[15] Bažant, Z.P., Vorechovsky, M., Novak, D. Asymptotic prediction of energetic-statistical size

effect from deterministic finite element solutions. *Journal of Engineering Mechanics* 128 (2007b), 153-162.

[16] Belgin, CM, Sener, S. Size effect on failure of overreinforced concrete beams. *Engineering Fracture Mechanics* 75(8) (2008), 2308-2319.

[17] Benkemoun, N., Poullain, Ph., Al Khazraji, H., Choinska, M., Khelidj, A. Meso-scale investigation of failure in the tensile splitting test: Size effect and fracture energy analysis. *Engineering Fracture Mechanics* 168 (2016), 242–259.

[18] Bhandari, A.R., Inoue, J. Experimental study of strain rates effects on strain localization characteristics of soft rocks. *Soils and Foundations* 45(1) (2005), 125-140.

[19] Biolzi, L., Cangiano, S., Tognon, G., Carpintieri, A. Snap-back softening instability in high strength concrete beams. *Materials and Structures* 22 (1989), 429-436.

[20] Bobiński, J., Tejchamn, J. Numerical simulations of localization of deformation in quasi–brittle materials within non–local softening plasticity. *Computers and Concrete* 1(4) (2004), 433–455.

[21] Bobiński, J., Tejchman, J. Modelling of concrete behaviour with a non–local continuum damage approach. *Archives of Hydro–Engineering and Enivronmental Mechanics* 52(2) (2005), 85–102.

[22] Bobiński, J., Tejchman, J., Górski, J. Notched concrete beams under bending – calculations of size effects within stochastic elasto-plasticity with non-local softening. *Archives of Mechanics* 61 (3-4) (2009), 283-307.

[23] Bobinski, J. and Tejchman, J. Comparison of continuous and discontinuous constitutive models to simulate concrete behaviour under mixed mode failure conditions. *Int. J. Num. Anal. Meths Geom*. 40 (2016a), 406-435.

[24] Bobiński, J. and Tejchman J. A coupled constitutive model for fracture in plain concrete based on continuum theory with non-local softening and eXtended Finite Element Method. *Finite Elements in Analysis and Design* 114 (2016b), 1-21.

[25] Bolander, J.E. and Sukumar, N. Irregular lattice model for quasistatic crack propagation Irregular lattice model for quasistatic crack propagation. *Physical Review* 71 (2005), 094106.

[26] Caballero, A., Carol, I., Lopez, CM. 3D meso–mechanical analysis of concrete specimens under biaxial loading. *Fatigue and Fracture of Engineering Materials and Structures* 30(9) (2007), 877–886.

[27] Carmeliet, J., Hens, H. Probabilistic nonlocal damage model for continua with random field properties. *Journal of Engineering Mechanics* 120 (1994), 2013-2027.

[28] Carmona, S., Gettu, R., Aguado, A. Study of the post-peak behaviour of concrete in the splitting-tension test, *Fracture Mechanics of Concrete Structures, Proceedings FRAMCOS-3,*

Aedificatio Publishers, D-79104 Freiburg, Germany (1998), 111-120.

[29] Carol, I., López, C.M., Roa, O. Micromechanical analysis of quasi-brittle materials using fracture-based interface elements. *International Journal for Numerical Methods in Engineering* 52 (2001), 193-215.

[30] Carpinteri, A. Decrease of apparent tensile and bending strength with specimen size: two different explanations based on fracture mechanics. *International Journal of Solids Structures* 25(4) (1989), 407-29.

[31] Carpintieri, A., Ferro, G. Size effect on tensile fracture properties: a unified explanation based on disorder and fractuality of concrete microstructure. *Materials and Structures* 27 (1994), 563-571.

[32] Carpintieri, A., Chiaia, B., Ferro, G. Size effects on nominal tensile strength of concrete structures: multifractality of material ligaments and dimensional transition from order to disorder. *Materials and Structures* 2 (1995), 311-317.

[33] Carpintieri, A., Ferro, G. Anomalous and irregular mechanical behavior in heterogeneous materials: snap-back instabilities and fractal cracking. *Journal of Mechanical Behavior of Materials* 11 (2000), 23-29.

[34] Carpintieri, C., Carmona, JR, Ventura, G. Failure Mode Transitions in Reinforced Concrete Beams Part 2: Experimental Tests. *ACI Structural Journal* 108 (2011), 286-293

[35] Chen, W. Yi, W., Hwang, H.J. Cracking strut-and-tie model for shear strength evaluation of reinforced concrete deep beams. *Engineering Structures* 163 (2018), 396-408

[36] Chen, W. & Konietzky, H. Simulation of heterogeneity, creep, damage and lifetime for loaded brittle rocks. *Tectonophysics* 633 (2014), 164-175.

[37] Cho, N., Martin, C.D., Sego, D.C. A clumped particle model for rock. *International Journal of Rock Mechanics & Mining Sciences* 44 (2007), 997–1010.

[38] Cundall, P.A., Hart, R.D. Numerical modelling of discontinue. *Engineering Computations* 9(2) (1992), 101-113.

[39] Cundall, P., Strack, O.D.L. A discrete numerical model for granular assemblies. *Geotechnique* 29 (1979), 47–65.

[40] Cusatis, G., Bažant, ZP, Cedolini, L. Confinement–shear lattice model for concrete damage in tension and compression: I. Theory. *ASCE Journal of Engineering Mechanics* (2003), 1439–1448.

[41] Cusatis, G., Bažant, Z., Cedolin, I. Confinement-shear lattice CSL model for fracture propagation in concrete. *Computer Methods in Applied Mechanics and Engineering* 195(52) (2006), 7154-7171.

[42] de Borst, R., Pamin, J., Geers, M. On coupled gradient-dependent plasticity and damage theories with a view to localization analysis. *European Journal of Mechanics A/Solids* 18(6) (1999),

939–962.

[43] Dempsey, J.P., Adamson, R.M., Mulmule, S.V. Scale effects on the in-situ tensile strength and fracture of ice. Part II: First-year sea ice as Resolute, N.W.T. International Journal of Fracture 95(1/4) (1999), 347-366.

[44] di Prisco, M., Mazars, J. Crush-crack: a non-local damage model for concrete. *Mechanics of Cohesive–Frictional Materials* 1(4) (1996), 321–347.

[45] Donze, F.V., Magnier, S.A., Daudeville, L. et al. Numerical study of compressive behaviour of concrete at high strain rates. *Journal for Engineering Mechanics* 122(80) (1999), 1154-1163.

[46] Dragon, A., Mróz, Z. A continuum model for plastic–brittle behaviour of rock and concrete. *International Journal for Engineering Science* 17(2) (1979), 121–137.

[47] Duan, K. & Hu, Z. Specimen boundary induced size effect on quasi-brittle fracture. *Strength Fracture and Complexity* 2(2) (2004), 47-68.

[48] Dupray, F., Malecot, Y., Daudeville, L., et al. Mesoscopic model for the behaviour of concrete under high confinement. *International Journal for Numerical and Analytical Methods in Geomechanics* 33 (2009), 1407-1423.

[49] Eliâŝ, J. and Stang, H. Lattice modeling of aggregate interlocking in concrete. *International Journal Fracture* 175 (2012), 1-11.

[50] Elices, M., Guinear, G.V., Planas, J. Measurment of the fracture energz using three point bending testŁ Part 3 – influence of cutting the p-δ tail. *Materials and Structures* 25 (1992), 327-334

[51] Ergenzinger, C., Seifried, R., Eberhard, P.A. Discrete element model to describe failure of strong rock in uniaxial compression. *Granular Matter* 12(4) (2011), 341-364.

[52] Elsharief, A., Cohen, MD., Olek, J. Influence of aggregate size, water cement ratio and age on the microstructure of the interfacial transition zone. *Cement and Concrete Research* 33 (2003), 1837–1849.

[53] Ferrara, L., Gettu, R. Size effect in splitting tests on plain and steel fiber-reinforced concrete: a non-local damage analysis. P*roceedings of 4th International Conference on Fracture Mechanics of Concrete and Concrete Structures*, Cachan, France 1 (2001), 677-684.

[54] Ferro, G. Effecti di scalla sulla resistenza a tratzione de materiali. PhD thesis. 1994. Politecnico di Torino

[55] Fleissner, F., Gaugele, T., Eberhard, P. Applications of the discrete element method in mechanical engineering. *Multibody Syst Dyn* 18 (2007), 81–94.

[56] Frantziskonis, G.N. Stochastic modeling of heterogeneous materials – a process for the analysis and evaluation of alternative formulations. Mechanics of Materials 27 (1998), 165-175.

[57] Gitman, I.M., Askes, H.. and Sluys, L.J. Coupled-volume multi-scale modelling of quasi-brittle

material. *European Journal of Mechanics Solids* 27 (2008), 302-327.

[58] Grassl, P., Bažant, ZP, Random lattice-particle simulation of statistical size effect in quasi-brittle structures failing at crack initiation. *Journal of Engineering Mechanics* 135 (2) (2009), 85-92.

[59] Groh, U., Konietzky, H., Walter, K., et al. Damage simulation of brittle heterogeneous materials at the grain size level. *Theoretical and Applied Fracture Mechanics* 55 (2011), 31-38.

[60] Grondin, F., Matallah, M. How to consider the Interfacial Transition Zones in the finite element modelling of concrete? *Cement and Concrete Research* 58 (2014), 67–75

[61] Gutierrez, M.A., de Borst, R. Energy dissipation, internal length scale and localization patterning – a probabilistic approach. *Computational Mechanics* (S. Idelsohn, E. Onate, E. Dvorkin, eds,), CIMNE, Barcelona, (1998) 1-9.

[62] Gutierrez, M.A. Size sensitivity for the reliability index in stochastic finite element analysis of damage. *International Journal of Fracture* 137 (1-4) (2006), 109-120.

[63] Hasegawa, T., Shioya, T., Okada, T. Size effect on splitting tensile strength of concrete. *Proceedings of the Japan Concrete Institute, 7th Conference* (1985), 309-312.

[64] He, H. Computational modeling of particle packing in concrete. PhD Thesis, Delft University of Technology, Netherlands, 2010.

[65] He, H., Guo, Z., Stroeven, P., et al. Influence of particle packing on elastic properties of concrete. In: Proc. *First International Conference on Computational Technologies in Concrete Structures* (CTCS'09), Jeju, Korea, May 2009, 1177-1197.

[66] Hentz, S., Daudeville, L., Donze, F. Identification and validation of a Discrete Element Model for concrete. *Journal of Engineering Mechanics ASCE* 130(6) (2004), 709-719.

[67] Hillerborg A. The theoretical basis of a method to determine the fracture energy of concrete. *Materials and Structures* 18 (1976), 291-296.

[68] Hoover, C.G, Bažant, Z.P. Universal size-shape effect law based on comprehensive concrete fracture tests. *Journal of Engineering Mechanics* (2014), 473-479.

[69] Hu, X., Duan, K. Size effect and quasi-brittle fracture: The role of FPZ. *International Journal of Fracture* 154 (2008), 3–14.

[70] Hu, X., Duan, K. Mechanism behind the size effect phenomenon. *Journal of Engineering Mechanics.* 136(1) (2010), 60–68.

[71] Hu, X., Guan, J., Keating, A., Yang, S. Comparison of boundary and size effect models based on new developments. *Engineering Fracture Mechanics* 175 (2017), 146–167.

[72] Hu, X., Wittman, F. Size effect on toughness induced by crack close to free surface. *Engineering Fracture Mechanics* 65 (2000), 209–221.

[73] Jebli, M., Jamim, F., Malachanne, E., Garcia-Diaz, E., El Youssoufi M.S. Experimental characterization of mechanical properties of the cement past- aggregate interface in concrete. *EPJ Web of Conferences* 140 (2017) Powders & Grains 2017

[74] Johnson, K.L. Contact mechanics. *Cambridge University Press* (1985).

[75] Kaderova, J., Vorechovsky, M. Experimental testing of statistical size effect in civil engineering structures. *An International Journal of Science* (2013), 516-523.

[76] Kadlecek, V., Modry, S., Kadlecek, Jr. V. Size effect of test specimens on tensile splitting strength of concrete: general relation. *Materials and Structures* 35 (2002), 28-34.

[77] Kani, G. N. J. How safe are our large concrete beams? *ACI Journal Proceedings* 64(3) (1967), 128-42.

[78] Ketterhagen, W.R.,Ende, M.T., Hancock, B.T. Process Modeling in the Pharmaceutical Industry using the Discrete Element Method. *Journal of Pharmaceutical Sciences* 98(2) (2009), 442-470.

[79] Kim, JK, Park, YD. Shear strength of reinforced high-strength concrete beams without web reinforcement. *Mag Concr Res* 46(166) (1994), 7–16.

[80] Klisiński, M., Mróz, Z. Description of inelastic deformation and degradation for concrete. *International Journal of Solids and Structures* 24(4) (1988), 391–416.

[81] Koide, H., Akita, H., Tomon, M. Probability model of flexural resistance on different length of concrete beams. Proc., 8th Int., Conf. on Application of Safety and Probability, Balkema, Rotterdam, The Netherlands 8(2) (1999), 1053-1058.

[82] Kosteski, L., Iturroz, I., Batista R.G., Cisilino, A.P. The truss-like discrete element method in fracture and damage mechanics. *Engineering Computations* 28(6) (2011), 765-787

[83] Königsberger, M., Pichler, B., Hellmich, Ch. Micromechanics of ITZ-aggregate interaction in concrete Part II: strength upscaling. *Journal of American Ceramic Society* 97 (2014), 543-551.

[84] Königsberger, M., Hlobil, M., Delsaute, B., Staquet S., Hellmich, C., Pichler, B. Hydrate failure in ITZ governs concrete strength: A micro-to-macro validated engineering mechanics model. *Cement and Concrete Research* 103 (2018), 77–94.

[85] Kompfner, TA. Ein finites Elementmodell für die geometrisch und physikalisch nichtlineare Berechnung von Stahlbetonschalen. *PhD Thesis* (1983), University of Stuttgard.

[86] Korol, E., Bobiński, J., Górski, J., Tejchman, J. Numerical investigations of size effects in notched and un-notched concrete beams under bending. *Computational Modelling of Concrete Structures*/ ed. eds. N. Bićanić, R. de Borst, [et al.]. London: Taylor & Francis Group (2010), 729-736

[87] Korol, E., Tejchman, J., Mróz, Z. FE calculations of a deterministic and statistical size effect in

concrete under bending within stochastic elasto-plasticity and non-local softening, *Engineering Structures* 48 (2013) 205-219.

[88] Korol, E. & Tejchman, J. Experimental investigations of size effect in reinforced concrete beams failing by shear. *Engineering Structures* 58 (2014a) 63–78.

[89] Korol, E., Tejchman, J., Mróz, Z. FE analysis of size effects in reinforced concrete beams without shear reinforcement based on stochastic elasto-plasticity with non-local softening. *Finite Elements in Analysis and Design* 88 (2014b), 25-41.

[90] Korol, E., Tejchman, J., Mróz, Z. The effect of correlation length and material coefficient of variation on coupled energetic-statistical size effect in concrete beams under bending. *Engineering Structures* 103 (2015), 239-259.

[91] Kozicki, J. Application of Discrete Models to Describe the Fracture Process in Brittle Materials. *PhD Thesis*, (2007), Gdańsk University of Technology.

[92] Kozicki, J., Donze, F.V. A new open-source software developer for numerical simulations using discrete modeling methods. *Computer Methods in Applied Mechanics and Engineering* 197 (2008a), 4429-4443.

[93] Kozicki, J., Tejchman, J. Modelling of fracture processes in concrete using a novel lattice model. *Granular Matter* 10 (2008b), 377-388.

[94] Kozicki, J., Tejchman, J., Mróz, Z. Effect of grain roughness on strength, volume changes, elastic and dissipated energies during quasi-static homogeneous triaxial compression using DEM. *Granular Matter* 14(4) (2012), 457–468.

[95] Kozicki, J., Niedostatkiewicz, M., Tejchman, K., Műhlhaus, H.B. Discrete modelling results of a direct shear test for granular materials versus FE results. *Granular Matter* 15(5) (2013), 607-627.

[96] Kozicki, J., Tejchman, J., Műhlhaus, H.B. Discrete simulations of a triaxial compression test for sand by DEM. *International Journal of Numerical Analysis Methods in Geomechanics*. 38(2014), 1923-1952.

[97] Kozicki, J., Tejchman, J. Investigations of quasi–static vortex structures in 2D sand specimen under passive earth pressure conditions based on DEM and Helmholtz-Hodge vector field decomposition. *Granular Matter*19(31) (2017)

[98] Kozicki, J., Tejchman, J. Relationship between vortex structures and shear localization in 3D granular specimens based on combined DEM and Helmholtz–Hodge decomposition. *Granular Matter* 20(48) (2018).

[99] Kuwabara, G., Kono, K. Restitution coefficient in a collision between two spheres. *Japan Journal of Applied Physics* 26 (1987), 1230–1233.

[100] Kuorkoulis, Ch.F. Markides, P.E. Chatzistergos. The standarized Brazilian disc test as

a contact problem. International Journal of Rock Mechanics & Mining Sciences 57 (2013a) 132–141.

[101] Kuorkoulis, S. K., Markides, Ch.F., Bakalis, G. Smooth elastic contact of cylinders be caustics: the contact length in the Brazilian disc test. *Archives of Mechanics* 65 (4) (2013b), 313–338.

[102] Lamond, J.F. Significance of tests and properties of concrete and concrete-making materials. *ASTM International*, Pielert (eds.), Barr Harbour Drive, 2006.

[103] Laubie, H., Monfared, S., Radjai, F., Pellenq, R. Ulm, F.J. Disorder-induced stiffness degradation of hoghly disordered porous materials. *Journal of the Mechanics and Physics of Solids* 000 (2017a), 1-22.

[104] Laubie, H., Radjai, F., Pellenq, R. Ulm, F.J. A potential-of-mean-force approach for fracture mechanics of heterogeneous materials using the lattice element method. *Journal of the Mechanics and Physics of Solids* 105 (2017b), 116-130.

[105] Laubie, H., Radjai, F., Pellenq, R. Ulm, F.J. Stress transmission and failure in disordered porous media. *Physical Review Letters*. 119 (2017c).

[106] Le Bellego, C., Gérard, B., Pijaudier-Cabot, G. Chemomechanical effects in mortar beams subjected to water hydrolysis. *Journal of Engineering Mechanics ASCE* 126 (2000), 266–272.

[107] Lilliu, G., van Mier J.G.M. 3D lattice type fracture model for concrete. *Engineering Fracture Mechanics* 70 (2003) ,927-941.

[108] Liu, TCY., Nilson, H., Slate, FO. Biaxial stress–strain relations for concrete. *ASCE Journal of the Structural Division* 98(5) (1972), 1025–1034.

[109] Love, A.E.H. A Treatise of Mathematical Theory of Elasticity. (1927) Cambridge University Press, Cambridge.

[110] Lubell, A, Sherwood, T., Bentz, E., Collins, M. Safe shear design of large, wide beams. *Concrete International* 26(1) (2004) 66-78.

[111] Lunding, S. Introduction to Discrete Element Methods. *EJECE Discrete modelling of geomaterials* 12 (2008).

[112] McNamara, S., Young, W. R. Inelastic collapse in two dimensions. *Phys. Rev. E*, 50(1) (1994), R28-R31.

[113] Mahabadi, O.K., Cottrell, B.E., Grasselli, G. An example of realistic modelling of rock dynamics problems: FEM/DEM simulation of dynamic Brazilian test on Barre granite, *Rock Mech Rock Eng* 43 (2010), 707-716.

[114] Marquard, D.W. An algorithm for Least-Squares estimation of nonlinear parameters. *Journal of the Society for Industrial and Applied Mathematics* 11(2), (1963), 431-441.

[115] Marzec, I., Bobiński, J., Tejchman, J. Simulations of spacing of localized zones in reinforced concrete beams using elasto–plasticity and damage mechanics with non–local softening. *Computers and Concrete* 4(4) (2007), 377–403.

[116] Marzec, I., Tejchman, J. Enhanced coupled elasto-plastic-damage models to describe concrete behaviour in cyclic laboratory tests: Comparison and improvement. *Archives of Mechanics* 64 (2012), 227-259.

[117] Marzec, I., Skarżynski, L., Bobiński J., Tejchman J. Modelling of reinforced concrete beams under mixed shear-tension failure with different continuous FE approaches. *Computers and Concrete* 12(4) (2013), 377-392.

[118] Marzec, I., Tejchman, J., Mróz, Z. Numerical analysis of size effect in RC beams scaleń along height Or length Rusing elasto-plastic-damage model enhanced by non-local softening. *Finite Elements in Analysis and Design* 157 (2019), 1-20.

[119] Miguel, L.F.F., Riera, J.D., Iturrioz, I., Aráoz, G.F. Influence of the width of the loading strip in the Brazilian tensile test of concrete and other brittle materials, *Journal of Materials in Civil Engineering* 28(11), (2016).

[120] Mondal, P., Shah, S.P., Marks, L.D. Nanomechanical properties of interfacial transition zone in concrete. *Nanotechnology in Construction* 3 (2009), 315-320.

[121] Mróz, Z. Mathematical models of inelastic concrete behavior. University Waterloo Press (1973).

[122] Nitka, M., Tejchman, J. Modelling of concrete behaviour in uniaxial compression and tension with DEM. *Granular Matter* 17(1) (2015), 145-164.

[123] Nosewicz, S., Rojek, J., Pietrzak, K., Chmielewski, M. Viscoelastic discrete element model of powder sintering. *Powder Technology* 246, (2013) 157-168.

[124] Nosewicz, S., Rojek, J., Chmielewski, M., Pietrzak, K. Discrete Element Modeling of Intermetallic Matrix Composite Manufacturing by Powder Metallurgy. *Materials* 12, 281 (2019) 1-22.

[125] Ollivier, JP., Maso, JC., Bourdette, B. Interfacial Transition Zone in Concrete. *Advanced Cement Based Materials* 2(1995), 30-38.

[126] Pamin, J., de Borst, R. Simulation of crack spacing using a reinforced concrete model with an integral length parameter. *Archive of Applied Mechanics* 68 (1998), 613-625.

[127] Pamin, J. *Gradient-enhanced continuum models: formulation, discretization and applications.* Habilitation monograph, Cracow University of Technology, Poland (2004).

[128] Peterson, P. Crack growth and development of fracture in plain concrete and similar materials, Report TVBM-1006 (1981), Div of Bldg Mat, Lund IT, Lund Sweden.

[129] Petersen F., Ulm FJ. Phase-field modeling of cement paste: Where particle physics meets continuum mechanics. *Computational Modelling of Concrete Structures EURO-C*. Bad Hofgastein, February 26 – March 1, 2018 ed. G. Meschke, B. Pichler and JG Rots.

[130] Pietruszczak S., Jiang, J., Miraza, F. A. An elastoplastic constitutive model for concrete. *International Journal for Solids and Structures* 24(7) (1988), 705–722.

[131] Podgorniak-Stanik, BA. The influence of concrete strength, distribution of longitudinal reinforcement, amount of transverse reinforcement and member size on shear strength of reinforced concrete members. MSc thesis. Toronto (CA): University of Toronto; 1998.

[132] Poinard, C., Piotrowska, E., Marin, P., Malecont, Y., Daudeville, L. Mesoscopic scale modeling of concrete under triaxial loading using X-ray tomographic images. II International Conference on Particle-based Methods – Fundamentals and Applications PARTICLES 2011 E. Oñate and D.R.J. Owen (Eds).

[133] Proudhon, H. Using X-ray micro-tomography to probe microstructure and damage of structural materials. WEMESURF contact course (2010).

[134] Reineck et al., KH, Kuchma, D, Kim KA, Marx, S. Shear database for reinforced concrete members without shear reinforcement. *ACI Structural Journal* 100(2) (2003).

[135] Ren, W., Yang. Z., Sharma, R. el al. Two-dimensional X-ray CT image based meso-scale fracture modelling of concrete. *Engineering Fracture Mechanics* 133 (2015), 24-39.

[136] Rechenmacher, A.L., Finno, R.J. Digital image correlation to evaluate shear banding in dilative sands. *Geotechnical Testing Journal* 27(1) (2004), 13-22.

[137] Rocco, CG. Influencia del tamano y mecanismos de rotura del ensayo de compresiondiametral. PhD thesis (1995). Dep. Cicnia de materials, Univesidad Politecnica de Madrid, ETS de Ingenieros de Caminos, Ciudad Universitatria, 28040 Madrid, Spain.

[138] Rocco, C., Guinea, G.V., Planas, J., Elices, M. Size effect and boundary conditions in the Brazilian test: Experimental verification. *Materials and Structures* 32 (1999), 210-217.

[139] Rocco, C., Guine, GV., Planas, J., Elices, M. Review of the splitting-test standards from a fracture mechanics point of view. *Cement and Concrete Research* 31 (2001), 73-82.

[140] https://rocky.esss.co/index.php?pg=particle_shapes

[141] Rojek, J., Zubelewicz, A., Madan, N., Nosewicz, S. The discrete element method with deformable particles. *Int J Numer Methods Eng*. 114 (2018), 828–860.

[142] Ruiz, G., Ortiz, M., Pandolfi, A. Three-dimensional finite-element simulation of the dynamic Brazilian tests on concrete cylinders, *Int. J. Numer. Meth. Engng*. 48 (2000), 963-994.

[143] Saksala, T. M., Hokka, A., Kuokkala, V.T., Makinen, J. Numerical modeling and experimentation of dynamic Brazilian disc test on Kuru granite. *International Journal of Rock*

Mechanics & Mining Sciences 59 (2013), 128–138.

[144] Salami, Y., Dano, C., Hicher, P., Colombo, G., Denain, P. The effects of the coordination on the fragmentation of a single grain. *IOP Conference Series: Earth and Environmental Science* 26(1) (2015).

[145] Sato, Y., Tadokoro, T., Ueda, T. Diagonal Tensile Failure Mechanism of Reinforced Concrete Beams. *J. Adv. Concr. Technol.*2(3) (2004), 327-341.

[146] Scholtès, L. and Donzé, F.V. A DEM model for soft and hard rocks: Role of grain interlocking on strength. *Journal of the Mechanics and Physics of Solids* 61(2) (2013), 352-369.

[147] Schlangen, E., Garboczi, E.J. Fracture simulations of concrete using lattice models: computational aspects. *Engineering Fracture Mechanics* 57 (1997), 319–332.

[148] Scrivener, K.L., Nemati, K.M. The percolation of pore space in the cement paste/aggregate interfacial zone of concrete. *Cement and Concrete Research* 26(1) (1996), 35-40.

[149] Scrivener, K.L., Crumbie, A.K.. and Laugesen, P. The interfacial transition zone (ITZ) between cement paste and aggregate in concrete. *Interface Science* 12 (2004), 411-421.

[150] Shioya, T., Iguro, M., Nojiri, Y., Akiyama, H., Okada, T. Shear strength of large reinforced concrete beams. *ACI SP* 118 (1989), 259-279.

[151] Simo, J.C., Ju, J. Strain- and stress-based continuum damage models-I formulation. *International Journal for Solids and Structures* 23 (7) (1987), 821-840.

[152] Skarżyński, Ł. and Tejchman, J. Calculations of fracture process zones on meso-scale in notched concrete beams subjected to three-point bending. *European Journal of Mechanics Solids* 29(4) (2010), 746-760.

[153] Skarżyński, Ł., Korol, E., Tejchman, J. Measurements and calculations of the width of the fracture process zones on the surface of notched concrete beams. *Journal of Strain Analysis for Engineering Design*. 47(1) (2011), 319-332.

[154] Skarżyński, Ł., Tejchman, J. Experimental investigations of fracture process in plain and reinforced concrete beams under bending. *Strain* 49 (2013a), 521-543.

[155] Skarżyński, Ł., Tejchman, J. Modelling the effect of composition on the tensile properties of concrete. *Understanding the tensile properties of concrete* (edited by Jaap Weerheijm). London: Woodhead Publishing Limited, 2013b, pp. 52-97.

[156] Skarżyński, Ł., Nitka, M., Tejchman, J. Modelling of concrete fracture at aggregate level using FEM and DEM based on x-ray μCT images of internal structure. *Engineering Fracture Mechanics* 10(147) (2015), 13-35.

[157] Skarzyński, Ł., Tejchman, J. Experimental investigations of fracture process in concrete by means of x-ray micro-computed tomography. *Strain* 52 (2016), 26-45.

[158] Skarżyński, L., Marzec, I., Tejchman, J. Fracture evolution in concrete compressive fatigue experiments based on X-ray micro-CT images. *International Journal of Fatigue* 122 (2019), 256–272.

[159] Słomiński, C., Niedostatkiewicz, M., Tejchman, J. Application of particle image velocimetry (PIV) for deformation measurement during granular silo flow. *Powder Technology* 173(1) (2007), 1-18.

[160] Šmilauer et al. Dem formulation. In Yade Documentation 2nd ed. The Yade Project , DOI 10.5281/zenodo.34044 (2015).

[161] Suchorzewski, J., Tejchman, J., Nitka, M. DEM simulations of fracture in concrete under uniaxial compression based on its real internal structure, *International Journal of Damage Mechanics* 27(4), (2018a) 578-607.

[162] Suchorzewski, J., Tejchman, J., Nitka, M. Experimental and numerical investigations of concrete behaviour at meso-level during quasi-static splitting tension. *Theoretical and Applied Fracture Mechanics* 96, (2018b) 720-739.

[163] Suchorzewski, J., Korol, E., Tejchman, J., Mróz, Z. Experimental study of shear strength and failure mechanisms in RC beams scaled along height or length. *Engineering Structures* 157, (2018c) 203-223.

[164] Suchorzewski, J., Tejchman, J, Nitka, M., Bobinski, J. Meso-scale analyses of size effect in brittle materials using DEM. *Granular Matter* 21, 9 (2019) 1-19.

[165] Tan, KH, Lu, HY. Shear behaviour of large reinforced concrete deep beams and code comparisons. *ACI Structural Journal* 96(5) (1999), 836-845.

[166] Tan, KH, Cheng, GH, Cheong, HK. Size effect in shear strength of large beams-behaviour and finite element modelling. *Mag Concrete Res* 57(8) (2005), 497-509.

[167] Tanabe, T., Itoh, A., Ueda, N. Snapback failure analysis for large scale concrete structures and its application to shear capacity study of columns. *Journal of Advanced Concrete Technology* 2(3) (2004), 275-288.

[168] Tejchman, J., Bobiński, J. *Continuous and discontinuous modelling of fracture in concrete using FEM*. Berlin-Heidelberg: Springer (eds. W Wu and RI Borja), 2013.

[169] Timoshenko, S., Goodier, J.N. *Theory of Elasticity*. McGraw-Hill Book Company, 1977.

[170] Torrent, R.J. A general relation between tensile strength and specimen geometry for concrete - like materials. *Materials and Structures* 10 (1977), 187-196.

[171] Tran, V.T, Donze, F.V., Marin, P. Discrete element model of concrete under high confining pressure. *Fracture Mechanics of Concrete and Concrete Structures -Recent Advances in Fracture Mechanics of Concrete* B.H. Oh, et al.(eds) (2010) Korea Concrete Institute, Seoul.

[172] Tran, V.T., Donzé, F.V., Marin, P. A discrete element model of concrete under high triaxial loading. *Cement and Concrete Compoitess* 33 (2011) 936– 948.

[173] van Vliet, M.R.A., van Mier, J.G.M. Experimental investigation of size effect in concrete and sandstone under uniaxial tension. *Engineering Fracture Mechanics* 65 (2000), 165-188.

[174] van Vliet, MRA. Size effect in tensile fracture of concrete and rock. *PhD Thesis*, Delft University of Technology, Netherlands, 2000.

[175] van Mier, J.G.M. Multiaxial strain-softening of concrete. Part I: Fracture. *Materiaux et Constructions* 19 (1986), 111.

[176] van Mier, JGM et al. Strain-softening of concrete in uniaxial compression. *Materials and Structures* 30 (1997), 195-209.

[177] Vorechovsky, M. Interplay of size effects in concrete specimens under tension studied via computational stochastic fracture mechanics. *International Journal of Solids and Structures* 44 (2007), 2715–2731.

[178] Walraven, JC. The Influence of Depth on the Shear Strength of Lightweight Concrete Beams without Shear Reinforcement. Stevin Laboratory Report No.5-78-4, Delft University of Technology, 36 (1978).

[179] Walraven, J.C. Fundamental analysis of aggregate interlock. *J. Struct. Div*. 107(11) (1981), 2245-2270.

[180] Walraven, J., Lehwalter, N. Size effects in short beams loaded in shear. *ACI Structural Journal* 91(5) (1994), 585–593.

[181] Walsh, PF. Fracture of plain concrete. *Indian Concrete Journal* 46(11) (1972).

[182] Walton, OR, Braun, RL. Viscosity, granular temperature, and stress calculations for shearing assemblies of inelastic, frictional disks. *Journal of Rheology* 30 (1986), 949–980.

[183] Wang, XH., Jacobsen, S., He, JY., Zhang, ZL., Lee, SF., Lein, HL. Application of nanoindentation testing to study of the interfacial transition zone in steel fiber reinforced mortar. *Cement and Concrete Research* 39 (2009), 701–715.

[184] Wang, YS, Hu, XZ, Li, L, Zhu, WC. Determination of tensile strength and fracture toughness of concrete using notched 3-p-b specimens. *Engineering Fracture Mechanics* 160 (2016), 67–77.

[185] Wei, X. X., Chau, K. T. Three dimensional analytical solution for finite circular cylinders subjected to indirect tensile test. *International Journal of Solids and Structures* 50(14) (2013), 2395–2406.

[186] Weibull, W. A statistical theory of the strength of materials. *Proc. Roy. Swedish Inst. Eng. Res*. 151:1 (1939).

[187] Weibull, W. A statistical distribution function of wide applicability. *Journal of Applied Mechanics* 18(9) (1951), 293-297.

[188] Widulinski, L., Tejchman, J., Kozicki, J., Leśniewska, D. Discrete simulations of shear zone patterning in sand in earth pressure problems of a retaining wall. *International Journal of Solids and Structures* 48(7-8) (2011), 1191-1209.

[189] Wittman, F., Sadouki, H., Steiger, T. Siye effect on fracture energz of concrete. Engineering Fracture Mechanics, 35 (1990), 107-115.

[190] Wu, S., Ma, J., Cheng, Y., Xu, M., Hunag, X. Numerical Analysis of the Flattened Brazilian Test: Failure Process, Recommended Geometric Parameters and Loading Conditions. *Acta Geotecnica.* (in press)

[191] Wright, PJF. The effect of the method of test on the flexural strength of concrete. *Magazine of Concrete Research* 11 (1952), 67-76.

[192] Xiao, J., Wengui, L., Zhihui, S. et al. Properties of interfacial transition zones in recycled aggregate concrete tested by nanoindentation. *Cement & Concrete Composites* 37 (2013), 276-292.

[193] Yang, KH, Chung, HS, Eun, HC. Shear characteristics of high-strength concrete deep beams without shear reinforcements. *Engineering Struc*tures 25(10) (2003), 1343-1352.

[194] Yang, Z. Hu, X.F. A heterogeneous cohesive model for quasi-brittle materials considering spatially varying random fracture properties. Computer Methods in Applied Mechanics and Engineering 197 (45-48) (2008), 4027-4039.

[195] Yoshida, Y. Shear reinforcement for large lightly reinforced concrete members. MSc thesis. Toronto (CA): University of Toronto; 2000.

[196] Yu, Q., Le, JL., Hoover, CG., Bažant ZP. Problems with Hu-Duan Boundary Effect Model and Its Comparison to Size-Shape Effect Law for Quasi-Brittle Fracture. *Journal of Engineering Mechanics* 6 (2010) 40-50.

[197] Zhang, N., Tan, KH. Direct strut-and-tie model for single span and continuous deep beams. *Engineering Structures* 29 (2007a), 2987-3001.

[198] Zhang, N., Tan, KH. Size effect in RC deep beams: Experimental investigation and STM verification. *Engineering Structures* 29 (2007b), 3241–3254.

[199] Zhu, W.C., Tang, C.A. Numerical simulation of Brazilian disk rock failure under static and dynamic loading, *Int J Rock Mech Min Sci* 43 (2006), 236-252.

[200] EN12390-6:2000 – European standard Testing hardened concrete Part 6: Tensile splitting strength of test specimens, European Committee for Standardization, 2000.

[201] ASTM, Standard Test Method for Splitting Tensile Strength of Cylindrical Concrete Specimens, C496M-04, 2004.

[202] EN 1992-1-1 (2008): Design of concrete structures: Part 1-1: General rules and rules for buildings.

[203] EN 12390-1 (2012): Testing of hardened concrete: Part 1: Shape, dimensions and other requirements of specimens and moulds

[204] ACI 318-14: Building code requirements for structural concrete, American Concrete Institute, 2014

[205] ACI 224R-01: Control of cracking in concrete structures, American Concrete Institute, 2001

[206] ACI 435R-95: Control of deflection in concrete structures, American Concrete Institute, 2000

[207] BS 8110-1:1997: Structural use of concrete. Code of practice for design and construction, 1997

[208] Code of practise of structural use of concrete. Building Department, Hong-Kong, 2013

Acknowledgments

The research performed in this thesis has been carried out within the project "*Experimental and numerical analysis of coupled deterministic-statistical size effect in brittle materials*" financed by the Polish National Science Centre NCN (UMO-2013/09/B/ST8/03598).

I would like to express my sincere gratitude to my supervisor prof. J. Tejchman for his guidance, help and support throughout four years of my research works. I thank him for both constant encouragements in numerical calculations and laboratory experiments and fruitful and interesting discussions.

I would like to thank all my colleagues and friends from the Gdańsk University of Technology (Chair of Building Structures and Material Engineering). First of all, I thank dr Michał Nitka for his patience in introducing me into programming and a discrete element method and dr Ewelina Korol for guiding me in performing large scale experiments. I am also very grateful to dr Łukasz Skarżyński for sharing his time and knowledge with respect to micro-CT, to dr hab. Jerzy Bobiński, dr hab. Michał Wójcik and dr Ireneusz Marzec for advising me in theoretical and practical issues of building structures. I would like to thank Eugeniusz Grześ for preparing concrete specimens and experimental setups for my research works. Finally, I would like to express my acknowledgements to my roommate dr Jarosław Florczuk for his support, advice and help.

I wish to express my gratitude to my parents for their inexpressible and unconditional support. Last but certainly not least, I deeply thank my wife Marta for her devoted participation in my research life, help, understanding and patience.

List of own publications

Publications from the list of the JCR database

[1] **Suchorzewski, J**., Nitka, M., Tejchman, J. Discrete element method simulations of fracture in concrete under uniaxial compression based on its real internal structure. *International Journal of Damage Mechanics,* 27(4), 578-607, 2018 (35 pkt. na liście ministerstwa).

[2] **Suchorzewski, J.,** Nitka, M., Tejchman, J. Experimental and numerical investigations of concrete behaviour at meso-level during quasi-static splitting tension. *Theoretical and Applied Fracture Mechanics*, 96 720-739, 2018 (30 pkt. na liście ministerstwa).

[3] **Suchorzewski, J.,** Kolor, E., Tejchman, J., Mróz, Z. Experimental study of shear strength and failure mechanisms in RC beams scaled along height or length. *Engineering Structures*, 157, 203-223, 2018 (40 pkt. na liście ministerstwa).

[4] Skarżyński, Ł., **Suchorzewski, J.** Mechanical and fracture properties of concrete reinforced with recycled and industrial steel fibers using Digital Image Correlation technique and X-ray micro computed tomography. *Construction and Building Materials,* 183, 283-299, 2018 (40 pkt. na liście ministerstwa).

[5] **Suchorzewski, J.,** Tejchman, J., Nitka, M., Bobiński, J. Meso-scale analyses of size effect in brittle materials using DEM. *Grannular Matter,* 21, 1-19, 2019. (30 pkt. na liście ministerstwa).

[6] Korol, E., **Suchorzewski, J.,** Tejchman, J., Mróz, Z. Experimental investigations of shear strength and failure mechanisms in RC beams with stirrups scaled along height or length. *Engineering Structures* (in review), 2019. (40 pkt. na liście ministerstwa).

Conference proceedings from the list of the Web of Science database

[1] **Suchorzewski, J**., Tejchman, J. Experimental and numerical investigations of concrete behavior at meso-level during quasi-static splitting tension. *V International Conference on particle-based methods. Fundamentals and Applications PARTICLES 2017*. Hanover, Germany, September 26-28, 2017. ed. P. Wriggers, M. Bischoff , E. Oñate, D.R.J. Owen and T. Zohdi

[2] **Suchorzewski, J**., Tejchman, J. Size effect in concrete under splitting tension. *Computational Modelling of Concrete Structures EURO-C*. Bad Hofgastein, February 26 – March 1, 2018 ed. G. Meschke, B. Pichler and JG Rots.

[3] **Suchorzewski, J.,** Marzec, I., Korol, E., Tejchman, J. Investigations on strength and fracture in RC beams scaled along height or length. *Computational Modelling of Concrete Structures EURO-C*. Bad Hofgastein, February 26 - March 1, 2018 ed. G. Meschke, B. Pichler and JG Rots.

Other peer-reviewed publications

[1] **Suchorzewski, J.,** Nitka, M., Tejchman, J. Modelowanie jednoosiowego rozciągania i ściskania betonu na poziomie kruszywa. *Przegląd Budowlany* 11 22-26, 2015.

[2] Korol, E., Ostaszewska, M., **Suchorzewski, J.,** Tejchman J. Wyniki doświadczeń nad efektem skali w belkach betonowych ze zbrojeniem bazaltowym. *Inżynieria i Budownictwo* 1, 44-46, 2016.